Topics in Viscous Potential Flow of Two-Phase Systems

A DISSERTATION
SUBMITTED TO THE FACULTY OF THE GRADUATE SCHOOL
OF THE UNIVERSITY OF MINNESOTA
BY

Juan Carlos Padrino Inciarte

IN PARTIAL FULFILLMENT OF THE REQUIREMENTS
FOR THE DEGREE OF
DOCTOR OF PHILOSOPHY

Daniel D. Joseph, Advisor

February 2010

Acknowledgments

I am thankful to the Creator, the Source of all wisdom and knowledge for giving me the eagerness to learn, to grasp the simple beauty of Nature. He has calmed my anxiety, and granted me the resources, patience and humility needed to face the challenges inherent to this journey of discovery.

I want to express my deepest gratitude to my advisor, Prof. Daniel D. Joseph. During times of unexpected, drastic changes in my life Prof. Joseph had the willingness to put me under his guidance and support my studies. His profound knowledge in the field of fluid mechanics and applied mathematics as well as scientific expertise have been of great benefit to my education and have influenced my research throughout. He has brought to my attention attractive projects that entail innovative ideas. He has encouraged me to show my work and accomplishments in research without being pedantic. He has set example of persistence and confidence while navigating the turbulent waters of scientific publishing, even in the face of tough criticism. I am the most grateful for the confidence he has shown in my skills, the level of freedom he has gave me to conduct my research, the respect for my stances on scientific matters, and the opportunities to stand and talk about my research in front of an audience.

I am grateful to the rest of my thesis committee: Prof. Ellen Longmire, Prof. Krishnan Mahesh and Prof. Peter Olver. I had the privilege of attending classes on theoretical and computational fluid mechanics brilliantly taught by Dr. Longmire and Dr. Mahesh. I was fortunate to have Dr. Olver as instructor in the courses of partial differential equations, where, with mastery on the subject, I was introduced to methods of applied mathematics useful for my research. I thank them for serving as members of my thesis committee. I am also indebted to Prof. Jian Sheng, who kindly accepted to be part of the jury for my final defense. I extend my gratitude to the University of Minnesota, Twin Cities, in particular, to the department of Aerospace Engineering and Mechanics, for providing world class instruction, and also spaces and resources to conduct my academic endeavors in an environment where the highest standards of scholastic honesty and integrity are demanded and encouraged.

Special thanks to my former and current office-mates and fellow graduate students, Dr. Todd Hesla, Dr. Jing Wang, Dr. Haoping Yang and Flavia Viana. They set examples not only of hard work, but also of discipline, serenity, patience, team work and good humor. Dr. Hesla, a thoughtful mathematician, fluid mechanician and teacher, has always been open

to motivating discussions and to take my questions with genuine interest. His suggestions are always very useful. I was lucky to come along with Dr. Wang when he was finishing his doctoral degree. We collaborated in various projects and I very much benefited from our talks and his various publications on the subject of potential flow of viscous fluids. I also have great appreciation for the visiting scholars that came to work with Prof. Joseph while I have been in his group: Prof. Toshio Funada of Numazu College of Technology, Japan, and Dr. Hyungjun Kim, an alumnus of KAIST in South Korea, with whom I have cooperated in different projects and have had the opportunity to publish research articles. I acknowledge enlightening discussions with Prof. William A. Sirignano of the University of California, Irvine, who has been the host of the visits that my advisor and I have made to this Institution. I also thank Prof. Eph Sparrow and Mr. Dave Hultman of the University of Minnesota for their kind cooperation in the design, construction and testing of a device to carry out experiments on heat transfer through fluids with nanoparticles.

I would like to say "Thank you" to Dr. Shankar Ghosh, a good friend and former graduate student in this department, who came to this program at the same time I did. He has been kindly helpful in affairs of every-day life. Our conversations about scientific topics have been as engaging as the most frequent ones about divine and mundane matters. With heart-felt gratitude, I thank my friends Silvia Alvarez and Walter Davila, and their children, whose warmness has made me feel that I am part of their household, showing their fondness in various ways. I extend my gratitude to all my other friends and colleagues, whose names I do not mention for the sake of space.

I gratefully acknowledge the support of the National Science Foundation, through grant No 0302837. Also, I acknowledge the support of the University of Minnesota Graduate School Dissertation Fellowship, awarded for the academic year 2007-2008. Computational resources used to carry out this investigation have been provided by the Minnesota Supercomputer Institute for Advance Computational Research at the University of Minnesota; I am grateful to their Technical Support Staff, in particular to Dr. Shuxia Zhang and Dr. H. Birali Runesha, for their timely help and guidance with software housed at the Institute. I am indebted to Prof. Roger Fosdick of the University of Minnesota who brought the central idea for the proof in Appendix C. I thank Prof. David Leppinen of the University of Birmingham for his kindness in providing his code for computing quintic splines that served as basis for our own code.

I am highly indebted to my beloved parents, Norka de Padrino and Carlos Padrino, and to my brother Leonardo, whose affection has been a source of inspiration throughout my career. The values that they have instilled in me have been a guiding light in times of self-doubt. They encouraged and supported my decision to come to Minnesota to pursue graduate studies. Their help during the days of preparation for this trip was outstanding and they kindly continue running things back home with diligence. Despite the distance, I felt them close as I know they keep me in their thoughts and prayers. This dissertation is also dedicated to the memory of Olga and Amilcar, pillars of our family, who were here before us and have already departed.

To my parents and brother

Abstract

Two-phase flows are ubiquitous, from natural and domestic environments to industrial settings. However, due to their complexity, modeling these fluid systems remains a challenge from both the perspective of fundamental questions on the dynamics of an individual, smooth interface, and the perspective of integral analyses, which involve averaging of the conservation laws over large domains, thereby missing local details of the flow. In this work, we consider a set of five problems concerning the linear and non-linear dynamics of an interface or free surface and the study of cavitation inception. Analyses are carried out by assuming the fluid motion to be irrotational, that is, with zero vorticity, and the fluids to be viscous, although results from rotational analyses are presented for the purpose of comparison.

The problems considered here are the following: First, we analyze the non-linear deformation and break-up of a bubble or drop immersed in a uniaxial extensional flow of an incompressible viscous fluid. The method of viscous potential flow, in which the flow field is irrotational and viscosity enters through the balance of normal stresses at the interface, is used in the analysis. The governing equations are solved numerically to track the motion of the interface by coupling a boundary element method with a time-integration routine. When break-up occurs, the break-up time computed here is compared with results obtained elsewhere from numerical simulations of the Navier–Stokes equations, which thus keeps vorticity in the analysis, for several combinations of the relevant dimensionless parameters of the problem. For the bubble, for Weber numbers $3 \leqslant We \leqslant 6$, predictions from viscous potential flow shows good agreement with the results from the Navier–Stokes equations for the bubble break-up time, whereas for larger We, the former underpredicts the results given by the latter. Including viscosity increases the break-up time with respect to the inviscid case. For the drop, as expected, increasing the viscous effects of the irrotational motion produces large, elongated drops that take longer to break up in comparison with results for inviscid fluids. In the second problem, we compute the force acting on a spherical bubble of variable radius moving within a liquid with an

outer spherical boundary. Viscous potential flow and the dissipation method, which is another purely irrotational approach stemming from the mechanical energy equation, are both systematically implemented. This exposes the role of the choice of the outer boundary condition for the stress on the drag, an issue not explained in the literature known to us. By means of the well-known "cell-model" analysis, the results for the drag are then applied to the case of a swarm of rising bubbles having a certain void fraction. Computations from the dissipation method for the drag coefficient and rise velocity for a bubble swarm agree with numerical solutions; evaluation against experimental data for high Reynolds and low Weber numbers shows that all the models considered, including those given in the literature, overpredict the bubble swarm rise velocity. In the next two problems, we apply the analysis of viscous potential flow and the dissipation method to study the linear dynamics of waves of "small" amplitude acting either on a plane or on a spherical interface separating a liquid from a dynamically inactive fluid. It is shown that the viscous irrational theories exhibit the features of the wave dynamics by comparing with the exact solution. The range of parameters for which good agreement with the exact solution exists is presented. The general trend shows that for long waves the dissipation method results in the best approximation, whereas for short waves, even for very viscous liquids, viscous potential flow demonstrates better agreement. Finally, the problem of cavitation inception for the flow of a viscous liquid past a stationary sphere is studied by means of the theory of stress-induced cavitation. The flow field for a single phase needed in the analysis is found from three different methods, namely, the numerical solution of the Navier–Stokes equations, the irrotational motion of a viscous fluid, and, in the limit of no inertia, the Stokes flow formulation. The new predictions are then compared with those obtained from the classical pressure criterion. The main finding is that at a fixed cavitation number more viscous liquids are at greater risk to cavitation.

Table of Contents

List of Tables

List of Figures

Nomenclature

Roman symbols

a	Bubble or drop radius
A	Surface area (Ch. 3); inverse of the bubble vertical velocity variance normalized by the square of the mean bubble velocity (Ch. 3)
A, B	Parameter in the direct formulation of the boundary element method (Ch. 2)
A_c, B_c, $\tilde{A}_c$, $\tilde{B}_c$	Four order degree polynomials of parameter $m_1 = 1 - m$
A_ℓ, C_ℓ, $B_{\ell m}$	Complex constants (Ch. 5)
A_l, B_l	Real coefficients (Ch. 3)
B	Bubble
B_{ij}	Cartesian components of a second order tensor
c	Speed of traveling waves
c.c.	Complex conjugate of previous term in a given expression
c_p	Pressure coefficient
C	Generic function (Chs. 1 and 3); spline coefficients (Ch. 2)
C_D	Drag coefficient
D	Volume region (Chs. 3 and 4); axial dimension of a bubble or drop (Ch. 2); force (Ch. 3)
D_f	Deformation parameter
D_{ij}	Component of the strain-rate tensor
D_{11}, D_{22}, D_{33}	Principal strain rates
$\mathbf{D}$	Strain-rate tensor
$\tilde{\mathbf{D}}$	Dimensionless strain-rate tensor
$\mathbf{e}$	Unit vector
E	Kinetic energy
f	Generic function

$f_{\alpha,j}$	Shape function
$\mathcal{F}$	Function defining the position of the points on the interface
$F_{\ell m}$	Real constants
$F_{z'}$	Drag force
g, h	Axisymmetric kernels of the direct formulation of the boundary element method
g	Acceleration of gravity (magnitude)
$\mathbf{g}$	Acceleration of gravity (vector)
G	Fundamental solution (Ch. 2)
G_{ij}, H_{ij}	Component of squared matrices $\mathbf{G}$, $\mathbf{H}$, respectively
$\mathbf{G}$, $\mathbf{H}$	Squared matrices from the direct formulation of the boundary element method
$\mathscr{G}$	Integral of the second axisymmetric kernel, g
h_j	Spline parameter step
H	Position of outer spherical edge of computational domain (Ch. 6)
$\mathscr{H}$	Integral of the first axisymmetric kernel, h
i	Imaginary number
$\mathbf{1}$	Identity tensor
J	Jacobian (Ch. 2); squared of Ohnesorge number (Ch. 5)
k	Wavenumber
K, E	Complete elliptic integrals of the first and second kind, respectively (Ch. 2)
K	Cavitation number (Ch. 6)
K_{c}	Critical cavitation number
$\hat{l}$	Density ratio
ℓ	Spline parameter (Ch. 2); index; mode number (Ch. 5)
L	Characteristic length
m	Parameter in the direct formulation of the boundary element method
$\hat{m}$	Viscosity ratio
M	Parameter that determines the magnitude of the principal strain-rate in a uniaxial straining motion
n	Coordinate along normal direction given by $\mathbf{n}$ (Ch. 2); exponent (Ch. 3)
$\mathbf{n}$	Unit normal vector
N	Number of elements or subdivisions on a plane curve
N_p, $\tilde{N}_p$	Number of Gaussian integration points

N_R	Characteristic pressure scale
O, O'	Centers of external and internal spherical boundaries, respectively
Oh	Ohnesorge number
p	Pressure
$\hat{p}$	Pressure in the disturbed state
p_c	Cavitation threshold
P	Pressure of the basic state
P_n	Legendre polynomial of order n
$P_\ell^{\|m\|}$	Associated Legendre function of order ℓ and rank m
q	Normal derivative of the velocity potential (Ch. 2); velocity along normal direction (Ch. 3); parameter in the exact solution for a drop or bubble of small oscillations about the spherical shape (Ch. 5)
Q^J	Parameter in the exact solution for a drop or bubble of small oscillations about the spherical shape
$\mathbf{Q}$	Vector of normal derivatives of the potential, q
r, $\hat{r}$, R	Radial coordinate in a cylindrical coordinate system (Ch. 2)
r	Radial coordinate in a spherical coordinate system (Chs. 3, 5 and 6)
r	Radial position of bubble interface (Ch. 3)
r'	Radial coordinate in a cylindrical coordinate system (Ch. 6)
R	Radius of a sphere (Chs. 2 and 3)
Re	Reynolds number
s	Arc length
S	Polynomial spline (Ch. 2)
S, $\mathcal{S}$	Surface
S_ℓ	Surface harmonics of integral order
t	Time
t_b	Break-up time
$\hat{t}$	Independent variable in spline interpolation
$\mathbf{t}$	Unit vector tangential to a surface
T_{11}, T_{22}, T_{33}	Principal stresses
$\mathbf{T}$	Stress tensor
$\mathbf{u}$	Velocity vector; velocity field in the inertial reference frame (Ch. 3)

U	Velocity scale based upon surface tension (Ch. 5); bubble velocity (Ch. 3); far field velocity (Ch. 6)
$\mathcal{U}$	Velocity ratio
U_∞	Bubble velocity in the limit of infinite dilution from the dissipation method
$U_{\alpha=0}$	Bubble velocity in an unbounded medium
$\mathbf{v}$	Velocity field in the noninertial reference frame
V	Volume region (Chs. 3 and 4); velocity scale based upon surface tension and viscosity (Ch. 5)
$\mathcal{V}$	Volume region (Ch. 3)
w	Generic potential function; weight factor for Gauss quadrature
W	Power integrals
We	Weber number
We_c	Critical Weber number
x, y	Cartesian coordinates
x_s	Separation length
y	Set of ordinates (Ch. 2)
Y_ℓ^m	Spherical harmonics
$\mathbf{x}$	Position vector
z, $\hat{z}$, Z	Axial coordinate of a cylindrical coordinate system (Ch. 2)
z'	Axial coordinate of a cylindrical coordinate system (Ch. 6)

Greek symbols

α	Index (Ch. 2); void fraction (Ch. 3); effective exponent (Ch. 4); parameter in the exact solution for a drop or bubble of small oscillations about the spherical shape (Ch. 5); angle of rotation (Ch. 6)
β	Dynamic viscosity ratio (Ch. 2); angle of rotation (Ch. 6)
γ	Surface tension coefficient
Γ	Designates a plane curve (Ch. 2); boundary in three dimensions (Ch. 3)
δ_{ij}	Kronecker delta
ϵ	Radius of a "small" ball (Ch. 2); "small" radial perturbation of the spherical interface of a drop or bubble (Ch. 2); dimensionless viscosity (Ch. 5); separation between centers of spheres (Ch. 3)
ε_{ijk}	Permutation symbol
ζ	Azimuthal angle in a cylindrical or spherical coordinate system (Ch. 2); disturbance of a spherical interface (Ch. 5)
$\zeta_{0\ell}$	Complex constant

η	Local intrinsic coordinate (Ch. 2); free surface elevation (Ch. 4)
η_0	Constant
θ	Polar angle in a spherical coordinate system (Chs. 2, 3, 5 and 6); parameter (dimensionless) in the dispersion relation for capillary-gravity waves (Ch. 4)
θ_s	Polar separation angle
θ'	Azimuthal coordinate in a cylindrical coordinate system (Ch. 6)
κ	Mean curvature
λ	Ratio of consecutive spline-parameter steps (Ch. 2); period in space (Ch. 4)
Λ	Density ratio
μ	Dynamic viscosity
ν	Kinematic viscosity
$\boldsymbol{\xi}$	Position vector
$\tilde{\xi}$	Local intrinsic coordinate
$\boldsymbol{\Xi}$	Vector of values of φ
ρ	Density
σ	Radial coordinate in a spherical coordinate system (Ch. 2); complex growth rate (eigenvalue) (Ch. 4); surface tension (Ch. 3)
$\tilde{\sigma}$	Dimensionless complex growth rate (Ch. 4)
$\hat{\sigma}$	Dimensionless complex growth rate (Ch. 5)
τ	Time to break-up, $t_b - t$ (Ch. 2); tangential stress (Ch. 3)
τ_{ij}	Component of the viscous stress tensor
$\boldsymbol{\tau}$	Deviatoric or viscous stress
ϕ, $\hat{\phi}$	Velocity potential
$\boldsymbol{\Phi}$	Vector of velocity potentials, ϕ
φ	Difference function (Ch. 2); azimuthal angle of a spherical coordinate system (Chs. 5 and 6)
ψ	Generic function (Ch. 2); stream function (Ch. 6)
ω	Vorticity magnitude

Subscripts

1, 2	Fluids 1 or 2 (Ch. 1); surfaces 1 and 2, respectively (Ch. 3)
c	Subscript
b	Bubble
B	Bubble

D	Drop
end	Refers to the right end of the bubble or drop on the axis of symmetry
G	Gas
i, e	Inner and outer fluids, respectively
I	Imaginary part of a complex number
j	Index
l, a	Fluids on this side or the other of the spherical interface of a drop or bubble
m	Index
max	Maximum value
min	Minimum value
M	Mixture
n	Index
r, θ, φ	Radial, polar and azimuthal coordinates in a spherical-polar coordinate system, respectively
R	Real part of a complex number
reg	Regular integral
sng	"Weakly" singular integral
s	Scaled coordinate
$\mathcal{S}$	Interface
z, r	Axial and radial coordinates in a cylindrical coordinate system, respectively
z', r', θ'	Axial, radial and polar coordinates in a cylindrical coordinate system, respectively
α	Index
ϵ	"Small" ball of radius ϵ
ξ	Point $\boldsymbol{\xi}$
∞	Far field in an infinite domain

Superscripts

j	Index
m	Index
T	Transpose
z, r	Refers to the axial and radial coordinates in a cylindrical coordinate system, respectively

Operators

$\langle\ \ \rangle$	Average of a quantity on a given region
$(\bar{\ })$	Complex conjugate
Δ	Difference
:	Double contracted product
∇	Gradient
$[\![\ \ ]\!] = (\ \ )_{r=a^+} - (\ \ )_{r=a^-}$	Jump across the interface at $r = a$
∇^2	Laplacian
$\frac{D}{Dt}$	Material derivative
$\frac{\mathrm{d}}{\mathrm{d}\ell}$	Ordinary derivative with respect to the spline parameter ℓ
$\frac{\mathrm{d}}{\mathrm{dt}}$	Ordinary derivative with respect to time
$\frac{\partial}{\partial n}$	Partial derivative with respect to the normal direction
$\frac{\partial}{\partial t}$	Partial derivative with respect to time
$\frac{\partial}{\partial s}$	Partial derivative with respect to the arc length
$\frac{\partial}{\partial x}$, $\frac{\partial}{\partial y}$	Partial derivatives with respect to the Cartesian coordinates
Re( )	Real part of a complex number
L^2	Spherical Laplacian
Im( )	Imaginary part of a complex number
$(\hat{\ })$	Relative to a noninertial reference frame
$\nabla_{\parallel}$	Surface gradient operator
$\otimes$	Tensor product
$(\dot{\ })$	Time differentiation
tr( )	Trace
$(\ddot{\ })$	Double time differentiation

Abbreviations

BEM	Boundary element method
DM	Dissipation method
IPF	Inviscid potential flow
NS	Navier–Stokes
PISO	Pressure-implicit with splitting of operators
PNSCC	Principal normal stress cavitation criterion
QUICK	Quadratic upwind interpolation for convective kinematics
VCVPF	Viscous correction of viscous potential flow
VPF	Viscous potential flow

Chapter 1

Introduction

The motion of two-phase systems in which both phases are immiscible fluids occurs in a wide variety of contexts, from natural and every day, domestic environments, to the industrial scale, as in the cases of chemical, oil and gas, and nuclear applications. Two-phase flows have been the subject of abundant research from both the theoretical and experimental sides over the years. One of the reasons for which this topic has received so much attention is the complexity associated with the modeling of the dynamics of such fluid systems. This difficulty comes not only from the fact that the numbers of parameters and unknowns describing the motion of each phase duplicates because another phase is present, but chiefly because the position of the interface being shared by the two fluids has to be determined as part of the solution and is usually time-dependent. In two-phase systems, the interface may be well defined and continuous, as in the case of separated or stratified flows, or may be diffused, as in the case of bubbly flows. In this work we are interested, for the most part, in the analysis of two-fluid systems sharing a well-defined interface. We consider several problems as listed below. We rely on both analytical and numerical methods to carry out the study. Our main working assumption is that the fluids are viscous and their motion is irrotational. A fluid element along its trajectory can simultaneously undergo translation, stretching and compression due to normal stresses, tilting due to shear, and solid-body-like rotation about an axis passing through its center of mass. The vorticity is a vector field that quantifies the local angular velocity of a fluid element. The term "irrotational" is used to described the flow of fluid elements that do not locally rotate as they deform, that is, a flow for which the vorticity is zero everywhere. Irrotational or nearly irrotational flows exist in fluid regions outside boundary or shear layers and wakes. Mathematically, irrotational motions are of great interest because their treatment is possible by means

of the potential theory, an elegant body of work that has been developed for more than two centuries. Hence, irrotational flows are also known as potential flows.

In the vast majority of analyses conducted with potential flow, the fluids have been considered inviscid. This is because a motion that starts from an irrotational initial state remains as such as time passes for an inviscid fluid, provided the density is a constant or the pressure is a sole function of the density, and that the body forces are conservative, as stated by Kelvin's theorem. On the other hand, in the flow of viscous fluids with a zero-vorticity initial condition, vorticity may be generated at boundaries and interfaces as a result of the no-slip condition. However, even in this context, purely irrotational theories have been able to successfully approximate the fluid dynamics of viscous fluids in various problems, describing its relevant features, not only for Newtonian fluids but also for non-Newtonian ones. The idea of analyzing the motion of viscous fluids with potential flow seems to have been introduced by Stokes (1851) in his work on the attenuation of small-amplitude waves on a gas-liquid interface by the energy viscous dissipation. Examples of analyses for which only the viscous effects of the irrotational motion are retained include instabilities of the Rayleigh-Taylor, Kelvin-Helmholtz and capillary type, decay of waves on the surface of planar free surfaces, decay of the oscillations on the surface of drops and bubbles, Faraday waves, flow-induced arrays of particles, drag on a translating bubble, and boundary-layer analysis for flow past rigid objects. These results and a few others have been collected in the treatise by Joseph, Funada, and Wang (2007) and references therein.

This thesis comprises the study of five problems. Each problem is considered in a separate chapter. Literature surveys pertinent to each problem are included in the corresponding chapter. The objectives sought in the investigation, the manner in which this thesis is organized and a brief account of each problem are given in what follows.

Objectives

In this work we focus on the analysis of a set of problems in the fluid mechanics of two-phase fluids. For this set of problems, the following objectives are listed:

- Model the non-linear (large) deformation of an interface including the viscous effects of the irrotational motion and surface tension using the boundary element method for the case of a bubble or drop immersed in a uniaxial extensional flow. Compare predictions for the break-up time with those obtained from solutions of the equations of motion retaining rotational effects (Chapter 2).

- Compute the force acting on a spherical bubble with a time-dependent radius translating in a liquid bounded externally by a spherical surface of variable radius using two approaches, namely, viscous potential flow and the dissipation method. Use this result and the so-called "cell-model" analysis to write the expressions for the drag force experienced by a bubble moving within a dilute swarm of bubbles with the same void fraction as the cell (already presented in the literature), elucidating the role of the choice of the outer boundary condition (not discussed in the literature). Compare the predictions from these formulas with predictions from other models, numerical analysis and experimental measurements (Chapter 3).

- Model viscous effects in the dynamics of "small" waves acting on a plane (Chapter 4) or spherical free surface (Chapter 5) using viscous potential flow and the dissipation method. Discuss the performance of the irrotational methods in comparison with the exact solutions available from the literature.

- Use the maximum tension criterion to predict the regions of the fluid domain at most risk to cavitation for viscous flow past a sphere, allowing vorticity in the analysis. Compare these new predictions with those from the classic pressure criterion, viscous potential flow and, when inertia is negligible, the slow-flow approximation (Chapter 6).

A brief description of each of the problems considered is given in what follows.

Content and organization

The first problem, which is considered in Chapter 2, concerns the deformation of a bubble or drop in an axially symmetric straining flow. The modeling of the dynamics on both sides of the interface assumes the motion of the viscous fluids to be irrotational. Both the fluid filling the bubble or drop and the surrounding fluid are incompressible. In this approach, viscosity enters the analysis through the balance of normal stresses at the interface with the stress due to surface tension. The tracking of the interface motion is achieved by integration of the set of differential equations furnished by the conservation of linear momentum and kinematic conditions, coupled with a boundary element method formulated over the interface as a result of conservation of mass. This methodology is thus employed to investigate the influence of a finite Reynolds number on the time evolution, up to break-up, of the drop or bubble for various Weber numbers. Our main interest is to compare the numerical results obtained here from viscous potential flow with results presented

in the literature from the numerical solution of the incompressible Navier–Stokes equations, which allows vorticity.

In Chapter 3 we examine the dynamics of a viscous incompressible fluid with an outer spherical boundary surrounding a spherical bubble in rectilinear motion simultaneously experiencing volume changes. Two purely irrotational methods of analysis are used, namely, viscous potential flow and the dissipation method. The forces that the liquid produces on the bubble and on the outer spherical boundary of the liquid are determined from these two approaches at the instant when the bubble is concentric with the outer surface. Viscous potential flow involves surface integration of the irrotational normal stress; the dissipation method stems from the mechanical energy balance, including the dissipation integral, evaluated in potential flow. In the inner boundary, zero tangential stress is enforced. Two choices for the tangential stress condition on the outer boundary are considered: Zero tangential stress or irrotational tangential stress. In a sense, this is an extension to include viscous effects of the inviscid analysis by Sherwood (1999). To the added-mass forces associated with the bubble acceleration and rate of change of the bubble radius determined by Sherwood, a viscous contribution is added here that depends upon the instantaneous bubble velocity and the inner and outer instantaneous radii of the bubble-liquid cell. If the inner and outer radii are held fixed, results from the cell model may be used to approximate the drag on a bubble moving in a bubbly flow with the same volume fraction as the cell. The analysis yields two results for the viscous drag on the bubble contingent on the boundary condition applied on the outer sphere. These formulas have been presented in the literature, although regarded as contradictories. By emphasizing the role of the tangential stress on the outer boundary, it is shown that both results are valid as they depend on the choice of the outer dynamic boundary condition. These results agree to first order in the volume fraction. The terminal rise velocity of a bubble swarm is derived using the drag from the viscous irrotational theories. We close this chapter with the comparison of the results for the drag coefficient and bubble rise velocity obtained here with other theoretical results, as well as data from numerical simulations and experiments, with emphasis in the regime of high Reynolds and low Weber numbers. For the bubble swarm rise velocity, we concluded that the models over-predicts the experimental data; among the models derived in this work, the dissipation method with and irrotational-tengential-stress external boundary condition renders the least discrepancies, and is second to the model by Spelt and Sangani (1998). For the drag coefficient and the bubble swarm rise velocity, the models presented here agree with results from numerical simulations.

In Chapter 4, we model the effect of viscosity on the decay and oscillation of capillary-gravity waves by means of two purely irrotational theories of the flow of a viscous fluid, namely, viscous potential flow and the dissipation method. The phenomenon is set by small two-dimensional periodic perturbations of the infinite planar free-surface of a liquid below a passive ambient fluid. The instantaneous velocity field in the viscous liquid is assumed to be irrotational in the modeling. In particular, the dissipation approximation used in this analysis gives rise to a viscous correction of the frequency of the oscillations which was not obtained in the well-known dissipation calculation carried out by Lamb (1932). Moreover, our dissipation method goes beyond Lamb's in the sense that it yields an eigenvalue relation valid for the entire continuous spectrum of wave numbers. Comparisons are presented between the purely irrotational theories and Lamb's solution of the linearized Navier–Stokes equations, showing good to reasonable agreement for long, progressive waves and for short, standing waves, even for very viscous liquids. The performance of the irrotational approximations deteriorates within an interval of wave-numbers containing the cut-off where traveling waves become standing ones.

In Chapter 5, the same viscous irrotational theories used in the previous chapter are now applied to the analysis of the linear dynamics of small perturbations on the surface of a sphere instead of a plane. We treat the problem of the decay of small disturbances on a viscous drop surrounded by gas of negligible density and viscosity and a bubble immersed in a viscous liquid. The results show that the viscous irrotational theories exhibit most of the features of the wave dynamics described by the exact solution. In particular, the viscous irrotational theories give rise to a viscous correction for the frequency that determines the crossover from oscillatory to monotonically decaying waves. Good to reasonable quantitative agreement with the exact solution is also shown for certain ranges of modes and dimensionless viscosity: For large viscosity and short waves, viscous potential flow is a very good approximation to the exact solution. For "small" viscosity and long waves, the dissipation method furnishes the best approximation.

Finally, in Chapter 6 we consider the phenomenon of cavitation, a problem that has drawn the attention of researchers over many years and has important implications in industry. A cavitation event can be defined as the formation, expansion and collapse of a cavity or void in a liquid. Specifically, the problem of cavitation of a viscous liquid in the streaming flow past a stationary sphere is studied in this chapter by applying the theory of stress-induced cavitation. This theory is a revision of the pressure theory which states that a flowing liquid will cavitate when and where the pressure drops below a cavitation threshold, or breaking strength, of the

liquid. In the theory of stress-induced cavitation, the liquid will cavitate when and where the maximum tensile stress exceeds the breaking strength of the liquid. For example, liquids at atmospheric pressure which cannot withstand tension will cavitate when and where additive tensile stresses due to motion exceed one atmosphere. A cavity will open in the direction of the maximum tensile stress, which is 45^o from the plane of shearing in pure shear of a Newtonian fluid. Flow of a single phase (liquid) is considered in the analysis. Therefore, the only boundary in the problem is the surface of the solid sphere. The treatment of this problem differs from those in the previous chapters in that the core of the results are obtained without neglecting the vorticity by solving the incompressible Navier–Stokes equations using a commercial solver. In addition, an analytical solution for the flow is obtained in the limit of zero Reynolds number. In both analyses, non-slip is enforced at the sphere's surface. For comparison, results from viscous potential flow are also included. The analysis leads to a dimensionless expression for the maximum tensile stress as a function of position which depends on the cavitation and Reynolds numbers. The main conclusion is that, at a fixed cavitation number, the extent of the region of flow at risk to cavitation increases as the Reynolds number decreases. This prediction that more viscous liquids at a fixed cavitation number are at greater risk of cavitation seems not to be addressed, affirmed nor denied, in the cavitation literature known to us. Our study on stress-induced cavitation describes a novel application of the maximum-tensile-stress criterion to predict the onset of cavitation not only for viscous potential flow but also for flows with non-zero vorticity, whose governing equations can be solved by commercial software available to the industry.

1.1 Interfacial potential flow of viscous fluids

In the motion of two immiscible fluids sharing a common interface, it is quite frequent to encounter a flow field in which vorticity is restrited to narrow layers neighboring the interface; beyond this region, the flow is nearly irrotational. At the interface, no-slip requires that the tangential velocities of both fluids be continuous and, if Marangoni stresses* are insignificant, as in the case of uniform surface tension over the interface, the tangential stresses must also match. The presence of vorticity layers assures the continuity of the tangential components of velocity and stress. In addition to these constraints, along the direction normal to the interface, the velocity components must also be continuous whereas normal stresses are not, in general, and its jump across the interface must be balanced by surface tension forces associated

*Stresses originated by gradients of surface tension.

with the local curvature. If the flow motion is assumed to be purely irrotational, the interfacial conditions must be relaxed because continuity of tangential components of velocity and stress cannot be satisfied. A rotational[†] flow field would have to be added to the irrotational one for the actual flow field to satisfy these matching conditions at the interface. Nevertheless, in the purely irrotational approximation, continuity of normal velocities and the balance of normal stresses can be enforced. In solid boundaries, the normal velocity of the fluid must match the normal component of the velocity of the solid and slip occurs in the tangential direction.

The theoretical aspects in the analysis of the irrotational flow of viscous fluids are founded in the well-developed or "mature" mathematical theory of potentials. The reason being that for an irrotational flow field the velocity vector is curl-free (i.e. vorticity is identically zero); therefore, the velocity can be expressed as the gradient of a scalar field or potential that, by virtue of mass conservation, turns out to be harmonic. To find the potential, Laplace's equation must be solved subject to boundary conditions of the type described above, which are projections along the normal direction at points on the boundary. Boundary conditions on the velocity, that is, specification of the normal velocity component or of the potential itself (e.g., in the far field for unbounded domains), are sufficient to determine the velocity field everywhere, and stresses, including the pressure, can be computed *a posteriori* using the statement of momentum balance. In problems of interfacial flow in which the position of the interface is unknown, the dynamical interfacial constraint given by the balance of normal stresses is also necessary. This is exemplified by the problem studied in Chapter 2.

For an incompressible Newtonian fluid the constitutive equation for the stress tensor is

$$\mathbf{T} = -p\mathbf{1} + 2\mu\mathbf{D}, \tag{1.1}$$

with the strain-rate tensor

$$\mathbf{D} = \frac{1}{2}\left[\nabla\mathbf{u} + (\nabla\mathbf{u})^T\right]. \tag{1.2}$$

where $\mathbf{u}$ is the velocity field, p is the pressure and μ is the dynamic viscosity.

With the stress-strain-rate relation (1.1), conservation of linear momentum for a fluid particle in an incompressible Newtonian fluid of density ρ leads to the incompressible Navier–Stokes equations

$$\rho\left(\frac{\partial\mathbf{u}}{\partial t} + \mathbf{u}\cdot\nabla\mathbf{u}\right) = -\nabla p + \mu\nabla^2\mathbf{u}, \tag{1.3}$$

[†]Vorticity is not zero, as opposed to "irrotational" flows.

with

$$\nabla \cdot \mathbf{u} = 0. \tag{1.4}$$

Consider now the motion of two immiscible incompressible Newtonian fluids that share a common smooth interface $\mathcal{S}$. Each fluid occupies a domain that may be bounded or may extend with no boundaries (other than the interface). We assume that the velocity of the fluid is equal to the (known) velocity on those boundaries or is given in the far field of an unbounded domain. Let $\mathcal{F}(\mathbf{x}(t), t) = 0$ define the position of the points of the interface $\mathbf{x}(t)$ for all times. Thus, the unit vector normal to the interface is $\mathbf{n} = \nabla\mathcal{F}/|\nabla\mathcal{F}|$ where $\mathcal{F}$ is such that $\mathbf{n}$ points from fluid 1 to fluid 2. Differentiation of $\mathcal{F}$ with respect to time yields the kinematic condition

$$\frac{\partial \mathcal{F}}{\partial t} + \mathbf{u}_{\mathcal{S}} \cdot \nabla\mathcal{F} = \frac{\partial \mathcal{F}}{\partial t} + \mathbf{u}_{\mathcal{S}} \cdot \mathbf{n}|\nabla\mathcal{F}| = 0 \tag{1.5}$$

where $\mathbf{u}_{\mathcal{S}}$ refers to the velocity of the interface $\mathcal{S}$ at point $\mathbf{x}$. If no mass transfers across the interface $\mathbf{u}_{\mathcal{S}} \cdot \mathbf{n} = \mathbf{u}_j \cdot \mathbf{n}$ for $j = 1, 2$ (Joseph and Renardy, 1993), and we have continuity of the normal component of velocity

$$\mathbf{u}_1 \cdot \mathbf{n} = \mathbf{u}_2 \cdot \mathbf{n}. \tag{1.6}$$

By this equality and the definition of $\mathbf{n}$ in terms of $\mathcal{F}$, we can replace $\mathbf{u}_{\mathcal{S}} \cdot \mathbf{n}$ with $\mathbf{u}_j \cdot \mathbf{n}$ in (1.5), the tangential component of $\mathbf{u}_{\mathcal{S}}$ being irrelevant (Joseph et al., 2007).

If the surface tension is a constant coefficient γ over the extension of the interface, the balance of normal stresses at the interface is

$$\mathbf{n} \cdot \mathbf{T}_1 \cdot \mathbf{n} - \mathbf{n} \cdot \mathbf{T}_2 \cdot \mathbf{n} = \gamma \nabla_{\parallel} \cdot \mathbf{n}, \tag{1.7}$$

where the stress tensor is given by (1.1). The surface gradient operator is $\nabla_{\parallel} = \nabla - \mathbf{n}(\mathbf{n} \cdot \nabla)$[‡] and $-\nabla_{\parallel} \cdot \mathbf{n} = 2\kappa$ is twice the mean curvature at a given point on the interface, that is, the sum of the reciprocal of the principal radii of curvature for that point (Joseph and Renardy, 1993).

With a vector $\mathbf{t}$ such that $\mathbf{t} \cdot \mathbf{n} = 0$, continuity of the tangential component of velocity and stress at the interface may be written as

$$\mathbf{u}_1 \cdot \mathbf{t} = \mathbf{u}_2 \cdot \mathbf{t}, \qquad \mathbf{n} \cdot \mathbf{T}_1 \cdot \mathbf{t} = \mathbf{n} \cdot \mathbf{T}_2 \cdot \mathbf{t}, \tag{1.8}$$

where the latter holds because surface tension is assumed to be constant.

Let us now constrain the flow to be irrotational, hence $\nabla \times \mathbf{u} = 0$ as mentioned

[‡]Notice that $\nabla_{\parallel} \cdot \mathbf{n} = \nabla \cdot \mathbf{n}$ because $\mathbf{n} \cdot (\mathbf{n} \cdot \nabla\mathbf{n}) = \mathbf{n} \cdot \nabla|\mathbf{n}|^2/2 = 0$.

above and we can write

$$\mathbf{u} = \nabla\phi, \tag{1.9}$$

where ϕ is the velocity potential. By the incompressibility constraint, the velocity field is solenoidal (divergence-free) and the potential is thus harmonic as it satisfies Laplace's equation. For an irrotational velocity field, the velocity gradient $\nabla\mathbf{u}$ is symmetric and, by virtue of (1.2), the stress tensor becomes

$$\mathbf{T} = -p\mathbf{1} + 2\mu\nabla \otimes \nabla\phi. \tag{1.10}$$

For irrotational flows, the viscous term in the Navier–Stokes equations (1.3) vanishes identically because

$$\mu\nabla^2\mathbf{u} = \mu\nabla\nabla^2\phi = 0,$$

leading to Euler's equations. With $\mathbf{u} = \nabla\phi$, these equations can be integrated resulting in Bernoulli's equation

$$\frac{\partial\phi}{\partial t} + \frac{p}{\rho} + \frac{|\mathbf{u}|^2}{2} = C(t). \tag{1.11}$$

The function of time $C(t)$ can be put together with the potential and the right-hand side of (1.11) can be set to zero with no loss of generality.

Continuity of the normal velocity component requires simply that

$$\mathbf{n} \cdot \nabla\phi_1 = \mathbf{n} \cdot \nabla\phi_2. \tag{1.12}$$

and substitution of (1.10) into the normal stress balance statement (1.7) leads to

$$(-p_1 + \mathbf{n} \cdot 2\mu_1\nabla \otimes \nabla\phi_1 \cdot \mathbf{n}) - (-p_2 + \mathbf{n} \cdot 2\mu_2\nabla \otimes \nabla\phi_2 \cdot \mathbf{n}) = \gamma\nabla_{\|} \cdot \mathbf{n}, \tag{1.13}$$

with no conditions imposed for the tangential components of velocity and stress for fluids 1 and 2 at the interface.

Finally, it should be mentioned that if the material density and viscosity of one of the fluids are neglected, the interface becomes a free surface, and rotational motions are subjected to a zero tangential stresses boundary condition. Purely irrotational motions, on the other hand, cannot satisfy this condition as the viscous irrotational stress at the interface on the side of the fluid does not vanish, in general.

Viscous potential flow versus the dissipation method

In the irrotational analysis encompassing expressions (1.10) to (1.13), the viscosity of the fluids enters the analysis only through the balance of normal stresses given by the latter. This formulation, labeled as viscous potential flow, is "the natural and obvious way to express the equations of balance when the flow is irrotational and the fluid viscous" (Joseph, Funada, and Wang, 2007).

Viscous potential flow is not the only purely irrotational theory considered in this work. The dissipation method is another approach based upon the irrotational solution of the flow field that can be used to model interfacial phenomena. The dissipation method can be traced back to the works of Stokes (1851) and later of Lamb (1932), the former on the estimation of the decay rate of small waves on otherwise planar interfaces and, the latter on the attenuation of the oscillations of drops and bubbles about the spherical form. The working equation for the dissipation approximations is the mechanical energy equation, which is obtained by taking the inner or "dot" product of the incompressible Navier–Stokes equation (1.3) with the velocity vector—in the case of a Newtonian incompressible fluid—and then integrate it over the volume of the entire fluid region. After applying the divergence theorem, one is left with a balance involving the rate of change of the kinetic energy, the viscous energy dissipation and the power of the stresses acting on the boundaries, where the boundary conditions of the type satisfied by a Navier–Stokes motion can be enforced. In the case of an interface shared by two fluids, the mechanical energy equations written for each of them can be added and constraints (1.6) through (1.8) for the continuity of normal and tangential velocities and tangential stresses, and for the balance of normal stresses can be applied. Then, the remaining surface integrals as well as the volume integrals for the kinetic energy and viscous dissipation are evaluated using the potential flow solution. This is the key feature of the method. It is an *ad hoc* approximation, and one may expect it to work if the regions of vorticity are narrow layers such as, for instance, shear layers at an interface, and thus the velocity field is nearly irrotational in most of the fluid domain. The dissipation method is implemented in chapters 3, 4 and 5 of this work; there, the mathematical description adapted to each particular application is presented in detail.

As shown above, the theory of viscous potential flow does not arise from energy arguments, whereas the dissipation method does rely on them. Therefore, the outcomes from these two irrotational theories will be different, in general.

Chapter 2

Viscous irrotational analysis of the deformation and break-up time of a bubble or drop in uniaxial straining flow

The large deformation of a bubble or drop initially spherical driven by an axially symmetric straining motion is studied in this chapter. Both the fluid within the bubble or drop and the exterior fluid are considered incompressible. The initial shape of the bubble o drop is spherical. The motion is assumed to be irrotational but the viscosity of both fluids is finite and non-zero. Viscous effects enter the analysis through the balance of normal stresses at the interface. The evolution of the interface is tracked by numerical integration of the equations of momentum conservation, which must be coupled with a boundary integral equation that results from the statement of mass conservation.

2.1 Introduction

2.1.1 Motivation – A simple model for bubble and drop turbulent break-up

The break-up of bubbles and drops by a turbulent immiscible flow plays a key role in transfer phenomena occurring in engineering applications and natural settings. The rate of mass, heat and momentum transfer between a dispersed phase and a continuous phase strongly depends on the existing contact or interfacial area,

which in turn is determined by the deformation and break-up of the fluid particles. For instance, this is of paramount importance for the performance of gas-liquid and liquid-liquid chemical reactors and separators. Also, the exchange of carbon dioxide, water vapor and other species between the oceans and the atmosphere, which has large-scale environmental implications, is known to be associated with the bubble size distribution resulting from interaction of the turbulence within the bulk of the water with the air entrained by the dynamics of sea waves (Melville, 1996; Martínez-Bazán, Montañes, and Lasheras, 1999a,b, and references therein). Therefore, an understanding of the mechanism of turbulent break-up of bubbles or drops has been central to developing predictive models applicable to these and many other processes. In particular, the particle break-up time is an essential parameter in the description of these phenomena.

After the pioneering works of Kolmogorov (1949) and later of Hinze (1955), it has been established that turbulent break-up of a fluid particle result as a consequence of the overcoming of the shape-preserving surface tension forces by the pressure fluctuations acting on the particle. Moreover, it has been ascertained that characterizing the local turbulent fluid dynamics prevailing around the bubble or drop suffices to describe the changes in its morphology. Another break-up mechanism, first described by Risso and Fabre (1998) and known as subcritical break-up, in opposition to the supercritical mechanism just presented, consists in the occurrence of bubble resonance with a series of consecutive subcritical (i.e. moderate) turbulent eddies that lead to large oscillations and eventual break-up of the bubble.

After examining available experimental data obtained by Rodríguez-Rodríguez (2004) and Eastwood, Armi, and Lasheras (2004) for the break-up of bubbles and drops, respectively, in a turbulent water stream, and by performing numerical simulations, Rodríguez-Rodríguez, Gordillo, and Martínez-Bazán (2006) has convincingly shown that this phenomenon can be modeled, as a first approximation, by considering a bubble or drop, initially spherical, immersed in a uniaxial straining flow of an incompressible fluid using a reference frame that moves with the mean velocity of the background flow. Although simple, this model retains the most relevant features of the process, thus avoiding expensive three-dimensional numerical computations involving the tracking of deforming interfaces in a turbulent flow characterized by unsteady structures with various length scales. Indeed, the images observed by Rodríguez-Rodríguez et al. (2006) revealed that the bubbles or drops follow a "cigar-shape" elongation leading to break-up that is nearly axisymmetric. Moreover, their observations suggest that a single turbulent eddy is the cause of breakage and "whose characteristic turnover time is larger than the break-up time",

thereby justifying the assumption of a steady flow in the far field (i.e. fluctuations are discarded as the cause of break-up). Indeed, Risso and Fabre (1998) observed in experiments that an initially non-deformed bubble may be deformed and broken by turbulent eddies strong enough to generate abrupt break-up. Rodríguez-Rodríguez et al. (2006) further assume that the particle characteristic size falls within the inertial subrange of the turbulent energy spectrum, hence the fluids are considered inviscid. In their simulations, the velocity field is irrotational. The numerical simulations are carried out by Rodríguez-Rodríguez et al. (2006) using the boundary element method and the bubble or drop break-up time is predicted as a function of the Weber number, which measures the relative importance of the outer flow inertia versus the force due to surface tension, and the inner to outer density ratio. Thus, values of the Weber number and density ratio must be entered before running a simulation. To be able to specify a Weber number representative of the characteristics of the turbulent flow, Rodríguez-Rodríguez et al. (2006) derived a formula that links the magnitude of the Weber number to the dissipation rate of turbulent kinetic energy per unit mass. Their simulations result in particle break-up when the actual Weber number is larger than a critical Weber number; otherwise, the bubble or drop oscillates and does not break-up in agreement with experimental evidence. For the case of the bubble, binary break-up is predicted, that is, the bubble breaks into two equal pieces in accord with experiments (Martínez-Bazán et al., 1999b; Rodríguez-Rodríguez, Martínez-Bazán, and Montañes, 2003; Andersson and Andersson, 2006); the computed break-up time also agrees with experimental measurements by Martínez-Bazán et al. (1999a) and Rodríguez-Rodríguez (2004).

On the other hand, in the case of the drop, the break-up is tertiary (e.g., Andersson and Andersson, 2006) as two symmetric daughter drops are formed at both ends of an intermediate ligament that becomes slender, with length larger than the initial drop radius for large Weber numbers, as the inner to outer density ratio becomes of order one. For Weber numbers close to the critical value, the central satellite drop is small in volume. In this case, Rodríguez-Rodríguez et al. (2006) point out that predictions for the break-up time and critical Weber number do not agree with the experimental measurements. They assert that this discrepancy results because the drop takes the form of a long ligament with a length much larger than the size of the breaking eddy. The elongated drop thus turns around itself as observed in the experiments. Therefore, the approximation of the local fluid motion as an axisymmetric straining motion is no longer valid. Beyond this weakness, those authors state that the simple model is able to qualitatively describe important features of the process as the tertiary break-up and the size of the intermediate ligament.

Revuelta et al. (2006) add a viscous correction to the inviscid break-up time predicted by Rodríguez-Rodríguez et al. (2006) by solving the unsteady incompressible Navier–Stokes equations for a bubble immersed in the uniaxial extensional flow of a liquid using a level set method on a fixed mesh. Since viscosity enters the analysis, two additional dimensionless parameters appear in the formulation, namely, the inner to outer viscosity ratio and a Reynolds number based upon the liquid properties, the bubble initial radius and the principal strain rate. In terms of this Reynolds number, the correction to the break-up time is $O(Re^{-1})$. They found that for a fixed Weber number, the smaller the Reynolds number, the longer takes the bubble to break up. Therefore, the break-up time computed for inviscid fluids, i.e. $Re \to \infty$, determines a lower bound. Moreover, they obtained that for a fixed Reynolds number, the break-up time reaches a plateau as the Weber number increases. They also found that the critical Weber number $We_c = 2.22 \pm 0.005$, which is almost the same as that found by Rodríguez-Rodríguez et al. (2006), is independent of the Reynolds number for $Re \geqslant 20$. In addition, Revuelta et al. also considered a fluctuating principal strain rate in the far field to model the mechanism of resonance of the bubble with passing turbulent structures, a process that has been described above.

A relevant antecedent of Revuelta's work is the paper by Kang and Leal (1987) on the dynamics of a bubble in a uniaxial extensional flow with a steady strain rate. They focused on finding the maximum critical Weber number for which a steady solution exists by solving the unsteady incompressible Navier–Stokes equations for the outer liquid. However, they do not present results on either the break-up time or the bubble morphology in an event of break-up. Kang and Leal (1990) also studied the bubble dynamics when the uniaxial straining motion in the far field is time-periodic. In the case of a drop in a uniaxial extensional flow of another liquid, the literature search revealed, surprisingly, that the numerical solution of the incompressible Navier–Stokes equations has been carried out only by Ramaswamy and Leal (1997) dropping the unsteady term. Therefore, information on the drop break-up time is not provided and their results are concerned with the critical Weber number below which a steady shape exists. The vast majority of the computational work for the transient of this flow configuration has been conducted neglecting inertia in the limit of Stokes flow as shown, for example, in the review paper by Guido and Greco (2004).

In Chapter 1, we have mentioned that the theories of potential flow of viscous fluids, i.e. viscous potential flow and the dissipation method, have been applied to problems of *linear* stability analysis of diverse origin, as well as to problems of *small* wave dynamics on an interface or free surface. Results from these analyses have

shown that excellent to reasonable agreement can be obtained with exact solutions from the linearized Navier–Stokes equations, which retain the effects of vorticity, or with experimental data. We wonder to what extent the viscous irrotational theories, in particular, viscous potential flow, can be used to predict the *nonlinear* motion of an interface. To investigate this question, in the particular case of the deformation of a bubble or drop in a uniaxial straining flow, we conduct this research.

2.1.2 Scope

In this work, the dynamics of the interface of a bubble or drop of an incompressible fluid immersed in another incompressible fluid subjected to a uniaxial extensional flow is studied. The fluids in this system are viscous and the motion is assumed to be irrotational for all time. For the bubble, the inner to outer fluid density ratio is set to be very small in comparison to unity and, for the case of the drop, this ratio is of order one. The solution of the governing equations is sought through a numerical method that couples a boundary integral formulation with a time integration scheme following the algorithm proposed by Rodríguez-Rodríguez et al. (2006). In a sense, this is an extension of the work of Rodríguez-Rodríguez et al. (2006) for inviscid fluids to include the viscous effects of the irrotational motion via the dynamic balance at the interface that contains the viscous normal stresses. The main objective is the comparison of the interfacial shapes as time advances and the break-up time computed using the viscous irrotational approximation with published results obtained from the solution of the incompressible fully-viscous Navier–Stokes equations, which keep the rotational component of the flow field, for the case of the bubble (Revuelta et al., 2006). For the case of the drop, we present numerical results from the viscous potential flow theory; however, we are not able to compare with results from a transient analysis of a Navier–Stokes flow because, as mentioned above and to the best of our knowledge, no works have been presented in the literature in which these computations have been performed.

This chapter is organized as follows. This section follows with literature reviews on the evolution of an interface near break-up in the next subsection and on the boundary element method applied to the problem of interfacial flows for both inviscid and viscous fluids in §2.1.4. Next, in §2.2 the representation formula for the direct formulation of the boundary integral method is derived. In §2.3 the problem formulation and the numerical method are described in detail. In §2.4, the validation of the numerical method (§2.4.1) and the results for the non-linear deformation of a bubble (§2.4.2) and drop (§2.4.3) with viscous effects are presented and discussed. Finally, concluding remarks are given in §2.5.

2.1.3 Brief literature survey on interface dynamics near break-up

Although it is not part of the core of this study, we should mention that in the last fifteen years or so, theoreticians, experimentalists and computational researchers alike have dedicated great effort to the study of the (axisymmetric) pinching-off of a liquid thread and the collapsing of a cavity in a liquid focusing on the stages of the motion when the breaking of the continuum is imminent. This phenomenon, characterized by the approaching and reaching of a singularity in a finite time, is attractive because of its striking beauty and richness of the underlying physics. In the case of liquid rupture, the interface shapes approaching the singularity have been shown to be self-similar because of the large differences between the local length scales and the global ones, and universal in the sense that no imprint of the initial and boundary conditions is retained. Analyses have focused on finding scaling theories relating the local length scales with the time before pinch-off for various flow regimes determined by the relative importance of inertia, viscosity and capillarity. In this regard, on the side of inviscid fluids, after the pioneering work of Keller and Miksis (1983), several works followed that considered different fluid density ratios (Chen and Steen, 1997; Day, Hinch, and Lister, 1998; Leppinen and Lister, 2003), describing the scaling of the thread neck radius $r_{\min} \sim \tau^{2/3}$, where τ is the time to pinch-off and $r_{\min}$ and τ are made dimensionless with appropriate scales. Viscous effects in the pinch-off of a liquid thread surrounded by a passive ambient fluid has been studied by Papageorgiou (1995) in the limit of motion with no inertia, and by Eggers (1993) adding inertia to viscosity and capillarity. He found $r_{\min} \sim \tau$ when the viscous effects of the thread become important. Lister and Stone (1998) accounted for the effect of the external fluid viscosity using scaling arguments so that transition between and scaling for different regimes are described. In the limit of inertialess motion, viscous capillary pinch-off of a fluid thread has been studied by Sierou and Lister (2003) obtaining self-similarity for a wide range of inner to outer viscosity ratios. After an unexpected experimental finding, Doshi et al. (2003) report that universality is violated when the outer fluid viscosity is larger than the inner fluid viscosity by several orders of magnitude and, for certain conditions, a long, slender thread is formed bridging the two larger pieces of liquid. The reader is referred to the very recent and comprehensive review article by Eggers and Villermaux (2008) covering the developments in the study of liquid pinch-off. On the other hand, the collapse of a gas cavity (bubble), which has received less attention than its liquid (drop) counterpart, has been described as not self-similar and non-universal (Suryo, Doshi, and Basaran, 2004; Keim et al., 2006). This phenomenon has been studied in the frame of the detachment of a bubble coming out of a nozzle due to buoyancy,

as in the experiments by Burton, Waldrep, and Taborek (2005), Thoroddsen, Etoh, and Takehara (2007) and Bolaños-Jiménez et al. (2009), and simulations by Quan and Hua (2008) and others. These works have represented the variation of the minimum bubble neck radius $r_{\min}$ with the time to pinch-off as $r_{\min} \sim \tau^{\alpha}$, where α is an *effective* exponent, $\alpha > 0.5$ and $\alpha \approx 1$ for high viscous liquids ($\alpha \approx 0.57$ for water in air), the exact value of α depending upon the initial and boundary conditions of the flow (Bolaños-Jiménez et al., 2009). For liquids with intermediate and large viscosities, Bolaños-Jiménez et al. (2009) found that the exponent α is better described as a function of τ. Analytical studies on the process of cavity pinch-off have also been conducted (Gordillo et al., 2005; Eggers et al., 2007; Gordillo and Fontelos, 2007, and others) yielding relations for the evolution of the neck radius approaching break-up that have a more complicated form than those for a liquid thread. Also, Rayleigh-like models have recently been developed by Gordillo (2008) yielding predictions in very good agreement with experiments. We remark that our interest is focused here in the study of the overall morphology of the bubble or drop throughout the entire motion rather than in the local analysis during the short time period preceding rupture.

2.1.4 The boundary element method applied to the study of interfacial potential flows

A major objective in the solution of interfacial flow problems is a highly accurate description of the interface. Therefore, boundary integral techniques are a fitting choice for the analysis, since they seek solutions of integral equations involving information only on the interface. This feature reduces the dimensionality of the problem by one. Thus, when an approximate solution is sought, a fine mesh can be afforded on the interface especially in regions with high curvature, without having to discretize the neighboring domain. This attribute is particularly important for an unbounded domain, in which case appropriate boundary conditions at infinity can be satisfied automatically by the governing integral equations. A survey of the literature on free-surface or interfacial flows indicates that boundary integral methods have been applied mostly to problems in two-dimensions or three-dimensions with axial symmetry since domain discretization simply takes place over a curve in the plane for these cases.

The application of the boundary integral method relies on the existence of a "fundamental solution" for the partial differential equation on hand. In particular, this solution is known for Laplace's equation. Therefore, boundary integral methods becomes a useful tool for incompressible potential flow problems because the velocity

potential is harmonic. Boundary integral formulations have also been developed for Stokes flow (e.g., Pozrikidis, 1992).

In general, boundary integral methods can be grouped into two major categories, namely, the indirect and the direct formulations (Banerjee and Butterfield, 1981; Brebbia, Telles, and Wrobel, 1984). In the indirect formulation an integral equation is written in terms of the density distribution over the boundary of a unit singular solution of the partial differential equation of interest. Numerical techniques are then applied to compute this density profile which may have no explicit physical connotation. Once the density function over the boundary has been determined, the physical variables of the problem inside the domain can be obtained by integration. On the other hand, the direct formulation poses integral equations on the boundaries in terms of the physical parameters of interest. By enforcing the boundary conditions, one can solve for the unknown field on the boundary first and then at particular locations on the interior. For instance, the normal derivative of the potential at the boundary can be computed in the Dirichlet problem or the potential over the boundary in the Neumann problem. Also, mixed boundary conditions can be easily handled.

For most of the problems of interest in science and engineering, finding a solution of the boundary integral equations is possible only in an approximate manner, by use of numerical techniques. A widely used approach is the boundary element method (BEM). In general terms, this method sets marker points or nodes on the boundary. A number of segments or "elements" connecting the nodes are used to approximate this boundary. In two dimensions, these elements may be straight segments or, if greater accuracy is desired, of higher order, including circular, parabolic or cubic representations. In three dimensions, triangular or quadrilateral elements may be chosen. Regarding the fields functions taken to the boundary (e.g., the potential and its normal derivative), they are approximated with a truncated polynomial over each element. For instance, the simplest choice is to hold the function constant on the element. To improve accuracy, the linear expansion or higher-order approximations may be used. The coefficients of the expansion correspond to the values of the function at particular locations on the element, which may be those of the nodes. Next, the integrals on the boundary integral equation are split into integrals evaluated over each element, and the local expansions for the field functions are substituted. Then, the discretized equation is satisfied at a set of collocation points on the boundary. This process gives rise to a set of algebraic equations that may be solved for the vector of unknowns. Detailed descriptions on the implementation of BEM can be found in monographs on the subject, such as those by Brebbia et

al. (1984), Pozrikidis (1992), and Wrobel (2002), among others. A fairly rigorous mathematical treatment of boundary integral equations and their numerical solution is given by Jaswon and Symm (1977).

For problems involving the deformation of a free surface or interface, the application of BEM to solve Laplace's equation as previously described is carried out at a given time with known geometry and boundary conditions. To advance the position of the boundary and the conditions on it to the next time level, the boundary integral solution algorithm has to be coupled with a time-marching scheme. This scheme is applied to the time integration of the kinematic and dynamic boundary conditions, together with the transport of momentum for points on the interface written in Lagrangian form. Starting from the initial conditions, the coupling of boundary integral and time-marching algorithms is repeated until the final time is reached.

Boundary integral methods for inviscid potential flow

Examples of the applications of boundary integral methods to problems involving free-surface flows are abundant. For instance, in the case of steady motion, the inviscid analysis of free surfaces is carried out by Byatt-Smith and Longuet-Higgins (1976) for a steep solitary wave, by Miksis, Vanden–Broeck, and Keller (1981) to study the deformation of an axisymmetric bubble in a uniform flow using a direct formulation and by Meiron and Saffman (1983) for interfacial gravity waves applying the indirect formulation.

The accurate description of the unsteady motion of free surfaces or fluid-fluid interfaces bounding regions of inviscid irrotational flow can be performed using boundary integral techniques. An approach that arises from the indirect double-layer potential formulation is the generalized vortex method. This method was presented and developed by Baker, Meiron, and Orszag (1980, 1982, 1984) in a series of publications. They obtained an integral equation for the Lagrangian time derivative of the dipole density distribution over the boundary. Solving for this time derivative allows updating the dipole density which is used to march the interface forward in time. Baker et al. (1980) used the vortex method to simulate the Rayleigh-Taylor instability in its classical form while Verdon et al. (1982) considered the acceleration of a thin fluid layer. Baker et al. (1982) applied the method to the breaking of surface waves and interacting triads of surface and interfacial waves. Lundgren and Mansour (1988, 1991) studied the oscillations of an inviscid axisymmetric drop in a dynamically inactive fluid (e.g., vacuum) and the motion of toroidal gas bubbles in an inviscid liquid, respectively, with a modified version of the generalized vortex

method. Mansour and Lundgren (1990) also applied this approach to model satellite formation in capillary jet break-up. The vortex method based upon the indirect approach has been used to study the dynamic break-up of an inviscid liquid bridge by Chen and Steen (1997) and capillary pinch-off of an inviscid drop surrounded by an ambient inviscid fluid by Leppinen and Lister (2003).

The direct formulation of the boundary integral method for inviscid fluids was used by Keller and Miksis (1983) to model a breaking sheet of liquid and the flow near the intersection of a solid boundary with the free surface of a liquid. Several papers by Oğuz and Prosperetti (1989, 1990, 1993) on the effect of surface tension in the contact of liquid surfaces, bubble entrainment by the impact of drops on liquid surfaces, and dynamics of bubble growth with detachment from a needle, respectively, use the direct formulation of boundary integral methods. Hilbing, Heister, and Spangler (1995) applied the direct formulation of BEM to study the atomization of a finite liquid jet coming out of a circular orifice discharging into a passive ambient fluid. Heister (1997) conducted a BEM analysis using the direct formulation for inviscid two-fluid interfacial flows and tested it for various problems. They found that increasing the outer to inner density ratio towards one degrades the stability an accuracy of the scheme. More recently, Yoon and Heister (2004) applied the direct form of BEM to study the primary atomization of a liquid jet considering boundary layer effects by placing a ring vortex at the nozzle exit plane. Park and Heister (2006) have used the direct formulation of BEM to study a pressure swirl atomizer. This formulation is also applied by Machane and Canot (1997) for various 2D and axisymmetric free-surface problems and by Day et al. (1998) and Rodríguez-Rodríguez et al. (2006) to problems of capillary pinchoff.

An interesting application of boundary integral methods is in the description of the motion of nonlinear waves. Longuet-Higgins and Cokelet (1976) used the direct formulation to study the deformation of steep, periodic, solitary waves in deep liquid. A condensed review of BEM analysis of nonlinear waves was given by Ligguet and Liu (1984). The phenomena of generation, propagation, shoaling, break-up and absorption of 2-D nonlinear waves have been studied by Grilli et al. (1989, 1994, 1996, 1997) through the direct formulation of BEM. The numerical modeling of a 3-D nonlinear wave over complex bottom topography was carried out by Grilli, Guyenne, and Dias (2001). Their model is able to predict wave overturning. Boundary conditions of the absorbing or reflective type can be indicated on lateral boundaries.

Boundary integral methods for viscous potential flow

BEM has been extended to accommodate the effects of viscosity in a purely irrotational flow by Georgescu, Achard, and Canot (2002) to study a gas bubble bursting at a free surface and by Canot et al. (2003) in their numerical simulation of the buoyancy-driven bouncing of a 2-D bubble at a horizontal wall using the direct formulation. Another kind of viscous potential flow analysis of the deformation of a rising 3-D bubble was given by Miksis, Vanden–Broeck, and Keller (1982). They converted their problem into a system of integro-differential equations which they solved under the conditions of small Weber numbers and large Reynolds numbers. Very recently, Gordillo (2008) studied the necking and break-up of a bubble under the action of gravity generated from a submerged vertical nozzle by modifying the code of Rodríguez-Rodríguez et al. (2006) for inviscid fluids to include the viscous effects of the irrotational motion of the liquid through the viscous normal stress at the interface, whereas the rotational effects in the gas (vorticity) are retained through a mechanistic model based upon the incompressible Navier–Stokes equations assuming a slender neck region that splits the gas pressure as an inviscid plus a viscous contribution. Predictions of the instantaneous position of the interface from this code are compared with those from a set of two-dimensional Rayleigh-like equations, deduced with the assumption that the liquid velocity field is irrotational, and excellent agreement was found. These Rayleigh-like equations were used later by Bolaños-Jiménez et al. (2009) to study bubble pinch-off in liquids more viscous than water and good agreement with their experimental data was reported. They justified the hypothesis of an irrotational liquid velocity field by stating that "the velocities induced by any of the possible sources of vorticity in our setup, i.e., the boundary layer at the needle wall and the interface curvature, are much smaller than the typical radial velocities associated to the collapse of the neck."

Lundgren and Mansour (1988) also included the effect of a small viscosity by decomposing the velocity field into the sum of an irrotational and a rotational velocity, in which the former is expressed as the gradient of a potential and the latter is written as the curl of a vector potential. Substitution of this decomposition into the incompressible Navier–Stokes equations and applying order-of-magnitude arguments under the assumption of a thin vortical layer at the free surface of the drop yields a new set of differential equations for the potentials. These equations carry weak viscous effects and are coupled with the boundary integral formulation for potential flow based on the vortex method.

The BEM calculations of Georgescu et al. (2002) and Canot et al. (2003) neglect vorticity but the viscous effects in the purely irrotational flow are not restricted to

small viscosity.

2.2 Direct formulation of the boundary integral method

Consider a three-dimensional region (volume) D bounded by a smooth surface $\mathcal{S}$. Consider any pair of functions ϕ and ψ defined on D and its boundary. Green's second identity may be written for these functions as

$$\int_D \left(\phi\nabla^2\psi - \psi\nabla^2\phi\right) \mathrm{d}\mathcal{V} = \int_{\mathcal{S}} \left(\phi\frac{\partial\psi}{\partial n} - \psi\frac{\partial\phi}{\partial n}\right) \mathrm{d}S. \tag{2.1}$$

where $\partial(\ )/\partial n = \mathbf{n}\cdot\nabla(\ )$, $\mathbf{n}$ being the outward unit normal vector on $\mathcal{S}$. This formula is readily obtained from Green's first identity, which can be regarded as the three-dimensional statement of integration by parts (Strauss, 1992).

Consider the field

$$G(\mathbf{x},\boldsymbol{\xi}) = \frac{1}{4\pi\,|\mathbf{x}-\boldsymbol{\xi}\,|}. \tag{2.2}$$

This function solves Laplace's equation, that is,

$$\nabla^2_{\xi} G = 0 \tag{2.3}$$

for all $\boldsymbol{\xi}$ except for $\boldsymbol{\xi} = \mathbf{x}$. The subscript in (2.3) indicates differentiation with respect to $\boldsymbol{\xi}$. Now, consider a point $\mathbf{x}$ that belongs to D but does not belong to boundary $\mathcal{S}$, and let us define the region D_ϵ as the region left after removing from domain D a "small" ball of radius ϵ centered at $\mathbf{x}$ (Figure 2.1). Also, let ϕ be harmonic. Clearly, function (2.2) is non-singular in D_ϵ and (2.1) can be applied with $\psi = G(\mathbf{x},\boldsymbol{\xi})$, yielding

$$\int_{\mathcal{S}} \left(\phi\frac{\partial G}{\partial n_\xi} - G\frac{\partial\phi}{\partial n_\xi}\right) \mathrm{d}S_\xi + \int_{\mathcal{S}_\epsilon} \left(\phi\frac{\partial G}{\partial n_\xi} - G\frac{\partial\phi}{\partial n_\xi}\right) \mathrm{d}S_\xi = 0, \tag{2.4}$$

because the left-hand side of (2.1) vanishes identically. Here, $\mathcal{S}_\epsilon$ denotes the spherical boundary centered at $\mathbf{x}$ with radius ϵ and $\partial(\ )/\partial n_\xi = \mathbf{n}_\xi\cdot\nabla_\xi(\ )$. Here $\mathbf{n}_\xi$ is the outward unit normal vector to either $\mathcal{S}$ or $\mathcal{S}_\epsilon$ (Figure 2.1). For convenience, let $\mathbf{x}$ be the origin of a spherical coordinate system. Therefore, $G(\mathbf{x},\boldsymbol{\xi}) = 1/(4\pi R)$, where R is the radial coordinate. Moreover,

$$\frac{\partial G}{\partial n_\xi} = -\frac{\partial}{\partial R}\left(\frac{1}{4\pi R}\right) = \frac{1}{4\pi R^2}. \tag{2.5}$$

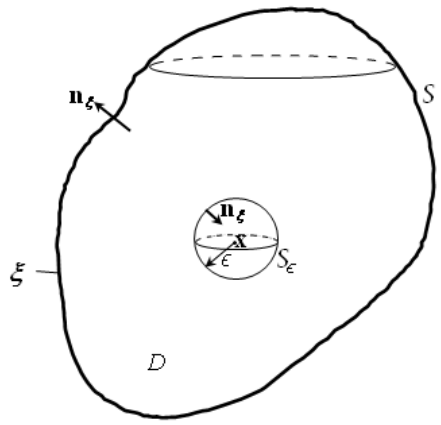

Figure 2.1: Three-dimensional domain D bounded by the smooth surface S containing the sphere $\mathcal{S}_\epsilon$ with radius ϵ centered at point $\mathbf{x}$. The harmonic potential ϕ is defined over the entire region D.

Thus, for the integrals on the sphere $\mathcal{S}_\epsilon$ appearing in (2.4) we have

$$\int_{\mathcal{S}_\epsilon} \phi \frac{\partial G}{\partial n_\xi} \mathrm{d}S_\xi = \frac{1}{4\pi\epsilon^2} \int_{\mathcal{S}_\epsilon} \phi \, \mathrm{d}S_\xi = \langle \phi \rangle, \tag{2.6}$$

and

$$\int_{\mathcal{S}_\epsilon} G \frac{\partial \phi}{\partial n_\xi} \mathrm{d}S_\xi = \frac{1}{4\pi\epsilon} \int_{\mathcal{S}_\epsilon} \frac{\partial \phi}{\partial n_\xi} \mathrm{d}S_\xi = \epsilon \left\langle \frac{\partial \phi}{\partial n_\xi} \right\rangle, \tag{2.7}$$

where "$\langle\ \rangle$" denotes the average of a quantity on the sphere $\mathcal{S}_\epsilon$. After passing the limit as $\epsilon \to 0$ in expressions (2.6) and (2.7), we have

$$\int_{\mathcal{S}_\epsilon} \left(\phi \frac{\partial G}{\partial n_\xi} - G \frac{\partial \phi}{\partial n_\xi} \right) \mathrm{d}S_\xi = \phi(R = 0) = \phi(\mathbf{x}), \tag{2.8}$$

because ϕ is continuous and $\partial\phi/\partial n_\xi$ is bounded (Strauss, 1992). Substitution of (2.8) into (2.4) leads to Green's representation formula

$$\phi(\mathbf{x}) + \int_{\mathcal{S}} \phi(\boldsymbol{\xi}) \frac{\partial G}{\partial n_\xi}(\mathbf{x}, \boldsymbol{\xi}) \mathrm{d}S_\xi = \int_{\mathcal{S}} G(\mathbf{x}, \boldsymbol{\xi}) \frac{\partial \phi}{\partial n_\xi}(\boldsymbol{\xi}) \mathrm{d}S_\xi. \tag{2.9}$$

Taking point $\mathbf{x}$ to boundary $\mathcal{S}$ yields (e.g., Wrobel, 2002)

$$\frac{1}{2}\phi(\mathbf{x}) + \int_{\mathcal{S}} \phi(\boldsymbol{\xi}) \frac{\partial G}{\partial n_\xi}(\mathbf{x}, \boldsymbol{\xi}) \mathrm{d}S_\xi = \int_{\mathcal{S}} G(\mathbf{x}, \boldsymbol{\xi}) \frac{\partial \phi}{\partial n_\xi}(\boldsymbol{\xi}) \mathrm{d}S_\xi. \tag{2.10}$$

This expression is obtained after extending domain D by adding the fraction of a small ball of radius ϵ centered at a point $\mathbf{x}$ located on the smooth surface $\mathcal{S}$. In this extended domain, $\mathbf{x}$ becomes an interior point and expression (2.9) can be used. After passing the limit $\epsilon \to 0$, the original domain is recovered and (2.10) is obtained.

This formula is known as the direct formulation of the boundary integral method. It is our working equation to solve Laplace's equation for the unknown on the boundaries. Notice hat (2.10) involves the distributions of potential ϕ and its normal derivative exclusively on boundary $\mathcal{S}$. For instance, if Dirichlet boundary conditions are imposed, i.e. ϕ is known, then (2.10) can be used to solve for the normal derivative of ϕ on the boundary. For Neumann boundary conditions, one has to exert caution as the solution is unique up to an arbitrary constant and the distribution of the normal derivative of the harmonic potential is constrained by virtue of the divergence theorem. Robin and mixed boundary conditions can also be handled with this boundary integral representation. When both the potential and its normal derivative are known on the boundary, expression (2.9) can be used to obtain the potential at an internal point. Usually, one is interested in applying boundary integral equations to problems in complex geometries, in which case numerical approximations are the best choice. The most commonly used numerical technique to solve boundary integral equations like (2.10) is the boundary element method, which is adopted in the present work.

Expression (2.10) was obtained considering a bounded domain. Turning our attention to the exterior problem, we can write an expression valid for an unbounded domain. Consider again a three-dimensional region D bounded by the smooth surface $\mathcal{S}$. We are interested in finding a boundary integral equation for the harmonic potential ϕ and its normal derivative on the interior boundary $\mathcal{S}$, such that $\phi \sim \phi_\infty$ as $|\mathbf{x}| \to \infty$, where ϕ_∞ is a prescribed function satisfying Laplace's equation for all points of the space. To derive the desire formula, let us assume that volume D is completely immersed within a region bounded by a spherical surface $\mathcal{S}_\infty$ centered at a point $\mathbf{x} \in \mathcal{S}$, and no point of $\mathcal{S}$ belongs to $\mathcal{S}_\infty$. Let D_∞ be the region of the space bounded internally by $\mathcal{S}$ and externally by $\mathcal{S}_\infty$. Define $w \equiv \phi - \phi_\infty$ so that w is harmonic in D_∞ and $w \to 0$ as $|\mathbf{x}| \to \infty$. Applying expression (2.10) to region D_∞ we may write

$$\frac{1}{2}w(\mathbf{x}) + \int_{\mathcal{S}} w(\boldsymbol{\xi})\frac{\partial G}{\partial n_\xi}(\mathbf{x},\boldsymbol{\xi})\mathrm{d}S_\xi + \int_{\mathcal{S}_\infty} w(\boldsymbol{\xi})\frac{\partial G}{\partial n_\xi}(\mathbf{x},\boldsymbol{\xi})\mathrm{d}S_\xi = \int_{\mathcal{S}} G(\mathbf{x},\boldsymbol{\xi})\frac{\partial w}{\partial n_\xi}(\boldsymbol{\xi})\mathrm{d}S_\xi + \int_{\mathcal{S}_\infty} G(\mathbf{x},\boldsymbol{\xi})\frac{\partial w}{\partial n_\xi}(\boldsymbol{\xi})\mathrm{d}S_\xi. \quad (2.11)$$

Choosing a spherical coordinate system centered at $\mathbf{x}$ with radial coordinate R, with $G = 1/(4\pi R)$ and $\partial(\ )/\partial n_\xi = \partial(\ )/\partial R$, where $\mathbf{n}_\xi$ denotes here the outward unit normal vector on $\mathcal{S}_\infty$, one can show that, in the limit $R \to \infty$, both integrals over $\mathcal{S}_\infty$ in (2.11) vanish identically, provided w satisfy the regularity condition $w \sim 1/R$ as $R \to \infty$ (Wrobel, 2002).

Expression (2.11) thus becomes

$$\frac{1}{2}\phi(\mathbf{x}) - \frac{1}{2}\phi_\infty(\mathbf{x}) + \int_{\mathcal{S}} \phi(\boldsymbol{\xi}) \frac{\partial G}{\partial n_\xi}(\mathbf{x}, \boldsymbol{\xi}) \mathrm{d}S_\xi - \int_{\mathcal{S}} \phi_\infty(\boldsymbol{\xi}) \frac{\partial G}{\partial n_\xi}(\mathbf{x}, \boldsymbol{\xi}) \mathrm{d}S_\xi = \int_{\mathcal{S}} G(\mathbf{x}, \boldsymbol{\xi}) \frac{\partial \phi}{\partial n_\xi}(\boldsymbol{\xi}) \mathrm{d}S_\xi - \int_{\mathcal{S}} G(\mathbf{x}, \boldsymbol{\xi}) \frac{\partial \phi_\infty}{\partial n_\xi}(\boldsymbol{\xi}) \mathrm{d}S_\xi. \quad (2.12)$$

By virtue of (2.10), ϕ_∞ satisfies

$$\int_{\mathcal{S}} \phi_\infty(\boldsymbol{\xi}) \frac{\partial G}{\partial n_\xi}(\mathbf{x}, \boldsymbol{\xi}) \mathrm{d}S_\xi - \int_{\mathcal{S}} G(\mathbf{x}, \boldsymbol{\xi}) \frac{\partial \phi_\infty}{\partial n_\xi}(\boldsymbol{\xi}) \mathrm{d}S_\xi = -\int_{\mathcal{S}} \phi_\infty(\boldsymbol{\xi}) \frac{\partial G}{\partial n_\xi^*}(\mathbf{x}, \boldsymbol{\xi}) \mathrm{d}S_\xi + \int_{\mathcal{S}} G(\mathbf{x}, \boldsymbol{\xi}) \frac{\partial \phi_\infty}{\partial n_\xi^*}(\boldsymbol{\xi}) \mathrm{d}S_\xi = \frac{1}{2}\phi_\infty(\mathbf{x}) \quad (2.13)$$

where $\mathbf{n}_\xi^* = -\mathbf{n}_\xi$ is the outward unit normal vector to D on $\mathcal{S}$. Thus, (2.12) finally becomes

$$\frac{1}{2}\phi(\mathbf{x}) + \int_{\mathcal{S}} \phi(\boldsymbol{\xi}) \frac{\partial G}{\partial n_\xi}(\mathbf{x}, \boldsymbol{\xi}) \mathrm{d}S_\xi = \phi_\infty(\mathbf{x}) + \int_{\mathcal{S}} G(\mathbf{x}, \boldsymbol{\xi}) \frac{\partial \phi}{\partial n_\xi}(\boldsymbol{\xi}) \mathrm{d}S_\xi. \quad (2.14)$$

which is our working equation for the exterior potential problem, that is, for ϕ satisfying Laplace's equation in a domain that extends unbounded towards infinity where ϕ behaves as ϕ_∞, and with suitable boundary conditions prescribed on an inner boundary $\mathcal{S}$.

2.3 Problem formulation and numerical method

In what follows, we adopt the notation used in the inviscid analysis by Rodríguez-Rodríguez et al. (2006) for the most part. Differences with their formulation arise with the inclusion here of the viscous effects of the irrotational motion, which are not considered in their work. Regarding the numerical method, the algorithm we applied in this work follows the major steps of the algorithm presented by those authors. However, the numerical technics applied here in the implementation of several of these steps differ from those employed by Rodríguez-Rodríguez et al. (2006).

2.3.1 Statement of the problem

Consider a bubble or drop initially of spherical shape with radius a containing an incompressible Newtonian fluid of density ρ_i and viscosity μ_i and immersed in an unbounded incompressible Newtonian fluid of density ρ_e and viscosity μ_e. The entire smooth interface $\mathcal{S}$ is characterized by a uniform surface tension γ. It will be assumed that the bubble or drop moves with the mean velocity of the flow. With respect to a reference frame that moves with this mean velocity, we will describe the evolution of the bubble or drop interface as a result of a steady uniaxial extensional flow. That is, far away from the interface, the following velocity potential is prescribed

$$\hat{\phi}_\infty = \frac{M}{a}\left(2\hat{z}^2 - \hat{r}^2\right), \tag{2.15}$$

and the corresponding (irrotational) velocity field is $\hat{\mathbf{u}}_\infty = \hat{\nabla}\hat{\phi}_\infty$. In representing the problem, we have adopted a cylindrical coordinate system $(\hat{z}, \hat{r}, \zeta)$, in which the $\hat{z}$-axis is coincident with the axis of symmetry and $\hat{\zeta}$ is the azimuthal angle about the z-axis (figure 2.3). From the potential in (2.15), the strain rate along the $\hat{z}$-direction, which is a principal direction, is $\partial^2\hat{\phi}/\partial\hat{z}^2 = 4M/a$, whereas the stain rates along the other two principal axes are the same and equal to $-2M/a$. Thus, the parameter M determines the magnitude of the principal strain rates. In formulating the problem, we also make the usual assumption of neglecting the effects of gravity including those associated with the variation of the hydrostatic pressure. This is a necessary condition for the interface deformation to be axisymmetric as discussed in Ramaswamy and Leal (1997). In order to write the governing equations in dimensionless form, the magnitudes $a, a/(8M)$ and $\rho_e(8M)^2$ are adopted as the characteristic length, time and pressure scales, respectively.

We will also assumed that the inner and outer velocity fields are irrotational for all times. Hence, conservation of mass leads to a pair of Laplace's equations

$$\nabla^2\phi_i = 0, \qquad \nabla^2\phi_e = 0, \tag{2.16}$$

where the subscripts i and e denote the inner and outer fluids, respectively. Dimensionless variables are written with no "ˆ". For the irrotational motion of a viscous fluid, as discussed in §1.1, conservation of linear momentum is given by the Bernoulli's equation

$$\Lambda\left(\frac{\partial\phi_i}{\partial t} + \frac{|\nabla\phi_i|^2}{2}\right) + p_i = 0, \qquad \frac{\partial\phi_e}{\partial t} + \frac{|\nabla\phi_e|^2}{2} + p_e = 0, \tag{2.17}$$

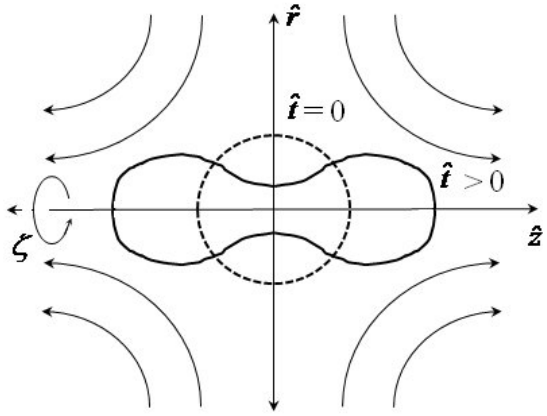

Figure 2.2: Two-phase flow system considered in this study: A bubble or drop of an incompressible fluid being deformed by an axially symmetric extensional incompressible flow. The shape of the interface is initially spherical.

for the inner and outer flows, respectively, and $\Lambda = \rho_i/\rho_e$. The solution of (2.16) and (2.17) must satisfy the following boundary conditions for points at the interface

$$\frac{\partial \phi_i}{\partial n_i} = -\frac{\partial \phi_e}{\partial n_e}, \tag{2.18}$$

$$\left[-p_e + \frac{2}{\mathrm{Re}}\frac{\partial^2 \phi_e}{\partial n_i^2}\right] - \left[-p_i + \frac{2\beta}{Re}\frac{\partial^2 \phi_i}{\partial n_i^2}\right] = \frac{1}{We}\nabla_{\|} \cdot \mathbf{n}_i, \tag{2.19}$$

where the former establishes continuity of the normal velocity across the interface and the latter expresses that the jump of normal stresses across the interface is balanced by surface tension forces. Both are adapted from (1.12) and (1.13). Here, $\beta = \mu_i/\mu_e$, and the dimensionless numbers $Re = \rho_e(8M)a/\mu_e$ and $We = \rho_e(8M)^2 a/\gamma$ are the Reynolds and Weber numbers, respectively. The first number represents the ratio of inertia to viscous forces and the second represents the ratio of inertia to surface tension forces. In equations (2.18) and (2.19), $\mathbf{n}_i$ is the unit vector normal to the interface pointing away from the inner fluid and $\mathbf{n}_e$ is the unit vector normal to the interface pointing towards the inner fluid, thus $\mathbf{n}_i = -\mathbf{n}_e$ (figure 2.3). Moreover, n_i (n_e) is the dimensionless coordinate along and increasing in the direction of $\mathbf{n}_i$ ($\mathbf{n}_e$). Notice that the term added to the pressure within the brackets corresponds to the viscous normal stress on this or that side of interface $\mathcal{S}$. Obviously, these terms, which account for the viscous effects of the irrotational motion, were not considered in the inviscid analysis by Rodríguez-Rodríguez et al.

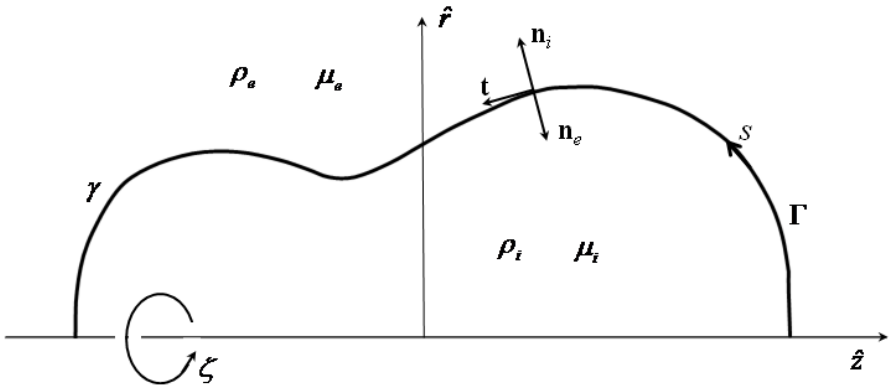

Figure 2.3: Sketch of the axially symmetric domain showing the cylindrical coordinate system $(\hat{z}, \hat{r}, \zeta)$ and the local orthogonal curvilinear coordinate system (n_i, s, ζ). Curve Γ represents the intersection of the axisymmetric interface $\mathcal{S}$ with a plane containing the z-axis. The material properties of the inner and outer fluids, as defined in §2.3.1, are included.

(2006).

The notation used in (2.19) for the normal component of the viscous stress comes from standard vector differential formulae presented in terms of a local orthogonal curvilinear coordinate system (see Batchelor, 1967, Appendix 2) that describes the position of points on the interface and includes coordinate n_i as defined above. With this aid, one can readily show that the normal component of the dimensionless strain rate at points on the interface can be written as

$$\mathbf{n}_i \cdot \nabla \otimes \nabla \phi_{(i,e)} \cdot \mathbf{n}_i = \frac{\partial^2 \phi_{(i,e)}}{\partial n_i^2} \tag{2.20}$$

and the two subscripts i and e are needed because this quantity, in general, is discontinuous across the interface (see below). This identity has been used in (2.19).

For an axisymmetric problem, it is convenient to introduce the set of local orthogonal curvilinear coordinates (n_i, s, ζ), where n_i and ζ have been defined above and s is the (dimensionless) arc length measured on a meridian curve Γ that results from the intersection of the surface $\mathcal{S}$ representing the interface with a plane containing the axis of symmetry (z-axis); s increases in the counterclockwise direction according to figure 2.3. Because $\partial(\ )/\partial\zeta = 0$, and using Laplace's equations for the potentials $\phi_{(i,e)}$ written in terms of these curvilinear coordinates, one can show that

$$\mathbf{n}_i \cdot \nabla \otimes \nabla\phi \cdot \mathbf{n}_i = \frac{\partial^2 \phi}{\partial n_i^2} = -\frac{\partial^2 \phi}{\partial s^2} + 2\kappa \frac{\partial \phi}{\partial n_i} - \frac{1}{r}\frac{\partial r}{\partial s}\frac{\partial \phi}{\partial s}, \qquad \text{for } r > 0, \text{ and} \tag{2.21a}$$

$$\mathbf{n}_i \cdot \nabla \otimes \nabla\phi \cdot \mathbf{n}_i = \frac{\partial^2 \phi}{\partial n_i^2} = -2\frac{\partial^2 \phi}{\partial s^2} + 2\kappa \frac{\partial \phi}{\partial n_i}, \qquad \text{for } r = 0, \tag{2.21b}$$

where κ denotes the mean curvature of the interface (see below). For simplicity, ϕ is written in (2.21) without subscripts (i, e). Notice that even though $\partial\phi/\partial n_i$ is continuous across the interface by condition (2.18), the second derivatives $\partial^2\phi_i/\partial n_i^2 \neq \partial^2\phi_e/\partial n_i^2$, in general, because tangential derivatives $\partial\phi/\partial s$ and $\partial^2\phi/\partial s^2$ are discontinuous as a consequence of the jump in potential ϕ.

Regarding the surface tension term in the right-hand side of (2.19), as mentioned in §1.1, the term $-\nabla_\parallel \cdot \mathbf{n}_i$ equals twice the mean curvature κ of the surface at a point. By using the set of orthogonal coordinates (n_i, s, ζ), we have

$$-\nabla_\parallel \cdot \mathbf{n}_i = 2\kappa = -\frac{\partial z}{\partial s}\frac{\partial^2 r}{\partial s^2} + \frac{\partial r}{\partial s}\frac{\partial^2 z}{\partial s^2} + \frac{1}{r}\frac{\partial z}{\partial s}, \qquad \text{for } r > 0, \text{ and} \tag{2.22a}$$

$$-\nabla_\parallel \cdot \mathbf{n}_i = 2\kappa = 2\frac{\partial^2 z}{\partial s^2}, \qquad \text{for } r = 0, \tag{2.22b}$$

where the latter expression is obtained by recognizing that $\partial z/\partial s = 0$ and $\partial r/\partial s = 1$ at $r = 0$. Similar expressions to those in (2.21) and (2.22) have been presented by Georgescu et al. (2002).

Turning now to the evolution of the interface, let $\mathbf{u}_\mathcal{S} = \mathrm{d}\mathbf{x}/\mathrm{d}t$ be the velocity of the interface $\mathcal{S}$ at point $\mathbf{x}$. By writing it in terms of its components

$$\mathbf{u}_\mathcal{S} = (\mathbf{u}_\mathcal{S} \cdot \mathbf{n}_i)\mathbf{n}_i + (\mathbf{u}_\mathcal{S} \cdot \mathbf{t})\mathbf{t}, \tag{2.23}$$

where $\mathbf{t}$ is the unit vector tangential to $\mathcal{S}$ along the s direction, with $\mathbf{u}_\mathcal{S} \cdot \mathbf{n}_i = \partial\phi/\partial n_i = \partial\phi_i/\partial n_i = \partial\phi_e/\partial n_i$ by continuity of the normal velocity component, and setting

$$\mathbf{u}_\mathcal{S} \cdot \mathbf{t} = 0 \tag{2.24}$$

arbitrarily because this tangential component is irrelevant in tracking the motion of the interface as commented in §1.1, the position of surface particles can be obtained from the equation

$$\frac{\mathrm{d}\mathbf{x}}{\mathrm{d}t} = \frac{\partial \phi}{\partial n_i}\mathbf{n}_i, \qquad \mathbf{x} \in \mathcal{S}. \tag{2.25}$$

Choices other than (2.24) are found in the literature for the tangential velocity $\mathbf{u}_\mathcal{S} \cdot \mathbf{t}$. For instance, Heister (1997) set this value equal to the tangential velocity

of the inner fluid at the boundary, whereas Leppinen and Lister (2003) used the average of the inner and outer fluid tangential velocities.

Finally, in the far field $(|z|, r) \to \infty$,

$$\phi_e \to \phi_\infty(z, r) = \frac{z^2}{4} - \frac{r^2}{8}. \tag{2.26}$$

The set of equations (2.16)-(2.17), together with boundary conditions (2.18),(2.19), (2.25) and (2.26) describe the evolution of the interface of the bubble or drop starting from an initial state that has $\mathcal{S}$ as a sphere of unit radius. The prescription of the initial conditions is discussed below. In the next subsection, the partial differential equations (2.16) are recast as boundary integral equations and those in (2.17) are written in a way that is convenient for time integration using the boundary conditions. Notice that the dimensionless parameters governing the problem are the Reynolds number Re, the Weber number We, and the density and viscosity ratios, Λ and β, respectively, and need to be prescribed.

2.3.2 Formulation of the boundary integral equations

Conservation of mass for an incompressible irrotational flow led to Laplace's equations (2.16) for the inner and outer regions. Instead of solving these equations, we can consider two boundary integrals equations, one for the inner region given in (2.10) and one for the outer region given in (2.14), obtained from Green's representation formula as discussed in §2.2. These integral equations involve the values of the potential and its normal derivative only at the surface representing the interface. For an axisymmetric problem, it turns out that the surface integrals can be simplified by considering integration in the azimuthal direction. To illustrate this, it is convenient to introduce the spherical coordinate system (σ, θ, ζ), where σ is the radial coordinate, with $\sigma = 0$ coincident with the origin of our original cylindrical coordinate system $(z = 0, r = 0)$; θ is the polar angle ($\theta = 0$ coincides with the positive z semi-axis), and ζ is the azimuthal angle as defined above. Using this coordinate system, the integrals in (2.10) and (2.14) become

$$\begin{aligned}\int_{\mathcal{S}} G(\mathbf{x}, \boldsymbol{\xi}) \frac{\partial \phi}{\partial n_{i,\xi}}(\boldsymbol{\xi}) \mathrm{d}S_\xi &= \int_{\theta=0}^{\pi} \left[\int_{\zeta=0}^{2\pi} G(\mathbf{x}, \boldsymbol{\xi}) \mathrm{d}\zeta \right] \frac{\partial \phi}{\partial n_{i,\xi}}(\boldsymbol{\xi}) \sigma^2 \sin\theta \mathrm{d}\theta \\ &= \int_{\Gamma} \left[\int_{\zeta=0}^{2\pi} G(\mathbf{x}, \boldsymbol{\xi}) \mathrm{d}\zeta \right] \frac{\partial \phi}{\partial n_{i,\xi}}(\boldsymbol{\xi}) R \mathrm{d}s_\xi \end{aligned} \tag{2.27a}$$

and

$$\int_{\mathcal{S}} \frac{\partial G}{\partial n_{i,\xi}}(\mathbf{x},\boldsymbol{\xi})\phi(\boldsymbol{\xi})\mathrm{d}S_\xi = \int_{\theta=0}^{\pi}\left[\int_{\zeta=0}^{2\pi}\frac{\partial G}{\partial n_{i,\xi}}(\mathbf{x},\boldsymbol{\xi})\mathrm{d}\zeta\right]\phi(\boldsymbol{\xi})\sigma^2\sin\theta\mathrm{d}\theta$$
$$= \int_{\Gamma}\left[\int_{\zeta=0}^{2\pi}\frac{\partial G}{\partial n_{i,\xi}}(\mathbf{x},\boldsymbol{\xi})\mathrm{d}\zeta\right]\phi(\boldsymbol{\xi})R\mathrm{d}s_\xi \tag{2.27b}$$

where $\mathbf{x}=(z,r)$ and $\boldsymbol{\xi}=(Z,R)$ are points on the surface boundary $\mathcal{S}$ and integration takes place over $\boldsymbol{\xi}$ with $\mathbf{x}$ fixed. We used $R=\sigma\sin\theta$ and $\mathrm{d}s_\xi=\sigma\mathrm{d}\theta$. Notation $\partial\phi_i/\partial n_{i,\xi}=\mathbf{n}_i\cdot\nabla_\xi\phi_i$ with $\mathbf{n}_i$ at point $\boldsymbol{\xi}$.

The integrals in the azimuthal direction ζ (within brackets) in (2.27) can be carried out analytically resulting in expressions involving complete elliptic integrals, which are written below (see, for instance, Jaswon and Symm, 1977, or Becker, 1992). Therefore, the surface integrals are reduced to line integrals over the plane curve Γ (figure 2.3). With this reduction in the dimensionality of the problem, for a point $\mathbf{x}=(z,r)$ on this smooth curve, the following integral equations can be written

$$\phi_i(\mathbf{x}) = \int_\Gamma g_i(\mathbf{x},\boldsymbol{\xi})\frac{\partial\phi_i}{\partial n_{i,\xi}}(\boldsymbol{\xi})\mathrm{d}s_\xi - \int_\Gamma h_i(\mathbf{x},\boldsymbol{\xi})\phi_i(\boldsymbol{\xi})\mathrm{d}s_\xi, \tag{2.28}$$

and

$$\phi_e(\mathbf{x}) = 2\phi_\infty(\mathbf{x}) + \int_\Gamma g_e(\mathbf{x},\boldsymbol{\xi})\frac{\partial\phi_e}{\partial n_{e,\mathbf{x}}}(\boldsymbol{\xi})\mathrm{d}s_\xi - \int_\Gamma h_e(\mathbf{x},\boldsymbol{\xi})\phi_e(\boldsymbol{\xi})\mathrm{d}s_\xi, \tag{2.29}$$

for the inner and outer domains, respectively. Integration occurs over points $\boldsymbol{\xi}=(Z,R)$ on the boundary Γ. The axisymmetric kernels are

$$g_{(i,e)} = \frac{2R}{\pi A^{1/2}}K(m), \tag{2.30a}$$

$$h_{(i,e)} = \frac{2RE(m)}{\pi A^{1/2}}\left[\frac{n^r_{(i,e)}}{2R}+\frac{(z-Z)n^z_{(i,e)}+(r-R)n^r_{(i,e)}}{B}\right] - \frac{K(m)n^r_{(i,e)}}{\pi A^{1/2}}, \tag{2.30b}$$

where $K(m)$ and $E(m)$ are the complete elliptic integrals of the first and second kind, respectively, and

$$A=(r+R)^2+(z-Z)^2, \qquad B=(r-R)^2+(z-Z)^2, \qquad m=\frac{4Rr}{A}, \tag{2.31}$$

where n_i^z and n_i^r denote the projections of $\mathbf{n}_i$ at point $\boldsymbol{\xi}$ in the z and r directions,

respectively. Moreover,

$$g_e = g_i, \qquad h_e = -h_i, \tag{2.32}$$

because the boundary is common for the inner and outer fluids, so that $\mathbf{n}_i = -\mathbf{n}_e$. The dependence of $g_{(i,e)}$ and $h_{(i,e)}$ on $\mathbf{x}$ and $\boldsymbol{\xi}$ is implicit here.

2.3.3 Differential equations tracking the evolution of the interface

We may write two scalar equations resulting from the projection of the kinematic condition (2.25) onto the axial and radial directions, respectively. This leads to

$$\frac{\mathrm{d}z}{\mathrm{d}t} = n_i^z \frac{\partial \phi}{\partial n_i}, \qquad \frac{\mathrm{d}r}{\mathrm{d}t} = n_i^r \frac{\partial \phi}{\partial n_i}. \tag{2.33}$$

Therefore, points at the interface evolved in time by moving them normal to the interface.

To track the time evolution of a scalar field defined on points moving with the interface, let us consider f to be any smooth field defined on a domain enclosing the entire interface $\mathcal{S}$. If $\mathbf{x}$ is a point on the interface, differentiation of $f(\mathbf{x}(t), t)$ with respect to time yields

$$\frac{\mathrm{d}f}{\mathrm{d}t} = \frac{\partial f}{\partial t} + \mathbf{u}_{\mathcal{S}} \cdot \nabla f = \frac{\partial f}{\partial t} + (\mathbf{u}_{\mathcal{S}} \cdot \mathbf{n}_i)\mathbf{n}_i \cdot \nabla f = \frac{\partial f}{\partial t} + \frac{\partial \phi}{\partial n_i}\frac{\partial f}{\partial n_i}, \tag{2.34}$$

according to decomposition (2.23) and the discussion following it. Expression (2.34) establishes that quantities for points at the interface are advected by the normal component of the velocity. Notice that it is not possible to define a material derivative in terms of the velocity vector for points at the interface by virtue of the jump in the tangential velocities, $\partial\phi_i/\partial s \neq \partial\phi_e/\partial s$ as a result of the discontinuity of the velocity potential across the interface.

Assume now that velocity potentials $\phi_{(i,e)}$ both belong to the same class of functions as f. Therefore, by expression (2.34) and continuity of normal velocities, we can write

$$\frac{\mathrm{d}\phi_{(i,e)}}{\mathrm{d}t} = \frac{\partial \phi_{(i,e)}}{\partial t} + \left(\frac{\partial \phi}{\partial n_i}\right)^2. \tag{2.35}$$

Introducing the difference function,

$$\varphi \equiv \phi_e - \Lambda\phi_i, \tag{2.36}$$

and eliminating the pressures in (2.19) by used of Bernoulli's equations (2.17), we

find, after rearranging terms using (2.35),

$$\frac{\mathrm{d}\varphi}{\mathrm{d}t} = \frac{1}{We}\nabla_{\parallel}\cdot\mathbf{n}_i + \frac{1}{2}(1-\Lambda)\left(\frac{\partial\phi}{\partial n_i}\right)^2 - \frac{1}{2}\left[\left(\frac{\partial\phi_e}{\partial s}\right)^2 - \Lambda\left(\frac{\partial\phi_i}{\partial s}\right)^2\right] - \frac{2}{Re}\left[\frac{\partial^2\phi_e}{\partial n_i^2} - \beta\frac{\partial^2\phi_i}{\partial n_i^2}\right], \tag{2.37}$$

for the rate of change of φ for points that advance in time according to (2.33).

Integration of the set of differential equations (2.33) and (2.37), which are coupled with (2.28) and (2.29), gives the shape of the interface after start-up. In order to solve this system of equations, we prescribe an initial shape and the distribution of φ on the interface. Initially, we consider the bubble (drop) to have a spherical interface. For φ, we choose

$$\varphi = 0. \tag{2.38}$$

To justify this choice, consider a spherical bubble (drop) immersed in an unbounded incompressible fluid and assume that the inner and outer fluids are at rest with respect to a frame that moves with the mean velocity of the flow (see §2.3.1). In the absence of gravity, this is a stable condition, in the sense that it will not change with time. It is also an irrotational solution of the Navier–Stokes equations. The velocity potentials ϕ_i and ϕ_e can take each the value of an arbitrary constant. Let us choose $\phi_e = 0$ for convenience. Therefore, according to (2.36), φ will be constant over the spherical interface. In order to modify this state, an external agent must act. Consider that this state of rest is the state of the system for time $t < 0$, say, where $t = 0$ is an arbitrary reference time. If at time $t = 0$, a steady uniaxial extensional flow abruptly starts in the far field as a result of a step change in parameter M from zero to $M > 0$ in the expression for the velocity potential $\hat{\phi}_\infty$ in (2.15), the bubble (drop) will begin to deform. It is reasonable to assume a continuous variation of φ with time across the instant of start-up $t = 0$. We have said that φ is a constant for $t < 0$. With this criterion and because the choice for the constant is arbitrary, we choose (2.38) as the initial condition ($t = 0$) for all points over the (spherical) boundary. Notice that $\partial\phi_{(i,e)}/\partial n_i$ is not zero everywhere on the interface at $t = 0$ immediately after start-up since the velocity potential ϕ_e is governed by Laplace's equation and must tend to ϕ_∞ in the far field.

The set of equations (2.33) and (2.37) can be integrated numerically with initial condition (2.38) and the boundary points (z, r) starting from the semicircle $z^2+r^2 = 1$, $r \geqslant 0$, to track the deformation of the interface as time advances. In the next section, we show, within the framework of the numerical method, that knowing the

position of the boundary and the distribution of φ on it, at a given time, suffices to determine, via equations (2.28) and (2.29), the distribution of potentials ϕ_i and ϕ_e, and the normal derivative $\partial\phi/\partial n_i$, for points on the boundary.

2.3.4 Numerical method

Considering that the bubble or drop will undergo large deformations depicting somewhat complex shapes driven by the uniaxial extensional flow imposed in the far field, the solution of the system of equations established in §§2.3.2 and 2.3.3 must be sought by numerical means. In this section, we describe how the approximate solution methods for these equations may be implemented in a computer program. This program will perform three major tasks, namely,

- Implementation of the boundary element method to solve the system of integral equations for the fluids normal velocity component at the interface at a given time. This requires discretization of the interface; interpolation of the geometry, potential and normal derivative of the potential; numerical evaluation of the integrals, and assembling and solution of two linear systems of algebraic equations obtained with the collocation method.

- Numerical integration of the system of differential equations governing the time evolution of discrete points on the interface to obtain its position at discrete times. Adaptive time stepping is implemented in this stage.

- Refinement and smoothing of the grid to improve resolution in regions of the curve approaching the axis of symmetry when pinch-off is imminent and to avoid interfacial instabilities of numerical origin.

These stages are coupled. The solution of the potential problem as described in the first task must be accomplished for each time step. Its results are used in the time integration procedure to march to the next time level. Then, the updated boundary position and potential distribution are inputs for the potential problem solver to perform again and a cycle is established. Refinement and smoothing of the mesh does not necessarily occur after each time step.

Here, we adopt the general algorithm originally presented by Rodríguez-Rodríguez et al. (2006) with several modifications in the details of its implementation. In various parts of the procedure, we make choices of numerical methods that differ from those selected by those authors. The details on the implementation of the stages listed above are presented in the following subsections.

Solution of the set of integral equations with the boundary element method

In this section we seek numerical solutions of the system of boundary integral equations (2.28) and (2.29) by means of the boundary element method using the collocation approach.

The curve representing the interface is divided into N connected subintervals or "elements". In this analysis, the end points of each element are considered as "nodal points" or simply "nodes". No nodal points are placed in the interior of the element. The values of the spatial coordinates and field variables (potential and normal derivative of the potential) are stored at the nodes and the advancing of the interface will be given discretely by the advancing of the nodes. Two consecutive elements share a node. Therefore, there are $N+1$ nodes after subdivision including one at each end of the open curve Γ on the axis of symmetry. The values of the variables stored at a given node are shared by the two elements having that node at their ends. This type of element is called "continuous". Nodes are labeled in sequential ascending order starting with 1 up to $N+1$, increasing in the counterclockwise direction (figure 2.3). Hence the jth-element is bounded by the nodal points j and $j+1$. We also introduce the local bookkeeping index α for the jth-element by identifying the nodes j and $j+1$ with the tags $\alpha=1$ and $\alpha=2$, respectively, on that element. This local element-wise notation is convenient because it allows easier generalization of the discrete equations if one wishes to use higher order approximations for the field variables over the element.

After subdivision, the integrals (2.28) and (2.29) over the entire curve Γ can be expressed as a sum of integrals over the N elements. That is, with no approximation,

$$\int_\Gamma g\,\frac{\partial\phi}{\partial n_{i,\xi}}\;\mathrm{d}s_\xi=\sum_{j=1}^{N}\int_{\Gamma_j} g\,\frac{\partial\phi}{\partial n_{i,\xi}}\;\mathrm{d}s_\xi,\qquad \int_\Gamma h\,\phi\;\mathrm{d}s_\xi=\sum_{j=1}^{N}\int_{\Gamma_j} h\,\phi\;\mathrm{d}s_\xi \tag{2.39}$$

The variation of the geometry and field variables must be described over each element. To approximate the geometry of curve Γ, the values of the coordinates (z,r) are interpolated between nodes using quintic splines taking ℓ as the spline parameter. The values of ℓ at the nodes, ℓ_j say, are computed from the linear distance between consecutive nodes,

$$\ell_{j+1}-\ell_j=\sqrt{(z_{j+1}-z_j)^2+(r_{j+1}-r_j)^2},$$

with $\ell_1=0$. Therefore, the values of ℓ_j for $1\leqslant j\leqslant N$ can be determined given the nodes coordinates. The interpolating quintic splines for z and r are given by the

piecewise polynomials

$$S_z^{(j)}(\ell) = z_j + \sum_{m=1}^{5} C_{z,m}^{(j)}(\ell - \ell_j)^m \tag{2.40a}$$

$$S_r^{(j)}(\ell) = r_j + \sum_{m=1}^{5} C_{r,m}^{(j)}(\ell - \ell_j)^m \tag{2.40b}$$

for $\ell_j \leqslant \ell < \ell_{j+1}$ and $1 \leqslant j \leqslant N$. Here, at a given instant of time, coordinates (z_j, r_j) are known for all nodes and the splines satisfy $z_j = S_z^{(j)}(\ell_j)$ and $r_j = S_r^{(j)}(\ell_j)$ with $z_{N+1} = S_z^{(N)}(\ell_{N+1})$ and $r_{N+1} = S_r^{(N)}(\ell_{N+1})$. Piecewise polynomials (2.40) are used to interpolate z and r within the jth-element, that is,

$$z(\ell) = S_z^{(j)}(\ell) \qquad \text{and} \qquad r(\ell) = S_r^{(j)}(\ell),$$

for $\ell_j \leqslant \ell < \ell_{j+1}$. For the interior nodes (z_j, r_j), with $2 \leqslant j \leqslant N$, continuity of derivatives $\mathrm{d}^p S_z^{(j)}/\mathrm{d}\ell^p$ and $\mathrm{d}^p S_r^{(j)}/\mathrm{d}\ell^p$ for $1 \leqslant p \leqslant 4$ is enforced. In addition, since the surface $\mathcal{S}$ is a surface of revolution, certain attributes of the smooth plane curve Γ at the end points can be used to set the following boundary conditions for the splines

$$\mathrm{d}S_z^{(1)}/\mathrm{d}\ell = \mathrm{d}^3 S_z^{(1)}/\mathrm{d}\ell^3 = 0, \qquad \mathrm{d}^2 S_r^{(1)}/\mathrm{d}\ell^2 = \mathrm{d}^4 S_r^{(1)}/\mathrm{d}\ell^4 = 0, \tag{2.41a}$$

for $\ell = 0$, and

$$\mathrm{d}S_z^{(N)}/\mathrm{d}\ell = \mathrm{d}^3 S_z^{(N)}/\mathrm{d}\ell^3 = 0, \quad \mathrm{d}^2 S_r^{(N)}/\mathrm{d}\ell^2 = \mathrm{d}^4 S_r^{(N)}/\mathrm{d}\ell^4 = 0, \tag{2.41b}$$

for $\ell = \ell_{N+1}$, as a result of the even character of z and odd character of r at $r = 0$, where curve Γ touches the axis of symmetry. With these boundary conditions, the set of spline coefficients $C_{z,m}^{(j)}$ and $C_{r,m}^{(j)}$ in (2.40) are uniquely determined. Details on these calculations are presented in Appendix A.

Linear variation with arc-length s is assumed for the field variables over the j-th element

$$\phi(s) = \phi_{1,j} f_{1,j}(s) + \phi_{2,j} f_{2,j}(s), \qquad q(s) = q_{1,j} f_{1,j}(s) + q_{2,j} f_{2,j}(s) \tag{2.42}$$

where $q_{\alpha,j} = (\partial\phi/\partial n_i)_{\alpha,j}$, with $\alpha = 1, 2$, and shape functions

$$f_{1,j}(s) = \frac{s_{2,j} - s}{\Delta s_j}, \qquad f_{2,j}(s) = \frac{s - s_{1,j}}{\Delta s_j}. \tag{2.43}$$

Here, local element-based notation is used for convenience and indices $\alpha = 1$ and 2 refer to nodes 1 and 2 of the jth-element and Δs_j is the length of this element. As explained above, this notation implies that $\phi_{1,j} = \phi_j$ and $\phi_{2,j} = \phi_{j+1}$ and similarly for q, s and ℓ.

The length $s - s_{1,j}$ of the arc within the j-th element associated with the interval $(\ell_{1,j}, \ell)$, with $\ell_{1,j} < \ell < \ell_{2,j}$ is given by

$$s(\ell) - s_{1,j} = \int_{\ell_{1,j}}^{\ell} \sqrt{\left(\frac{\mathrm{d}z}{\mathrm{d}\tilde{\ell}}\right)^2 + \left(\frac{\mathrm{d}r}{\mathrm{d}\tilde{\ell}}\right)^2}\, \mathrm{d}\tilde{\ell}. \tag{2.44}$$

The derivatives of z and r are approximated using the spline interpolation (2.40). By letting $\ell = \ell_{2,j}$, this expression gives the element length, $\Delta s_j = s_{2,j} - s_{1,j}$. The integral is evaluated in an approximate manner using standard Gauss-Legendre quadrature (see below).

Turning now to the complete elliptic integrals $K(m)$ and $E(m)$ appearing in the kernels (2.30), function $E(m)$ is bounded in $0 \leqslant m \leqslant 1$, but function $K(m)$ shows a logarithmic singularity and grows unbounded as $m \to 1$. However, this singularity is integrable in the classical sense. Evaluation of these elliptic integrals is carried out with the explicit formulae found in Abramowitz and Stegun (1964), valid for $0 \leqslant m < 1$ and with errors of $O(10^{-8})$,

$$K(m) \approx A_c(m_1) + B_c(m_1) \ln(1/m_1) \tag{2.45a}$$

$$E(m) \approx \tilde{A}_c(m_1) + \tilde{B}_c(m_1) \ln(1/m_1)\,, \tag{2.45b}$$

where,

$$m_1 = 1 - m = \frac{B}{A}, \tag{2.46}$$

and A, B and m are given in (2.31). A_c, B_c, $\tilde{A}_c$ and $\tilde{B}_c$ are known fourth-order degree polynomials in m_1.

The integrals over the j-th element appearing in expressions (2.39) may thus be written as

$$\int_{\Gamma_j} g\, \frac{\partial \phi}{\partial n_{i,\xi}}\, \mathrm{d}s_\xi \approx \sum_{\alpha=1}^{2} q_{\alpha,j} \int_{\ell_{1,j}}^{\ell_{2,j}} f_{\alpha,j}\, g\, J\, \mathrm{d}\ell, \quad \int_{\Gamma_j} h\, \phi\, \mathrm{d}s_\xi \approx \sum_{\alpha=1}^{2} \phi_{\alpha,j} \int_{\ell_{1,j}}^{\ell_{2,j}} f_{\alpha,j}\, h\, J\, \mathrm{d}\ell, \tag{2.47}$$

with Jacobian

$$J(\ell) = \sqrt{\left(\frac{\mathrm{d}z}{\mathrm{d}\ell}\right)^2 + \left(\frac{\mathrm{d}r}{\mathrm{d}\ell}\right)^2}, \tag{2.48}$$

and again the derivatives of z and r are computed using the spline interpolation

(2.40). With the above expressions, boundary integral equations (2.28) and (2.29) may be expressed as

$$\begin{aligned}\phi(\mathbf{x}) = \psi(\mathbf{x}) &+ \sum_{j=1}^{N}\sum_{\alpha=1}^{2} q_{\alpha,j}\int_{\ell_{1,j}}^{\ell_{2,j}} f_{\alpha,j}\, g(\mathbf{x},\boldsymbol{\xi}(\ell))J\,\mathrm{d}\ell \\ &- \sum_{j=1}^{N}\sum_{\alpha=1}^{2} \phi_{\alpha,j}\int_{\ell_{1,j}}^{\ell_{2,j}} f_{\alpha,j}\, h(\mathbf{x},\boldsymbol{\xi}(\ell))J\,\mathrm{d}\ell, \end{aligned} \tag{2.49}$$

where $\psi(\mathbf{x}) = 0$ for the inner fluid and $\psi(\mathbf{x}) = 2\phi_\infty(\mathbf{x})$ for the outer fluid. The subscripts (i,e) have been omitted from ϕ, q, and kernels g and h to alleviate the clutter in notation. Expression (2.49) is valid for any point on the boundary.

By the collocation method two systems of $(N+1)\times(N+1)$ linear algebraic equations can be generated by applying equation (2.49) to each node $\mathbf{x}_k$ in turn. We have assumed that for both the inner and outer domains the nodes occupy the same position. Continuity of potential and normal velocity components across elements implies that $\phi_{2,j-1} = \phi_{1,j}$ and $q_{2,j-1} = q_{1,j}$, respectively. The resulting systems of equations my be written in matrix form as

$$\mathbf{H}_i\boldsymbol{\Phi}_i = \mathbf{G}_i\mathbf{Q}_i, \qquad \mathbf{H}_e\boldsymbol{\Phi}_e = 2\boldsymbol{\Phi}_\infty + \mathbf{G}_e\mathbf{Q}_e. \tag{2.50}$$

Here, the kth-component of vectors $\boldsymbol{\Phi}_{(i,e)}$, $\mathbf{Q}_{(i,e)}$ and $\boldsymbol{\Phi}_\infty$ corresponds to the value of $\phi_{(i,e)}$, $q_{(i,e)}$ and ϕ_∞, respectively, at node k. Here, it should be clear that notation

$$q_{(i,e)} = \frac{\partial\phi_{(i,e)}}{\partial n_{(i,e)}}. \tag{2.51}$$

Elements of matrices $\mathbf{H}_{(i,e)}$ and $\mathbf{G}_{(i,e)}$ are formed by the integrals of the first and second axisymmetric kernels, $h_{(i,e)}$ and $g_{(i,e)}$, respectively. The elements of $\mathbf{H}_{(i,e)}$ and $\mathbf{G}_{(i,e)}$ are given by

$$H_{kj} = \delta_{kj} + \int_{\ell_{1,j-1}}^{\ell_{2,j-1}} f_{2,j-1}\, h\left(\mathbf{x}_k,\boldsymbol{\xi}(\ell)\right)J\,\mathrm{d}\ell + \int_{\ell_{1,j}}^{\ell_{2,j}} f_{1,j}\, h\left(\mathbf{x}_k,\boldsymbol{\xi}(\ell)\right)J\,\mathrm{d}\ell, \tag{2.52a}$$

and

$$G_{kj} = \int_{\ell_{1,j-1}}^{\ell_{2,j-1}} f_{2,j-1}\, g\left(\mathbf{x}_k,\boldsymbol{\xi}(\ell)\right)J\,\mathrm{d}\ell + \int_{\ell_{1,j}}^{\ell_{2,j}} f_{1,j}\, g\left(\mathbf{x}_k,\boldsymbol{\xi}(\ell)\right)J\,\mathrm{d}\ell, \tag{2.52b}$$

respectively, where $1 \leqslant k \leqslant N+1$, $2 \leqslant j \leqslant N$, and

$$\delta_{kj} = \begin{cases} 1, & \text{if } k = j, \\ 0, & \text{if } k \neq j, \end{cases} \tag{2.53}$$

is the Kronecker delta. For $j = 1$ ($j = N+1$), the first (last) integral in both expressions (2.52) must be excluded.

Adding matrix equations for the inner and outer fluids in (2.50), and applying equations (2.18), (2.32) and (2.36), leads to

$$(\mathbf{H}_i + \Lambda \mathbf{H}_e)\, \boldsymbol{\Phi}_i = 2\boldsymbol{\Phi}_\infty - \mathbf{H}_e \boldsymbol{\Xi}, \tag{2.54}$$

where the element $[\boldsymbol{\Xi}]_k$ is the value of φ at nodal point k.

With the distribution of φ on the nodal points known at a given time, one solves the system (2.54) for $\boldsymbol{\Phi}_i$. Then, with this vector already computed, one turns to either of the equations in (2.50) to obtain the nodal values of the normal velocities $\boldsymbol{Q}$ (recall that $\boldsymbol{Q} = \boldsymbol{Q}_i = -\boldsymbol{Q}_e$). These values are needed in the right-hand side of the differential equations (2.33) and (2.37) that are used to advance the interface to the next time level. Since the matrices in the left-hand sides of (2.50) and (2.54) are fully populated, these linear systems are solved using LU decomposition.

Due to the initial shape and the boundary conditions satisfied by the solution of the problem subject of analysis, the flow field is symmetric with respect to the plane $z = 0$. Therefore, one can substantially reduce the computational effort needed in the solution of the linear systems (2.50) and (2.54) by enforcing equatorial symmetry in the geometry coordinates, potentials $\phi_{(i,e)}$ and normal velocity $\partial\phi/\partial n_i$ in equation (2.49). This reduces the number of equations and unknowns to $N/2+1$ for each system, where the number of elements N is constrained to be even as an input to the code. Of course, the elements of $\mathbf{H}$ and $\mathbf{G}$ have to be computed considering the imposed symmetry. In summary, in this work we have two algorithms for the solution of (2.50) and (2.54), namely, one in which equatorial symmetry is not assumed and two $(N+1) \times (N+1)$ systems of equations must be solved, and another in which equatorial symmetry is enforced and each linear system to be solved becomes of size $(N/2+1) \times (N/2+1)$, with even N.

The integrals resulting in the components of $\mathbf{H}$ and $\mathbf{G}$ must be evaluated numerically. For this purposes and considering integration over the jth-element, two cases need to be distinguished, namely, when the collocation point $\mathbf{x}_k$ does not belong to this element, that is, when k is neither j nor $j+1$, and when the collocation point does belong to it, i.e. $k = j$ (node $\alpha = 1$) and $k = j+1$ (node $\alpha = 2$). In the former

case, one has regular integrals because both axisymmetric kernels g and h are not singular, whereas for the latter case, the complete elliptic function of the first kind $K(m)$ is singular at $m = 1$, for which $\boldsymbol{\xi} = \mathbf{x}_k$ at one end of the integral. This is a weak (logarithmic) singularity that is integrable in the classical sense. It requires, however, special care when carrying out the numerical evaluation of the integrals, being necessary a scheme that is different from the one used with the regular integrals. The process of numerical integration is discussed below, where we follow, for the most part, the discourse of Hilbing et al. (1995).

Regular integrals

When the collocation point does not belong to the element where the integrals are evaluated, the kernels g and h are not singular. To carry out its integration, we define an intrinsic coordinate η, $-1 \leqslant \eta \leqslant 1$, that is local to any particular element and takes the value $\eta = -1$ at node $\alpha = 1$ and $\eta = 1$ at node $\alpha = 2$ of that element. It is related to parameter ℓ according to

$$\ell(\eta) = \ell_{1,j}\frac{1-\eta}{2} + \ell_{2,j}\frac{1+\eta}{2}. \tag{2.55}$$

The variation of η from -1 to 1 is not chosen arbitrarily. This interval is the same as the one used in standard quadrature for numerical integration as shown below. With transformation (2.55), the regular integrals in (2.49) become

$$\int_{\ell_{1,j}}^{\ell_{2,j}} f_{\alpha,j}\, gJ\, \mathrm{d}\ell = \frac{\Delta\ell_j}{2}\int_{-1}^{1} f_{\alpha,j}\, g\, J\, \mathrm{d}\eta, \quad \int_{\ell_{1,j}}^{\ell_{2,j}} f_{\alpha,j}\, hJ\, \mathrm{d}\ell = \frac{\Delta\ell_j}{2}\int_{-1}^{1} f_{\alpha,j}\, h\, J\, \mathrm{d}\eta, \tag{2.56}$$

with $\Delta\ell_j = \ell_{2,j} - \ell_{1,j}$. The integrands in (2.56) are well behaved and their integration can be carried out using standard Gauss-Legendre quadrature

$$\int_{-1}^{1} F[\ell(\eta)]\mathrm{d}\eta \approx \sum_{n=1}^{N_p} F[\ell(\eta_n)]w_n, \tag{2.57}$$

where N_p is the number of integration points, η_n is the coordinate of a Gaussian point and w_n its corresponding weight (e.g., Stroud and Secrest, 1966). We use $N_p = 6$ in our code.

Weakly singular integrals

When the collocation point lies on one or the other end of the element over which the integral is computed, one has to deal with a weakly singular integral because

the integrand has a logarithmic singularity. We proceed by splitting the fit of the complete elliptic integral of the first kind

$$K(m) \approx [A_c(m_1) + B_c(m_1) \log A] - B_c(m_1) \ln B, \tag{2.58}$$

into a nonsingular part (within brackets) and a singular part (last term). The development that follows depends on the relative position of the singularity in the element.

If the nodal point is at position $\alpha = 1$, the last term in (2.58) may be conveniently written as (Bialecki et al., 1996)

$$\ln B = 2 \ln \left[\frac{B^{1/2}}{(\ell - \ell_{1,j})/\Delta\ell_j} \right] + 2 \ln \left[\frac{\ell - \ell_{1,j}}{\Delta\ell_j} \right], \tag{2.59}$$

where the first term on the right-hand side is no singular and the second is singular. With the substitution of (2.59) into (2.58), the integral of the second axisymmetric kernel g may be split into a regular integral and a weakly singular integral $\mathscr{G}_{1,\text{reg}} + \mathscr{G}_{1,\text{sng}}$. That is,

$$\int_{\ell_{1,j}}^{\ell_{2,j}} f_{\alpha,j}\, gJ \, \mathrm{d}\ell = \mathscr{G}_{1,\text{reg}} + \mathscr{G}_{1,\text{sng}}. \tag{2.60}$$

With the variable transformation

$$\ell - \ell_{1,j} = \frac{1}{2}(1 + \eta)\Delta\ell_j, \tag{2.61}$$

where $-1 \leqslant \eta \leqslant 1$, the regular integral may be written as

$$\mathscr{G}_{1,\text{reg}} = \frac{\Delta\ell_j}{\pi} \int_{-1}^{1} f_{\alpha,j} \frac{r}{A^{1/2}} \left[A_c(m_1) + B_c(m_1) \left\{ \ln A - 2 \ln \left(\frac{2B^{1/2}}{1 + \eta} \right) \right\} \right] J \mathrm{d}\eta, \tag{2.62}$$

and can be computed with standard Gauss-Legendre quadrature. For the integral of the singular term, the following variable change is adequate

$$\ell - \ell_{1,j} = \tilde{\xi}\Delta\ell_j, \tag{2.63}$$

where $0 \leqslant \tilde{\xi} \leqslant 1$. The integral of the singular term thus becomes

$$\mathscr{G}_{1,\text{sng}} = \frac{4\Delta\ell_j}{\pi} \int_{0}^{1} f_{\alpha,j} \frac{r}{A^{1/2}} B_c(m_1) J \ln \left(\frac{1}{\tilde{\xi}} \right) \mathrm{d}\tilde{\xi}. \tag{2.64}$$

These limits of integration, given by rule (2.63), are chosen so that the integral

(2.64) has the exact form needed for the application of logarithmically weighted Gaussian quadrature schemes. Therefore, numerical evaluation of this integral can be achieved by using

$$\int_0^1 F[\ell(\tilde{\xi})] \ln\left(\frac{1}{\tilde{\xi}}\right) \mathrm{d}\tilde{\xi} \approx \sum_{n=1}^{\tilde{N}_p} F[\ell(\tilde{\xi}_n)] w_n, \tag{2.65}$$

where $\tilde{N}_p$ is the number of Gaussian points, and $\tilde{\xi}_n$ and w_n denote their coordinates and the associated weights, respectively (e.g., Stroud and Secrest, 1966). We chose $\tilde{N}_p = 6$ in our computations.

Turning now to the integrals with the first axisymmetric kernel h, according to (2.30b), this may be written as

$$h = h^* - \frac{n^r}{\pi A^{1/2}} K(m), \tag{2.66}$$

where h^* is regular and the last term in the right-hand side has the singularity due to the presence of $K(m)$. This last term may be treated as in the case of the integrals with kernel g above. After repeating that procedure, we have that the integrals with kernel h and singularity at the nodal point $\alpha = 1$ may be written as the sum of a regular integral and a weakly singular integral, $\mathscr{H}_{1,\mathrm{reg}} + \mathscr{H}_{1,\mathrm{sng}}$, i.e.

$$\int_{\ell_{1,j}}^{\ell_{2,j}} f_{\alpha,j}\, hJ \,\mathrm{d}\ell = \mathscr{H}_{1,\mathrm{reg}} + \mathscr{H}_{1,\mathrm{sng}}, \tag{2.67}$$

where

$$\begin{aligned}\mathscr{H}_{1,\mathrm{reg}} =& \frac{\Delta\ell_j}{2} \int_{-1}^{1} f_{\alpha,j} \left[h^* - \frac{n^r}{\pi A^{1/2}} \left\{ A_c(m_1) \right.\right. \\ &\left.\left. + B_c(m_1) \left\{ \ln A - 2 \ln\left(\frac{2B^{1/2}}{1+\eta}\right) \right\} \right\} \right] J \mathrm{d}\eta,\end{aligned} \tag{2.68}$$

and

$$\mathscr{H}_{1,\mathrm{sng}} = -\frac{2\Delta\ell_j}{\pi} \int_0^1 f_{\alpha,j} \frac{n^r}{A^{1/2}} B_c(m_1) J \ln\left(\frac{1}{\tilde{\xi}}\right) \mathrm{d}\tilde{\xi}, \tag{2.69}$$

and their numerical treatment follows as in the cases of $\mathscr{G}_{1,\mathrm{reg}}$ and $\mathscr{G}_{1,\mathrm{sng}}$, respectively.

Consider now the case in which the collocation point is at nodal point $\alpha = 2$. The treatment of this singularity follows similarly as in the case of the singularity

at the other end, but instead of (2.59) and (2.61), we use

$$\ln B = 2\ln\left[\frac{B^{1/2}}{(\ell_{2,j}-\ell)/\Delta\ell_j}\right] + 2\ln\left[\frac{\ell_{2,j}-\ell}{\Delta\ell_j}\right] \tag{2.70}$$

and

$$\ell_{2,j} - \ell = \frac{1}{2}(1-\eta)\Delta\ell_j, \tag{2.71}$$

respectively. Therefore, the integral associated with the second axisymmetric kernel g is split into its regular and weakly singular parts $\mathscr{G}_{2,\mathrm{reg}} + \mathscr{G}_{2,\mathrm{sng}}$, where

$$\mathscr{G}_{2,\mathrm{reg}} = \frac{\Delta\ell_j}{\pi}\int_{-1}^{1} f_{\alpha,j}\frac{r}{A^{1/2}}\left[A_c(m_1) + B_c(m_1)\left\{\ln A - 2\ln\left(\frac{2B^{1/2}}{1-\eta}\right)\right\}\right] J\mathrm{d}\eta, \tag{2.72}$$

and the integral $\mathscr{G}_{2,\mathrm{sing}}$ of the weakly singular term is computed with the same expression as (2.64), except that the transformation

$$\ell_{2,j} - \ell = \tilde{\xi}\Delta\ell_j, \tag{2.73}$$

$0 \leqslant \tilde{\xi} \leqslant 1$, must be used to evaluate the integrand. The integral with the first axisymmetric kernel h is also computed as the sum of its regular and weakly singular parts, $\mathscr{H}_{2,\mathrm{reg}} + \mathscr{H}_{2,\mathrm{sng}}$, where

$$\begin{aligned}\mathscr{H}_{2,\mathrm{reg}} =& \frac{\Delta\ell_j}{2}\int_{-1}^{1} f_{\alpha,j}\left[h^* - \frac{n^r}{\pi A^{1/2}}\left\{A_c(m_1)\right.\right.\\ &\left.\left. + B_c(m_1)\left\{\ln A - 2\ln\left(\frac{2B^{1/2}}{1-\eta}\right)\right\}\right\}\right] J\mathrm{d}\eta,\end{aligned} \tag{2.74}$$

and integral $\mathscr{H}_{2,\mathrm{sng}}$ of the weakly singular term is given by the right-hand side of (2.69), but the integrand must be computed using transformation (2.73).

Rodríguez-Rodríguez et al. (2006) reported the use of the singularity substraction technique (Oğuz and Prosperetti, 1993) to handle the singular integrals instead of the special logarithmic Gaussian quadrature method employed here.

Numerical integration of the differential equations for the motion of the interface

The integration of the system of equations (2.33) and (2.37) is carried out using a fourth-order Runge-Kutta method with adaptive time stepping. This scheme requires four evaluations of the functions for each time step. Even though the

significant computational cost, this method has the benefit of needing no information from previous time steps. This feature allows for implementation of re-gridding and refinement by changing the number and position of the nodal points as time advances. The time step is dynamically modified in order to properly resolve the shape of the interface when approaching pinch-off and its value is found by requiring that no nodal point will move beyond a fraction of the smallest element size. The time step employed is the minimum of all time steps computed as the ratio of that maximum distance to the nodal velocity and cannot be larger than both the time step needed to resolve inviscid capillary waves with the smallest grid dimension (Leppinen and Lister, 2003) given by (see Lamb, 1932; Padrino, Funada, and Joseph, 2008)

$$\Delta t \leqslant 2\pi(\Delta s)^{3/2}\left[\frac{\pi^3}{(1+\Lambda)We}\right]^{-1/2}, \tag{2.75}$$

and a maximum allowable time increment set from the start as an input (see Hilbing et al., 1995).

The evaluation of the tangential derivatives $\partial\phi_{(i,e)}/\partial s$ at the nodal points needed in the right-hand side of (2.37) is carried out by differentiation of the quintic spline (of the "z-type", see Appendix A) fitted to the discrete distribution of potentials $\phi_{(i,e)}$, whereas the normal derivative comes from the solution of the boundary integral equation described above. The first and second derivatives of z and r with respect to arc-length s needed in the computation of the viscous normal stress (2.21) and the mean curvature (2.22) are obtained from the quintic splines formulae interpolating the nodal coordinates. By virtue of the chain rule for differentiation, these computations require the values of $\mathrm{d}s/\mathrm{d}\ell$ and $\mathrm{d}^2s/\mathrm{d}\ell^2$ at the nodes, for which relation (2.44) between s and ℓ becomes useful.

Grid refinement and smoothing

In a number of works that apply the boundary element method coupled with a time integration scheme to track the motion of an interface or free surface, it has been reported the developing of "zigzag" instabilities when simulations run for relatively long time intervals (Longuet-Higgins and Cokelet, 1976; Lundgren and Mansour, 1988; Hilbing et al., 1995; Heister, 1997). This might be associated with the clustering of the nodes over certain regions of the boundary, on which the element size gets reduced, thereby requiring a smaller time step to maintain the stability of the time advancing algorithm (Lundgren and Mansour, 1988). Several strategies have been implemented to alleviate this problem. One choice is to apply a smoothing function of the boundary shape or the boundary potential as time pro-

gresses (Longuet-Higgins and Cokelet, 1976; Hilbing et al., 1995); an alternative is to modify the surface potential by adding a five point formula for the discrete spatial fourth-order derivative of the potential, as described by Lundgren and Mansour. Remeshing the nodes as time advances so that they are kept evenly spaced has also been utilized as an strategy to smooth out the numerical instabilities (Lundgren and Mansour, 1988; Hilbing et al., 1995; Heister, 1997). The remeshing technique has been modified by Oğuz and Prosperetti (1990) to generate a staggered grid. This is achieved by setting the length between consecutive nodes equal to a constant value, Δs say, which is determined from the total arc-length of the boundary at the current time, except for arc segments defined by the first and last pairs of nodes on the grid, whose length is made equal to $\Delta s/2$. Then, a time-integration step is performed after which staggering occurs again, this time by placing the nodes so that the arc-length between adjacent nodes, including the first and last pair, is the same. This amounts to dynamically increasing and decreasing the number of nodes. Oğuz and Prosperetti (1990) also proposed the alternative approach of damping the curvature by adding to it a term proportional to the rate of change of the curvature. Filtering schemes have also been used, as in the case of Rodríguez-Rodríguez et al. (2006), based upon the fast Fourier transform of the discrete boundary functions and the elimination of the high-frequency components.

In certain situations, it is desirable to have grid refinement by having shorter separation between nodes in particular regions of the boundary. This technique seems to contradict the strategy of having nearly constant grid spacing, as described above. Nevertheless, grid refinement has been applied successfully in problems of bubble and drop dynamics. For instance, Chen and Steen (1997) implemented an algorithm to have a higher concentration of nodes in the regions of large curvature in their numerical method for bubble break-up, whereas, in their work on axisymmetric capillary pinch-off of a drop, Leppinen and Lister (2003) set the distance between consecutive nodes proportional to the distance from each node to the point on the axis of symmetry with the same abscissa as the location of the minimum neck radius. With this strategy, it was possible to resolve the shape of the boundary with great detail at the instants before pinch-off.

In the present computations, we adopt a refinement scheme similar to the one by Leppinen and Lister (2003). Interpolating the coordinates of the nodes on the boundary using quintic splines, the separation between adjacent nodal points $\{\mathbf{x}_j, \mathbf{x}_{j+1}\}$ was set to $0.1D$, where D is the distance between point $\mathbf{x}_j$ and the point $(z_{\min}, 0)$, where $(z_{\min}, r_{\min})$ are the coordinates of the nodal point on the interface with the minimum neck radius, that is, the node closest to the axis of symmetry

in the neck region. In this notation, the index $j = 1$ corresponds to the node with coordinates $(z_{\min}, r_{\min})$ and increases towards both ends of the boundary. This grid spacing was restricted to be no larger than an upper bound defined as an input to the code. This grid refinement strategy was applied in the version of the code for which equatorial symmetry was considered in the solution of the discrete boundary integral equation [see the discussion after (2.54)]. This version of the code is used in the case of a drop, where break-up takes place, because of symmetry, simultaneously at two different points away from the plane $z = 0$. Of course, the algorithm just described also works when the node with minimum neck radius lies on the plane $z = 0$. In the version of the code that does not enforce equatorial symmetry, the grid refinement strategy described above is modified by setting $z_{\min} = 0$ for all times, this abscissa being associated with the node $N/2+1$, with N being the (even) total number of elements. This version of the code is used to simulate the deformation of a bubble, i.e. small Λ, in which case the minimum radius of the neck occurs at $z_{\min} = 0$ or, if a (small) satellite bubble is formed, the actual z-coordinates for the (two) nodes with the minimum neck radius will not be zero but in the neighborhood of $z = 0$, and therefore the level of grid refinement will also be satisfactory around those points.

In our code, this grid refinement method has been combined with the smoothing strategy of node staggering in a manner similar to that implemented by Oğuz and Prosperetti (1990) as presented above. Of course, in this case the nodes are not evenly spaced as inter-nodal spacing is affected by grid refinement. In the code, one can deactivate either the grid refinement or the node staggering, or both, at will. For instance, in the subcritical case, in which no break-up takes place, grid refinement may be of no advantage. When grid refinement is deactivated and node staggering is carried out, the resulting grid can be enforced to have equally spaced nodes except, perhaps, for the first and last pair of nodes. We do not usually call for node staggering after each time step, but after several time steps have been executed.

2.4 Results and discussion

The problem described in §§2.3.1-2.3.3 is solved numerically using the procedure detailed in §2.3.4. Here, we present and discuss the results of the simulations for the case of a bubble, for which the density ratio is very small, and for the case of a drop, for which the density ratio is $O(1)$. Before doing so, we discuss the validation stage for the numerical method employed.

2.4.1 Validaton of the numerical set-up

The validation of the axisymmetric solver is carried out first by comparing its predictions with analytic results for the small oscillations of a bubble or drop about the spherical shape from both inviscid (Lamb, 1932) and viscous potential flow (Joseph et al., 2007; Padrino et al., 2008, see chapter 5 of this thesis). In this case the motion is driven by capillary forces as a result of an initial deformation imposed on the interface in the absence of any prescribed flow in the far field. The dimensionless equations presented in §2.3.1 are still valid for this setting. However, since the flow strength $M = 0$ in the far field, one must choose a different velocity scale, $\sqrt{\gamma/(\rho_e a)}$ in this case, so that the Weber number is now fixed, $We = 1$, and the Reynolds number is $Re = \sqrt{\rho_e \gamma a}/\mu_e$, which is simply Oh_e^{-1}, where Oh_e is the Ohnesorge number for the exterior fluid. Two independent modes of oscillation are considered, namely, the second and fourth modes, which are set by an initial interfacial shape of the form $1+\epsilon P_n(\cos\theta)$ with $n = 2$ and 4, respectively, and ϵ is a "small" number; P_n are the Legendre polynomials of order n. With these modes, equatorial symmetry of the evolved interface is guaranteed.

Figure 2.4 shows the variation with time of the normalized amplitude of the right end of the bubble or drop obtained with the numerical method presented above for both inviscid and viscous fluids and 128 elements. In the latter case, we chose $Re = 100$ and a viscosity ratio $\beta = 0.01$ for the bubble and $\beta = 0.1$ for the drop. These choices give a decay rate such that the interface oscillates over several time periods without decaying too fast, thereby allowing the analysis of the signal. Figures 2.4(a) and 2.4(b) correspond to the second mode and $\epsilon = 0.05$, whereas figures 2.4(c) and 2.4(d) correspond to the fourth mode and $\epsilon = -0.05$. Density ratio in these cases is $\Lambda = 0.0012$ (bubble case). The frequency of oscillations increases by increasing n. In the inviscid case (figure 2.4(a) and 2.4(c)), non-linear effects can presumably be observed as the amplitude of the oscillations slightly deviates from a constant value. In figures 2.4(e) through 2.4(f) the initial deviation of the bubble interface is reduced (in absolute value) to $\epsilon = -0.005$. By comparing (c) and (e), one can notice that the amplitude of the oscillations tend to a constant value as ϵ becomes smaller in the inviscid case. Finally, figures 2.4(g) and 2.4(h) show the change in amplitude for a drop ($\Lambda = 0.8$), $n = 4$ and $\epsilon = -0.005$. Results for a drop and $\epsilon = -0.05$ were also obtained but are not shown here as they conform to those results already depicted. In all the cases, the frequency of the oscillations shows excellent agreement with the theoretical results obtained in the linearized case by Lamb (1932) for fluids with zero viscosity and by Joseph et al. (2007) for two viscous fluids (see Padrino et al., 2008, and also chapter 5). The relative error

in all the cases lies within 0.4%. In the viscous case, figure 2.4 also demonstrates very good match between the theoretical and numerical results for the decay rate of the oscillations.

This is perhaps the first time in which the linear viscous potential flow theory for the small oscillations of a bubble or drop is used to validate a numerical method developed to solve the non-linear deformation of an interface shared by two viscous fluids whose motion is assumed to be irrotational. Indeed, the linear inviscid theoretical result by Lamb (1932) has been used elsewhere to validate, in the small deformation case, algorithms solving boundary integral equations to simulate the inviscid motion of an interface or free surface (Hilbing et al., 1995; Rodríguez-Rodríguez et al., 2006). It should also be mentioned that the boundary integral formulation of Lundgren and Mansour (1988) used to study the oscillations of a drop with "weak" viscous effects, which is different from the viscous potential flow approach followed here, was validated using the result from Lamb's linear viscous dissipation approximation. The linearized viscous dissipation approximation differs from the linearized viscous potential flow method employed in the present validation, and therefore, one should not expect agreement between their results for all cases.

Results for the time evolution of a bubble or drop in a uniaxial straining flow from boundary integrals simulations by Rodríguez-Rodríguez et al. (2006) considering inviscid fluids are used to further validate our code in the case of large deformations. They considered that initially the interface is spherical. If the viscosity is set to zero, the parameters controlling the dynamics are the Weber number and the density ratio. Their results indicate that above a certain critical value of We, the bubble breaks up, whereas for values of We below that threshold, the bubble undergoes large oscillations without breaking up. For the case of a drop, .i.e. $\Lambda \sim O(1)$, those authors provide no information regarding the existence of a critical We. For the purpose of comparison, we have chosen some of the cases considered by Rodríguez-Rodríguez et al. (2006). First, we consider a bubble with density ratio $\Lambda = 0.0012$ and Weber numbers $We = 1.0$, 2.19, 10.0 and $We \to \infty$; the first two values correspond to subcritical conditions and the last two cases result in break-up. Rodríguez-Rodríguez et al. (2006) have found a critical Weber number $We_c = 2.3$. Figure 2.5 shows our numerical simulations using the numerical method presented in §2.3.4 for various times. For the final time in each case, the predictions by Rodríguez-Rodríguez et al. (2006) are shown with symbols and the agreement is excellent. It should also be mentioned that the final time t_b from our simulations agree very well with their final time, except for case (c), for which our $t_b = 1.221$

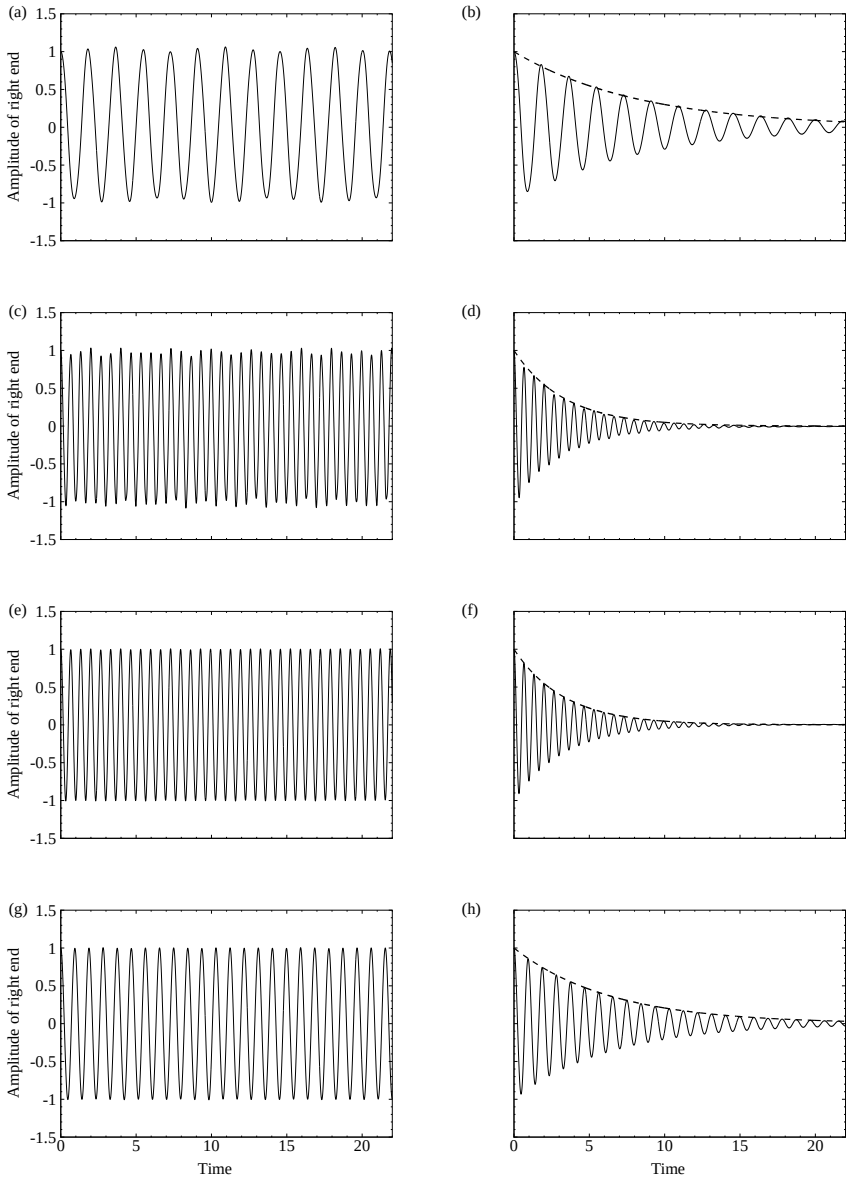

Figure 2.4: Amplitude of the right end of the bubble or drop $z_{\rm end}(t) = |\,\mathbf{x}_{\rm end}(t)\,|$, where $\mathbf{x}_{\rm end}(t) = (z(t), 0)$, as a function of time. This amplitude is presented in normalized fashion, $(z_{\rm end}(t) - 1)/\epsilon$. The motion of the system is due to an initial perturbation of the spherical interface of unit radius given by $|\mathbf{x}(0)| = 1 + \epsilon P_n(\cos\theta)$, where P_n are the Legendre polynomials of order either $n = 2$ or 4, and θ is the polar angle. The fluid is at rest in the far field (Caption continues on the next page).

Figure 2.4: (Continued from the previous page) The figures on the left correspond to inviscid potential flow, whereas the figures on the right result from viscous potential flow simulations with a Reynolds number $Re = 100$. Figures (a) and (b) are obtained with $n = 2$, $\epsilon = 0.05$ and density ratio $\Lambda = 0.0012$ (bubble). For figures (c) and (d), $n = 4$, $\epsilon = -0.05$ and $\Lambda = 0.0012$, whereas for figures (e) and (f), $n = 4$, a much smaller (in absolute value) deviation $\epsilon = -0.005$ and $\Lambda = 0.0012$. Figures (g) and (h) results from $n = 4$, $\epsilon = -0.005$ and $\Lambda = 0.8$ (drop). The frequency and decay rate of the oscillations are compared with the linear, viscous potential flow theory, from which the dashed lines shown in the figures on the right are obtained.

and theirs $t_b = 1.230$, which amount to a discrepancy of -0.7% that we consider satisfactory. Since the fluids are incompressible, the volume of the bubble or drop must remain constant; by numerical integration of a body of revolution around the z-axis, this volume has been computed after every time step and errors within 0.02%* where obtained for the four cases shown in figure 2.5. This demonstrates the mass preserving attribute of the numerical scheme used in this work.

The results shown in figure 2.5 were computed using 128 elements, with node staggering and grid refinement. Because of the latter feature, the number of elements increased with time leading to a number of elements in the order of 350 at the last instant of the computations. Test computations with double the initial number of elements lead to the same profiles as those shown here. In addition, using a maximum allowable time step of 10^{-5} (recall that we are using an adaptive time stepping) instead of our standard maximum of 10^{-4} did not rendered significant changes either. Similar tests were also conducted for a few of the cases reported below for the inviscid drop as well as for the calculations concerning the irrotational motion of viscous fluids, and the results presented here show insignificant variation with both the increment of the number of elements at start-up and the reduction of the maximum time-step size.

Due to the symmetry imposed by the initial and boundary conditions, when the necking regions develops, the minimum radius is attained at the equatorial plane. If the coordinates of the interface are normalized by the minimum radius $r_{\min}$ (figure 2.6), the normalized profile becomes slender as time progresses, since the length scale in the radial direction decreases faster than the scale along the axial direction, as reported by Gordillo et al. (2005). A parabolic function fits these curves very well.

In figure 2.7 we show the variation of the minimum neck radius $r_{\min}$ with the

*As a reference, with 129 nodes, the relative error (%) in the computation of the volume for the initial sphere is about 2×10^{-12}.

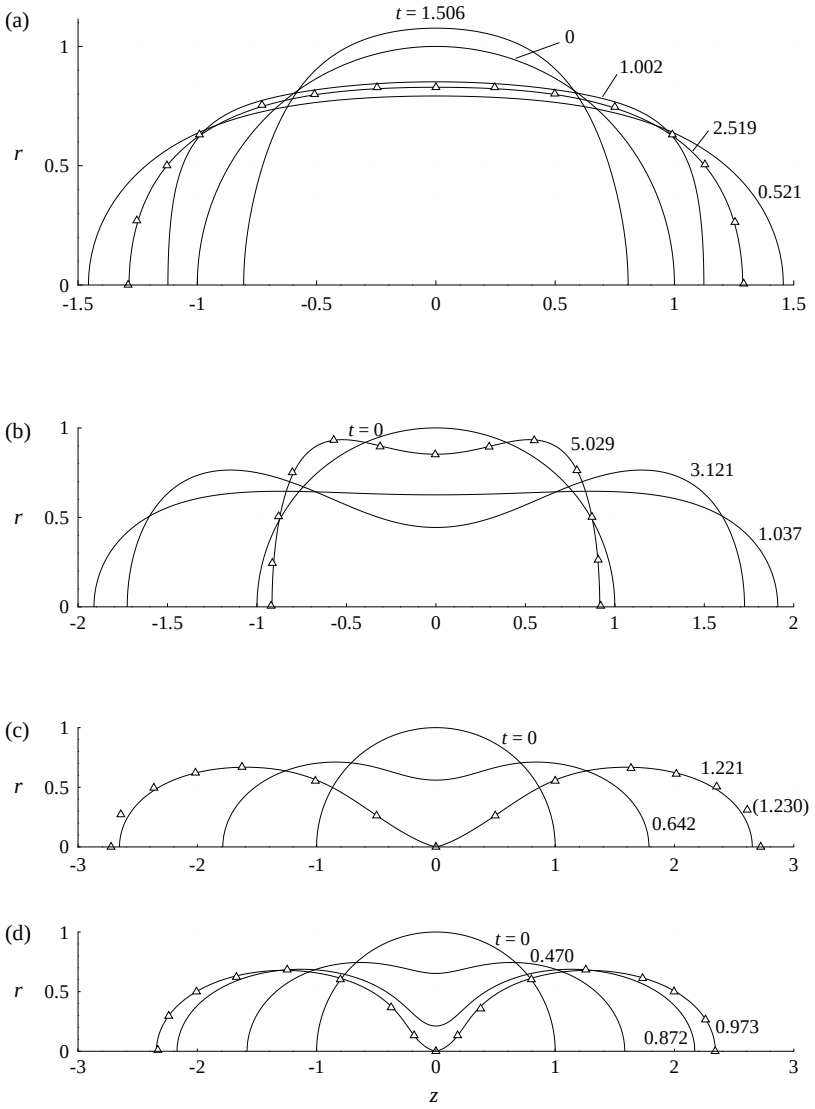

Figure 2.5: Deformation of a bubble in a uniaxial straining flow from an inviscid potential flow analysis with density ratio $\Lambda = 0.0012$ and different Weber numbers. (a) $We = 1.0$, (b) $We = 2.19$, (c) $We = 10.0$ and (d) $We \to \infty$. The solid lines represent the results from the present work and the $\triangle$ denotes results from Rodriguez-Rodriguez et al. (2006). This comparison is part of the validation stage of the computational code developed in this work.

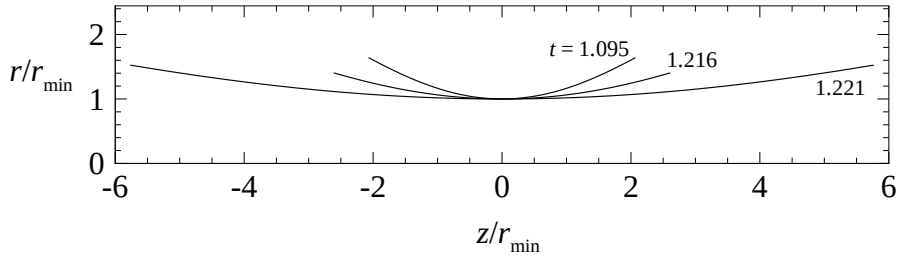

Figure 2.6: Normalized bubble profile approaching pinch-off for a Weber number $We = 10.0$, density ratio $\Lambda = 0.0012$ and inviscid fluids. Here, $r_{\min}$ denotes the minimum radius of the bubble neck. The various curves are very well fitted by the parabolic profile $z/r_{\min} = 1 + ar^2/r_{\min}^2$, where $r_{\min} = 0.220$ and $a = 0.152$ for $t = 1.095$; $r_{\min} = 0.035$ and $a = 0.060$ for $t = 1.216$, and $r_{\min} = 0.002$ and $a = 0.016$ for $t = 1.221$.

time to break-up $\tau = t_b - t$ for the inviscid cases, where t_b is the break-up time. The fitting of the law $r_{\min} \sim \tau^{\alpha}$, where α is an effective exponent, gives rise to values of α somewhat larger than 0.5, as expected (Gordillo et al., 2005), and closer to values determined from experimental data for a bubble detaching from a nozzle due to gravity ($\alpha = 0.56$ by Keim et al. (2006), and $\alpha = 0.57$ by Thoroddsen et al. (2007)). The slight difference with our results may be due to the fact that their experimental setting is different from the configuration studied here, as the precise value of α depends on the initial and boundary conditions, and also, perhaps, to the range of $r_{\min}$ fitted in these graphs. We note that the ranges plotted here for τ and $r_{\min}$ are similar to the ones used by Gordillo et al. (2005).

Figure 2.8 depicts the time evolution of the interface for a drop with a density ratio $\Lambda = 0.8$ and two different Weber numbers. In contrast to the case of a bubble where break-up has been observed to be binary in experiments, for the case of a drop the tertiary break-up has been reported (see §2.1.1). This is reproduced by the simulations. For the smallest $We = 3$, the slender satellite drop and the two large droplets on the sides have similar axial length scales. On the other hand, for the largest $We = 10$ considered, a central elongated ligament is formed with axial length of about 12 times the initial drop length, and break-up occurs near the ends of the slender drop. Also, the break-up time is larger than those observed for the bubble. The length of this long liquid thread becomes of the same size of the eddy that tend to break it up and, therefore, the axisymmetric configuration is not preserved as the ligament is bent by the action of the background flow and the model assumed in this work does not longer hold on quantitative terms. However, some relevant features of the drop shape are still reproduced, i.e. the drop length

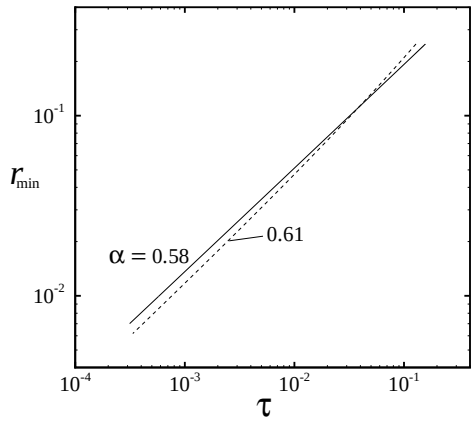

Figure 2.7: Minimum neck radius $r_{\min}$ as a function of the time to break-up $\tau = t_b - t$ for a bubble in uniaxial straining motion; the density ratio $\Lambda = 0.0012$ and the fluids are inviscid. For the interval shown the motion follows the scaling $r_{\min} \sim \tau^{\alpha}$, where α is an "effective" exponent. The thin solid line corresponds to a Weber number $We = 10$ and the dashed line corresponds to $We \to \infty$.

and break-up pattern. Comparison of the shapes predicted by our code with those by Rodríguez-Rodríguez et al. (2006) (symbols) for $We = 3$ demonstrate excellent agreement, which is also obtained for the break-up time. For $We = 10$, the drop shape predicted with viscous potential flow is similar to that by Rodríguez-Rodríguez et al.; however, discrepancies arise in the neck region (pinch-off area) and in the shape of the daughter drops at the tips. This is because we implemented grid refinement in our simulations, whereas Rodríguez-Rodríguez et al. did not. Indeed, when we disable grid refinement and enforce equally spaced nodes, our result with 513 nodes (not shown) and the one by Rodríguez-Rodríguez et al. (2006) coincide in shape. We also highlight that volume is preserved in the simulations for the drop up to the final time within 0.09%, even in the case where the axial length scale changes so dramatically ($We = 10$).

The evolution of the neck minimum radius $r_{\min}$ as pinch-off is approached for a drop ($\Lambda = 0.8$) is shown to follow the law $r_{\min} = \tau^{2/3}$ in figure 2.9 for both Weber numbers $We = 3$ and 10 in agreement with analyses and numerical predictions (Keller and Miksis, 1983; Chen and Steen, 1997; Day et al., 1998; Leppinen and Lister, 2003). Here, we show only the cone to the right of the equatorial plane $z = 0$. For a drop and $We = 3$, figure 2.10(a) shows the evolution of the interface in the neck region as it approaches pinch-off. Notice that the interface overturned before breaking up and so both the steep and shallow parts of the interface being

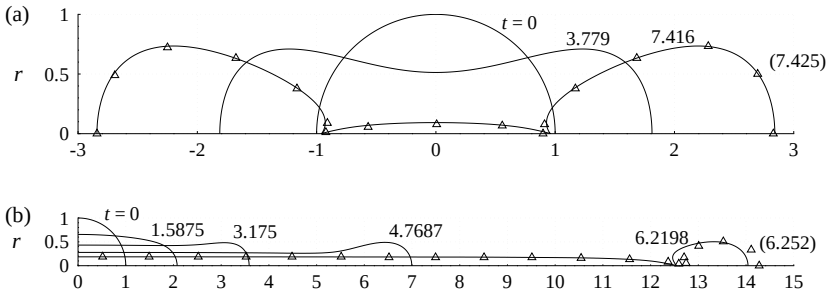

Figure 2.8: Deformation of a drop in a uniaxial straining flow from an inviscid potential flow analysis with density ratio $\Lambda = 0.8$ and Weber numbers (a) $We = 3.0$ and (b) $We = 10$. The solid lines represent the results from the present work and the $\triangle$ denotes results from Rodriguez-Rodriguez et al. (2006). This comparison is part of the validation stage of the computational code developed in this work.

connected by the necking region depict negative slopes with respect to the reference frame shown. As time progresses, the interface tend to attain a cone shape about the minimum radius and $r_{\min} \to 0$ in a finite time creating a kink. Also notice the dense grid for the last instant included in the figure, for which the interface is discretized by 605 nodal points (initially we set 129 nodes) and the final (adaptive) time steps are of order 3×10^{-9}. In figure 2.10(b), we present the scaled profiles near drop pinch-off r_s versus z_s using the coordinates of the neck $(z_{\min}, r_{\min})$ as indicated in the figure's caption at each instant depicted. With this new set of coordinates the profiles show a clear tendency to collapse onto a single smooth curve as the time to break-up τ and thus $r_{\min}$ both go to zero; therefore, in this scaled set of coordinates, this inviscid break-up process is self-similar, as expected (Leppinen and Lister, 2003).

2.4.2 Bubble - Viscous analysis

In this section, the time evolution of the interface of a bubble in a uniaxial extensional flow is computed using the numerical method described in §2.3.4 considering irrotational motion and the inner and outer fluids to be viscous. The goal is to compare the results obtained here under these assumptions with the results given very recently by Revuelta et al. (2006) from the numerical solution of the incompressible, fully viscous Navier–Stokes equations using a projection method with suitable spatial and time discretizations of the various terms combined with a level set method to track the evolution of the interface. They dimensionalized their governing equations with the same scales as those used in §2.3.1. In their numerical study, the initially

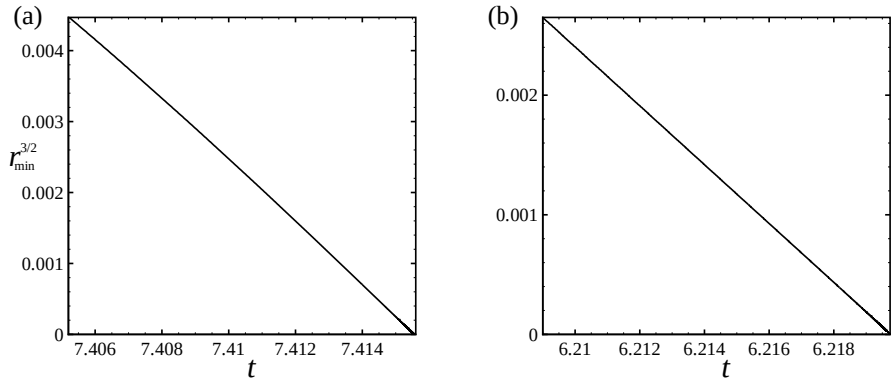

Figure 2.9: Power of the minimum neck radius $r_{\min}^{3/2}$ as a function of time t approaching pinch-off for an inviscid drop within another inviscid liquid with density ratio $\Lambda = 0.8$ and Weber number (a) $We = 3$ and (b) $We = 10$. The figures show that the minimum neck radius approaches pinch-off following the scaling $r_{\min} \sim \tau^{2/3}$ as the time to pinch-off $\tau = t_b - t \to 0$.

spherical bubble starts from rest, the density and viscosity ratios $\Lambda = 0.001$ and $\beta = 0.01$ and the remaining controlling parameters, i.e. the Reynolds and Weber numbers, as defined in §2.3.1, take different values. Revuelta et al. point out that the errors in the computation of the (bubble) mass were within 1%, except for high Reynolds numbers and low Weber numbers, where the errors where within 3%.

In figure 2.11, the change of the total axial dimension of the bubble D with time is presented for five different values of Re and also for the inviscid case, $Re \to \infty$, for a fixed $We = 1.5$. This magnitude is lower than the critical Weber number We_c above which inertia effects are strong enough to overcome the surface tension effects that tend to preserve the integrity of the bubble, thereby leading to break-up. Revuelta et al. (2006) found $We_c \approx 2.22 \pm 0.005$ and independent of Re for $Re \geqslant 20$. Therefore, for $We = 1.5$, the bubble does not break up. It is shown that the oscillations are more rapidly attenuated as the Reynolds number decreases as a result of viscous dissipation and the bubble shape quickly reaches steady state. The figures show very good agreement between the calculations from the potential flow of viscous fluids of the present work (solid lines) and the fully viscous Navier–Stokes equations by Revuelta et al. (2006) (symbols) for up to $t \approx 8$, indicating that viscous effects are mostly associated with the irrotational motion during this stage. Because the initial condition is irrotational, the viscous results for the largest Reynolds numbers, i.e. $Re = 200$, 500 and 1000, match the inviscid solution, at least for the first cycle, as in the case of $Re = 200$. This is not the case for the

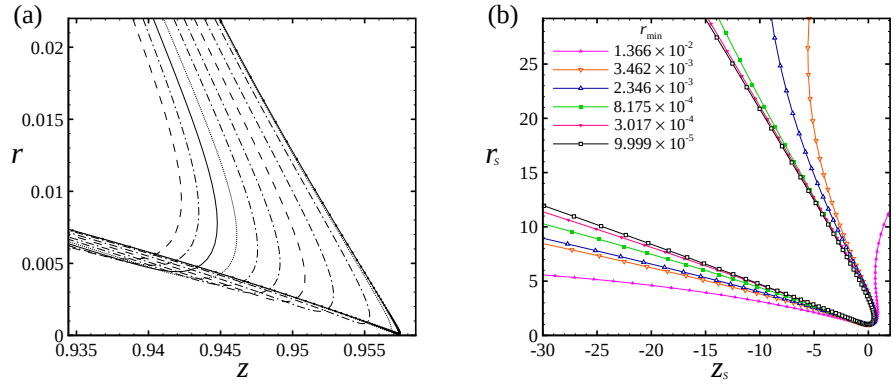

Figure 2.10: Interface shapes for various times approaching pinch-off for a drop of an inviscid fluid in another inviscid liquid; the density ratio is $\Lambda = 0.8$ and the Weber number is $We = 3$. In figure (a) the coordinates r vs. z are shown; for the last instant, the node distribution over the interface is depicted, highlighting the high nodal density of the grid around the neck region. In figure (b) the shapes tend to collapse onto a conical shape when rescaled with the minimum neck radius $r_{\min}$ and centered on $z_{\min}$, i.e., $z_s = (z - z_{\min})/r_{\min}$ and $r_s = r/r_{\min}$, thereby suggesting self-similarity. Two decades of variation of $r_{\min}$ with time are shown in the legend.

smallest values of Re considered, $Re = 20$ and 50, for which discrepancies with the inviscid results are evident almost from the start. Finally, note that the results from the fully viscous Navier–Stokes equations seem to get damped abruptly, especially for the largest Re, a phenomenon that may be regarded as unexpected and it is not discussed by Revuelta et al. (2006). In our numerical solutions for the sub-critical cases, the maximum error in the computation of the volume of the bubble lies within 0.02%. For the set of values of Re mentioned above, we conducted tests with our code and found about the same critical value We_c as that reported by Revuelta et al., with a very weak dependence on Re.

In passing, it should be mentioned that bubble break-up still may take place for subcritical $We < We_c$ if the strength M of the extensional flow in the far field is set to fluctuate and a mechanism of resonance occurs with the bubble oscillations (see Kang and Leal, 1990; Revuelta et al., 2006); however, this case is out of the scope of this research as the strength M does not change with time in the present analysis. Note also that Revuelta et al. (2006) predict that We_c decreases towards zero as $Re \to 0$. In comparing their critical values for We with those reported by Kang and Leal (1990) for intermediate and large Re, substantial discrepancies are obtained. Revuelta et al. (2006) explained these differences arguing that the initial conditions that they imposed and the criteria used to determine We_c are not the same as

those used by Kang and Leal (1990). We observe, however, that some of the results presented by Kang and Leal (1990) seem to have been obtained with the same initial conditions as in the case of Revuelta et al. (2006) but discrepancies in the outcome are surprisingly encountered, when one would have expected agreement.

Turning now our attention to the case of supercritical Weber numbers, figure 2.12 shows the break-up time t_b as a function of the Weber number We for several magnitudes of the Reynolds number Re obtained from the viscous potential flow computations. These predictions are compared with results from the solution of the fully-viscous Navier–Stokes equations. In addition, results for inviscid fluids are also included. The vertical dashed-dotted line corresponds to the critical value reported by Revuelta et al. ($We_c = 2.22$). As explained above, for higher values of We the bubble breaks up. For $3 \leqslant We \leqslant 6$, predictions from both theories show very good agreement. This result is important because it is known (Rodríguez-Rodríguez et al., 2006) that We of order 5 are found in practical applications (e.g., atomization). On the other hand, for $We > 6$, discrepancies become noticeable, with the largest differences found to be of 13% for $Re = 20$, the smallest value used in the analysis, as expected. For the largest Re, differences between viscous potential theory and the results from the Navier–Stokes equations are small. Note that viscous potential flow under-predicts the break-up time, that is, the bubble breaks up in shorter time for viscous potential flow than for the Navier–Stokes motion. Thus, as Re decreases and We increases, rotational effects (vorticity) generated at the interface become influential in the dynamics. From this figure, it is also evident that the break-up time increases as We decreases for fixed Re. Examining Revuelta's results one can notice that for the smallest Re considered in their work, a plateau is obtained in the graphs of break-up time versus We. That is, for fixed Re, there exists certain We above which break-up time becomes almost independent of the Weber number. This trend is not reproduced by the viscous potential flow results. It should be mentioned that the break-up time in most of the simulations presented in this work is obtained by stopping the computations when the minimum radius in the neck region reaches $r_{\min} < 2 \times 10^{-3}$ or, in some cases, 10^{-4}. For a typical initial bubble radius in the order of 1 mm, this criterion establishes a neck dimension smaller than 2 μm to stop the computations. The time for which the bubble or drop actually breaks up will be very shortly after the value set by the criterion (Gordillo et al., 2005). In other words, continuing the computations beyond the aforementioned limit will not significantly modify the break-up time reported in the figures.

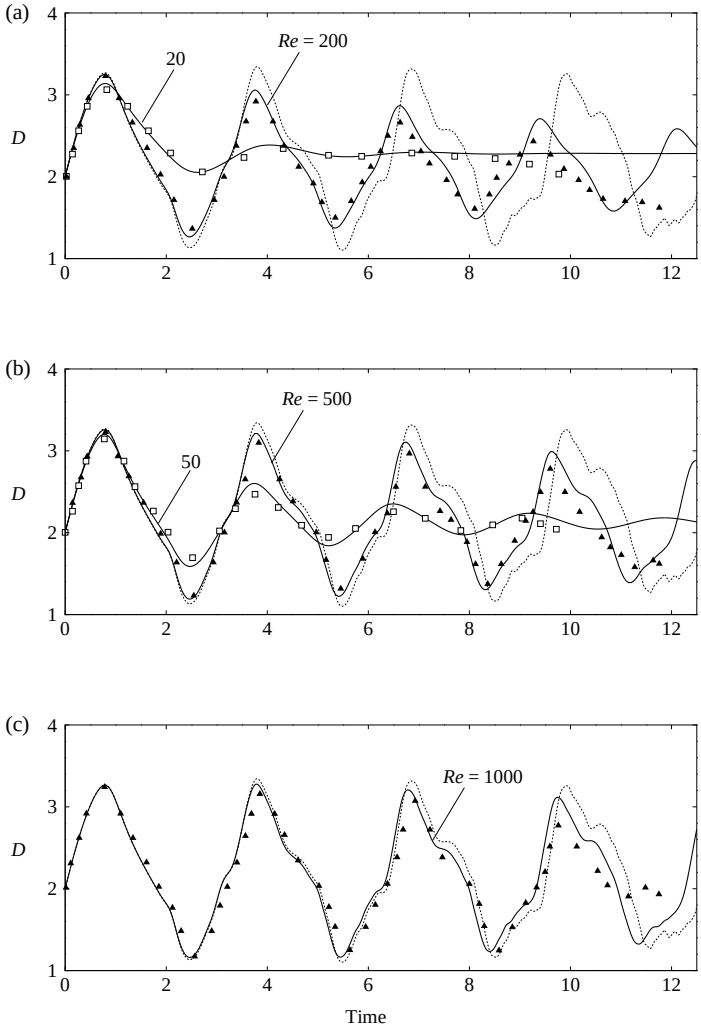

Figure 2.11: Total bubble axial dimension D as a function of time for various Reynolds numbers Re and a sub-critical Weber number, $We = 1.5$. Here, the density ratio $\Lambda = 0.001$ and viscosity ratio $\beta = 0.01$. The bubble shows an oscillatory motion with large amplitude. Decreasing the Reynolds number significantly damps the amplitude of the oscillations until steady state is reached. Therefore, the bubble reaches steady state faster for the lowest Re. Solid line, viscous potential flow results from the present work; dotted line, inviscid potential flow results from the present work; symbols, results from simulations of the fully viscous Navier–Stokes equations by Revuelta et al. (2006), where ▲ corresponds to the highest Re and □ to the smallest. Very good agreement is observed between these two approaches.

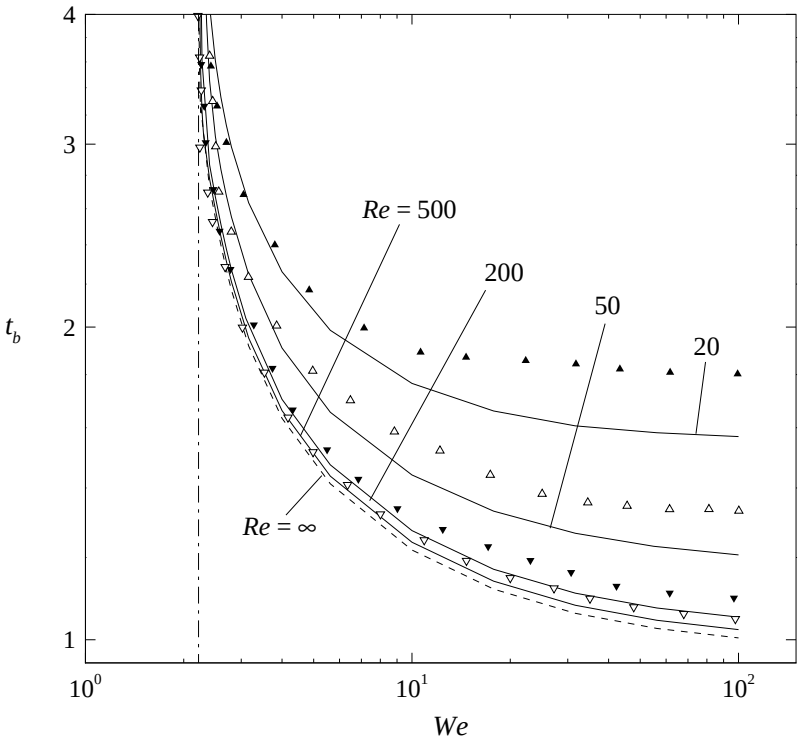

Figure 2.12: Bubble break-up time t_b as a function of the Weber number We for various Reynolds numbers Re. Here, the density ratio $\Lambda = 0.001$ and viscosity ratio $\beta = 0.01$. Solid line, viscous potential flow results from the present work; dashed line, inviscid potential flow results from the present work; symbols, results from simulations of the fully viscous Navier–Stokes equations by Revuelta et al. (2006), where ▲ corresponds to $Re = 20$, △ to $Re = 50$, ▼ to $Re = 200$, and ▽ to $Re = 500$. The vertical dashed line represents the cross-over from a subcritical condition (no break-up) to a super-critical condition (break-up).

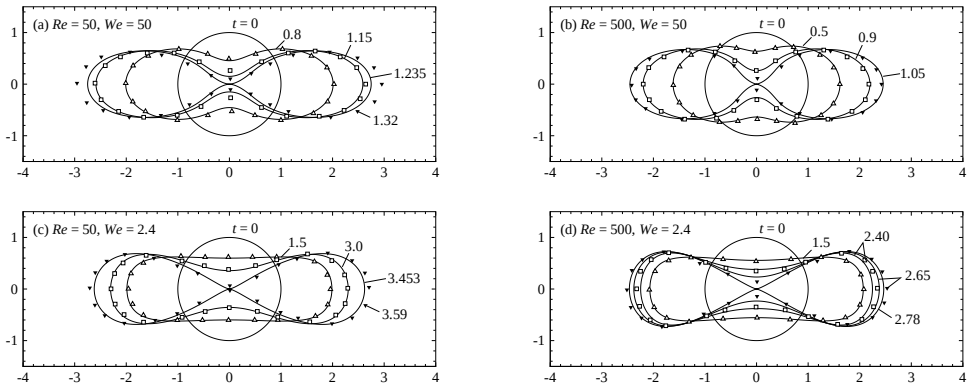

Figure 2.13: Bubble break-up profiles with density ratio $\Lambda = 0.001$, viscosity ratio $\beta = 0.01$, Reynolds numbers $Re = 50$ and 500, and Weber numbers $We = 2.4$ and 50. The solid lines represent results from the viscous potential flow analysis of the present work. Symbols correspond to results from simulations of the fully viscous Navier–Stokes equations given by Revuelta et al. (2006). The profiles by Revuelta et al. for the last instant shown in the figures, and denoted by ▼, do not correspond to the instant of break-up.

The time evolution of the bubble interface for different combinations of Re and We obtained with the method presented here is compared to the profiles presented by Revuelta et al. (2006) in figure 2.13. For the latter, three instants before pinch-off are presented. It should be mentioned that Revuelta et al. did not show the bubble interface at the instant of pinch-off, but *before* and *after* pinch-off (the latter is not reproduced here). Overall, the predictions from the boundary element formulation for viscous potential flow agrees well with the profiles given by the level set method used by Revuelta et al. coupled with a Navier–Stokes solver. In particular, the match is very good for the instants well before pinch-off as the effects of the vorticity created at the interface are still inconsequential. For cases (a), (b) and (c), our irrotational solution clearly underpredicts the break-up time; case (a), i.e. $Re = 50$ and $We = 50$, shows the most conspicuous difference since we predict $t_b = 1.235$ whereas Revuelta's et al. computations result in $1.32 < t_b < 1.4$. For case (d), however, the present computation predicts a larger break-up time $t_b = 2.78$, whereas Revuelta et al. indicate $2.65 < t_b < 2.72$. This is evidence that for supercritical We close to the critical value, there exists discrepancies between the viscous potential flow and the Navier–Stokes results. These differences are difficult to appreciate in figure 2.12.

In figure 2.14, graphs of minimum neck radius $r_{\min}$ as function of τ are shown

when the interface approaches pinch-off for four cases corresponding to super-critical conditions that combine the values $Re = 50$ and $Re = 500$, with $We = 2.4$ and $We = 50$. For the interval plotted, $r_{\min} \sim \tau^{\alpha}$, with the "effective" coefficient α ranging between 0.52 and 0.65. For $We = 50$, when Re decreases from 500 to 50 (i.e., increasing liquid viscosity with everything else fixed, including interfacial tension), the exponent increases from $\alpha = 0.60$ to 0.65, a result that follows a tendency observed in numerical simulations performed for a bubble detaching from a nozzle due to gravity (Quan and Hua, 2008). Although we are comparing different physical settings, the exponents α follow a similar tendency here and there. In any case, as mentioned above, α depends on the initial and boundary conditions (Bolaños-Jiménez et al., 2009). The increment of α with liquid viscosity has been obtained in experiments for a bubble coming out of a nozzle (Burton et al., 2005; Thoroddsen et al., 2007; Bolaños-Jiménez et al., 2009), even though in this case surface tension might vary as the liquids are changed to modify the viscosity. In contrast, for $We = 2.4$, decreasing Re also reduces the exponent α; we argue that this trend is due to the fact that this We is close to the critical value and thus the break-up times are longer (see figure 2.12 and figure 2.13), and the effects of the vorticity generated at the interface might therefore become important. Notice also that when the strain rate, fluid densities and viscosities, and bubble initial radius are held fixed and surface tension decreases, We increases with Re fixed and our model predicts an increment in α, a trend that agrees with previous numerical results for the collapse of a bubble coming out of a nozzle (Quan and Hua, 2008).

The steady shapes computed with the viscous irrotational formulation are presented in figure 2.15 for a bubble with Reynolds number $Re = 10$ and $Re = 100$ and several sub-critical Weber numbers. Starting with a spherical bubble and setting $\Lambda = 0.001$ and $\beta = 0.01$, the simulations are monitored until steady state is reached in each case. These results are compared with predictions by Ryskin and Leal (1984) obtained by solving the *steady* incompressible Navier–Stokes equations for a bubble in uniaxial extensional flow neglecting the material density and viscosity of the fluid within the bubble; in this case, a zero-shear-stress condition is imposed at the free surface. For $Re = 10$, the bubble tend to extent in the direction of the principal axis of strain (z-axis) due to the effect of the viscous stress distribution (Ryskin and Leal, 1984). For fixed Re, increasing We, that is, decreasing the restoring capillary forces, increases the axial dimension while decreases the radial dimension. For $Re = 100$, the dynamic pressure dominates because in this condition the viscous stresses are weak, so that the surface of the bubble is pushed inwards at the stagnation points. This situation resembles the extensional flow of an inviscid fluid over

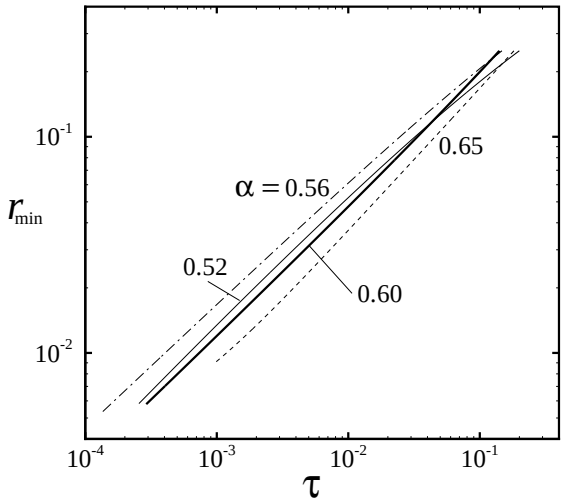

Figure 2.14: Minimum neck radius $r_{\min}$ as a function of the time to break-up $\tau = t_b - t$ for a bubble in uniaxial straining motion; the density ratio $\Lambda = 0.001$ and the fluids are viscous with viscosity ratio $\beta = 0.01$. For the interval shown the motion follows the scaling $r_{\min} \sim \tau^{\alpha}$, where α is an "effective" exponent. The thin solid line corresponds to a Reynolds number $Re = 50$ and Weber number $We = 2.4$; for the dashed line, $Re = 50$ and $We = 50$; for the dash-dotted line, $Re = 500$ and $We = 2.4$, and the thick solid line corresponds to $Re = 500$ and $We = 50$.

an non-deformable sphere, for which the pressure distribution reaches local maxima at the stagnation points; these occur at the points on the free surface on the axis of symmetry and on the circumference of the equatorial plane (i.e. z=0). Qualitatively, the viscous irrotational theories generate steady shapes that look like those determined by the motion of a viscous fluid with vorticity.

2.4.3 Drop - Viscous analysis

In this section we present results for the deformation of a drop in the uniaxial straining flow of a liquid. In this case, we set $\Lambda = 0.8$. The results discussed here are obtained from the viscous potential flow approach and the numerical method of §2.3.4. No comparison is presented for the evolution of the drop interface computed here with profiles resulting from numerical solutions of the *unsteady* incompressible Navier–Stokes equations, since, unexpectedly, this type of computations have not been found in the literature, as commented in §2.1.1.

Figure 2.16 shows the interface profiles for a drop in a uniaxial extensional flow according to the numerical results from the viscous potential flow theory, with

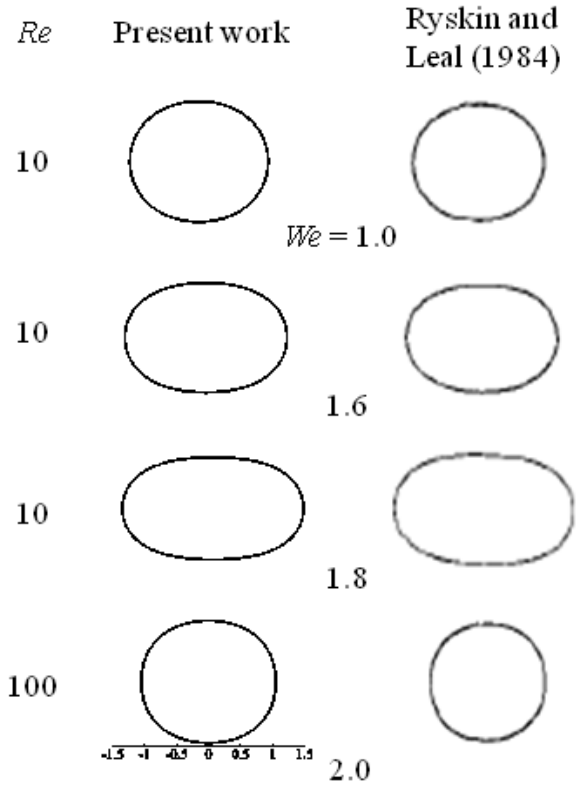

Figure 2.15: Comparison of the steady shape of a bubble in uniaxial straining flow as a function of the Reynolds Re and (sub-critical) Weber We numbers between the present computations using viscous potential flow and the computations of Ryskin and Leal (1984) solving the fully viscous Navier–Stokes equations.

density ratio $\Lambda = 0.8$, viscosity ratios $\beta = 0.1$ and $\beta = 1$, Reynolds numbers $Re = 20$ and $Re = 200$, and Weber number $We = 3$. We have chosen these values of Weber and Reynolds numbers because they are in the same order as those used for the bubble. In particular, $Re = 20$ should correspond to a regime in which both inertia and viscosity affect the flow dynamics. First, one notices that, as in the inviscid case for the drop, the break-up is tertiary. Comparing cases (a) and (b) for $Re = 200$ and cases (c) and (d) for $Re = 20$ indicates that increasing the viscosity ratio from $\beta = 0.1$ to 1 increases the break-up time, a result that can be anticipated because of the resistance that a more viscous liquid offers to motion. In addition, for a fixed β, decreasing Re, e.g., increasing the viscous effects in the flow, leads to higher break-up times and much more elongated drops; in particular, the length of the intermediate satellite drop considerably increases and the size of the daughter drops on the sides, which are large for $Re = 200$, substantially diminishes. A comparison between cases (a) and (b) reveals that for $Re = 200$ changing β from 0.1 to 1 is of little consequence for the drop morphology, whereas for $Re = 20$ the final length of the drop increases in a rather noticeable amount, although the overall shapes are similar. Contrasting with the inviscid case of figure 2.8(a), adding the viscous effects of the irrotational motion for $Re = 200$ in figure 2.16(a) and (b), yields a stretching of the axial drop dimension and, in particular, the intermediate satellite drop stretches about 26% at the time of break-up. Surprisingly, for $Re = 200$, cases (a) and (b), the drops break-up in a shorter time than for the inviscid case ($t_b = 7.425$). This is contrary to the bubble case in which the break-up time for the inviscid system is a *lower* bound for the viscous system (see figure 2.12). Performing computations with $Re > 200$, for $We = 30$ and $\Lambda = 0.8$ (not shown here), we obtained break-up times increasing with Re towards the inviscid limit. The difference in the trends of the break-up time for these two Re in comparison with the inviscid case perhaps has to do with the unequal distribution of the liquid in the drop: For $Re = 200$, it mostly occupies two big lateral drops each of them having similar axial length as the slender satellite drop bridging them. On the other hand, for $Re = 20$, cases (c) and (d), the drops attain large elongations of about four times those attained in the case of $Re = 200$, hence the process of deformation takes longer before pinch-off in comparison with the inviscid case of figure 2.8(a). Finally, the volume changes in the drop during the entire deformation resulting from the numerical solutions are within 0.07% for all the cases presented in figure 2.16.

The evolution of the drop minimum neck radius $r_{\min}$ with time when the interface approaches pinch-off is plotted in figure 2.17 for $We = 3$, $\beta = 0.1$ and two values $Re = 20$ and 200. Figure 2.17(b) shows that $r_{\min} \sim \tau^{2/3}$ for $Re = 200$, in agreement

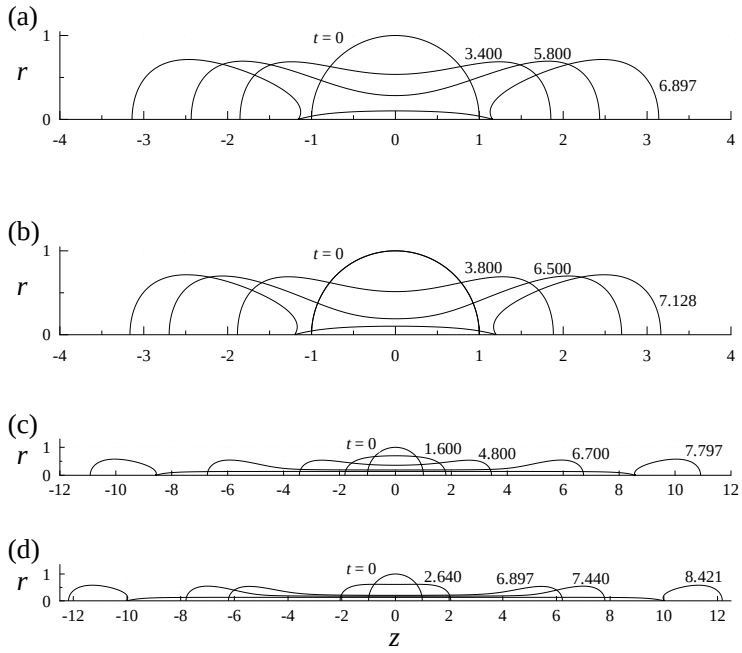

Figure 2.16: Deformation of a drop in a uniaxial straining flow from a viscous potential flow analysis with density ratio $\Lambda = 0.8$, Weber number $We = 3.0$ and (a) $\beta = 0.1$ and $Re = 200$, (b) $\beta = 1.0$ and $Re = 200$, (c) $\beta = 0.1$ and $Re = 20$, and (d) $\beta = 1.0$ and $Re = 20$.

with the inviscid potential regime (Leppinen and Lister, 2003), as expected for such a large value of the Reynolds number. This scaling law is governed by inertia and surface tension. On the other hand, in figure 2.17(a), obtained for $Re = 20$, a transition is observed as $r_{\min} \to 0$ and $\tau = t_b - t \to 0$ from the inviscid scaling to the scaling $r_{\min} \sim \tau$, which corresponds to a regime where viscous effects are significant for the dynamics of the interface (Eggers, 1993; Lister and Stone, 1998). The transition to this regime occurs for $r_{\min} \approx 3 \times 10^{-3}$ as shown in the insert of figure 2.17(a). This insert also shows that the change in $r_{\min}$ unexpectedly starts to deviate from the latter scaling at about $r_{\min} \approx 10^{-3}$ as $\tau \to 0$, a response that may be explained by the next figure. In figure 2.18(a), we plot interface profiles for various times approaching pinch-off for $Re = 20$, $We = 3$, $\Lambda = 0.8$ and $\beta = 0.1$. We notice that as $r_{\min} \to 0$, the interface develops a cylindrical section whose length increases with time; this cylinder seems to start forming at about $r_{\min} = 1.5 \times 10^{-3}$ in accord with the deviation depicted in the insert of plot 2.17(a). In figure 2.18(b), we observe that the scaled profiles r_s vs. z_s do not tend to collapse as $\tau \to 0$, and hence are not self-similar with respect to this scaling, as the necking region

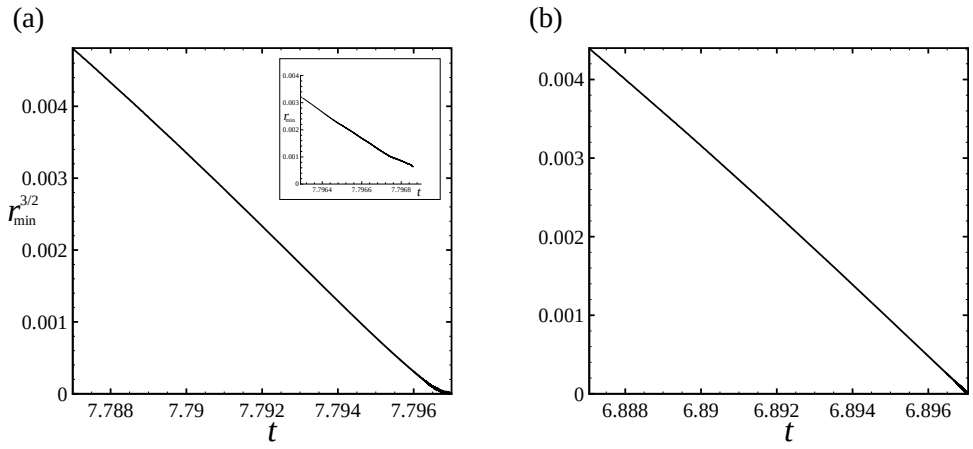

Figure 2.17: Power of the minimum neck radius $r_{\min}^{3/2}$ as a function of time t approaching pinch-off for an viscous drop within another viscous liquid with density ratio $\Lambda = 0.8$, Weber number $We = 3$, viscosity ratio $\beta = 0.1$ and Reynolds number (a) $Re = 20$ and (b) $Re = 200$. The figures show that the minimum neck radius approaches pinch-off following the scaling $r_{\min} \sim \tau^{2/3}$ as the time to pinch-off $\tau = t_b - t \to 0$. In figure (a) a change to the scaling $r_{\min} \sim \tau$ occurs when rupture is imminent.

adopts the shape of a cylindrical thread. This behavior is in contrast with the tendencies described in figure 2.10 for the inviscid case, in which the interface forms cones with an apex-like necking region and the scaled coordinates evolve in a self-similar manner towards pinch-off. Experiments by Cohen et al. (1999) for a viscous drop dripping through another viscous liquid and simulations by Sierou and Lister (2003) for a large range of viscosity ratios have shown self-similar behavior for the drop pinch-off; however, in their studies, the limit of no inertia (i.e. Stokes flow) is guaranteed even at macroscopic scales, and thus their conditions differ from those in our simulations. On the other hand, Doshi et al. (2003) conducted experiments for a water drop dripping through a very viscous liquid such that $\beta = 10^{-4}$, which is much lower than the value used here, and they observed the formation of a long thread bridging two conical sections of the drop. Another difference is that in those experiments, overturning of the steep side of the interface around the neck does not occur when the thread is formed and its slope remains lower than 90^o measured from the positive z-semi-axis. In sum, we do not know whether the predicted formation of a cylindrical necking section for $\beta = 0.1$ is physically realizable or it is an artifact resulting from the lack of vorticity in our model.

In addition, we performed simulations with $\beta = 1$ and found (not plotted here)

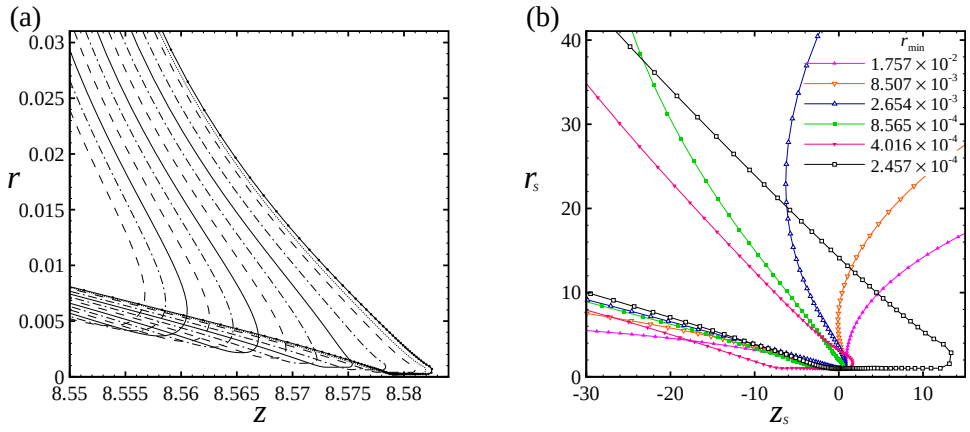

Figure 2.18: Interface shapes for various times approaching pinch-off for a drop of a viscous liquid in another viscous liquid computed with the viscous potential flow approach; the density ratio is $\Lambda = 0.8$, the viscosity ratio is $\beta = 0.1$, the Reynolds number is $Re = 20$ and the Weber number is $We = 3$. In figure (a) the coordinates r vs. z are shown; for the last instant, the node distribution over the interface is depicted, highlighting the high density of the grid around the neck region. In figure (b) the shapes are rescaled with the minimum neck radius $r_{\min}$ and centered on $z_{\min}$, i.e., $z_s = (z - z_{\min})/r_{\min}$ and $r_s = r/r_{\min}$ but they do not tend to collapse and the formation of a cylindrical section is predicted. Two decades of variation of $r_{\min}$ with time are shown in the legend.

that, after transitioning from the inviscid scaling, the linear scaling region $r_{\min} \sim \tau$ persists all the way towards the last instant considered in the simulations, for which $r_{\min} = 1.8 \times 10^{-3}$; this value of $r_{\min}$ is about an order of magnitude higher than the final $r_{\min}$ for $\beta = 0.1$ (see figure 2.18(b)). Perhaps, continuing the computations would have revealed the formation of a cylindrical neck section; unfortunately, continuing the simulation was impractical for this case. The point of transition to the linear scaling is observed at $r_{\min} \approx 8 \times 10^{-3}$ in agreement with the predictions of the theory $r_{\min} \sim \beta^{-1} Oh_i^2$ (Lister and Stone, 1998), obtained from scaling arguments that takes into account viscous effects of the inner and outer fluids, and valid when both fluids have comparable viscosities or the inner fluid is more viscous than the outer fluid. Here, $Oh_i \equiv \mu_i / \sqrt{\rho_i \gamma a}$ is the Ohnesorge number based upon the properties of the inner fluid, which can be easily computed combining We, Re, Λ and β to eliminate parameter M. With $\beta = 1$ and the other parameters known as well ($We = 3$, $Re = 20$, $\Lambda = 0.8$), we have $Oh_i = 0.097$ and $r_{\min} = 9 \times 10^{-3}$.

Even though data for the transient of interface deformation from the solution of the unsteady incompressible Navier–Stokes equations have not been found for

the problem considered here, comparison with data from computations of rotational flows is still possible in the case of steady shapes, since Ramaswamy and Leal (1997) obtained numerical solutions for those equations, dropping the unsteady terms, for the case of a drop in a uniaxial extensional flow for a wide range of density and viscosity ratios, varying the Weber number, and considering several values of the Reynolds number. They presented the results in terms of the deformation parameter, $D_f \equiv (l_z - l_r)/(l_z + l_r)$, where l_z and l_r are half the dimension of the drop measured on the z-axis and on the r-axis (plane z=0), respectively (see figure 2.3); D_f is identically zero for a spherical interface. Results assuming the potential flow of viscous fluids for $\Lambda = 1$, $\beta = 1$ lead to $D_f = 0.13$ for the pair $(Re, We) = (10, 1)$, $D_f = 0.05$ for $(100, 2)$, and $D_f = 0.07$ for $(100, 2.4)$, whereas they reported, $D_f = 0.16$ for $(10, 1)$, $D_f = 0.09$ for $(100, 2)$, and $D_f = 0.12$ for $(100, 2.4)$, using our notation. Therefore, although qualitatively our predictions follow the trend of their results, large quantitative differences are appreciated and their results are underpredicted by ours. Because a very long time period passes between start-up and the reaching of the steady state in comparison with typical break-up times in the super-critical conditions (steady state is reached in time periods about an order of magnitude longer than typical drop break-up times, roughly), diffusion of vorticity in the actual flow away from the interface where it is generated presumably produces strong deviations of the actual velocity field from irrotationality. Thus, in terms of the prediction of the deformation parameter for a steady drop, viscous potential flow turns out to be an inadequate approximation for the cases considered in this exercise.

2.5 Concluding remarks

The deformation of a bubble or drop in a uniaxial extensional flow starting from a spherical shape is studied in this work. Based on experimental and numerical evidence, this model has been regarded as a suitable first approximation to the phenomenon of bubble break-up in a turbulent flow; for drop break-up, although quantitatively has not been satisfactory, qualitatively it does describe the main features of the deformation. The problem formulation adopted here assumes the potential flow of two viscous, incompressible fluids; hence, the effects of the vorticity, which is generated at a fluid-fluid interface in an actual fluid motion due to continuity of the tangential components of velocity and stresses, are neglected in this approximation. Viscosity enters the analysis via the balance of normal stresses at the interface which includes capillary forces. The parameters governing the bubble or drop break-up

process studied here are the ratios of inner to outer fluids density and viscosity, Λ and β, respectively, and the Reynolds and Weber numbers, Re and We, respectively, defined in terms of the outer fluid properties and the principal strain rate in the far field. We aimed to evaluate the performance of the viscous irrotational approximation by comparing with solutions of the fully-viscous Navier–Stokes equations, where available.

Due to the irrotational assumption, a boundary integral method for axisymmetric potential problems on both interior and exterior domains with appropriate constraints at the interface is the best choice. The equations describing the evolution of the interface are given by the kinematic condition and the conservation of linear momentum. This set of equations is solved adopting the numerical method proposed by Rodríguez-Rodríguez et al. (2006), who considered the same physical setup although for the flow of inviscid fluids. Some differences in our implementation of their numerical method are worth of highlighting, namely, the application of quintic splines instead of quartic ones, and the use of grid refinement to improve resolution in the interface region approaching pinch-off. The code has been validated by comparing its predictions for the amplitude and frequency of small oscillations about the spherical shape of a bubble or a drop with theoretical predictions from the linear theory of potential flow of inviscid and, perhaps for the first time, viscous fluids. Moreover, computations of nonlinear deformations of a bubble or drop in a uniaxial straining flow showed excellent agreement with predictions by Rodríguez-Rodríguez et al. (2006). Also, from the results for the inviscid nonlinear case, the evolution of the minimum neck radius towards pinch-off is shown to follow a well-known scaling with the time to pinch-off, and the interface shapes approach rupture in a self-similar fashion after appropriate rescaling. From our computations, mass (volume) for the bubble or drop during the entire process of deformation was conserved to within errors in the order of 0.1% at most.

On one hand, boundary element methods are suitable for the tracking of an interface because the dimensionality of the problem is reduced by one and discretization is only required at the interface and therefore all the computational effort can be concentrated there. Moreover, in problems where the domain extends with no bounds, conditions in the far-field appear as an additional term in the *exact* integral equation, i.e. before discretization. On the other hand, formulating a boundary integral equation requires a fundamental solution of the partial differential equation on hand. For flow of fluids in which both viscosity effects and inertia are relevant, the motion is governed by the Navier–Stokes equations; no fundamental solution exists for this nonlinear equations and thus writing boundary integral formulations

for them is complicated and generates volume integrals (Wrobel, 2002). For problems of incompressible potential flow, Laplace's equation, for which a fundamental solution exists, comes into play and boundary integral equations that involve information only at the boundaries can be written. In the vast majority of the cases, boundary integral methods has been applied to problems of flow of inviscid fluids, with a very few exceptions. To the best of our knowledge, for the first time, the viscous effects of the irrotational motion for the fluids *on both sides* of the interface are considered in a problem in which the boundary integral method is applied to model the interface dynamics.

We presented the comparison of the results obtained here for the bubble with results from computations involving the unsteady, incompressible Navier–Stokes equations carried out by Revuelta et al. (2006) using a level-set method. Such a comparison was not possible for the drop, since numerical works of this class have not been reported in the literature known to us. From the analysis of the results presented in this work, the following conclusions can be drawn. First, for the case of the *bubble* for which the density and viscosity ratios $\Lambda \ll 1$ and $\beta \ll 1$, we have,

- Two different paths for the evolution of the bubble interface were distinguished in our simulations in agreement with the patterns described in the literature: If the Weber number is larger than a critical value, $We_c = 2.22$ for the bubble, independent of the Reynolds number for $Re \geqslant 20$ (Revuelta et al., 2006), for fixed ratios of density and viscosity, the bubble breaks up at a finite time into two symmetric pieces. If the Weber number is smaller than a critical value, the bubble undergoes nonlinear oscillations and does not break up, eventually reaching a steady-state shape as a consequence of viscous damping.

- For the sub-critical condition, $We < We_c$, the results from the viscous irrotational solution show good agreement with the predictions from the Navier–Stokes solver for the time variation of the bubble axial dimension and during various cycles of oscillations, not only for the largest Reynolds numbers considered, i.e. $Re = 200$, 500 and 1000, but also for $Re = 20$ and $Re = 50$, for which the amplitude of the oscillations are rapidly damped. This tendency is a consequence of the irrotational initial condition. Moreover, steady bubble shapes resemble those presented in the literature from the numerical solution of the steady Navier–Stokes equations

- For the super-critical condition, the viscous potential flow computations result in interface shapes evolving towards pinch-off that are very similar to the bubble shapes obtained from the solution of the Navier–Stokes equations. For

a fixed Reynolds number, the break-up time decreases as the Weber number increases. For a set of intermediate and large Reynolds numbers, the break-up time computed here shows good agreement with Revuelta's predictions in the interval $3 \leqslant We \leqslant 6$. For $We > 6$ and up to the maximum value considered in this study ($We = 100$), viscous potential flow tends to underpredict the break-up time, especially for the lowest Reynolds numbers considered, namely, $Re = 20$ and $Re = 50$. Moreover, for these values of Re, the Navier–Stokes motion gives rise to a plateau in the break-up time for $We \gtrsim O(10)$ that is not predicted by the viscous irrotational solution. For the largest Re, differences are relatively small between the irrotational and rotational theories. The predictions from the inviscid theory provide a lower bound for the break-up time, which decreases with increasing Re for fixed We. In the interval $We_c < We < 3$, discrepancies between both theories become noteworthy. The minimum neck radius evolves towards pinch-off following scalings with time to pinch-off similar to those reported from experiments and numerical simulations.

In the case of the *drop*, with density ratio $\Lambda = 0.8$, we highlight the following findings from the computations performed considering potential flow of two viscous fluids,

- For the cases presented in this work, the drop deforms and breaks up into three daughter drops, where the intermediate drop takes a slender form, and the deformation pattern exhibits reflectional symmetry, which is a consequence of the initial and boundary conditions.

- From the evolution of the shape of a drop computed for a Reynolds number $Re = 200$, viscosity ratios $\beta = 0.1$ and 1 and Weber number $We = 3$, the morphology and length scales are similar to those for the inviscid case. Decreasing to $Re = 20$ renders totally different shapes: Approaching pinch-off, the drop becomes very elongated and slender, with lateral daughter drops having a much smaller volume than the much larger intermediate cylindrical daughter drop. For these elongated drops with $Re = 20$, the break-up time is longer than for the $Re = 200$ case. Unexpectedly, the break-up time for $Re = 200$ was shorter than for the inviscid case, contrary to the more viscous case of $Re = 20$. Increasing the viscosity ratio from $\beta = 0.1$ to 1 makes the drop length slightly larger, especially for the intermediate Reynolds numbers, i.e. $Re = 20$.

- The deformation parameter, which gives a measure of the degree of deformation suffered by the fluid particle, is computed for a drop that has reached a steady shape for sub-critical conditions, several values of Re and viscosity ratio $\beta = 1$, and compared with results given in the literature from numerical solutions of the *steady*, incompressible Navier–Stokes equations and large discrepancies are encountered. Under these conditions, the vorticity field seems to significantly affect the actual flow and, consequently, the performance of the viscous potential flow approximation in predicting the deformation parameter becomes unsatisfactory.

- Even though our focus here was in the macroscopic morphology of the deformation of a drop or bubble from the undeformed state up to break-up, we plotted the interface shapes in the necking region for several times and the evolution of the minimum radius approaching pinch-off. For the two cases determined by $Re = 20$ and $Re = 200$, $We = 3$, $\Lambda = 0.8$ and $\beta = 0.1$, the neck minimum radius evolves with time towards pinch-off as $r_{\min} \sim \tau^{2/3}$ following the inviscid scale; however, for $Re = 20$, a transition occurs to the scaling $r_{\min} \sim \tau$, for which viscous effects become relevant for the interface motion. As the motion proceeds, the change in the neck radius deviates from this linear variation presumably because of the formation of a cylindrical thread. Finally, for $Re = 20$, rescaled interface shapes with the coordinates of the point for which the neck radius is minimum were plotted for various times and their approach to pinch-off was not self-similar.

Future work may include the application of the code developed in this work to pursue more insight on the interfacial dynamics in the proximity of bubble and drop pinch-off. In particular, the problem of pinch-off of a bubble from a nozzle due to gravity is an interesting prospect since a generous amount of data from meticulous experiments have been presented for this setup and also numerical solutions of the governing equations including vorticity are readily available. The formulation followed here can be modified to include the gravitational body force and the numerical method can also be adapted. The numerical algorithm may also be improved by implementing higher orders approximations for the field functions, i.e. the potential and its normal derivative at the interface, instead of the linear interpolation applied here.

Chapter 3

Viscous irrotational theories and the force on an expanding bubble–A cell-model analysis*

We examine the dynamics of a viscous incompressible fluid bounded internally and externally by spherical shells of variable radius, with an internal boundary (bubble) that translates in rectilinear motion with respect to the outer boundary. The forces acting on the bubble are derived from two purely viscous irrotational theories, namely, viscous potential flow and the dissipation method in a systematic way that highlights the importance of the choice of the outer boundary condition for the stress in the formulation, a treatment that is not given in prior work known to us. By invoking the well-known "cell model", these results are extended for a dilute bubble swarm rising in the limits of high Reynolds and low Weber numbers. Then, results for the drag and bubble swarm rise velocity are compared with numerical simulations and experimental data along with other models presented in the literature.

3.1 Introduction

Bubbly flows in the regime of high Reynolds and low Weber numbers exhibit bubbles that are spherical or nearly spherical. Here these groups are defined in the usual way: the former is defined as $Re \equiv 2Ua/\nu$ and the latter is defined as $We \equiv 2\rho U^2 a/\sigma$ (where U is the bubble velocity, a the bubble radius, ρ the density of the liquid, ν

*Reproduced with permission from Padrino, J. C.; Joseph, D. D. *Ind. Eng. Chem. Res.*, Vol. 48, Number 1, 110–127, 2009.

the kinematic viscosity of the liquid, and σ the interfacial tension). In general, for very high Reynolds numbers, of the order $O(1000)$, say (Levich, 1962), the Weber number is likely greater than unity and the bubble shows important deviations from the spherical shape. Experimentally, the dual limit of high Reynolds and low Weber numbers have been realized with $Re = O(100)$ and $We = O(1)$, respectively (Zenit, Kock, and Sangani, 2001). For instance, bubbles with a diameter in the order of 1 mm rising in water satisfy the dual condition of high Reynolds and low Weber numbers (Sangani and Didwania, 1993; Zenit et al., 2001). Moreover, in this regime, with a clean liquid, that is, free of impurities and surfactants, vorticity effects are confined to a thin boundary layer on the bubble surface and to a wake in a minute neighborhood of the bubble rear end (Levich, 1962). Therefore, liquid motion in the bulk can be considered irrotational. Because of these features, bubbly flows in this regime are particularly suited for analysis. Further simplification is attained by considering bubbles of the same diameter, that is, a monodispersed suspension. In practice, small variation about the mean bubble diameter may be achieved by preventing coalescence with the addition of certain chemicals to the mixture in such low concentration that the gas-liquid interface does not behave as the boundary of a rigid particle, in which case a recirculation zone would appear at the rear side of the bubble, thereby breaking down the irrotational hypothesis (Zenit et al., 2001; Kang, Sangani, Tsao, and Koch, 1997).

For bubbles rising under the action of gravity, the problem have also been described, besides the Reynolds number, by the Eötvös number, which is a characteristic of the bubble size, and the Morton number, which is a group that involves physical properties with no bubble size-dependent quantities (Sankaranarayanan, Shan, Kevrekidis, and Sundaresan, 2002). Small Eötvös numbers are associated with nearly spherical bubbles, whereas larger Eötvös indicates highly distorted bubbles. The Weber number can be recovered by combining those three dimensionless groups. Instead of the Morton number, the Archimedes number may be used (Esmaeeli and Tryggvason, 2005).

In modeling bubbly flows in the regime of low Weber and high Reynolds numbers, viscous drag is usually computed from the liquid potential flow solution exploiting the fact that rotational (viscous) deviations from irrotational motion are confined to thin regions adjacent to the bubbles. In this regard, the dissipation method, based upon the mechanical energy balance, has been a commonly used approach. A boundary layer on a clean bubble interface conforms to the zero-shear-stress boundary condition, because of the large viscosity of the liquid compared to the small viscosity of the gas, rather than to the no-slip constraint enforced on a solid particle.

This boundary layer remains attached almost over the entire bubble interface, as separation occurs only around the rear end. Since vorticity is contained in these narrow regions, it is assumed that the rate of viscous dissipation is given entirely by the irrotational motion (Landau and Lifshitz, 1959).

For a sphere translating in rectilinear motion with constant speed within an infinite liquid, the dissipation approximation seems to have been applied first by Bateman in 1931 (see Dryden, Murnaghan, and Bateman, 1956, p. 157) who obtained the drag $12\pi a\mu U$, where μ is the liquid dynamic viscosity. Later, Ackeret (1952) repeated this dissipation calculation. For a bubble in rectilinear motion, Levich (1949) applied the dissipation method and attained the result given above. This drag is close to the measured value for Reynolds numbers above 20, say (Joseph and Liao, 1994a). It should be noted that for a rigid sphere, with the no-slip condition enforced at its surface, or a spherical bubble of constant volume, for which the tangential component of the traction vanishes at the interface, the dissipation calculation based on potential flow gives rise to the same drag (Joseph and Liao, 1994a). Moore (1963) found the drag $12\pi a\mu U$, which in dimensionless form is written as $48/Re$, by computing the momentum deficit. In addition, he determined the structure of the boundary-layer flow and used this information to improve upon the Re^{-1} result by adding a $Re^{-3/2}$ contribution from the dissipation in the boundary layer and wake. Kang and Leal (1988) and, recently, Joseph and Wang (2004) used different methods to add a viscous correction to the normal stress and obtained $48/Re$. It should be noted that Moore (1959) computed a viscous drag by direct integration of the irrotational normal stress around the bubble, thereby enforcing the zero shear stress at the interface. He found the drag to be $8\pi a\mu U$, which fell short of the dissipation result. Evidently, this discrepancy is resolved by adding a viscous correction to the irrotational normal stress (Moore, 1963; Kang and Leal, 1988; Joseph and Wang, 2004). Tam (1982) extended Moore's (1963) analysis to the case of a translating bubble undergoing acceleration and found the same form of the viscous drag. The approach of potential flow with viscous normal stresses at a gas-liquid interface was employed by Miksis et al. (1982) to compute numerically the shape of a rising bubble using a boundary-integral formulation.

The effect of a varying bubble radius on the force experienced by a bubble translating in an unbounded liquid has been the subject of a number of works. Magnaudet and Legendre (1998) examined this case by means of a frame transformation under which the bubble radius becomes fixed while conserving dynamic similarity. The total force on the bubble is presented for both the inertia-dominated flow and the creeping flow limits. Ohl, Tijink, and Prosperetti (2003) conducted experimental

investigations of this bubble motion, whereas Yang, Prosperetti, and Takagi (2003) carried out numerical simulations. Both works included simplified dynamic models accounting for the forces acting on a bubble that compare favorably with the experimental and numerical data. Takemura and Magnaudet (2004) studied experimentally the history force on a shrinking bubble rising at finite Reynolds number. Recently, Léger and Askovic (2006) carried out the modeling of the boundary layers outside and within a slowly deforming spherical bubble in rectilinear motion. Comprehensive reviews on the advances in the understanding of single bubble dynamics have been given by Magnaudet and Eames (2000) and Kulkarni and Joshi (2005).

Dynamic simulations of the motion of a set of N bubbles moving in a liquid at rest at infinity have been examined in several papers (Voinov and Golovin, 1970; Gavrilyuk and Teshukov, 2005; Ilinskii, Hamilton, and Zabolotskaya, 2007). Smereka (1993) studied the motion of a set of bubbles in a box in a periodic assembly, so that the entire space is filled with an array of boxes. Wang and Smereka (2003) took the continuum limit of the equations of motion for a finite set of bubbles in an unbounded liquid to obtain effective equations in terms of the void fraction. In these works, potential flow is assumed for the liquid motion and viscous effects are given by the dissipation method. Sangani and Didwania (1993) and Kushch, Sangani, Spelt, and Koch (2002) performed dynamic simulations with the viscous drag determined from a leading order viscous correction to the irrotational pressure computed from the analysis of the boundary layer flow around the bubbles. The former also estimated the viscous drag on the bubbles with the gradient of the rate of energy dissipation in potential flow. The latter considered arrays of ellipsoids to account for bubble shape deformation such that flows with finite Weber numbers may be simulated. On the other hand, averaged equations for bubbly flows derived from first principles have been presented by Sangani (1991) and Spelt and Sangani (1998) considering the irrotational motion of a viscous fluid, and in Zhang and Prosperetti (1994) for an inviscid fluid. Recently, the buoyant rise of a set of nearly spherical bubbles as well as deformable ones at $O(100)$ Reynolds number in a periodic box has been studied through direct numerical simulations of the incompressible Navier–Stokes equations by Esmaeeli and Tryggvason (2005) with a front-tracking/finite-volume method. Earlier, these authors (Esmaeeli and Tryggvason, 1998, 1999) applied a similar method to study nearly spherical bubbles at $Re = O(1)$ and $Re \approx 20$. Using the same technique, Bunner and Tryggvason (2002a,b) considered a much larger number of bubbles for the latter Reynolds-number regime. By placing a single bubble in a periodic box, a regular array of bubbles of the same size was simulated by Sankaranarayanan et al. (2002) and Yin, Koch, and Verberg (2006)

using the lattice Boltzmann method for the intermediate-Reynolds-number regime, i.e. $O(10)$. In this regime, the wake effects in the bubble-liquid dynamics cannot be neglected. Careful experiments and detailed measurements have been carried out by Zenit et al. (2001) to study bubbly flow for small Weber and large Reynolds numbers and by Martínez-Mercado, Palacios-Morales, and Zenit (2007) for intermediate and high Reynolds numbers in the range 10 to 500.

Effective properties of particulate flows including hydrodynamic transport coefficients have been modeled by means of effective-medium theories. According to these approximate theories, the conditionally-averaged field satisfies the suspending fluid equations within a suitably sized exclusion region that encloses a reference particle or bubble and the unconditionally-averaged fields in the effective medium occupying the rest of the space (Spelt et al., 2001). The method does not bear the ambiguity of the choice of proper constraints at the interface between the effecttive medium and the exclusion region. Kushch et al. (2002) determined the added mass and viscous drag coefficients for a suspension of oblate spheroidal bubbles using an effective medium theory showing remarkable agreement with dynamic simulations. Detailed descriptions of the effective medium theory applied in various contexts can be found elsewhere (Dodd, Hammer, Sangani, and Koch, 1995; Sangani and Mo, 1997; Koo and Sangani, 2002, 2003).

A simplified approach to examine the hydrodynamics of bubbly flow for small or moderate gas volume fraction is obtained through the so-called "cell-model" representation. For nearly spherical bubbles, the bubbly flow is assumed to be composed of identical unit spherical cells. Each cell consists of a spherical bubble surrounded by a liquid bounded by an outer spherical envelope concentric with the bubble. The outer sphere radius is such that the cell void fraction is identical to the void fraction of the bubbly flow (Happel and Brenner, 1965). The underlying hypothesis is that the dynamics within the reference cell is representative of the dynamics in the entire bubbly flow. The choice of the outer boundary condition in the cell model has been subject of debate (see Chhabra, 1995, and references there in). Happel and Brenner (1965) argue that each cell should be a unit independent of the rest of the assemblage, so no energy exchange takes place with its surroundings. They thus consider that a frictionless outer boundary is adequate. Other boundary conditions, however, have been applied in the literature. For particulate flows in the limit of creeping motion, Cunningham (1910) applied the cell model with no-slip conditions on the inner and outer spherical boundaries. Happel (1958) considered the same problem although imposing a zero-tangential-stress constraint on the outer envelope. Kuwabara (1959) applied a zero-vorticity boundary condition on the outer

sphere and computed the drag from the dissipation integral evaluated in Stokes flow. However, in his formulation, as pointed out by El-Kaissy and Homsy (1973), the term accounting for the work of the tangential stress on the outer envelope is missing. The zero-vorticity constraint implies that mechanical energy is transferred between the reference cell and the rest of the domain. For higher Reynolds numbers, Marrucci (1965) employed the cell model to predict the drag on the bubble evaluating the dissipation integral from the potential flow solution in the cell. Recently, Kendoush (2001) revisited Marrucci's analysis obtaining a different drag. We shall review this discrepancy in §3.3. LeClair and Hamielec (1971) presented the numerical solution of the Navier–Stokes equations for the liquid motion within a unit cell with zero shear stress on the bubble surface and zero vorticity on the outer sphere. They computed the drag on the bubble with the numerical flow field. Reasonably good agreement with experimental data was reported. A similar numerical analysis was performed by Manjunath et al. (1994) enforcing, on the contrary, a zero-tangential-stress condition on the outer boundary. Chhabra (1995) also presented numerical results for a viscous liquid in a cell model enclosing a bubble to elucidate the effect on the drag of the choice of either zero tangential stress (free surface) or zero vorticity on the outer boundary. He concluded that the viscous force shows a stronger dependence on the void fraction in the zero-vorticity model than in the free-surface model. All these works have considered a cell enclosing a bubble of constant volume. More recently, Sherwood (1999) modeled the dynamics of a translating spherical bubble with a time dependent radius surrounded by an inviscid imcompressible fluid bounded externally by a spherical surface. He presented expressions for the force on the bubble and on the outer envelope.

After surveying the literature on the cell model, we are left with the impression that the implementation of the dissipation method lacks a systematic approach to deriving expressions for the forces starting from the mechanical energy equation with emphasis in the role of the cell boundary conditions from dynamics (stresses). The aim of this work is to extend Sherwood's analysis to include viscous effects by use of purely irrotational theories, namely, viscous potential flow and the dissipation approximation. The former approach computes the force on a given direction by direct integration of the irrotational normal stress over the boundary, whereas the latter predicts the drag from the mechanical energy balance evaluated in potential flow, so that the viscous effects arise from the rate of energy dissipation. First, working formulae for the drag is developed by applying these theories to the system defined by a spherical bubble with its center moving in a rectilinear path and undergoing volume changes within a bounded liquid domain with a deforming

outer boundary. The shape evolution of the inner and outer boundaries is assumed to be known, such that the incompressibility constraint is satisfied. Two different conditions for the tangential stress on the outer boundary are considered, namely, a zero-tangential-stress condition (i.e. free surface) and an irrotational-tangential-stress condition. In the inner boundary (i.e. bubble surface), zero tangential stress is enforced. This is the same as having two boundary-value problems. The dissipation method gives rise to different expressions for the force on the bubble on a given direction depending upon the tangential stress condition applied on the outer boundary of the reference cell. Viscous potential flow, on the other hand, gives the same bubble drag independently of the choice of the outer boundary condition. Next, the flow field is obtained from Sherwood's potential analysis. This potential flow is then entered in the machinery derived before to compute the forces on the spherical bubble and on the spherical outer envelope at the instant when both are concentric. This is the same geometric condition for which Sherwood computed the forces. The expressions for the drag on the bubble show the added-mass contribution given by the acceleration of the bubble translational motion and the rate of change of the bubble radius, already given in Sherwood's inviscid analysis, plus a viscous drag depending upon the instantaneous values of the velocity and inner and outer radii. When neither the inner nor the outer radius changes with time, the formulas for the drag are rewritten in terms of the cell void fraction. According to the cell model, these expressions can be used as an approximation for the drag on a typical bubble moving in a bubbly flow with the same average void fraction. These results for the viscous drag from the dissipation method have been given in the literature (Marrucci, 1965; Kendoush, 2001); however, the role of the dynamic boundary conditions, in particular, that of the tangential stress on the outer boundary, is not evident there. Because each of these two expressions for the drag corresponds to a different choice of the outer boundary condition for the stress, these results do not contradict each other, neither is one of them in error, as has been argued in the literature (Kendoush, 2001). Results indicate that the drag from the model with an irrotational tangential stress on the outer boundary shows a stronger dependence upon the void fraction than the drag from a free-surface cell model. Both results for the bubble drag from the dissipation method, however, match to first order in the void fraction. Using the formulae for the drag, expressions for the terminal rise velocity for a bubble swarm in dimensionless form are obtained. Finally, predictions from these analyses are compared with results from other theoretical approaches, numerical simulations and experiments.

3.2 Force on an expanding bubble within a bounded liquid

We present the analysis that gives rise to the formulae for the force acting on a spherical compressible bubble along its direction of motion within a liquid confined by a spherical surface. Two types of purely irrotational analysis are carried out, namely, viscous potential flow and the dissipation method.

3.2.1 Problem formulation

Consider a spherical bubble B moving within a viscous incompressible Newtonian fluid occupying the volume V in three dimensions. Let S_1 be the interface shared by the bubble B and the liquid in V and let S_2 be the outer spherical surface bounding V (figure 4.1). Both, S_1 and S_2 remain spherical during the entire motion. Suppose the center of the bubble moves on a straight line containing the center of the outer sphere S_2 along the direction $\mathbf{e}_x$ (fixed) with velocity U, which may be a function of time. Moreover, suppose the bubble volume can change with time but the bubble does not rotate. The pathline followed by the center of the bubble thus defines the axis of symmetry for this configuration. Let $\mathbf{u}$ be the velocity field in the laboratory (inertial) reference frame. Let $\mathbf{v}$ be the velocity field with respect to a noninertial reference frame whose origin moves with velocity $U\mathbf{e}_x$ relative to the laboratory frame, but it is not allowed to rotate. Velocities $\mathbf{u}$ and $\mathbf{v}$ are then related by

$$\mathbf{u} = U\mathbf{e}_x + \mathbf{v}. \tag{3.1}$$

The fluid dynamics within the bubble does not enter the analysis. Suppose the following boundary conditions are given:

On S_1,

$$\mathbf{n}_1 \cdot \mathbf{v} = \hat{q}_1, \tag{3.2}$$

$$\mathbf{n}_1 \cdot \mathbf{T} \cdot \mathbf{t}_1^{(\alpha)} = 0, \qquad \text{with} \quad \mathbf{t}_1^{(\alpha)} \perp \mathbf{n}_1, \tag{3.3}$$

On S_2,

$$\mathbf{n}_2 \cdot \mathbf{u} = q_2, \tag{3.4}$$

$$\mathbf{n}_2 \cdot \mathbf{T} \cdot \mathbf{t}_2^{(\alpha)} = \tau_2^{(\alpha)}, \qquad \text{with} \quad \mathbf{t}_2^{(\alpha)} \perp \mathbf{n}_2, \tag{3.5}$$

and $\alpha = 1, 2$. Here, $\mathbf{n}_1$ is the inward unit normal on S_1 to V (i.e. outward to

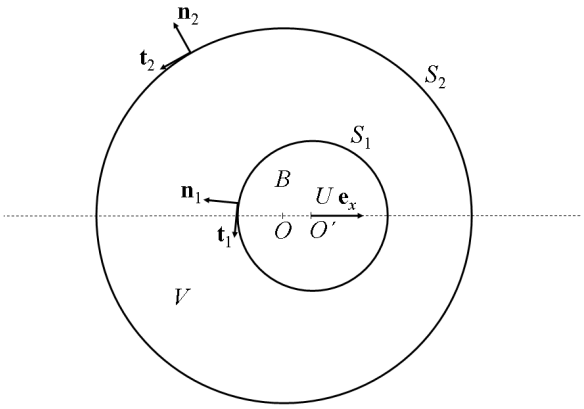

Figure 3.1: Sketch of a spherical bubble B centered at O' sharing interface S_1 with the incompressible fluid occupying volume V bounded externally by the spherical surface S_2 centered at O. The motion of the bubble B is such that O' moves along the fixed direction $\mathbf{e}_x$ with speed U, and its radius can change with time. The line containing the path of O' also contains O, which is fixed with respect to the laboratory frame. This line is therefore the axis of symmetry of the problem. The separation between O and O' is considered to be small. Because of the incompressibility of the fluid in V, changes in the radius of S_2 occur in accordance with changes in the radius of B. Symbol $\mathbf{n}_1$ denotes the inward unit vector to V on S_1 and $\mathbf{n}_2$ denotes the outward unit vector to V on S_2. Unit vectors $\mathbf{t}_1$ and $\mathbf{t}_2$ are orthogonal to $\mathbf{n}_1$ and $\mathbf{n}_2$, respectively.

the bubble) and $\mathbf{n}_2$ is the outward unit normal on S_2 to V; $\mathbf{t}_1^{(\alpha)}$ and $\mathbf{t}_2^{(\alpha)}$ are unit vectors. Each triad $\{\mathbf{n}_\beta, \mathbf{t}_\beta^{(1)}, \mathbf{t}_\beta^{(2)}\}$, with $\beta = 1, 2$, is orthogonal and right-handed. Symbol $\mathbf{T}$ denotes the stress tensor.

Constraint (3.3) is a standard interfacial condition for a bubble, in which case the gas dynamic viscosity is small in comparison to that of the liquid. We are assuming here that Marangoni stresses, which originate from surface tension gradients, are negligible. This is typical of a clean gas-liquid interface (e.g., free of impurities or surfactants). From (3.1) and (3.2), notice that $q_1 = \mathbf{n}_1 \cdot \mathbf{u} = U\mathbf{n}_1 \cdot \mathbf{e}_x + \hat{q}_1$ on S_1.

Two choices for $\tau_2^{(\alpha)}$ in (3.5) for the outer boundary are considered in this work, namely, (i) zero tangential stress and (ii) irrotational tangential stress. The latter is established from the potential flow in V, which is fully determined by kinematic boundary conditions as explained in §3.2.2.

Using (3.2) and (3.4), the incompressibility condition and divergence theorem lead to

$$\int_{S_1} \hat{q}_1 dA = \int_{S_2} q_2 dA, \tag{3.6}$$

which establishes a constraint that $\hat{q}_1$ and q_2 must satisfy.

The forces that the fluid in V exerts on S_1 and S_2 in the $\mathbf{e}_x$ direction are

$$D_1 \equiv \int_{S_1} \mathbf{n}_1 \cdot \mathbf{T} \cdot \mathbf{e}_x dA, \tag{3.7}$$

$$D_2 \equiv -\int_{S_2} \mathbf{n}_2 \cdot \mathbf{T} \cdot \mathbf{e}_x dA. \tag{3.8}$$

With the decomposition $\mathbf{e}_x = \mathbf{n}_\beta(\mathbf{n}_\beta \cdot \mathbf{e}_x) + \mathbf{t}_\beta^{(\alpha)}(\mathbf{t}_\beta^{(\alpha)} \cdot \mathbf{e}_x)$, for $\alpha = 1, 2$ and $\beta = 1, 2$, with summation over α but not over β, these expressions can be written as

$$D_1 = \int_{S_1} \mathbf{n}_1 \cdot \mathbf{T} \cdot \mathbf{n}_1(\mathbf{n}_1 \cdot \mathbf{e}_x) dA + \int_{S_1} \mathbf{n}_1 \cdot \mathbf{T} \cdot \mathbf{t}_1^{(\alpha)}(\mathbf{t}_1^{(\alpha)} \cdot \mathbf{e}_x) dA, \tag{3.9}$$

$$D_2 = -\int_{S_2} \mathbf{n}_2 \cdot \mathbf{T} \cdot \mathbf{n}_2(\mathbf{n}_2 \cdot \mathbf{e}_x) dA - \int_{S_2} \mathbf{n}_2 \cdot \mathbf{T} \cdot \mathbf{t}_2^{(\alpha)}(\mathbf{t}_2^{(\alpha)} \cdot \mathbf{e}_x) dA. \tag{3.10}$$

Invoking constraints (3.3) and (3.5), we have

$$D_1 = \int_{S_1} \mathbf{n}_1 \cdot \mathbf{T} \cdot \mathbf{n}_1(\mathbf{n}_1 \cdot \mathbf{e}_x) dA, \tag{3.11}$$

$$D_2 = -\int_{S_2} \mathbf{n}_2 \cdot \mathbf{T} \cdot \mathbf{n}_2(\mathbf{n}_2 \cdot \mathbf{e}_x) dA - \int_{S_2} \tau_2^{(\alpha)}(\mathbf{t}_2^{(\alpha)} \cdot \mathbf{e}_x) dA. \tag{3.12}$$

It is assumed in this analysis that the geometry of the fluid domain V is known

at any time. For the sake of simplicity, we have taken hydrostatics forces (i.e. buoyancy) out of the analysis.

3.2.2 Viscous potential flow

The viscous potential flow approximation of the forces on surfaces S_1 and S_2 is obtained by direct integration of the stress computed for purely irrotational motion. For a free-shear surface, where the actual tangential stress is zero, only the normal stress enters in the viscous potential flow computation even though the irrotational tangential stress is not zero.

For irrotational motion, the velocity field is $\mathbf{u} = \nabla\phi = U\mathbf{e}_x + \mathbf{v}$. For incompressible flow, the potential satisfy

$$\nabla^2\phi = 0, \tag{3.13}$$

with boundary conditions

$$\mathbf{n}_1 \cdot \nabla\phi = q_1 = U\mathbf{n}_1 \cdot \mathbf{e}_x + \hat{q}_1 \tag{3.14}$$

on S_1, and

$$\mathbf{n}_2 \cdot \nabla\phi = q_2 \tag{3.15}$$

on S_2. The irrotational pressure p satisfies the Bernoulli equation:

$$\frac{p}{\rho} + \frac{\partial\phi}{\partial t} + \frac{|\mathbf{u}|^2}{2} = C(t). \tag{3.16}$$

The forces on the boundaries of V are computed according to (3.11) and (3.12) for irrotational motion. For a Newtonian fluid, the stress tensor is thus given by

$$\mathbf{T} = -p\mathbf{1} + 2\mu\nabla \otimes \nabla\phi. \tag{3.17}$$

Hereinafter, for the sake of brevity, we use the symbol $\mathbf{D} \equiv \nabla \otimes \nabla\phi$ to refer to the strain-rate tensor in potential flow.

On the free-shear surface S_1 or bubble interface, the force in the $\mathbf{e}_x$ direction is

$$D_1 = \int_{S_1} \left(-p + \mathbf{n}_1 \cdot 2\mu\mathbf{D} \cdot \mathbf{n}_1\right) \mathbf{n}_1 \cdot \mathbf{e}_x dA. \tag{3.18}$$

The force on the outer free surface S_2 in the $\mathbf{e}_x$ direction is, for zero tangential

stress,

$$D_2 = -\int_{S_2} \left(-p + \mathbf{n}_2 \cdot 2\mu\mathbf{D} \cdot \mathbf{n}_2\right) \mathbf{n}_2 \cdot \mathbf{e}_x dA. \tag{3.19}$$

In the case of an outer boundary subject to a tangential stress given by the potential flow in the interior, that is,

$$\tau_2^{(\alpha)} = \mathbf{n}_2 \cdot 2\mu\mathbf{D} \cdot \mathbf{t}_2^{(\alpha)}, \tag{3.20}$$

the self-equilibration of irrotational viscous stresses on a closed surface (Appendix C) implies

$$\int_{S_1} \mathbf{n}_1 \cdot 2\mu\mathbf{D} \cdot \mathbf{e}_x dA = \int_{S_2} \mathbf{n}_2 \cdot 2\mu\mathbf{D} \cdot \mathbf{e}_x dA = 0. \tag{3.21}$$

Hence,

$$D_2 = -\int_{S_2} \left(-p\right) \mathbf{n}_2 \cdot \mathbf{e}_x dA. \tag{3.22}$$

Thus, the force on the outer boundary is obtained solely from the irrotational pressure in this case.

3.2.3 Dissipation method

In this section, the computation of the forces on the inner and outer boundaries of the fluid domain oriented along the direction of bubble translation are obtained by used of the dissipation approximation based upon irrotational motion. For the outer boundary, in addition to the kinematic constraint imposed on the normal velocity, two choices are considered for the shear stress, as in §3.2.2: (i) Zero tangential stress and (ii) irrotational tangential stress. Each of these possibilities leads to a set of results that are compared with those from viscous potential flow.

Suppose now that the fluid motion in V is governed by the incompressible Navier–Stokes equations with an appropriate set of boundary conditions that includes (3.2)-(3.5). The rate of change of kinetic energy in V is

$$\frac{dE}{dt} = \frac{d}{dt}\int_V \rho \frac{|\mathbf{u}|^2}{2} d\mathcal{V} = \int_V \mathbf{u} \cdot \rho \left(\frac{\partial \mathbf{u}}{\partial t} + \mathbf{u} \cdot \nabla \mathbf{u}\right) d\mathcal{V}. \tag{3.23}$$

The last equality in (3.23) follows from the fact that mass crosses neither S_1 nor S_2. The fluid has density ρ and dynamic viscosity μ. From (3.23), the Navier–Stokes

equations and divergence theorem lead to

$$\frac{dE}{dt} = -\int_{S_1} \mathbf{n}_1 \cdot \mathbf{T} \cdot \mathbf{u}\ dA + \int_{S_2} \mathbf{n}_2 \cdot \mathbf{T} \cdot \mathbf{u}\ dA - \int_V 2\mu \mathbf{D}[\mathbf{u}] : \mathbf{D}[\mathbf{u}]\ d\mathcal{V}, \quad (3.24)$$

where $\mathbf{T}$ is the stress tensor for a Newtonian fluid and the strain-rate tensor

$$\mathbf{D}[\mathbf{u}] = \frac{1}{2}(\nabla \mathbf{u} + \nabla \mathbf{u}^T). \quad (3.25)$$

Using (3.1) and (3.7), expression (3.24) leads to

$$UD_1 = -\frac{dE}{dt} - \int_{S_1} \mathbf{n}_1 \cdot \mathbf{T} \cdot \mathbf{v}\ dA + \int_{S_2} \mathbf{n}_2 \cdot \mathbf{T} \cdot \mathbf{u}\ dA - \int_V 2\mu \mathbf{D}[\mathbf{u}] : \mathbf{D}[\mathbf{u}]\ d\mathcal{V}. \quad (3.26)$$

Expanding the surface integrals, this expression may be written as

$$\begin{aligned} UD_1 = &-\frac{dE}{dt} - \int_{S_1} \mathbf{n}_1 \cdot \mathbf{T} \cdot \mathbf{n}_1 (\mathbf{n}_1 \cdot \mathbf{v})\ dA - \int_{S_1} \mathbf{n}_1 \cdot \mathbf{T} \cdot \mathbf{t}_1^{(\alpha)} \left(\mathbf{t}_1^{(\alpha)} \cdot \mathbf{v}\right)\ dA \\ &+ \int_{S_2} \mathbf{n}_2 \cdot \mathbf{T} \cdot \mathbf{n}_2 (\mathbf{n}_2 \cdot \mathbf{u})\ dA + \int_{S_2} \mathbf{n}_2 \cdot \mathbf{T} \cdot \mathbf{t}_2^{(\alpha)} \left(\mathbf{t}_2^{(\alpha)} \cdot \mathbf{u}\right)\ dA \\ &- \int_V 2\mu \mathbf{D}[\mathbf{u}] : \mathbf{D}[\mathbf{u}]\ d\mathcal{V}. \end{aligned} \quad (3.27)$$

With boundary conditions (3.2)-(3.5), we have

$$D_1 = \frac{1}{U}\left(-\frac{dE}{dt} - \int_V 2\mu \mathbf{D}[\mathbf{u}] : \mathbf{D}[\mathbf{u}]\ d\mathcal{V} + W\right), \quad (3.28)$$

where

$$W = -\int_{S_1} \mathbf{n}_1 \cdot \mathbf{T} \cdot \mathbf{n}_1 \hat{q}_1\ dA + \int_{S_2} \mathbf{n}_2 \cdot \mathbf{T} \cdot \mathbf{n}_2 q_2\ dA + \int_{S_2} \tau_2^{(\alpha)} \left(\mathbf{t}_2^{(\alpha)} \cdot \mathbf{u}\right)\ dA. \quad (3.29)$$

Expression (3.28) gives the force on S_1 in the $\mathbf{e}_x$-direction due to a Navier–Stokes flow in V satisfying an appropriate set of boundary conditions on S_1 and S_2 that includes those given in (3.2)–(3.5).

To evaluate the volume integrals in (3.28) we now assume that the fluid motion is irrotational, with velocity field $\mathbf{u} = \nabla\phi$. This approximation is satisfactory when the contribution of the rotational component of the fluid motion to the rate of change of kinetic energy and the viscous dissipation is assumed to be small in comparison with the irrotational contribution. This potential flow is obtained from the solution of the boundary-value problem (3.13)-(3.16). Clearly, such potential flow cannot satisfy, in general, the complete set of boundary conditions that the Navier–Stokes motion

does satisfy. With the potential flow assumption, (3.23) for the kinetic energy yields

$$\begin{aligned}\frac{dE}{dt} &= \int_V \nabla\cdot\left[\mathbf{u}\rho\left(\frac{\partial\phi}{\partial t}+\frac{|\mathbf{u}|^2}{2}\right)\right]d\mathcal{V} = \int_V \nabla\cdot\left[\mathbf{u}\left(\rho C(t)-p\right)\right]d\mathcal{V}\\ &= -\int_{S_1}(-p)\mathbf{n}_1\cdot\mathbf{u}dA+\int_{S_2}(-p)\mathbf{n}_2\cdot\mathbf{u}dA\\ &= -U\int_{S_1}(-p)\mathbf{n}_1\cdot\mathbf{e}_x dA-\int_{S_1}(-p)\mathbf{n}_1\cdot\mathbf{v}dA+\int_{S_2}(-p)\mathbf{n}_2\cdot\mathbf{u}dA, \qquad (3.30)\end{aligned}$$

with (3.16) and $\nabla\cdot\mathbf{u}=0$.

Regarding the dissipation integral, denoting $\mathbf{D}=\mathbf{D}[\mathbf{u}=\nabla\phi]$, one can readily show that for irrotational motion the following result holds

$$\begin{aligned}\int_V 2\mu\mathbf{D}:\mathbf{D}d\mathcal{V} &= -\int_{S_1}\mathbf{n}_1\cdot 2\mu\mathbf{D}\cdot\mathbf{u}dA+\int_{S_2}\mathbf{n}_2\cdot 2\mu\mathbf{D}\cdot\mathbf{u}dA\\ &= -U\int_{S_1}\mathbf{n}_1\cdot 2\mu\mathbf{D}\cdot\mathbf{e}_x dA-\int_{S_1}\mathbf{n}_1\cdot 2\mu\mathbf{D}\cdot\mathbf{v}dA\\ &\quad+\int_{S_2}\mathbf{n}_2\cdot 2\mu\mathbf{D}\cdot\mathbf{u}dA. \qquad (3.31)\end{aligned}$$

Zero tangential stress on the outer boundary

Suppose the outer boundary is also a free surface. Therefore, $\tau_2^{(\alpha)}\equiv 0$ in the last integral of (3.29) for W.

The discrepancy between the nonzero irrotational shear stress and the zero shear stress that the Navier–Stokes equations must satisfy at the free surface induces a (viscous) rotational correction to the irrotational normal stress that also enters the computation of the work integrals in (3.29). In the present formulation, this extra stress is ignored. With this assumption, W in (3.29) is computed in potential flow

$$W=-\int_{S_1}\left(-p+\mathbf{n}_1\cdot 2\mu\mathbf{D}\cdot\mathbf{n}_1\right)\hat{q}_1\ dA+\int_{S_2}\left(-p+\mathbf{n}_2\cdot 2\mu\mathbf{D}\cdot\mathbf{n}_2\right)q_2\ dA, \qquad (3.32)$$

and thus the entire right-hand side of (3.28) is furnished by a purely irrotational theory and a computable formula for D_1 is obtained.

In inertia-dominated problems, in which viscosity can be regarded as "small" and perturbations of the irrotational motion are confined to narrow boundary layers, evaluating the right-hand side of (3.28) from potential flow implies that the viscous contribution to the drag, to first order in the "small" viscosity μ, is assumed to arise solely from the rate of energy dissipation, thereby neglecting any possible first order viscous effect coming from the first and last terms in the right-hand side of (3.28).

In the particular case of $\hat{q}_1 = q_2 = 0$, the integrals in (3.29) are annihilated and the approximation of W is not an issue. This case represents an extension to a bounded domain of the analysis carried out by Joseph, Liao, and Hu (1993) and Joseph and Liao (1994a) that applies the dissipation approximation to a non-expanding bubble translating in an unbounded domain.

Substitution of (3.30)–(3.32) into (3.28), after some algebra, yields this expression for the force on the bubble surface in the $\mathbf{e}_x$-direction according to the dissipation method,

$$D_1 = \int_{S_1} \left(-p + \mathbf{n}_1 \cdot 2\mu\mathbf{D} \cdot \mathbf{n}_1\right) \mathbf{n}_1 \cdot \mathbf{e}_x dA + \frac{1}{U} \int_{S_1} \mathbf{n}_1 \cdot 2\mu\mathbf{D} \cdot \mathbf{t}_1^{(\alpha)} \left(\mathbf{t}_1^{(\alpha)} \cdot \mathbf{u}\right) dA$$
$$- \frac{1}{U} \int_{S_2} \mathbf{n}_2 \cdot 2\mu\mathbf{D} \cdot \mathbf{t}_2^{(\alpha)} \left(\mathbf{t}_2^{(\alpha)} \cdot \mathbf{u}\right) dA. \tag{3.33}$$

To determine the force D_2 on S_2 in the $\mathbf{e}_x$-direction by the dissipation method, we follow a procedure similar to that given above for D_1, with the difference that the governing equations are transformed to a noninertial reference frame that translates with velocity $U\mathbf{e}_x$. The steps are presented in Appendix B. There, an expression for the force on S_2 with respect to the noninertial frame is written from the transformed mechanical energy equation. Then, an expression for the force D_2 with respect to the laboratory frame can be obtained by evaluating the integrals in potential flow and by employing the transformation rules that link both coordinate systems. The outlined procedure, detailed in Appendix B, gives rise to the relation

$$D_2 = -\int_{S_2} \left(-p + \mathbf{n}_2 \cdot 2\mu\mathbf{D} \cdot \mathbf{n}_2\right) \mathbf{n}_2 \cdot \mathbf{e}_x dA + \frac{1}{U} \int_{S_2} \mathbf{n}_2 \cdot 2\mu\mathbf{D} \cdot \mathbf{t}_2^{(\alpha)} \left(\mathbf{t}_2^{(\alpha)} \cdot \mathbf{v}\right) dA$$
$$- \frac{1}{U} \int_{S_1} \mathbf{n}_1 \cdot 2\mu\mathbf{D} \cdot \mathbf{t}_1^{(\alpha)} \left(\mathbf{t}_1^{(\alpha)} \cdot \mathbf{v}\right) dA. \tag{3.34}$$

Next, by used of (3.33) in (3.34), with the aid of (B.23) from Appendix B from the self-equilibration of irrotational viscous stresses, we obtain the net force that must be applied to the liquid system in the $\mathbf{e}_x$-direction

$$-(D_1 + D_2) = -\int_{S_1} (-p)\, \mathbf{n}_1 \cdot \mathbf{e}_x dA + \int_{S_2} (-p)\, \mathbf{n}_2 \cdot \mathbf{e}_x dA. \tag{3.35}$$

Clearly, the dissipation approximation is an irrotational theory that gives rise to results that are different from those obtained from viscous potential flow in §3.2.2. The discrepancy between these two irrotational methods, in the case of an outer free surface, is given by the last two terms in the right-hand side of (3.33) and (3.34).

Irrotational tangential stress on the outer boundary

The dissipation analysis given above can be slightly modified to consider an outer surface on which the tangential stress is constrained to be purely irrotational, computed from the solution of the boundary-value problem (3.13)–(3.16). A motivation for this alternative outer boundary condition is discussed in §3.3.3. In this case, boundary condition (3.5) becomes

$$\tau_2^{(\alpha)} = \mathbf{n}_2 \cdot 2\mu\mathbf{D} \cdot \mathbf{t}_2^{(\alpha)}, \tag{3.36}$$

on S_2, where $\mathbf{D} \equiv \nabla \otimes \nabla\phi$. Thus, there is no discrepancy between the irrotational tangential stress and the tangential stress condition that the Navier–Stokes motion must satisfy. Since (3.36) holds, the normal component of the stress on S_2 is also irrotational. Therefore, with no approximation, (3.29) now takes the form

$$\begin{aligned} W = &- \int_{S_1} \mathbf{n}_1 \cdot \mathbf{T} \cdot \mathbf{n}_1 \hat{q}_1 \; dA + \int_{S_2} \left(-p + \mathbf{n}_2 \cdot 2\mu\mathbf{D} \cdot \mathbf{n}_2\right) q_2 \; dA \\ &+ \int_{S_2} \mathbf{n}_2 \cdot 2\mu\mathbf{D} \cdot \mathbf{t}_2^{(\alpha)} \left(\mathbf{t}_2^{(\alpha)} \cdot \mathbf{u}\right) dA. \end{aligned} \tag{3.37}$$

This expression is used in (3.28). The next step consists in approximating the remaining terms in the right-hand side of (3.28) for potential flow satisfying (3.13)–(3.16). By used of (3.30)–(3.31), the entire analysis thus leads to

$$\begin{aligned} D_1 = &\int_{S_1} \left(-p + \mathbf{n}_1 \cdot 2\mu\mathbf{D} \cdot \mathbf{n}_1\right) \mathbf{n}_1 \cdot \mathbf{e}_x dA \\ &+ \frac{1}{U} \int_{S_1} \mathbf{n}_1 \cdot 2\mu\mathbf{D} \cdot \mathbf{t}_1^{(\alpha)} \left(\mathbf{t}_1^{(\alpha)} \cdot \mathbf{u}\right) dA. \end{aligned} \tag{3.38}$$

The force D_2 on the outer boundary S_2 is obtained by direct integration of the (irrotational) stresses using the fact that the viscous irrotational stresses are self-equilibrated on any closed surface (Appendix C). Thus,

$$D_2 = - \int_{S_2} \left(-p\right) \mathbf{n}_2 \cdot \mathbf{e}_x dA. \tag{3.39}$$

It is worth mentioning that the analysis in Appendix B would lead to a different result for the force on S_2 since the zero-tangential-stress boundary condition at the bubble surface would enter the integral analysis in the dissipation approximation giving rise to D_2. On the contrary, (3.39) is an "exact" result obtained here from direct integration over the outer boundary where the stress is known to be irrotational. Therefore, no information from the inner boundary is needed. These

formulae are used in the end of §3.3.3.

3.3 Computation of the forces from the potential flow solution

To compute the forces on the bubble interface and the outer liquid boundary by used of the formulae obtained in §3.2, the solution of the boundary-value problem (3.13)–(3.16) for the flow is needed. This problem was examined by Sherwood (1999). Because he considered an inviscid fluid, the forces were given solely by the irrotational pressure. Since the analysis is explanatory and for the sake of completeness, a version of Sherwood's analysis is presented here in §3.3.1. The resulting flow field is then used in the computation of the viscous irrotational effects that gives rise to a viscous drag.

3.3.1 Potential flow field

In the bubble-liquid system defined in §3.2.1, let R_1 be the radius of the bubble and R_2 the radius of the outer surface and let ϵ be the separation between the centers of the bubble and the outer sphere. Then, the translational velocity is $U = \dot{\epsilon}$. Recall that the center of the bubble moves along the fixed direction $\mathbf{e}_x$, and its pathline contains the center of the outer envelope, thereby defining the axis of symmetry for the flow field. According to the notation defined in §3.2.1, the bubble interface and the outer sphere are denoted as S_1 and S_2, respectively. The analysis that follows aims to predict the forces exerted by the liquid on the bubble and the outer container along $\mathbf{e}_x$ for $\epsilon = 0$. The analysis is thus carried out for $\epsilon/R_1 \ll 1$ and $\epsilon/R_1 \ll R_2/R_1 - 1$.

The volume occupied by the liquid for all time is $4\pi(R_2^3 - R_1^3)/3$. Then,

$$R_1^2 \dot{R}_1 = R_2^2 \dot{R}_2, \tag{3.40}$$

where the "dot" denotes time differentiation. Using spherical polar coordinates (r, θ) with orthonormal basis $\{\mathbf{e}_r, \mathbf{e}_\theta\}$, and the center of S_2 given by $r = 0$, the bubble surface is described by

$$r = \epsilon \cos\theta + R_1 \left[1 - \left(\frac{\epsilon}{R_1} \right)^2 \sin^2\theta \right]^{1/2}. \tag{3.41}$$

Expanding around $\epsilon = 0$,

$$r = R_1 + \epsilon \cos\theta + O(\epsilon^2). \tag{3.42}$$

The harmonic velocity potential ϕ that gives rise to an axisymmetric flow field is

$$\phi = \frac{B_0}{r} + \sum_{l=1}^{\infty} \left(A_l r^l + B_l r^{-l-1} \right) P_l(\cos\theta), \tag{3.43}$$

such that $\mathbf{u} = \nabla\phi$. In (3.43), P_l denotes the Legendre polynomial of degree l (see Strauss, 1992, p. 275). This potential must satisfy the boundary conditions,

$$\mathbf{n}_1 \cdot \nabla\phi\big|_{S_1} = q_1 = U\mathbf{n}_1 \cdot \mathbf{e}_x + \hat{q}_1 = \dot{R}_1 + \dot{\epsilon}\cos\,\theta - \frac{\epsilon\dot{\epsilon}}{R_1}\sin^2\theta + O\left(\epsilon^2\right), \tag{3.44}$$

and

$$\mathbf{n}_2 \cdot \nabla\phi\big|_{S_2} = q_2 = \dot{R}_2, \tag{3.45}$$

where $\hat{q}_1 = \dot{R}_1$ and, to first order in ϵ,

$$\mathbf{n}_1 = \mathbf{e}_r + \mathbf{e}_\theta \frac{\epsilon}{R_1}\sin\theta, \tag{3.46}$$

and $\mathbf{n}_2 = \mathbf{e}_r$. Condition (3.45) yields

$$B_0 = -R_2^2\dot{R}_2 = -R_1^2\dot{R}_1, \tag{3.47}$$

and

$$A_l l R_2^{l-1} = B_l(l+1)R_2^{-l-2} \quad \text{for} \quad l \geqslant 1. \tag{3.48}$$

With the potential given in expression (3.43), the velocity field components in the (r,θ) frame are obtained, $\mathbf{u} = \mathbf{e}_r u_r + \mathbf{e}_\theta u_\theta = \mathbf{e}_r \partial\phi/\partial r + \mathbf{e}_\theta \partial\phi/r\partial\theta$,

Turning to the bubble surface S_1, boundary condition (3.44) allows us to find the coefficients in (3.43). In so doing, it is convenient to expand these coefficients as a power series in ϵ. That is,

$$A_l = A_l^{(0)} + A_l^{(1)}\epsilon + A_l^{(2)}\epsilon^2 + \cdots, \qquad B_l = B_l^{(0)} + B_l^{(1)}\epsilon + B_l^{(2)}\epsilon^2 + \cdots, \tag{3.49}$$

for $l \geqslant 1$, where $A_l^{(j)}$ and $B_l^{(j)}$ are related through (3.48). Sherwood (1999) obtained,

for $l = 1$,

$$A_1 = -\frac{R_1^3(\dot{\epsilon} + 2\epsilon\dot{R}_1 R_1^{-1})}{R_2^3 - R_1^3}, \qquad B_1 = -\frac{R_1^3 R_2^3(\dot{\epsilon} + 2\epsilon\dot{R}_1 R_1^{-1})}{2(R_2^3 - R_1^3)}, \tag{3.50}$$

to first order in ϵ. Some detail on the computations of these coefficients by imposing constraint (3.44) is given in Appendix D, where expressions for A_2 and B_2, to leading order, are also presented. There, we also show that $A_l^{(0)} = B_l^{(0)} = 0$ for $l \geqslant 2$ and that $A_l^{(1)} = B_l^{(1)} = 0$ for $l \geqslant 3$. Since the forces on S_1 and S_2 in the $\mathbf{e}_x$-direction are computed for $\epsilon = 0$, it suffices to find the coefficients B_0, A_1, B_1, A_2 and B_2 to first order in ϵ and then calculate their time derivatives. These computations will show, however, that only $l = 1$ terms—and thus A_1 and B_1—are actually needed because of orthogonality properties of Legendre polynomials.

The fluid pressure p distribution on S_1 and S_2 can be obtained from Bernoulli equation (3.16). The derivative $\partial\phi/\partial t$ needed to compute p is obtained from (3.43) by differentiating the coefficients and then putting $\epsilon = 0$, with $r = R_1$ or $r = R_2$.

Using standard formulae, the components of the strain-rate tensor in spherical-polar coordinates can be computed from $\mathbf{u} = \nabla\phi$, with ϕ given in (3.43), and $D_{rr} = \mathbf{e}_r \cdot 2\mu\mathbf{D}[\nabla\phi] \cdot \mathbf{e}_r$ and $D_{r\theta} = \mathbf{e}_r \cdot 2\mu\mathbf{D}[\nabla\phi] \cdot \mathbf{e}_\theta$. These computations yield

$$D_{rr} = \sum_{l=0}^{\infty} \left[l(l-1)A_l r^{l-2} + (l+1)(l+2)B_l r^{-l-3} \right] P_l(\cos\theta), \tag{3.51}$$

$$D_{r\theta} = \sum_{l=1}^{\infty} \left[(l-1)A_l r^{l-2} - (l+2)B_l r^{-l-3} \right] dP_l(\cos\theta)/d\theta. \tag{3.52}$$

For $\epsilon = 0$, at $r = R_1$, the velocity component u_r is given by (3.44) and the component $u_\theta = \partial\phi/r\partial\theta$; hence,

$$u_r = \dot{R}_1 + \dot{\epsilon}\cos\theta, \qquad u_\theta = -\left(A_1 + B_1 R_1^{-3}\right)\sin\theta. \tag{3.53}$$

At $r = R_2$, with $\epsilon = 0$, $u_r = \partial\phi/\partial r$ and $u_\theta = \partial\phi/r\partial\theta$ give

$$u_r = -B_0 R_2^{-2}, \qquad u_\theta = -\left(A_1 + B_1 R_2^{-3}\right)\sin\theta. \tag{3.54}$$

With $\epsilon = 0$, evaluating (3.51) and (3.52) at $r = R_1$ yields

$$D_{rr} = 2B_0 R_1^{-3} + 6B_1 R_1^{-4}\cos\theta, \qquad D_{r\theta} = 3B_1 R_1^{-4}\sin\theta, \tag{3.55}$$

and, at $r = R_2$, we have

$$D_{rr} = 2B_0 R_2^{-3} + 6B_1 R_2^{-4}\cos\theta, \qquad D_{r\theta} = 3B_1 R_2^{-4}\sin\theta. \tag{3.56}$$

In these results, B_0 is given by (3.47) and A_1 and B_1 are given in (3.50) with $\epsilon = 0$. It is worth noting that the alternative approach of computing the velocity potential from a boundary-value problem that considers two instantaneously growing or collapsing concentric spheres would have sufficed to obtain the strain-rate tensor $\mathbf{D}[\nabla\phi]$, since it only involves spatial partial differentiation.

Below, the forces on the bubble interface S_1 and the outer boundary S_2 are computed from the formulae of this section and §3.2 for $\epsilon = 0$. When the bubble and the outer surface are concentric, $\mathbf{n}_1 = \mathbf{n}_2 = \mathbf{e}_r$, $\mathbf{t}_1 = \mathbf{t}_2 = \mathbf{e}_\theta$, with $\mathbf{e}_r \cdot \mathbf{e}_x = \cos\theta$ and $\mathbf{e}_\theta \cdot \mathbf{e}_x = -\sin\theta$.

3.3.2 Forces—Viscous potential flow

The force on the bubble according to viscous potential flow is computed from (3.18). For the spherical bubble, with $\epsilon = 0$ at $r = R_1$, this expression becomes,

$$D_1 = 2\pi R_1^2 \int_0^\pi \left(-p + 2\mu D_{rr}\right)\big|_{R_1} \cos\theta \sin\theta d\theta. \tag{3.57}$$

With Bernoulli equation (3.16), computing $\partial\phi/\partial t$, and using (3.53) and (3.55), we get

$$D_1 = -\frac{4}{3}\pi\rho R_1^3 \left[\frac{\ddot{\epsilon}(2R_1^3 + R_2^3)}{2(R_2^3 - R_1^3)} + \frac{\dot{\epsilon}\dot{R}_1(15R_1^3 + 3R_2^3)}{2R_1(R_2^3 - R_1^3)} + \frac{6\nu\dot{\epsilon}}{R_1^2}\frac{R_2^3}{(R_2^3 - R_1^3)}\right]. \tag{3.58}$$

Taking $R_2 \to \infty$, this expression leads to

$$D_1 = -\frac{4}{3}\pi\rho R_1^3 \left[\frac{\ddot{\epsilon}}{2} + \frac{3\dot{\epsilon}\dot{R}_1}{2R_1} + \frac{6\nu\dot{\epsilon}}{R_1^2}\right]. \tag{3.59}$$

In particular, for a spherical bubble of constant volume that translates with constant velocity (i.e. $\dot{R}_1 = 0$ and $\ddot{\epsilon} = 0$), (3.59) reduces to $D_1 = -8\pi\mu\dot{\epsilon}R_1$ a result found by Moore (1959) from direct integration of the viscous normal stress in irrotational motion. If the fluid is considered inviscid, then the drag is zero (d'Alembert's paradox). When the acceleration $\ddot{\epsilon}$ is not zero, (3.59) gives rise to the apparent-mass.

With $\dot{R}_1 = 0$ and the void fraction $\alpha = (R_1/R_2)^3$, (3.58) reduces to

$$D_1 = -\frac{4}{3}\pi\rho R_1^3 \left[\frac{\ddot{\epsilon}(1+2\alpha)}{2(1-\alpha)} + \frac{6\nu\dot{\epsilon}}{R_1^2}\frac{1}{(1-\alpha)}\right], \tag{3.60}$$

which is in agreement, when $\nu = 0$, with (AI.11) of Zuber (1964) for the force on a spherical bubble moving within an inviscid liquid bounded by a spherical shell. This leads to the cell void fraction correction of the accelerated-apparent mass given in (3.59).

For "small" α, it is useful to write (3.60) in the form

$$D_1 = -\frac{4}{3}\pi\rho R_1^3 \left[\frac{\ddot{\epsilon}}{2}(1+3\alpha) + \frac{6\nu\dot{\epsilon}}{R_1^2}(1+\alpha)\right] + O(\alpha^2). \tag{3.61}$$

The force on the outer sphere, $r = R_2$, with $\epsilon = 0$, is obtained from (3.19) when the outer boundary is a free surface. This yields,

$$D_2 = -2\pi R_2^2 \int_0^\pi \left(-p + 2\mu D_{rr}\right)\big|_{R_2} \cos\theta \sin\theta d\theta. \tag{3.62}$$

Finding $\partial\phi/\partial t$, with (3.54) and (3.56), this formula gives,

$$D_2 = \frac{4}{3}\pi\rho R_2^3 \left[\frac{3\ddot{\epsilon}R_1^3}{2(R_2^3 - R_1^3)} + \frac{\dot{\epsilon}R_1^2\dot{R}_1(15R_2^3 + 3R_1^3)}{2R_2^3(R_2^3 - R_1^3)} + \frac{6\nu\dot{\epsilon}}{R_2^2}\frac{R_1^3}{(R_2^3 - R_1^3)}\right]. \tag{3.63}$$

Using (3.58) and (3.63), the total force that must be applied to the system is

$$-\left(D_1 + D_2\right) = -\frac{4}{3}\pi\rho R_1^3 \left[\ddot{\epsilon} + \frac{6\dot{\epsilon}\dot{R}_1}{R_1} - \frac{6\nu\dot{\epsilon}}{R_1^2}\frac{R_2(R_2^2 - R_1^2)}{(R_2^3 - R_1^3)}\right]. \tag{3.64}$$

For $\nu = 0$ (inviscid fluid), these results reduce to those obtained by Sherwood (1999). The force D_2 when the irrotational stress is specified on S_2 is given by (3.63) with $\nu = 0$. This follows from (3.22).

3.3.3 Forces—Dissipation method

The force D_1 on the bubble interface S_1 in the $\mathbf{e}_x$-direction can be obtained by used of (3.33) when a zero shear stress is prescribed on the outer boundary. This formula

can be written as,

$$D_1 = 2\pi R_1^2 \int_0^\pi \left(-p + 2\mu D_{rr}\right)\big|_{R_1} \cos\theta \sin\theta d\theta + \frac{2\pi R_1^2}{\dot{\epsilon}} \int_0^\pi \left(2\mu D_{r\theta} u_\theta\right)\big|_{R_1} \sin\theta d\theta$$
$$- \frac{2\pi R_2^2}{\dot{\epsilon}} \int_0^\pi \left(2\mu D_{r\theta} u_\theta\right)\big|_{R_2} \sin\theta d\theta. \tag{3.65}$$

With (3.16) for the pressure, (3.53) and (3.55), (3.65) leads to

$$D_1 = -\frac{4}{3}\pi\rho R_1^3 \left[\frac{\ddot{\epsilon}(2R_1^3 + R_2^3)}{2(R_2^3 - R_1^3)} + \frac{\dot{\epsilon}\dot{R}_1(15R_1^3 + 3R_2^3)}{2R_1(R_2^3 - R_1^3)} + \frac{9\nu\dot{\epsilon}}{R_1^2}\frac{R_2(R_2^5 - R_1^5)}{(R_2^3 - R_1^3)^2}\right]. \tag{3.66}$$

This expression, with $R_2 \to \infty$, reduces to

$$D_1 = -\frac{4}{3}\pi\rho R_1^3 \left[\frac{\ddot{\epsilon}}{2} + \frac{3\dot{\epsilon}\dot{R}_1}{2R_1} + \frac{9\nu\dot{\epsilon}}{R_1^2}\right]. \tag{3.67}$$

For a spherical bubble of constant volume moving with constant velocity $\dot{\epsilon}$ in an infinite fluid, (3.67) gives $D_1 = -12\pi\mu\dot{\epsilon}R_1$. This result has been obtained with the dissipation method in potential flow by several authors(Dryden et al., 1956; Joseph and Liao, 1994a; Levich, 1949; Ackeret, 1952; Moore, 1963; Joseph and Wang, 2004; Joseph et al., 1993).

Moore (1963) has examined the discrepancy between the viscous potential flow solution and the correct dissipation result for the drag over a spherical bubble of constant volume translating in an unbounded domain. Moore explains, citing an idea due to G. K. Batchelor, that the addition of an extra-pressure or viscous correction to the irrotational normal stress can compensate such discrepancy. From a boundary-layer type of analysis assessing the order of magnitude of the various terms in the steady governing equations, Moore (1963) concludes that the extra-pressure "contributes to the drag on the bubble to the same order as the viscous stresses", since he found that this extra-pressure is first order in the dimensionless viscosity. If the extra-pressure produces work, this is evidently neglected in the approach used here (that is, for nonzero choices of $\hat{q}_1$ and q_2), for W in (3.29) is approximated by the irrotational pressure and irrotational viscous normal stress.

For a bubble of variable radius in an unbounded fluid, the viscous part in (3.67) can be reduced from the multiple-bubble analysis by Voinov and Golovin (1970). They applied a Lagrangian formulation to examine the motion of a set of N bubbles of varying radius translating in a liquid otherwise at rest with dissipative forces computed from the rate of viscous dissipation evaluated in potential flow. Magnaudet and Legendre (1998) obtained (3.67) by transforming the original problem

to a reference frame in which the bubble radius remains fixed, while preserving the dynamic similarity in the transformation. In the limit when $Re >> 1$ or $\mathcal{U}Re >> 1$, where the Reynolds number $Re = R_1 U/\nu$ and the velocity ratio $\mathcal{U} = |\dot{R}_1|/U$, the boundary layer is thin. The transformed problem thus involves a bubble of constant radius in an unsteady flow and the drag force is computed to first order in the viscosity by evaluating the kinetic energy and the viscous dissipation from potential flow (see Tam, 1982). The force in physical space is then found by simply applying the known rules that link the transformed problem to the original one. This method contrasts with the approach described in §3.2.3 that gives rise to (3.67), in which the work of the normal stress due to the radial motion of the bubble interface and the contribution of this motion to the liquid kinetic energy are modeled by potential flow in a rather heuristic way. The fact that (3.67) agrees with the force given by Magnaudet and Legendre (1998) indicates that the combined viscous contribution from dE/dt and W in (3.28) is null up to order $O(Re^{-1})$. This may be explained by considering that the component of the total motion attributed to the bubble radial expansion and contraction is of the source-sink type and, hence, of an irrotational nature.

The result obtained above can be readily used to approximate the dynamics in a bubbly swarm with void fraction α by applying the cell model described in §3.1. In the case of $\dot{R}_1 = 0$, with the cell void fraction $\alpha = (R_1/R_2)^3$, (3.66) gives the added-mass and viscous contributions to the force acting on each bubble

$$D_1 = -\frac{4}{3}\pi\rho R_1^3 \left[\frac{\ddot{\epsilon}(1+2\alpha)}{2(1-\alpha)} + \frac{9\nu\dot{\epsilon}}{R_1^2}\frac{(1-\alpha^{5/3})}{(1-\alpha)^2} \right], \tag{3.68}$$

which agrees with Zuber's result for $\nu = 0$. The viscous part in (3.68) is the widely cited result obtained with the dissipation approximation by Marrucci (1965). For "small" α, (3.68) may be written as

$$D_1 = -\frac{4}{3}\pi\rho R_1^3 \left[\frac{\ddot{\epsilon}}{2}(1+3\alpha) + \frac{9\nu\dot{\epsilon}}{R_1^2}(1+2\alpha) \right] + O(\alpha^2). \tag{3.69}$$

It should be noted that (3.68) has been derived from a cell model with a frictionless outer boundary, such that no work is exchanged by the reference cell with the surroundings.

The force D_2 in the $\mathbf{e}_x$-direction on surface S_2 can be obtained from either (3.34)

or (3.35). The latter expression can be written as

$$D_1 + D_2 = 2\pi R_1^2 \int_0^\pi (-p)\,\big|_{R_1} \cos\theta \sin\theta d\theta - 2\pi R_2^2 \int_0^\pi (-p)\,\big|_{R_2} \cos\theta \sin\theta d\theta, \quad (3.70)$$

which, with (3.66), leads to

$$D_2 = \frac{4}{3}\pi\rho R_2^3 \left[\frac{3\ddot{\epsilon} R_1^3}{2(R_2^3 - R_1^3)} + \frac{\dot{\epsilon} R_1^2 \dot{R}_1 (15R_2^3 + 3R_1^3)}{2R_2^3(R_2^3 - R_1^3)} + \frac{9\nu\dot{\epsilon}}{R_2^2} \frac{R_1(R_2^5 - R_1^5)}{(R_2^3 - R_1^3)^2} \right]. \quad (3.71)$$

Again, Sherwood's results are recovered taking $\nu = 0$ in (3.66) and (3.71).

The total force that must be applied to the system is obtained from (3.70):

$$-(D_1 + D_2) = -\frac{4}{3}\pi\rho R_1^3 \left(\ddot{\epsilon} + \frac{6\dot{\epsilon}\dot{R}_1}{R_1} \right), \quad (3.72)$$

in agreement with the inviscid result by Sherwood.

Consider now an outer boundary S_2 in which the tangential stress is given by the irrotational motion satisfying the boundary-value problem (3.13)-(3.16), such that the zero-tangential-stress constraint does not hold. Under this framework, the formulae of §3.2.3 for the irrotational tangential stress on the outer boundary can be applied yielding an expression for the force D_1 on the bubble and the force D_2 on the outer spherical envelope. Applying (3.38), we obtain,

$$D_1 = -\frac{4}{3}\pi\rho R_1^3 \left[\frac{\ddot{\epsilon}(2R_1^3 + R_2^3)}{2(R_2^3 - R_1^3)} + \frac{\dot{\epsilon}\dot{R}_1(15R_1^3 + 3R_2^3)}{2R_1(R_2^3 - R_1^3)} + \frac{9\nu\dot{\epsilon}}{R_1^2} \frac{R_2^6}{(R_2^3 - R_1^3)^2} \right]. \quad (3.73)$$

With $\dot{R}_1 = 0$, in terms of the void fraction α, this expression becomes,

$$D_1 = -\frac{4}{3}\pi\rho R_1^3 \left[\frac{\ddot{\epsilon}(1 + 2\alpha)}{2(1 - \alpha)} + \frac{9\nu\dot{\epsilon}}{R_1^2} \frac{1}{(1 - \alpha)^2} \right]. \quad (3.74)$$

To first order in α, (3.74) also leads to (3.69). The viscous part of (3.74) has been given by Kendoush (2001), as discussed below. The force D_2, according to (3.39), can be obtained from either (3.63) or (3.71) taking $\nu = 0$. For the two outer boundary conditions examined here, note that the force on the bubble increases with the void fraction according to both irrotational theories.

3.4 Discussion

The force acting on a spherical compressible bubble in rectilinear motion within an incompressible fluid bounded externally by a spherical surface has been computed above at the instant in which both spheres are concentric. The analysis is carried out using two different irrotational approximations, namely, viscous potential flow (§§3.2.2 and 3.3.2), which directly integrates the irrotational normal stress over the bubble surface, and the dissipation method (§§3.2.3 and 3.3.3), in which the integration of the various terms in the mechanical energy equation, including the rate of energy dissipation, is carried out assuming irrotational motion, after satisfying actual boundary conditions for Navier–Stokes motion. The dissipation method stems from the fact that viscous irrotational stresses are self-equilibrated, but its power does not vanish (Joseph et al., 2007). In addition, the force on the outer surface is also computed. In particular, by keeping the bubble radius constant, one can use the results to approach the force on a bubble moving in a monodispersed homogeneous bubbly liquid having the same void fraction as the reference cell and satisfying the dual limit of large Reynolds and small Weber numbers, because, in this case, the velocity field differs very little from that in irrotational motion. This is in accord with the well-known cell-model approximation.

In the present formulation of the dissipation method, the tangential stress is set to zero on the inner boundary, but two possibilities are considered for the outer boundary, either a zero tangential stress or an irrotational tangential stress. Since the irrotational tangential stress on the outer boundary is not identically zero, this stress does work against the remainder of the domain, as shown in (3.37). This boundary condition thus contradicts the postulate by Happel and Brenner (1965) of regarding each cell as an independent entity in the sense that energy transfer should not occur between the unit cell and the neighboring fluid. This is the case with the model with zero tangential stress on both the inner and outer boundaries (i.e. free-surface cell model), leading to Marrucci's drag when the bubble speed is constant. Nevertheless, if the cell model is used to describe a bubbly flow with "weak" rotational effects confined to a thin layer adjacent to the bubble interface and a minute wake at the bubble rear, such that the liquid motion is essentially irrotational, the choice of irrotational stresses on the outer envelope appears reasonable.

The viscous drag from the viscous potential flow solution (3.60) is always lower than the viscous drag obtained from the dissipation method with either outer boundary condition, (3.68) or (3.74), for the same volume fraction α. It is well known (Moore, 1963) that the drag on a single bubble rising steadily in a liquid from the

integration of the viscous irrotational normal stress (i.e. viscous potential flow in this work) is 2/3 of that predicted by the dissipation method, which gives the correct trend for a large-Reynolds-number spherical bubble. Therefore, one may expect the results from the dissipation method to be closer to the actual viscous drag than those from viscous potential flow for nonzero α.

For a bubble moving with constant velocity, i.e. $\ddot{\epsilon} = 0$, (3.74) reduces to the drag found by Kendoush (2001) with the dissipation method using a cell model. Nonetheless, in his analysis, the dynamic constraint (stress) at the outer boundary is not stated. Expressions (3.73) and hence (3.74) were attained here by imposing an irrotational tangential stress on the outer boundary. Both Marrucci (1965) and Kendoush (2001) used the irrotational velocity profile determined by the domain configuration and the kinematic conditions (normal velocity component) on the inner and outer boundaries. Kendoush's working equation [his (5)] can be obtained from (3.38) by used of (3.1).

Kendoush also argues that Marrucci's result, given in (3.68) for $\ddot{\epsilon} = 0$, is incorrect, reasoning that the upper integration limit in Marrucci's dissipation integral should have been taken to infinity instead of using the outer radius, as originally specified by Marrucci. Although implementing this change in Marrucci's formulation does lead to (3.74) instead of (3.68), we find this modification rather contradictory since in the cell model the liquid is bounded, and the velocity profile employed is that of a confined fluid. The analysis that led to (3.68) verifies that Marrucci's formula for the viscous drag is correct; it is found here from the mechanical energy balance by considering frictionless inner and outer boundaries and irrotational motion in the bulk of fluid. It should be noted that Marrucci did not prescribe any external boundary condition from dynamics (i.e. stress), although he mentioned Happel's assumption of a free-surface condition for the outer boundary in a creeping-flow cell model as a prominent antecedent of his work. He only indicates that boundary-layers contributions to the total energy dissipation are neglected in his analysis.

While a zero tangential stress is the obvious choice for the bubble interface, an alternative constraint, that is, an irrotational stress condition, may be specified on the outer boundary. In sum, (3.68) and (3.74) arise through the dissipation method applied to the same configuration with the same frictionless condition on the inner boundary but each satisfying a different condition on the outer boundary, thereby yielding different results. Nonetheless, the drag is the same to first order in the void fraction.

3.4.1 Comparison with numerical and other analytical results

The viscous irrotational theories considered here can be compared with results from other analytical models, numerical simulations and experimental data. We have in mind the situation of gas being bubbled through a stagnant liquid in a continuous manner by injecting a constant gas flow rate or the case of a swarm of spherical bubbles rising by buoyancy in a liquid otherwise at rest. The latter case can be placed in the framework of the cell-model analysis carried out here by letting U be the velocity of the rising bubble swarm with respect to the container wall (Marrucci, 1965; LeClair and Hamielec, 1971). If a steady gas flow rate is bubbled through the same container, the actual bubble velocity U_b referred to the container walls is related to U by the expression $U_\mathrm{b} = U/(1-\alpha)$ as a result of mass conservation (Nicklin, 1962), where α is also the gas volume fraction in the bubbly flow. In this case, U also represents the gas drift velocity, that is, the difference of the actual gas velocity, U_b, and the gas volumetric flow rate per unit of cross sectional area being pushed into the system (Nicklin, 1962). It is assumed that the bubbles in the swarm are nearly spherical, homogeneously distributed, and with negligible variations of the equivalent bubble diameter with respect to the mean value. The equivalent bubble diameter is the diameter of the sphere with the same volume of the bubble. We are referring to this definition when we use the term "bubble diameter".

In Figure 3.2(a) the predictions by the irrotational theories for the drag coefficient C_D are presented and compared with those listed in Chhabra (1995) from the numerical solution of the steady incompressible Navier–Stokes equations using both the free-surface and the zero-vorticity cell-model approximations for $Re = 100$, where $Re = 2R_1U\rho/\mu$, thereby suitable for comparison with the viscous irrotational theories. Numerical results for $Re = 20$ are also included to illustrate the change in C_D with Re. Chhabra collected the results obtained by Manjunath et al. (1994) using the finite-element method for a cell model with zero tangential stress both on the inner and outer boundary and new results generated with the same numerical method solving the governing equations for the same physical domain and boundary conditions except that at the outer boundary the vorticity is set to zero instead of the tangential stress. The drag D on a bubble may be written in the form

$$D = \frac{1}{2}\rho U^2 \pi R_1^2 C_\mathrm{D}, \tag{3.75}$$

an expression that defines the drag coefficient C_D. Using the results for the viscous drag from (3.60), (3.68) and (3.74), expressions for the drag coefficient can thus be written, respectively, for viscous potential flow (VPF) and the dissipation method

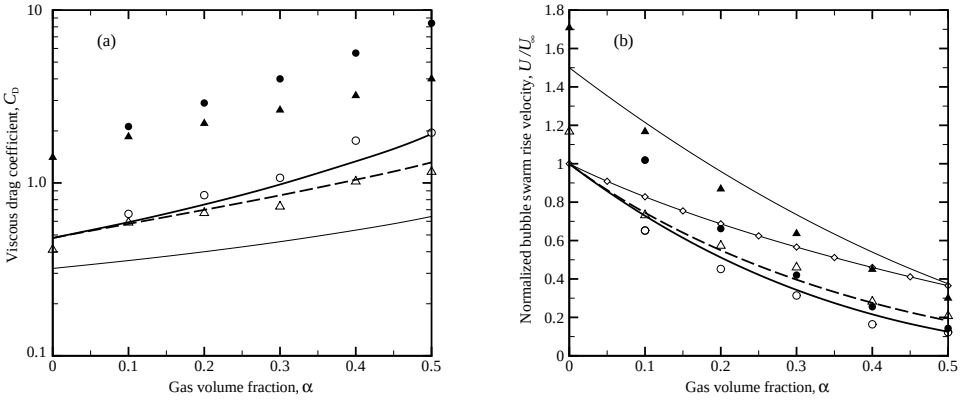

Figure 3.2: (a) Drag coefficient $C_{\rm D}$ as a function of the void fraction α. (b) Normalized bubble swarm rise velocity U/U_∞ as a function of the gas volume fraction α. The graphs for $C_{\rm D}$ vs. α are determined with Re=100, except where indicated. The curves of U/U_∞ vs. α are valid for $Re \gg 1$ but do not explicitly depend on Re. Thin solid line: VPF (3.76a) and (3.77a); thick dashed line: DM with zero tangential stress on the outer boundary (3.76b) and (3.77b); thick solid line: DM with irrotational tangential stress on the outer boundary (3.76c) and (3.77c); thin solid line with ⋄: Marrucci (1965); ▲ and △: numerical simulations with free-surface cell model by Chhabra (1995) for Re=20 and Re=100, respectively, where (3.80) is used for the normalized velocity; • and ○: numerical simulations with zero-vorticity cell model by Chhabra for Re=20 and Re=100, respectively. DM stands for the dissipation method and VPF stands for viscous potential flow. The symbols for $\alpha = 0$ correspond to the numerical results by Manjunath et al. (1994) using a free-surface cell model. U_∞ denotes the single bubble rise velocity from the dissipation method.

(DM) with either a zero tangential stress or an irrotational tangential stress on the outer boundary. In this order, we obtain,

$$C_{\rm D_1} = \frac{32}{Re}\frac{1}{(1-\alpha)}, \tag{3.76a}$$

$$C_{\rm D_2} = \frac{48}{Re}\frac{(1-\alpha^{5/3})}{(1-\alpha)^2}, \tag{3.76b}$$

$$C_{\rm D_3} = \frac{48}{Re}\frac{1}{(1-\alpha)^2}. \tag{3.76c}$$

Figure 3.2(a) shows that the DM with the irrotational-tangential-stress condition on the outer boundary exhibits fair agreement with the numerical results for the zero-vorticity cell model for the range of void fraction considered in the study. In this formulation of the dissipation approximation, the potential flow hypothesis

is brought from the bulk of the fluid to include the outer boundary. Predictions from the DM with the zero-tangential-stress condition on the outer surface are close to the numerical simulations using a cell model with the same constraint, as expected for $Re = 100$. VPF, on the other hand, consistently under-predicts the numerical solution, which is the extension to a bubbly suspension of the known result for a single bubble rising in an infinite medium (Moore, 1963). From the two curves rendered by DM, the cell model with an irrotational shear stress on the outer boundary predicts values for the drag coefficient C_{D} that display a stronger dependence on the void fraction than those from the cell model with a zero-shear-stress condition. A similar trend is described by the numerical results by Chhabra, who commented on this, for $Re = 100$ (represented by symbols), that is, results from the zero-vorticity cell model are more dependent upon the void fraction than results from the free-surface cell model. This trend agrees with that reported by Happel and Brenner (1965) and El-Kaissy and Homsy (1973). Happel and Brenner framed their discussion under the analysis of creeping flow; El-Kaissy and Homsy carried out regular perturbation techniques on the Navier–Stokes equations. A comparison of numerical predictions for the drag coefficient with Marrucci's drag [expression (3.76b)] has been presented by Manjunath et al. using the free-surface cell model.

Although numerical simulations and analytical models can predict the drag acting on a bubble in a bubbly suspension, perhaps the most convenient way of evaluating their performance is comparing theoretical results for the terminal rise velocity of the bubbles with experimental data. This is because measurements of this magnitude are somewhat abundant in the literature. The terminal velocity U of a swarm of spherical bubbles of equal size rising due to buoyancy can be determined by equating the drag on a bubble with the lift force that drives the bubble upwards, given by the buoyancy force corrected by the bubble weight, that is, $4\pi R_1^3(\rho_{\mathrm{M}} - \rho_{\mathrm{G}})g/3$, g being the acceleration of gravity, ρ_{G} the gas density and $\rho_{\mathrm{M}} \equiv \rho(1-\alpha) + \rho_{\mathrm{G}}\alpha$, the averaged density of the mixture (Zuber and Hench, 1962; Zuber, 1964; Kendoush, 2001). Using (3.60), (3.68) and (3.74) for the drag, we thus find,

$$\frac{U}{U_\infty} = \frac{3}{2}(1-\alpha)^2, \tag{3.77a}$$

$$\frac{U}{U_\infty} = \frac{(1-\alpha)^3}{(1-\alpha^{5/3})}, \tag{3.77b}$$

$$\frac{U}{U_\infty} = (1-\alpha)^3, \tag{3.77c}$$

for VPF, and the DM with either a zero tangential stress or an irrotational tangential stress at the outer boundary of the cell, respectively. Here, U_∞ is the bubble

velocity in the limit of infinite dilution, that is for $\alpha = 0$, computed from the DM (Levich, 1962), $U_\infty = R_1^2(\rho - \rho_G)g/9\mu$. Hence the bubble rise velocity for infinite dilution according to VPF is $3U_\infty/2$. Expression (3.77c) has been given by Kendoush (2001). Expression (3.77b) times the factor $(1-\alpha)^{-1}$ gives the rise velocity model by Marrucci (1965), who apparently used the density of the liquid ρ instead of the density of the mixture ρ_M in the buoyancy force. Richardson and Zaki (1954) favored the use of the density of the liquid over the density of the suspension ρ_M in computing the buoyancy force acting on solid particles settling in a liquid at the same rate, pointing out that each particle displaces its own volume of liquid, not of suspension. Kuwabara (1959) also used the density of the liquid instead of that of the suspension for the buoyancy force needed in the evaluation of the terminal settling velocity of spheres uniformly arranged in a liquid. Manjunath et al. proposed to compute the steady rise velocity of the bubble swarm with the buoyancy force determined by the density of the liquid. On the other hand, Zuber (1964) applied the one-dimensional momentum equation for two-phase flow to the case of steady vertical motion of particles in a fluid neglecting the friction at the walls, finding that the buoyancy force determined with the density of the mixture balances the drag force on a particle and its weight. Based upon experimental studies on the settling velocity of spheres in two-component solid-liquid suspensions, Poletto and Joseph (1995) affirmed that the effective density approaches the average density of the mixture in the case of a test particle of the same diameter as the suspended particles, or larger. Moreover, they entered the average density of the mixture to account for the effective buoyancy on a test particle in a model describing the settling of a test sphere in a suspension. Kendoush also used the density of the mixture in finding the terminal rise velocity of a bubble swarm. This approach was adopted above.

Expressions (3.77) are plotted in figure 3.2(b) as function of the void fraction. To use the numerical results for C_D compiled in Chhabra for fixed Reynolds number Re and varying α to predict the ratio U/U_∞, the drag D in (3.75) is equated to the buoyancy force minus the bubble weight. That is,

$$C_D \frac{1}{2}\rho U^2 \pi R_1^2 = \frac{4}{3}\pi R_1^3(\rho - \rho_G)g(1-\alpha). \tag{3.78}$$

Writing a similar expression in the infinite dilution limit, $\alpha = 0$, for a bubble of radius R_1 rising with velocity U_∞ in the same liquid, according to the dissipation method, the drag coefficient being $C_{D,\infty}$, and combining with (3.78), we find (Ishii

and Zuber, 1979)

$$\frac{U}{U_\infty} = (1-\alpha)^{1/2}\left(\frac{C_{\mathrm{D},\infty}}{C_\mathrm{D}}\right)^{1/2}. \tag{3.79}$$

With $C_{\mathrm{D},\infty}$ given by the known expression $C_{\mathrm{D},\infty} = 48/Re_\infty$, and $U/U_\infty = Re/Re_\infty$, (3.79) represents and implicit relation for Re_∞, for known values of α and Re, a pair that determines the drag coefficient C_D from the numerical analysis. Expression (3.79) can be written in explicit form,

$$\frac{U}{U_\infty} = (1-\alpha)\frac{48}{ReC_\mathrm{D}} \tag{3.80}$$

The results from (3.80) for Re=20 and 100 are represented with symbols in figure 3.2(b).

The trend depicted by the viscous irrotational theories in figure 3.2(b) indicates a decrease in the ratio U/U_∞ for the bubble swarm with increasing void fraction. For a given gas-liquid system for which the dual limit of large Reynolds number and small Weber number is satisfied, this trend indicates that increasing bubble concentration hinders the bubble swarm rise speed. DM with an irrotational tangential stress on the outer boundary of the cell model gives the lowest normalized velocity amongst the irrotational theories described in this chapter. Slightly higher values are obtained from the DM when a zero tangential stress is prescribed on the outer boundary for the same volume fraction. In addition, results from the former model are somewhat more dependent on the void fraction than results from the latter model. VPF predicts much higher normalized bubble swarm velocities than the other models considered in the analysis as the first order viscous correction to the irrotational pressure associated with the vortical layer is omitted, thereby predicting a lower drag. Marrucci's formula predicts dimensionless velocities that lie in between those from VPF and the other viscous irrotational theories and shows a less pronounced dependence on the gas volume fraction.

The results obtained here (plotted as symbols) from the drag coefficients reported in Chhabra from numerical simulations also show a decrease in U/U_∞ as the void fraction α increases. In the limit of infinite dilution, the points included in figure 3.2(b) are given in Manjunath et al. from their numerical solution. The remark stated above regarding the hindering effect due to increasing gas concentration cannot be drawn from the points determined by the numerical solution, as each data series corresponds to a fixed bubble swarm Reynolds number, Re. Since (3.80) with the numerical results for C_D in Chhabra for $Re = 20$ and 100 yields

an increasing Re_∞ as α increases, the ratio Re/Re_∞ and hence U/U_∞ ought to decrease. To investigate the effect of increasing gas volume concentration on bubble rise velocity using numerical simulations at finite Reynolds number, another type of plot is needed; this can be found elsewhere (LeClair and Hamielec, 1971; Kendoush, 2001, see below). For both Re =20 and 100 and $\alpha > 0$, the normalized velocity predictions from the free-surface cell model are larger than the results from the zero-vorticity cell model obtained by means of computational fluid dynamics analysis. As expected, this trend agrees with that shown by the DM results for U/U_∞ with the zero-tangential-stress model leading to a somewhat larger values in comparison with the model with an irrotational tangential stress on the exterior surface. Larger values of U/U_∞ are predicted for bubble swarms for which $Re = 20$ than for swarms with $Re = 100$ at a fixed gas volume fraction and for the same type of cell model. The difference between both series decreases as the gas volume fraction increases.

The decrease of the normalized bubble swarm velocity U/U_∞ as Re increases for fixed α may be explained by considering the limit of low Reynolds number. For creeping motion of a single bubble in an unbounded medium, the drag is known to be $4\pi\mu R_1 U$ (White, 1974). Therefore, the bubble terminal rise velocity is U/U_∞=3, which is well above the corresponding value for $Re = 20$, $U/U_\infty \approx$1.7 [see figure 3.2(b)]. As the Reynolds number increases towards the other limit $Re \gg 1$, U/U_∞ should tend to 1. This tendency is also observed for a bubble swarm, that is, for $\alpha > 0$.

As the Reynolds number increases, it is reasonable to expect that U/U_∞ for given α approaches the curves resulting from the DM, since these curves represent the limiting values for $Re \gg 1$. Whereas for $\alpha = 0$ and $Re = 100$, $U/U_\infty \approx 1.2$, and a decreasing trend should be expected, so that $U/U_\infty \to 1$ as Re increases, the data obtained from numerical experiments for $\alpha > 0$ using the free-surface cell model apparently have already reached their limit, given by the DM analysis for the same type of cell model. In the case of the data set corresponding to the zero-vorticity cell model, for $\alpha > 0$ the magnitudes of U/U_∞ are already slightly under their expected limiting values, given by the graph of the DM with an irrotational tangential stress on the exterior boundary. Discarding issues related to the approximations employed in the numerical scheme, one possible explanation for this result is the increasing trend of the product ReC_D with increasing Re that, by virtue of (3.80), leads to a decrease in U/U_∞. Should this trend be reversed, ReC_D would start decreasing slowly as Re continues increasing so that the limiting value would be closely approached, and U/U_∞ would become insensitive to changes in Re.

In closing, one should mention that results for $U/U_{\alpha=0}$ as function of the gas volume fraction, $U_{\alpha=0}$ being the velocity of a bubble rising in an unbounded medium ($U_{\alpha=0} \neq U_{\infty}$), were reported by LeClair and Hamielec (1971) for infinite dilution Reynolds numbers up to $Re_{\alpha=0}$=1000 from their numerical solutions employing the zero-vorticity cell model. There, the hindering of bubble motion as the bubble concentration increases is demonstrated from the simulations. They pointed out that a standing vortex ring in the bubble rear stagnation region was not present. They assert that for such a high Reynolds number, the limit given by potential flow theory is approached. From the dissipation method, the drag coefficient defined in (3.75) leads to the result $C_{\mathrm{D}} \approx 0.048$ yet they plotted a drag coefficient, defined in the same manner, of $C_{\mathrm{D}} \approx 0.1$. Appreciable covective effects that overcome the capabilities of the numerical scheme (Jaiswal, Sundararajan, and Chhabra, 1992) are perhaps the cause of such a significant difference. Therefore, we opted not to include their data for such a high Reynolds number in the comparisons carried out in the present work.

3.4.2 Comparison of the theory against experimental data

Comparison of the theory with experimental data for the velocity U_{b} of the bubbles in a bubbly flow as a function of the void fraction is presented in figure 3.3. One dataset corresponds to the experiments conducted by Zenit et al. (2001) to study a monodispersed suspension of bubbles moving in a vertical channel satisfying the dual limit of large Reynolds and small Weber numbers. The mixture is produced by bubbling gas at a constant volumetric flow rate through a stagnant liquid. They used a dilute aqueous electrolyte solution with gas nitrogen. A monodispersed suspension is obtained with the addition of a salt to the liquid, that helps preventing bubble coalescence. The mean equivalent bubble diameter of the suspension increases from 1.364 mm to 1.696 mm for gas volume fraction in the interval $0 \lesssim \alpha \leqslant 0.20$. The aspect ratio decreases in this interval from 1.3 to 1.1 and the Reynolds and Weber numbers decrease with the void fraction from $Re_{\mathrm{b}} = 380$ and $We_{\mathrm{b}} = 1.5$ for $\alpha \approx 0$ to $Re_{\mathrm{b}} = 260$ and $We_{\mathrm{b}} = 0.5$ for $\alpha = 0.20$. For this data set, Zenit et al. gives the fitting $U_{\mathrm{b}} = U_0(1-\alpha)^n$, with $U_0 = 0.269$ m s^{-1} and $n = 2.796$. They report that $U_0 < U_{\infty} = 0.320$ m s^{-1}, measured from the rising of a single bubble in a larger pipe, a value that is just within 1% of the result predicted by the theory for an oblate ellipsoid (Moore, 1965). This sudden steep decrease in bubble velocity with gas concentration for very dilute suspensions has been attributed by Zenit et al. to the effects of bubble-wall collisions. They discuss this issue in depth while including additional experimental evidence, and the interested reader should refer

to their work. Another dataset is taken from the series of experiments performed by Martínez-Mercado et al. (2007) with a flux of gas nitrogen bubbling through a variety of stagnant liquids. We choose the set of measurements obtained with a mixture of water-glycerin (15% wt.) because the bubbles were nearly spherical and the Reynolds number was $O(100)$. In the experiments with this liquid, the mean bubble diameter decreases from 1.3 to 1.2 mm with increasing void fraction from 0 to 0.05, whereas the aspect ratio remained constant about 1.05. The measured Reynolds and Weber numbers decrease from $Re_\mathrm{b} = 120$ and $We_\mathrm{b} = 0.60$ to $Re_\mathrm{b} = 70$ and $We_\mathrm{b} = 0.22$ for void fraction increasing in the range $0 \lesssim \alpha \leqslant 0.05$. Again, a rapid decrease in the bubble velocity in the region of a very dilute suspension was observed as the velocity for a single bubble in an infinite medium is 0.287 m s^{-1} computed from the theory for a clean oblate ellipsoidal bubble of Moore (1965) (note that they reported the value of Re_∞ instead). They speculate that the sudden increase in the drag that slows down the bubbles might be caused by velocity fluctuations arising from bubble-wall collisions.

The predictions from the irrotational theories described here are compared with the experimental data for the dimensionless velocity U_b/U_∞ in figure 3.3, where U_∞ takes the values given above for both experimental datasets. In addition, Zenit et al. (2001) took the model by Spelt and Sangani (1998) for the drag coefficient and found an expression for the normalized bubble velocity U_b/U_∞ for vertical bubbly flow through stagnant liquid

$$\frac{U_\mathrm{b}}{U_\infty} = \frac{(1-\alpha)}{1+\frac{3}{20}\alpha A}. \tag{3.81}$$

Here the parameter A denotes the inverse of the bubble vertical velocity variance normalized by the square of the mean bubble velocity. A fit for $A = A(\alpha)$ with measurements by Zenit et al. (2001) is given in Kushch et al. (2002), $A = (0.02+0.5\alpha)^{-1}$. This fitting may be regarded as particular for the set of conditions of the experiments from which it is obtained. Predictions from (3.81) are included in figure 3.3. Note that A does not approach zero as $\alpha \to 0$; this is explained by the oscillations in the bubble trajectory associated with bubble-wall interactions observed in a single bubble experiment (Zenit et al.). The drag coefficient formula referred to above was derived by Spelt and Sangani by solving for a viscous potential that adds a first order correction in the dimensionless viscosity to the irrotational flow field. Their expression for the drag coefficient depends upon the void fraction and an additional parameter A, defined above, and is needed in their system of average equations for bubbly flow in the regime of large Reynolds and small Weber numbers. They

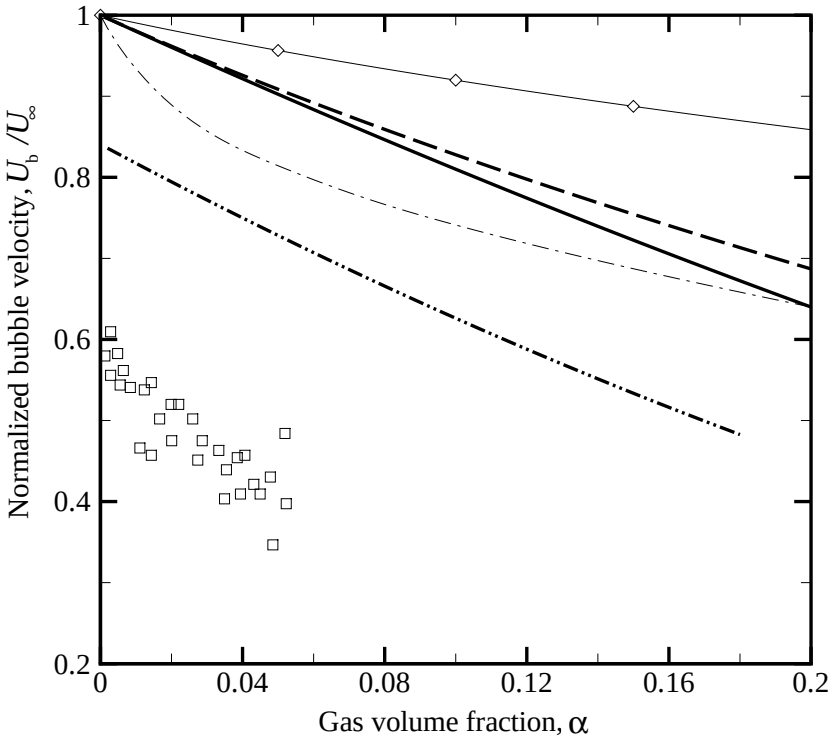

Figure 3.3: Normalized bubble velocity U_b/U_∞ as a function of the gas volume fraction α for gas bubbling continuously in a stagnant liquid. Two data sets from experiments are included for comparison. Thick dash-dot-dotted line: fitting of data from experiments with nitrogen in aqueous solution by Zenit et al. (2001); □: experiments with nitrogen in water-glycerin (15% wt.) by Martínez-Mercado et al. (2007); thick dashed line: DM with zero tangential stress on the outer boundary (3.77b); thick solid line: DM with irrotational tangential stress on the outer boundary (3.77c); thin dash-dotted line: model by Spelt and Sangani (1998) (3.81); thin solid line with ⋄: Marrucci (1965). DM stands for the dissipation method and VPF stands for viscous potential flow. Predictions are given by $U_\mathrm{b} = U/(1-\alpha)$. For the experimental data, U_∞ was determined from Moore's (1965) theory.

present comparisons with dynamics simulations, in which satisfactory agreement is demonstrated.

The experiments show that greater concentration of bubbles leads to a hindering of their motion and the models follow this trend. Figure 3.3 indicates that the theory over-predicts the measurements in the interval of gas volume fraction considered. This trend has been reported by Zenit et al. (2001) from the comparison of their data with the model by Spelt and Sangani (1998). This discrepancy was attributed to several factors, namely, bubble deformation, departures of the liquid dynamics from irrotational motion due to the presence of surface-active contaminants, and energy dissipation associated with bubble shape oscillations (Zenit et al.). A similar discrepancy was noted by Kushch et al. (2002) after comparing their model, derived using an effective-medium theory for oblate spheroidal bubbles, with the data by Zenit et al. They suggest that viscous dissipation originated by the container walls might be the cause of such a discrepancy. Figure 3.3 shows that the model by Spelt and Sangani for U_b/U_∞ presented in Zenit et al., with the fit for A obtained from their experimental data, gives the best approximation to the measurements. Moreover, the difference for all models is the least with the data by Zenit et al., for which the Reynolds number ($380 \geq Re_\mathrm{b} \geq 260$) is about three times that of Martinez-Mercado et al. This is consistent with the notion that the formulae considered here is valid for $Re_\mathrm{b} \gg 1$, and thus these models ought to be considered limiting cases as long as the bubbles remain nearly spherical (i.e., $We_\mathrm{b} < 1$).

From the set of viscous irrotational theories analyzed in §§3.2 and 3.3, that obtained from the dissipation method with an irrotational tangential stress on the outer boundary gives the smallest discrepancy and also depicts the same slope as the dataset by Zenit et al. Nevertheless, when the bubbles are modeled as oblate ellipsoids using Moore's (1965) model for U_∞, and the variation of the equivalent diameter of the bubbles and aspect ratio with the void fraction is accounted for, the curve of U/U_∞ versus α for the experimental data by Zenit et al. becomes rather concave, as presented in their work (not shown here), resembling the curvature of the graph rendered by the model of Spelt and Sangani.

3.5 Closing remarks

The assumed irrotational dynamics of the incompressible fluid surrounding a spherical bubble of variable radius and bounded externally by a spherical surface, is applied to the computation of the drag acting on the bubble and on the outer surface when a relative translation exists between them. A simpler computation of

the drag is given by the integration of the irrotational normal stress, including the viscous part. Another viscous irrotational formulation based upon the mechanical energy balance, namely, the dissipation method, is employed, leading to a different form of the drag. A major aspect of the formulation of the dissipation method presented here is the way the tangential stress boundary condition on the exterior surface enters the analysis. Two choices are considered for this boundary condition, namely, a zero tangential stress and an irrotational tangential stress. In particular, when the bubble volume is held constant, these expressions for the drag are taken as an approximation, in the sense of the classical cell model, of the drag acting on a swarm of identical bubbles. These results are then used to find expressions for the suitably normalized terminal rise velocity of the bubble swarm. These formulae are evaluated by comparing against other theoretical approaches, numerical simulations of the cell-model and experimental data for bubbly flow.

The results for the drag coefficient obtained by the dissipation approximation in a cell with either a zero tangential stress or an irrotational tangential stress on the exterior surface show fair agreement with results given in the literature from numerical solutions of the steady incompressible Navier–Stokes equations for a free-surface cell model or a zero-vorticity cell model, respectively, for a bubble-swarm Reynolds number Re=100. Similar trend is observed for the bubble swarm terminal rise velocity normalized by the terminal rise velocity of a bubble according to the dissipation method, U/U_∞, for nonzero gas volume fraction, $\alpha \geqslant 0.1$. This bubble swarm rise velocity is found by the equilibration of the viscous drag and bubble weight with the buoyancy force determined by the gas-liquid mixture density. In the infinite dilution limit, the bubble velocity is still larger than the value given by the dissipation method, which should be approached as Re increases. On the other hand, the simpler integration of the normal stress from viscous potential flow gives unsatisfactory predictions. The comparison with the experimental data for bubble velocity in bubbly flow through a stagnant liquid in the regime of high Reynolds and low Weber numbers, indicates that the model by Spelt and Sangani, which requires knowledge of the bubble vertical velocity variance, gives the best approximation; it is followed by predictions from the dissipation method with an exterior irrotational-tangential-stress boundary condition.

Chapter 4

Correction of Lamb's dissipation calculation for the effects of viscosity on capillary-gravity waves*

The decay and oscillations of capillary-gravity waves are modeled here by means of two purely viscous irrotational theories of the motion of a viscous liquid, namely, viscous potential flow and the dissipation method. Both approaches give rise to a viscous correction of the frequency of the oscillations, a feature that was not obtained by Lamb (1932) in his version of the dissipation method. This viscous correction to the frequency determines the cross over from progressives waves to standing ones. The resulting expressions for the decay rate and frequency of the oscillations are compared here with the solution of the linearized Navier–Stokes equations also obtained by Lamb.

4.1 Introduction

Stokes (1851) introduced the idea of the dissipation method "in which the decay of the energy of the wave is computed from the viscous dissipation integral where the dissipation is evaluated on potential flow" (Joseph , 2006). This method was implemented by Lamb (1932, §348) (§348) to study the effect of viscosity on the dynamics of free oscillatory waves on deep liquid. The waves are considered small departures

*Reprinted with permission from Padrino, J. C.; Joseph, D. D. *Phys. Fluids*, Vol. 19, Issue 8, 082105, 2007.

about a plane free surface. The result of his analysis was an estimate of the decay rate of the traveling waves. He also conducted the solution of the linearized Navier–Stokes equations for this problem using normal modes (§349; hereinafter 'exact solution'), in which the zero-shear-stress condition at the free surface is satisfied. Independently, Basset (1888) obtained the same dispersion relation as Lamb for the exact solution. Furthermore, Lamb applied his dissipation method to study viscous effects on small oscillations about the spherical shape of a liquid globule in a vacuum or a bubble surrounded by liquid (§355). Whereas the effect of viscosity in both the decay rate and frequency of the oscillations can be examined through the exact solution, Lamb's dissipation approximation does not give rise to a viscous correction of the frequency.

In this work, we carry out the integration of the mechanical energy equation assuming irrotational flow to obtain a relation for the effects of viscosity on the decay rate and frequency of the oscillations of small capillary-gravity waves. Viscosity is explicitly considered in the dissipation term of the mechanical energy balance and the shear stress is put to zero at the free surface. This purely irrotational formulation is referred to as the dissipation method (DM) here. Our irrotational method is similar to Lamb's in the sense that it is an irrotational approximation, but, unlike Lamb, we do not assume that the potential energy equals the kinetic energy and gravity is thus explicitly considered in our formulation. Unlike Lamb, our method of calculation yields a complex eigenvalue for progressive waves with the same growth rate as Lamb's but a different frequency which depends on viscosity. Lamb advertises his method as valid to estimate "the effect of viscosity on free oscillatory waves on deep water". However, his analysis did not yield viscous effects on the frequency of these waves. In fact, when the dissipation method is carried out as presented here, it gives rise to progressive and standing waves just like the exact solution. The progressive waves are associated with long waves and the standing waves with short waves where the cut-off wavenumber is a decreasing function of the viscosity. For standing waves, DM predicts effects of surface tension and gravity on the decay rate. Another purely irrotational theory of the motion of a viscous liquid is used in this study, namely, the theory of viscous potential flow (VPF). In this approach, the viscous normal stress at the free surface enters the potential flow analysis.

Joseph and Wang (2004) applied both VPF and the viscous correction of VPF (labeled as VCVPF) theories to the problem of free gravity waves in which capillary effects are neglected. In the latter approach, VPF theory is modified by adding a viscous pressure correction to the irrotational pressure to compensate the differ-

ence between the non-zero irrotational shear stress and the zero-shear stress at the free surface. Viscous effects in both the decay rate and the frequency were considered. The same decay rate obtained by Lamb's dissipation method was found from VCVPF. Wang and Joseph (2006) performed a thorough comparison showing good agreement between the viscous irrotational theories, VPF and VCVPF, with Lamb's exact solution for short and long gravity waves, respectively, even for liquids with viscosity 10^4 times that of water. The theories of irrotational flow of a viscous fluid (VPF, VCVPF and DM) are applied by Wang, Joseph, and Funada (2005a,b) to the problem of capillary instability and by Padrino et al. (2008) to study capillary-driven oscillations about the spherical shape of a drop or bubble. In these works, VCVPF and DM produced equivalent results. Although the study of nonlinear waves is beyond the scope of this work, we mention that among the abundant literature on nonlinear waves, we know only the work by Longuet-Higgins (1997) on the viscous effects on these waves. He computed the viscous decay of steep irrotational capillary-gravity waves through the dissipation method (see also Joseph et al., 2007).

Here, we compare and discuss predictions from the purely irrotational theories with the exact solution of the linearized problem. The method of calculating the dissipation applied in this work, which follows the steps of that used in the study of capillary instability (Wang et al., 2005a,b), leads to an excellent to reasonable approximation to the dispersion relation of the exact solution for long waves. For short waves, VPF gives the best approximation. The resulting performance may be cautiously used as a guide for application of the irrotational approximations in cases where the 'exact solution' is not known.

Neither Joseph and Wang (2004) nor Wang and Joseph (2006) applied the DM to waves on a plane free surface, although the former did review Lamb's dissipation approximation. The VPF calculation presented in this chapter in §4.2 expands the procedure outlined in Joseph and Wang (2004) to include surface tension effects. More importantly, it gives rise to intermediate results which are required by the DM in §4.3. To the best of our knowledge, for the first time, viscous effects in both the decay rate and frequency of oscillations of 'small' capillary-gravity waves about a plane free surface are obtained through the dissipation approximation.

4.2 Viscous potential flow analysis (VPF)

Consider two-dimensional small irrotational disturbances of the basic state of rest of an incompressible fluid occupying half of the space, $-\infty \leq y \leq 0$, where y is a

Cartesian coordinate such that the plane $y = 0$ corresponds to the free surface for the basic state. The fluid in the upper half is dynamically inactive. The basic state is given by $dP/dy = -\rho g$ where P is the pressure, ρ is the liquid density and g is the acceleration of gravity. We set, with no loss of generality, $P = 0$ at the free surface of the undisturbed state $y = 0$.

In the perturbed state, we look for functions which are periodic in the Cartesian coordinate x with period λ. The perturbed free surface has elevation $y = \eta(x, t)$. For irrotational flow, the velocity field is $\mathbf{u} = \nabla\phi$, such that the incompressibility condition implies the Laplace's equation $\nabla^2\phi = 0$ for the velocity potential ϕ.

Dynamical effects enter the analysis through the Bernoulli equation, which can be written as

$$\rho\frac{\partial\phi}{\partial t} + \frac{\rho}{2} \mid \nabla\phi \mid^2 + \hat{p} + \rho g y = 0, \qquad \text{at} \qquad y = \eta, \tag{4.1}$$

where $\hat{p}$ is the pressure in the disturbed state. The balance of the normal stress at the free surface yields

$$-\hat{p} + 2\mu\frac{\partial^2\phi}{\partial n^2} = -\gamma\nabla_{\mathrm{II}} \cdot \mathbf{n}, \qquad \text{at} \qquad y = \eta, \tag{4.2}$$

where $\nabla_{\mathrm{II}} = \nabla - \mathbf{n}(\mathbf{n} \cdot \nabla)$ (Joseph and Renardy, 1993). In this expression, μ is the liquid dynamic viscosity and γ is the surface tension; the symbol $\mathbf{n}$ denotes the unit outward normal vector from the fluid at the free surface, which determines the n direction, and the second term in the left-hand side of (4.2) accounts for the viscous normal stress at the interface. At the free surface, the kinematic condition can be written as

$$\frac{\partial\phi}{\partial y} = \frac{D\eta}{Dt} = \frac{\partial\eta}{\partial t} + \mathbf{u} \cdot \nabla\eta, \qquad \text{at} \qquad y = \eta. \tag{4.3}$$

The pressure in the disturbed state is now decomposed into small disturbances about the basic state, such that $\hat{p} = P + p$ with $P = -\rho g y$. The system of equations (4.1)-(4.3) is linearized assuming that the free-surface displacement is 'small' in comparison with the wavelength and has 'small' slopes, $\partial\eta/\partial x \ll 1$. This process

yields, at $y = 0$,

$$\rho\frac{\partial\phi}{\partial t} + p = 0, \tag{4.4}$$

$$-p + \rho g\eta + 2\mu\frac{\partial^2\phi}{\partial y^2} = \gamma\frac{\partial^2\eta}{\partial x^2}, \tag{4.5}$$

$$\frac{\partial\phi}{\partial y} = \frac{\partial\eta}{\partial t}. \tag{4.6}$$

Solutions of the Laplace's equation for ϕ in the domain $0 \leq x \leq \lambda$, $-\infty \leq y \leq 0$ with periodic boundary conditions for $x = 0$ and $x = \lambda$ can be written under the form

$$\phi = A\mathrm{e}^{\sigma t + \mathrm{i}kx + ky} + \text{c.c.}, \tag{4.7}$$

with $k = 2\pi j/\lambda$ and $j = 1,2,3, \ldots$, and c.c. denotes complex conjugate of the previous term. The time dependence has been separated to obtain normal-mode solutions. We assume that the shape of the disturbed interface is also given by a normal-mode expression

$$\eta = \eta_0\mathrm{e}^{\sigma t + \mathrm{i}kx} + \text{c.c.}, \tag{4.8}$$

where η_0 is a constant. Combining (4.4) and (4.5) to eliminate the pressure disturbance and using (4.7) and (4.8) gives rise to the expression

$$(\rho\sigma A + 2\mu Ak^2 + \rho g\eta_0 + \gamma k^2\eta_0)\mathrm{e}^{\sigma t + \mathrm{i}kx} + \text{c.c.} = 0 \qquad \text{at} \quad y = 0. \tag{4.9}$$

The linearized kinematic condition (4.6) is then used to find $Ak = \sigma\eta_0$. Applying this relation to eliminate η_0 in (4.9) yields the dispersion relation for VPF

$$\sigma^2 + 2\nu k^2\sigma + gk + \gamma' k^3 = 0, \tag{4.10}$$

which can be solved for the eigenvalues

$$\sigma = -\nu k^2 \pm \sqrt{\nu^2 k^4 - (gk + \gamma' k^3)}, \tag{4.11}$$

with $\gamma' = \gamma/\rho$ and the kinematic viscosity $\nu = \mu/\rho$. This result can be obtained as a special case from the more general expression derived by Funada and Joseph (2001) from the Kelvin-Helmholtz stability analysis of two viscous fluids. For $\gamma = 0$ in (4.10), our result agrees with the eigenvalue relation presented by Joseph and Wang (2004) using the theory of VPF for free gravity waves with no capillary effects.

In the case of $\nu k^2 \geq \sqrt{gk + \gamma' k^3}$ we have two real roots from (4.11) and the waves decay monotonically. The highest value gives the slowest decay rate. In the case of $\nu k^2 < \sqrt{gk + \gamma' k^3}$ we obtain the complex conjugate pair of roots

$$\sigma = -\nu k^2 \pm \mathrm{i}k\sqrt{(g/k + \gamma' k) - \nu^2 k^2}, \tag{4.12}$$

giving rise to progressive decaying waves. The decay rate is $-\nu k^2$ which is half of the value computed by Lamb using energy dissipation arguments. The speed of the traveling waves is

$$c = \sqrt{(g/k + \gamma' k) - \nu^2 k^2}, \tag{4.13}$$

and the speed is slower than the inviscid result $\sqrt{g/k + \gamma' k}$, as noticed by Joseph and Wang (2004) in the absence of surface tension.

For short waves or high viscosity, i.e. $\nu k^2 \gg \sqrt{gk + \gamma' k^3}$, the eigenvalues from (4.11) follow

$$\sigma = -2\nu k^2 \qquad \text{and} \qquad \sigma = -\frac{\gamma' k}{2\nu} - \frac{g}{2\nu k}, \tag{4.14}$$

and the latter gives the slowest decay rate for the standing waves. For zero surface tension, the damping of the waves follows the rate $-g/(2\nu k)$, which decreases for shorter waves. This decay rate was found by Lamb (1932) from the exact solution for large viscosity. For $\nu k^2 \ll \sqrt{gk + \gamma' k^3}$, traveling decaying waves are obtained and the eigenvalues behave as

$$\sigma = -\nu k^2 \pm \mathrm{i}k\sqrt{g/k + \gamma' k}, \tag{4.15}$$

such that the wave speed reaches the inviscid result.

4.3 Dissipation method (DM)

The dissipation method relies on the integration of the mechanical energy equation. To apply DM to capillary-gravity waves, the working equation is obtained after subtracting the basic state of rest $\nabla P = \rho \mathbf{g}$ from the incompressible Navier–Stokes equation and then taking the scalar ("dot") product with the velocity vector. Integration over the region of interest yields the mechanical energy balance for the flow

disturbances in integral form

$$\frac{\mathrm{d}}{\mathrm{d}t}\int_V \frac{\rho}{2}\left|\mathbf{u}\right|^2 \,\mathrm{d}V = \int_{\mathcal{S}} \mathbf{n}\cdot\mathbf{T}\cdot\mathbf{u}\mathrm{d}\mathcal{S} - \int_V 2\mu\mathbf{D}:\mathbf{D}\,\mathrm{d}V, \tag{4.16}$$

where $\mathbf{T}$ is the stress tensor for an incompressible Newtonian fluid in terms of pressure and velocity disturbances (see 4.17 below); $\mathbf{D}$ is the strain-rate tensor

$$\mathbf{D} = \frac{1}{2}\left[\nabla\mathbf{u} + \left(\nabla\mathbf{u}\right)^T\right],$$

where the superscript T denotes the transpose, and $\mathbf{n}$ is the outward normal vector from the fluid. The symbol V denotes the volume of integration enclosed by the surface $\mathcal{S}$. The last term in (4.16) gives the viscous dissipation. The double contracted product $\mathbf{D}:\mathbf{D} = D_{ij}D_{ji}$, and the repeated indexes imply summation according to Cartesian index notation in two dimensions.

The region of integration is defined by $0 \le x \le \lambda$ and $-\infty < y \le 0$. Periodic boundary conditions at $x = 0$ and $x = \lambda$ and disturbances (both velocity and pressure) that vanish as $y \to -\infty$ are considered. Therefore, the surface integral is reduced to an integral at $y = 0$.

The first integral in the right-hand side of (4.16) can be expanded by considering

$$\mathbf{n}\cdot\mathbf{T}\cdot\mathbf{u} = (-p + \tau_{yy})v + \tau_{xy}u. \tag{4.17}$$

The analysis follows with the assumption that the zero-shear-stress condition and the normal-stress balance are satisfied at the free surface. Therefore, we have, at $y = 0$,

$$\tau_{xy} = 0 \qquad \text{and} \qquad -p + \tau_{yy} = -\rho g\eta + \gamma\frac{\partial^2\eta}{\partial x^2} \tag{4.18}$$

Integrals in (4.16) are computed assuming that the fluid motion can be approximated as irrotational. The discontinuity of the zero shear stress at the free surface with the irrotational shear stress is resolved in a vorticity layer which is neglected in the analysis. For irrotational flow, the following identity holds,

$$\int_V 2\mu\mathbf{D}:\mathbf{D}\mathrm{d}V = \int_{\mathcal{S}} \mathbf{n}\cdot 2\mu\mathbf{D}\cdot\mathbf{u}\mathrm{d}\mathcal{S}, \tag{4.19}$$

Substitution of (4.17) and (4.19) into (4.16), using (4.18), yields

$$\frac{\mathrm{d}}{\mathrm{d}t}\int_V \frac{\rho}{2}\left|\mathbf{u}\right|^2 \mathrm{d}V = -\int_0^\lambda \rho g\eta v \,\mathrm{d}x + \int_0^\lambda \gamma\frac{\partial^2\eta}{\partial x^2}v \,\mathrm{d}x - \int_{\mathcal{S}} \mathbf{n}\cdot 2\mu\mathbf{D}\cdot\mathbf{u}\mathrm{d}\mathcal{S}. \tag{4.20}$$

Next, the integrals in (5.31) are carried out with the aid of the formula in Appendix E and using expressions (4.7) and (4.8) for ϕ and η together with the relation $Ak = \sigma\eta_0$, which stems from the irrotational assumption. With $|\mathbf{u}|^2 = u^2 + v^2$ and writing the components of the strain-rate tensor $\mathbf{D}$ in Cartesian coordinates, such that $\mathbf{n} \cdot 2\mu\mathbf{D} \cdot \mathbf{u} = \tau_{yy}v + \tau_{xy}u$ from potential flow, this series of integrals gives rise to

$$\frac{\mathrm{d}}{\mathrm{d}t}\int_V \frac{\rho}{2}\,|\mathbf{u}|^2\ \mathrm{d}V = \rho k A\bar{A}(\sigma+\bar{\sigma})\mathrm{e}^{(\sigma+\bar{\sigma})t}\lambda, \tag{4.21a}$$

$$\int_0^\lambda \rho g\eta v\ \mathrm{d}x = \rho g k^2 A\bar{A}\left(\frac{1}{\sigma}+\frac{1}{\bar{\sigma}}\right)\mathrm{e}^{(\sigma+\bar{\sigma})t}\lambda, \tag{4.21b}$$

$$\int_0^\lambda \gamma\frac{\partial^2\eta}{\partial x^2}v\ \mathrm{d}x = -\gamma k^4 A\bar{A}\left(\frac{1}{\sigma}+\frac{1}{\bar{\sigma}}\right)\mathrm{e}^{(\sigma+\bar{\sigma})t}\lambda, \tag{4.21c}$$

$$\int_{\mathcal{S}} \mathbf{n}\cdot 2\mu\mathbf{D}\cdot\mathbf{u}\mathrm{d}\mathcal{S} = 8\mu k^3 A\bar{A}\mathrm{e}^{(\sigma+\bar{\sigma})t}\lambda. \tag{4.21d}$$

Substitution of (4.21) into (5.31) yields the expression

$$\sigma + 4\nu k^2 + (gk+\gamma' k^3)\frac{1}{\sigma} + \text{c.c.} = 0, \tag{4.22}$$

which is satisfied if the following eigenvalue relation holds

$$\sigma^2 + 4\nu k^2\sigma + gk + \gamma' k^3 = 0. \tag{4.23}$$

with roots

$$\sigma = -2\nu k^2 \pm \sqrt{4\nu^2 k^4 - (gk+\gamma' k^3)}. \tag{4.24}$$

Putting $\gamma' = 0$ in (4.24) yields the same relation obtained in Joseph and Wang (2004) using the viscous correction of VPF, a method that follows a different path to the one described here. We regard (4.24) as an irrotational approximation for the exact solution.

For $2\nu k^2 \geq \sqrt{gk+\gamma' k^3}$, expression (4.24) gives two real roots and monotonically-decaying waves are obtained. On the contrary, if $2\nu k^2 < \sqrt{gk+\gamma' k^3}$, progressive decaying waves occur. In this case, it is convenient to write (4.24) in the form

$$\sigma = -2\nu k^2 \pm \mathrm{i}k\sqrt{(g/k+\gamma' k) - 4\nu^2 k^2}, \tag{4.25}$$

and the traveling waves decay with rate $-2\nu k^2$, which is the same value obtained by Lamb (1932) via the dissipation method. However, Lamb's approach did not

account for the effects of viscosity in the wave speed of traveling decaying waves. The wave speed is extracted from (4.25) as

$$c = \sqrt{(g/k + \gamma' k) - 4\nu^2 k^2}, \tag{4.26}$$

which is slower than the inviscid result $\sqrt{g/k + \gamma' k}$. Prosperetti (1976) finds (4.25) for small times and an irrotational initial condition from the solution of the initial-value problem for standing, capillary-gravity waves. He notes that this solution can apply to large viscosity. He also obtains Lamb's normal-mode solution (labeled "exact solution" here) as the asymptotic limit for large times, pointing out that validity of Lamb's solution for all times is restricted to small viscosity.

For $2\nu k^2 \gg \sqrt{gk + \gamma' k^3}$ (e.g., short waves or high viscosity), relation (4.24) yields the trend for the decay rates

$$\sigma = -4\nu k^2 \qquad \text{and} \qquad \sigma = -\frac{\gamma' k}{4\nu} - \frac{g}{4\nu k}, \tag{4.27}$$

and the second root, which is governed by surface tension, gives the slowest decay rate of the standing waves. If $2\nu k^2 \ll \sqrt{gk + \gamma' k^3}$, as for long waves or low viscosity, the eigenvalues from (4.25) behave as

$$\sigma = -2\nu k^2 \pm \mathrm{i}k\sqrt{g/k + \gamma' k} \tag{4.28}$$

and the progressive decaying waves travel with the inviscid speed. Lamb (1932) found that the exact solution reaches (4.28) in the case of "small" viscosity.

4.4 Discussion

Lamb (1932, §349) analyzed the viscous problem of small waves on the free surface of a deep liquid with capillary and gravity effects. The approach considers the solution of the linearized Navier–Stokes equations of an incompressible flow where the zero shear stress condition is satisfied at the free surface. Hence, vorticity is not set to zero. Lamb obtained the following eigenvalue relation, designated here as the exact solution,

$$\left[(\sigma + 2\nu k^2)^2 + \sigma_0^2\right]^2 = 16\nu^3 k^6 (\sigma + \nu k^2), \qquad \sigma_0^2 = gk + \gamma' k^3, \tag{4.29}$$

with $\mathrm{Re}[(\sigma + 2\nu k^2)^2 + \sigma_0^2] \geq 0$.

In this section we compare the predictions from the exact solution with results from the purely irrotational theories, namely, VPF, DM and IPF, the inviscid irrota-

tional theory. The latter is reached by setting $\nu = 0$ in either VPF or DM eigenvalue relations (4.12) and (4.25), respectively; hence, the eigenvalues are purely imaginary with zero decay rate.

The dispersion relations (4.12), (4.25) and (4.29) can be conveniently written in dimensionless form as follows

$$\text{VPF} \qquad \tilde{\sigma} = -\theta \pm \mathrm{i}\sqrt{1-\theta^2} \tag{4.30a}$$

$$\text{DM} \qquad \tilde{\sigma} = -2\theta \pm \mathrm{i}\sqrt{1-4\theta^2} \tag{4.30b}$$

$$\text{Exact solution} \qquad \left[(\tilde{\sigma}+2\theta)^2+1\right]^2 = 16\theta^3(\tilde{\sigma}+\theta) \tag{4.30c}$$

and $\tilde{\sigma} = \mathrm{i}$ for IPF. In these expressions, we have set $\tilde{\sigma} = \sigma/\sigma_0$ and $\theta = \nu k^2/\sigma_0$, a factor introduced by Lamb in his "exact solution". The analysis of (4.30) reveals that a threshold θ_c can be obtained that separates progressive waves ($\theta < \theta_c$, $\mathrm{Im}[\tilde{\sigma}] \neq 0$) from standing waves ($\theta \geq \theta_c$, $\mathrm{Im}[\tilde{\sigma}] = 0$) from each theory. We obtain $\theta_c = 1$ for VPF and $\theta_c = 0.5$ for DM. For the exact solution, (4.30c) gives rise to, nearly, $\theta_c = 1.3115$ (also reported in Prosperetti, 1976). We notice that the first order approximation in θ of (4.30b) for the dissipation method is equivalent to the first order approximation in this parameter of the exact solution presented by Lamb (1932) and Basset (1888). As noted by Landau and Lifshitz (1959), the vortical layer is thin when viscous effects are "weak" (small θ) and its contribution to the total energy dissipation is negligible in comparison to the dissipation from within the bulk of fluid.

From the definition of θ, we have that the respective cutoff wavenumber k_c can be obtained for each theory using the corresponding value of θ_c given above. When $k < k_c$, progressive waves decay, whereas for $k \geq k_c$, the waves decay monotonically.

To investigate the cross-over from progressive to standing waves according to the exact solution and the irrotational approximations, we choose three different liquids, namely, a highly mobile one as water, glycerin and SO10000, a very viscous oil at ambient temperature. The properties of these liquids used in the computations are indicated in Table 4.1. The kinematic viscosity varies several orders of magnitude from one fluid to another. The cutoff wave-number k_c from the exact solution, VPF and DM is shown in Table 4.2 for the three liquids. For the same liquid, DM gives the lowest k_c and the exact solution gives the largest. Therefore, traveling waves of certain length according to the exact solution may be predicted as standing waves by the irrotational approximations. Table 4.2 reveals that the cutoff wave-number decreases as the viscosity increases. Thus, the region of progressive decaying waves $0 < k < k_c$ shrinks with increasing viscosity. Waves for which $k < k_c$ oscillate with

Table 4.1: Properties of the liquids used in this study.

Property	Water	Glycerin	SO10000 oil
ν (m^2 s^{-1})	1.00×10^{-6}	6.21×10^{-4}	1.03×10^{-2}
ρ (kg m^{-3})	1.00×10^{3}	1.26×10^{3}	9.69×10^{2}
γ (N m^{-1})	7.28×10^{-2}	6.34×10^{-2}	2.10×10^{-2}

Table 4.2: Cutoff wavenumber k_c (m^{-1}) computed for DM, VPF and the exact solution for three different liquids: Water, glycerin and SO10000 oil.

Theory	Water	Glycerin	SO10000 oil
DM	1.82×10^{7}	196.81	28.50
VPF	7.28×10^{7}	344.64	45.29
Exact	1.25×10^{8}	445.18	54.30

a finite period whereas waves with $k > k_c$ can be though of as having an infinitely long period. This latter feature is clearly associated with the low mobility of highly viscous liquids.

Figure 4.1 shows the dimensionless decay rate $-\mathrm{Re}[\tilde{\sigma}]$ and frequency of the oscillations $\mathrm{Im}[\tilde{\sigma}]$ as a function of the dimensionless parameter θ from (4.30a), (4.30b) and (4.30c) for VPF, DM and the exact solution, respectively. IPF predictions for the frequency, $\mathrm{Im}[\tilde{\sigma}] = 1$, are also included. For $\theta > \theta_c$ only the slowest decay rate, given by the smallest real eigenvalue, is plotted. In these figures, only the cutoff θ_c given by the exact solution is presented, which hereinafter is referred to as θ_c'. An important feature of the dimensionless representation of the dispersion relations (4.30) is that their graphs of $\tilde{\sigma}$ versus θ are equally applicable to any incompressible Newtonian fluid, and no individual plots have to be presented for every liquid chosen.

Both viscous irrotational theories follow the trend described by the exact solution as shown in figure 4.1. With respect to the decay rate, this figure indicates that DM approaches the exact solution in the progressive-wave regime ($\theta < \theta_c'$) for $\theta \ll 1$. In particular, for $\theta \leq 0.02$ we found that the relative error for DM in absolute value remains below 10% and the agreement becomes outstanding as θ decreases since $\mathrm{Re}[\tilde{\sigma}] = -2\theta$ as indicated by (4.28). On the other hand, VPF is off the mark by 50% as can be anticipated from (4.15). In the standing-wave regime ($\theta \geq \theta_c'$), VPF shows excellent agreement with the exact solution; for $\theta \geq 2$ this irrotational theory predicts values of the decay rate with relative errors within 5% in absolute value and

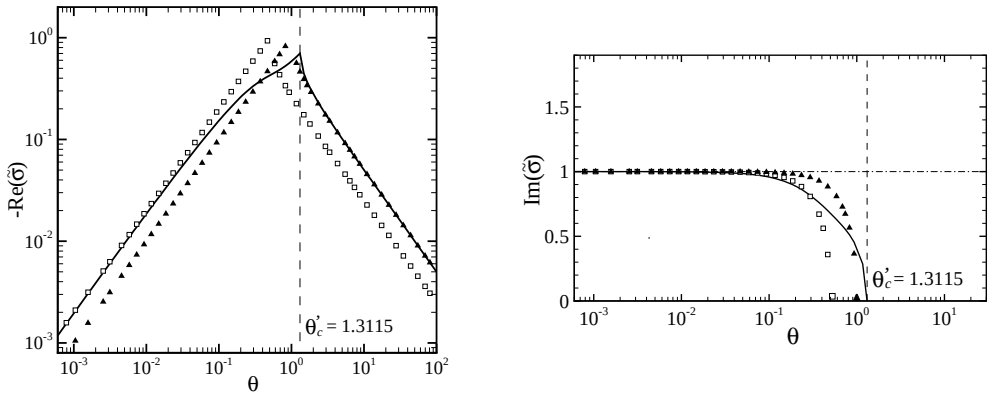

Figure 4.1: Dimensionless decay rate $-\mathrm{Re}[\tilde{\sigma}]$ and frequency of the oscillations $\mathrm{Im}[\tilde{\sigma}]$ as a function of the dimensionless parameter $\theta = \nu k^2/\sigma_0$ from the exact solution and the irrotational theories VPF, DM and IPF: Solid line, exact solution; ▲, VPF; □, DM; dashed-dotted line, IPF. In the latter case, the eigenvalues $\tilde{\sigma}$ are purely imaginary. The dimensionless eigenvalue is $\tilde{\sigma} = \sigma/\sigma_0$ where σ_0 is the inviscid frequency. For $\theta > \theta_c$, the solutions are purely real; in this case, only the slowest decay rate, given by the lowest real eigenvalue, is presented. The cutoff θ_c' corresponds to the exact solution.

the agreement with the exact solution improves substantially following $\tilde{\sigma} = -1/(2\theta)$ as θ increases as predicted by (4.14). By contrast, DM under-predicts the decay rate by 50% in this regime in accord with (4.27). In the transition region ($0.02 \leq \theta \leq 2$, say), neither of the viscous irrotational theories gives a good approximation of the exact decay rate for this entire interval. However, each of these approximations gives rise to a critical value θ_c that qualitatively resembles the cross-over from progressive to standing waves depicted by the exact solution.

Regarding the frequency of the oscillations, $\mathrm{Im}[\tilde{\sigma}]$, figure 4.1 1 reveals that viscous effects are significant when $\theta \geq 0.1$, for which the exact solution deviates from the inviscid result. The frequency becomes damped and, for $\theta \geq \theta_c'$, the oscillations are suppressed. These features in the dynamics of the waves are also described, on qualitative grounds, by the viscous irrotational approximations. This figure also illustrates what was computed above, namely, the lowest cross-over θ_c is given by DM and the highest is obtained from the exact solution; the cut-off from VPF lies in between. This cut-off between progressive and standing waves cannot be obtained from the dissipation calculation implemented by Lamb based on Stokes' idea.

An aspect that is worth mentioning and which may not be evident from the graph $-\mathrm{Re}(\tilde{\sigma})$ versus θ is the effect of surface tension in the decay of the waves. The slowest

decay rate for the exact solution and VPF goes as $-\gamma' k/(2\nu)$ as $k \to \infty$, whereas for DM, it goes as $-\gamma' k/(4\nu)$. Thus, as the waves become shorter, they are more rapidly damped by capillary effects. By contrast, the suppression of the regularizing effect of surface tension yields a decrease in the decay rate of the gravity waves as k increases as shown by Wang and Joseph (2006) (see expressions 4.14 and 4.27). In the case of the inviscid theory, the frequency continues increasing as $k \to \infty$ and the waves oscillate undamped. The shortest the wave, the highest the frequency, which contradicts the viscous theories. By taking into account viscous effects in the irrotational theories, the cross-over from the traveling-wave regime to the standing-wave regime is predicted by these approximations, in a similar fashion as the exact solution.

In this analysis, we have shown that the effect of viscosity on the frequency of capillary-gravity waves which Lamb (1932) assumed to be the same as in an inviscid fluid, can be obtained from the dissipation integral in the mechanical energy balance. Moreover, results from this dissipation method are not restricted to oscillatory waves, as it is the case with Lamb's dissipation calculation, but they also predict values for the decay rate of standing waves that follows the trend described by the exact solution. In sum, our dissipation method yields an eigenvalue relation for the entire spectrum of wave numbers and is in good agreement with the exact solution for sufficiently large waves. VPF is the best approximation for sufficiently short waves.

Chapter 5

Purely irrotational theories for the viscous effects on the oscillations of drops and bubbles*

The approximations of viscous potential flow and the dissipation method are applied to the problem of the decay of "small" waves on a drop or bubble about the spherical shape. The fluids are incompressible and viscous and the velocity field is assumed to be purely irrotational. Comparisons with the solution of the linearized incompressible Navier–Stokes equations given in the literature are presented and discussed.

5.1 Introduction

A viscous liquid drop surrounded by a quiescent gas or a gas bubble immersed in a viscous liquid tends to an equilibrium spherical shape if the effects of surface tension are significantly large in comparison with gravitational effects. When the spherical interface of the bubble or drop is slightly perturbed by an external agent, the bubble or drop will recover their original spherical configuration through an oscillatory motion of decreasing amplitude. In the case of the drop, depending upon its size and physical properties, the return to the spherical shape may consist of overdamped aperiodic waves that decrease monotonically. For a drop immersed in

*Reprinted with permission from Padrino, J. C.; Funada, T.; Joseph, D. D. *Int. J. Multiphase Flow.*, Vol. 34, Issue 1, 61–75, 2008.

another viscous liquid, decaying oscillatory waves always occurs at the liquid-liquid interface.

Early studies on the subject for inviscid liquids are due to Kelvin (1890) and Rayleigh (1896). Lamb (1881) considered fully viscous effects on the oscillations of a liquid spheroid by solving the linearized Navier–Stokes equations. Applying Stokes' ideas (Stokes, 1851), Lamb also approximated the effect of viscosity on the decay rate of the oscillations on a liquid globule by means of the dissipation method, in which an irrotational velocity field is assumed. His result is independent of the nature of the forces that drive the interface to the spherical shape. Furthermore, Lamb used energy arguments to compute the frequency of the oscillations governed by self-gravitation in the absence of viscosity, recovering the result due to Kelvin. In his book on hydrodynamics, Lamb (1932) included his dissipation calculation of the decay rate of the oscillations on a spherical globule and added the corresponding result for a spherical bubble in a viscous liquid. Chandrasekhar (1959) studied fully viscous effects on the small oscillations of a liquid globe with self-gravitation forces neglecting surface tension. The same form of the solution was also obtained by Reid (1960) when surface tension instead of self-gravitation is the force that tends to maintain the spherical shape. A good account of both solutions is presented in the treatise by Chandrasekhar (1961). Following Lamb's reasoning, Valentine, Sather, and Heideger (1965) applied the dissipation method to the case of a drop surrounded by another viscous liquid. They presented their result for two fluids with the same density. However, the dissipation approximation for the two-liquid case, according to Miller and Scriven (1968), underestimates the decay rate.

Comprehensive analyses of viscous effects in a drop embedded in liquid were presented by Miller and Scriven (1968) and Prosperetti (1980a) using normal modes. The latter found a continuous spectrum of eigenvalues for an unbounded outer fluid. Prosperetti (1977, 1980b) considered the initial-value, fully-viscous problem posed by small perturbations about the spherical shape of a drop or a bubble with no assumption about the form of the time dependence. The solution showed that the normal mode results are recovered for large times.

Finite size disturbances have received some attention. Tsamopoulos and Brown (1983) considered the small-to-moderate-amplitude inviscid oscillations using perturbations methods. Lundgren and Mansour (1988) and Patzek et al. (1991) studied the inviscid problem posed by large oscillations applying the boundary-integral and the finite-element methods, respectively. Lundgren and Mansour also investigated the effect of a "small" viscosity on drop oscillations. Basaran (1992) carried out the numerical analysis of moderate-to-large-amplitude axisymmetric oscillations of

a viscous liquid drop.

In this chapter, approximate solutions of the linearized problem for small departures about the spherical shape for a drop surrounded by a gas of negligible density and viscosity or a bubble embedded in a liquid are sought using viscous potential flow (VPF) and the dissipation method. VPF is a purely-irrotational-flow theory in which viscosity enters the problem through the viscous normal stress at the interface (Joseph and Liao, 1994a, 1994b; Joseph, 2003). If the viscosities of the fluids are neglected, the analysis reduces to inviscid potential flow (IPF). Another viscous irrotational approximation can be obtained by applying the dissipation method (Joseph and Wang, 2004). In this approximation, which requires the evaluation of the mechanical energy equation, viscous effects are accounted for through the computation of the viscous dissipation originated by the irrotational flow. In addition to his study of a viscous globule and a gas bubble, the dissipation method was used by Lamb (1932) in his analysis of the effect of viscosity on the decay of free gravity waves. He found the decay rate from the dissipation method in complete agreement with the exact solution for the decay rate of free gravity waves for "small" viscosity. However, his analysis did not render viscous effects for the frequency of the waves. The dissipation calculation presented here does give rise to a viscous correction for the wave frequency, thus predicting a crossover from oscillatory to monotonically decaying waves.

VPF was used by Funada and Joseph (2002) to study the problem of capillary instability. Their results for the growth rate were in much better agreement with Tomotika's (1935) exact normal-mode solution than inviscid potential flow. Wang, Joseph, and Funada (2005a) computed the growth rates for this configuration by adding a viscous correction to VPF, when either the interior or exterior fluid is a gas of negligible density and viscosity. They found good agreement between their results and the exact solution. The case of capillary instability of two viscous liquids was considered by Wang, Joseph, and Funada (2005b), obtaining good to reasonable agreement for the maximum growth rates whereas poor agreement for long waves. Wang et al. (2005a, 2005b) also used the dissipation method in the problem of capillary instability and obtained the same growth rate as the viscous correction of VPF. The decay of free gravity waves modeled as small disturbances about an infinite plane free surface was studied by Joseph and Wang (2004) and Wang and Joseph (2006) using VPF and the viscous correction of VPF. They found that the decay rate from VPF agrees with Lamb's exact solution for short waves, whereas the damping rate computed from the viscous correction of VPF for long waves agrees with both Lamb's dissipation result and his solution of the linearized Navier–Stokes

equations. A comprehensive review on the theory of irrotational flow of viscous fluids was given by Joseph (2006). The idea of a viscous correction of VPF is discussed in detail by Joseph, Funada, and Wang (2007). They present examples of its application and show its relation with the dissipation method.

Two viscous irrotational approximations are thus used in this study to determine the decay rate and frequency of the oscillations on drops and bubbles, namely,

VPF or viscous potential flow, in which viscosity enters the analysis through the viscous normal stress at the interface.

Dissipation method, which requires the integration of the mechanical energy equation with the approximation of irrotational motion yet zero-shear stress is satisfied at the free surface.

Results from these theories are compared to predictions from **IPF** or inviscid potential flow, in which the viscosity is set equal to zero, and the solution of the linearized incompressible Navier–Stokes equations using normal modes, hereinafter "**exact solution**", given in the literature.

This chapter is organized as follows: First, VPF analysis of a drop embedded in a viscous liquid is presented and the limiting cases of a drop in vacuum and a bubble in liquid are obtained. In §5.3, the dissipation method is applied to the spherical shape. In §5.4, the exact solution of the linearized fully viscous problem is summarized. Results are discussed in §5.5 where several final remarks are presented.

5.2 Viscous potential flow analysis of a spherical drop immersed in another fluid

Consider a single spherical drop of radius a filled with a fluid with density ρ_l and viscosity μ_l immersed in another fluid with density ρ_a and viscosity μ_a. The coefficient of interfacial tension is denoted as γ. Both fluids are incompressible and Newtonian with gravity neglected. At the basic or undisturbed state both fluids are at rest and the pressure jump across the spherical interface is balanced by surface tension.

When the basic state is disturbed with small irrotational perturbations, the resulting velocity field can be written as the gradient of a potential. The disturbance of the spherical interface is denoted by $\zeta \equiv \zeta(t, \theta, \varphi)$, $0 \leqslant \theta \leqslant \pi$, $0 \leqslant \varphi \leqslant 2\pi$; the interface position is $r = a + \zeta$.

For irrotational flow the incompressible Navier–Stokes equations reduce to the

Bernoulli equation. The resulting pressure field can be decomposed into the undisturbed pressure plus a "small" disturbance.

After subtracting the basic state from the disturbed fluid motion and performing standard linearization of the resulting expressions by neglecting products of the small fluctuations and products of their derivatives, one obtains, for the interior motion ($0 \leqslant r < a$),

$$\nabla^2 \phi_l = 0, \tag{5.1}$$

$$p_l = -\rho_l \frac{\partial \phi_l}{\partial t}, \tag{5.2}$$

and, for the exterior motion ($a < r < \infty$),

$$\nabla^2 \phi_a = 0, \tag{5.3}$$

$$p_a = -\rho_a \frac{\partial \phi_a}{\partial t}. \tag{5.4}$$

where ϕ is the velocity potential and p is the pressure disturbance. For irrotational motion, the boundary conditions at the interface require the continuity of the radial velocity and the balance of the normal stresses by interfacial tension. For small departures about the spherical shape, $a >> \zeta$ and the boundary conditions can be written as

$$u_r^l = u_r^a, \tag{5.5}$$

for the continuity of the radial velocity at $r = a$ and

$$\left[\left[-p + 2\mu \frac{\partial u_r}{\partial r}\right]\right] = \frac{\gamma}{a^2}(L^2 - 2)\zeta, \tag{5.6}$$

for the balance of normal stresses across the interface $r = a$, written in linearized form, accounting for the pressure balance in the undisturbed state. The notation $[[\cdot]] = (\cdot)_{r=a^+} - (\cdot)_{r=a^-}$ is being used to denote the jump across the interface located at $r = a$. The linearized kinematic condition is

$$u_r = \frac{\partial \zeta}{\partial t}, \tag{5.7}$$

at $r = a$ with, $u_r = \partial\phi/\partial r$. The right-hand side of (5.6) is obtained from the linearized form of the divergence of the outward unit normal vector to the disturbed interface for the interior fluid. The operator L^2 is also known as the spherical Laplacian and emerges, for instance, in the solution of the Laplace equation using spherical coordinates by applying the method of separation of variables. It is defined

as

$$-L^2\zeta = \frac{1}{\sin\theta}\frac{\partial}{\partial\theta}\left(\sin\theta\frac{\partial\zeta}{\partial\theta}\right) + \frac{1}{\sin^2\theta}\frac{\partial^2\zeta}{\partial\varphi^2}. \tag{5.8}$$

Solutions of (5.1) and (5.3) for the interior and exterior of a sphere, respectively, can be sought in the form

$$\phi_l(r,\theta,\varphi,t) = \sum_{\ell=0}^{\infty} A_\ell \left(\frac{r}{a}\right)^\ell e^{-\sigma_\ell t} S_\ell(\theta,\varphi) + \text{c.c.} \qquad 0 \leqslant r < a, \tag{5.9}$$

and

$$\phi_a(r,\theta,\varphi,t) = \sum_{\ell=0}^{\infty} C_\ell \left(\frac{r}{a}\right)^{-\ell-1} e^{-\sigma_\ell t} S_\ell(\theta,\varphi) + \text{c.c.} \qquad a < r < \infty, \tag{5.10}$$

such that ϕ_l is finite at $r = 0$ and ϕ_a remains bounded as $r \to \infty$; σ_ℓ is an eigenvalue to be determined. It will be shown that σ_ℓ does not depend upon the index m. The symbol c.c. designates the complex conjugate of the previous term. The functions S_ℓ are the surface harmonics of integral order

$$S_\ell(\theta,\varphi) = \sum_{m=-\ell}^{\ell} B_{\ell m} Y_\ell^m(\theta,\varphi), \tag{5.11}$$

which, with the choice $\bar{B}_{\ell m} = B_{\ell,-m}$, are real functions. The functions $Y_\ell^m(\theta,\varphi)$ are known as the spherical harmonics (Strauss 1992)

$$Y_\ell^m(\theta,\varphi) = P_\ell^{|m|}(\cos\theta)e^{\mathrm{i}\varphi}, \tag{5.12}$$

where $P_\ell^{|m|}$ are the associated Legendre functions. The spherical harmonics satisfy

$$L^2 Y_\ell^m(\theta,\varphi) = \ell(\ell+1)Y_\ell^m(\theta,\varphi), \tag{5.13}$$

for $\ell = 0, 1, 2, \ldots$ and $m = -\ell, \ldots, -1, 0, 1, \ldots, \ell$. The operator L^2 has been defined in (5.8). Expressions for the radial components of the velocity can be obtained from (5.9) and (5.10) by applying $u_r = \partial\phi/\partial r$. Then, the pressure disturbances p_l and p_a can be obtained from (5.2) and (5.4).

Let us write the disturbance of the spherical shape of the interface as a series expansion,

$$\zeta(\theta,\varphi,t) = \sum_{\ell=0}^{\infty} \zeta_\ell(\theta,\varphi)\mathrm{e}^{-\sigma_\ell t} + \text{c.c.} \tag{5.14}$$

By considering $\zeta_\ell(\theta,\varphi) = \zeta_{0\ell} S_\ell(\theta,\varphi)$, where $\zeta_{0\ell}$ is a constant, and using conditions (5.5) and (5.7) one obtains

$$-\sigma_\ell \zeta_{0\ell} = \left(\frac{\ell}{a}\right) A_\ell, \qquad \sigma_\ell \zeta_{0\ell} = \left(\frac{\ell+1}{a}\right) C_\ell. \tag{5.15}$$

In addition, we have

$$(L^2-2)\zeta = \sum_{\ell=0}^{\infty} \{\ell(\ell+1)-2\}\zeta_{0\ell} \mathrm{e}^{-\sigma_\ell t} S_\ell + \text{c.c.} = \sum_{\ell=0}^{\infty} (\ell+2)(\ell-1)\zeta_{0\ell} \mathrm{e}^{-\sigma_\ell t} S_\ell + \text{c.c.}, \tag{5.16}$$

by virtue of (5.13) and (5.14). Substituting normal-mode expressions for u_r and p, obtained using (5.9) and (5.10), into the left-hand side of (5.6), applying the result (5.16) and replacing A_ℓ and C_ℓ with (5.15) yields the dispersion relation for the eigenvalue σ_ℓ, which, after some manipulation, may be written as

$$\left(\rho_l(\ell+1)+\rho_a\ell\right)\sigma^2 - \left(\frac{2\mu_l}{a^2}(\ell+1)\ell(\ell-1) + \frac{2\mu_a}{a^2}(\ell+2)(\ell+1)\ell\right)\sigma + \frac{\gamma}{a^3}(\ell+2)(\ell+1)\ell(\ell-1) = 0, \tag{5.17}$$

where the subscript ℓ has been dropped from σ for convenience. Expression (5.17) may be written in dimensionless form with the following choices of dimensionless parameters (Funada and Joseph, 2002),

$$\hat{l} = \frac{\rho_a}{\rho_l}, \quad \hat{m} = \frac{\mu_a}{\mu_l}, \quad \hat{\sigma} = \sigma\frac{a}{U} \qquad \text{with} \qquad U = \sqrt{\frac{\gamma}{\rho_l a}}, \tag{5.18}$$

In dimensionless form, expression (5.17) becomes,

$$\left((\ell+1)+\hat{l}\ell\right)\hat{\sigma}^2 - \frac{2}{\sqrt{J}}\left((\ell+1)\ell(\ell-1) + \hat{m}(\ell+2)(\ell+1)\ell\right)\hat{\sigma} + (\ell+2)(\ell+1)\ell(\ell-1) = 0 \tag{5.19}$$

with a Reynolds number

$$J = \frac{\rho_l V a}{\mu_l} = Oh^2 \qquad \text{with} \qquad V = \frac{\gamma}{\mu_l}, \tag{5.20}$$

where Oh is the Ohnesorge number. In other words, $J^{-1/2}$ represents a dimensionless viscosity. Therefore, the eigenvalue $\hat{\sigma}$ for viscous potential flow (VPF) can be

computed from

$$\hat{\sigma} = \frac{(\ell+1)\ell(\ell-1) + \hat{m}(\ell+2)(\ell+1)\ell}{\sqrt{J}\left((\ell+1)+\hat{l}\ell\right)} \pm \sqrt{\left[\frac{(\ell+1)\ell(\ell-1)+\hat{m}(\ell+2)(\ell+1)\ell}{\sqrt{J}((\ell+1)+\hat{l}\ell)}\right]^2 - \frac{(\ell+2)(\ell+1)\ell(\ell-1)}{(\ell+1)+\hat{l}\ell}}, \quad (5.21)$$

which has two different real roots or two complex roots. In the former case, the interface does not oscillate and the disturbances are damped. In the latter case, $\hat{\sigma} = \hat{\sigma}_R \pm \mathrm{i}\hat{\sigma}_\mathrm{I}$ where the real part represents the damping coefficient while the imaginary part corresponds to the frequency of the damped oscillations.

When both fluids are considered inviscid (IPF), expression (5.21) simplifies to ($\hat{m} \to 0$ and $\sqrt{J} \to \infty$)

$$\hat{\sigma} = \pm\mathrm{i}\sqrt{\frac{(\ell+2)(\ell+1)\ell(\ell-1)}{(\ell+1)+\hat{l}\ell}}, \quad (5.22)$$

and undamped oscillations are predicted. This is the same expression found by Lamb (1932), §275.

5.2.1 VPF results for a spherical drop in a vacuum

If the external fluid has negligible density and viscosity ($\hat{l} \to 0$ and $\hat{m} \to 0$), a drop surrounded by a dynamically inactive ambient fluid is obtained, in which case expression (5.21) becomes,

$$\hat{\sigma} = \frac{\ell(\ell-1)}{\sqrt{J}} \pm \sqrt{\left[\frac{\ell(\ell-1)}{\sqrt{J}}\right]^2 - (\ell+2)\ell(\ell-1)}. \quad (5.23)$$

Moreover, for an inviscid drop $\sqrt{J} \to \infty$ and (5.23) reduces to

$$\hat{\sigma}_D = \pm\mathrm{i}\sqrt{(\ell+2)\ell(\ell-1)} = \pm\mathrm{i}\hat{\sigma}^*_\mathrm{D}, \quad (5.24)$$

and the drop oscillates undamped about the spherical form. This result was obtained by Lamb (1932).

Using the expression obtained from VPF in (5.23), one can readily find two roots for the decay rate as $\sqrt{J} \to 0$ in the drop (e.g., high viscosity) for the aperiodic

modes. The relevant root on physical grounds is given by

$$\hat{\sigma} = \hat{\sigma}_D^{*2}\sqrt{J}\frac{1}{2\ell(\ell-1)}. \tag{5.25}$$

In the case $\sqrt{J} \to \infty$ (low viscosity, say), the eigenvalues are complex, and then we encounter oscillatory decaying waves. These eigenvalues behave as

$$\hat{\sigma} = \frac{\ell(\ell-1)}{\sqrt{J}} \pm \mathrm{i}\hat{\sigma}_{\mathrm{D}}^{*}. \tag{5.26}$$

5.2.2 VPF results for a spherical bubble

By taking $\rho_l \to 0$ and $\mu_l \to 0$ in (5.17), the eigenvalue relation for a bubble of negligible density and viscosity embedded in a liquid is obtained for VPF

$$\hat{\sigma} = \frac{(\ell+2)(\ell+1)}{\sqrt{J}} \pm \sqrt{\left[\frac{(\ell+2)(\ell+1)}{\sqrt{J}}\right]^2 - (\ell+2)(\ell+1)(\ell-1)}, \tag{5.27}$$

where J is defined in terms of the liquid properties. In the limit of an inviscid external fluid $\sqrt{J} \to \infty$ in (5.27) and we obtain

$$\hat{\sigma}_B = \pm\mathrm{i}\sqrt{(\ell+2)(\ell+1)(\ell-1)} = \pm\mathrm{i}\hat{\sigma}_{\mathrm{B}}^{*}, \tag{5.28}$$

and the bubble oscillates about the spherical shape without damping. This expression was obtained by Lamb (1932).

The dispersion relation obtained from VPF in (5.27) can be used to study the trend followed by the disturbances when $\sqrt{J} \to 0$ in the case of the bubble. In this case, monotonically decaying waves are predicted with decay rate

$$\hat{\sigma} = \hat{\sigma}_B^{*2}\sqrt{J}\frac{1}{2(\ell+2)(\ell+1)}. \tag{5.29}$$

In the case of $\sqrt{J} \to \infty$, VPF analysis for the bubble yields

$$\hat{\sigma} = \frac{(\ell+2)(\ell+1)}{\sqrt{J}} \pm \mathrm{i}\hat{\sigma}_{\mathrm{B}}^{*}, \tag{5.30}$$

and decaying oscillations are found.

5.3 Dissipation approximation

Viscous effects can be included for irrotational motion through the dissipation method; neither vortical layers nor viscous pressure corrections enter into the analysis. This method stems from the evaluation of the mechanical energy equation on the fluid domain. In this equation, the viscous dissipation in the bulk of the liquid is approximated by potential flow, while the continuity of tangential stress is enforced at the gas-liquid interface; the shear stress is put to zero (the gas being considered of negligible density and viscosity). Here, the procedure described in the work by Wang et al. (2005a, 2005b) is applied to the spherical geometry. Our result goes further than Lamb's result, since the effect of viscosity in the frequency of the oscillations is predicted in the analysis that follows.

5.3.1 Dissipation approximation for a spherical drop in a vacuum

In the case of a liquid drop surrounded by a vacuum, the mechanical energy equation can be written as

$$\frac{d}{dt}\int_V \rho\frac{|\mathbf{u}|^2}{2}\mathrm{d}V = \int_{\mathcal{S}} \mathbf{n}\cdot\mathbf{T}\cdot\mathbf{u}\mathrm{d}\mathcal{S} - \int_V 2\mu\mathbf{D}:\mathbf{D}\mathrm{d}V, \tag{5.31}$$

where V is the volume of the liquid sphere of radius a in the linearized problem; $\mathcal{S}$ is the surface of the drop and $\mathbf{n}$ is the unit outward normal; $\mathbf{u}$ is the velocity field; $\mathbf{T}$ is taken as the stress tensor for Newtonian incompressible flow and $\mathbf{D}$ is the strain-rate tensor. The last term in (5.31) represents the viscous dissipation. For potential flow, the following identity holds,

$$\int_V 2\mu\mathbf{D}:\mathbf{D}\mathrm{d}V = \int_{\mathcal{S}} \mathbf{n}\cdot 2\mu\mathbf{D}\cdot\mathbf{u}\mathrm{d}\mathcal{S}, \tag{5.32}$$

where $\mathbf{D}:\mathbf{D} = D_{ij}D_{ij}$ using Cartesian index notation. Therefore, (5.31) becomes,

$$\frac{d}{dt}\int_V \rho\frac{|\mathbf{u}|^2}{2}\mathrm{d}V = \int_{\mathcal{S}}[(-p+\tau_{rr})u_r + \tau_{r\theta}u_\theta + \tau_{r\varphi}u_\varphi]\mathrm{d}\mathcal{S} - \int_{\mathcal{S}} \mathbf{n}\cdot 2\mu\mathbf{D}\cdot\mathbf{u}\mathrm{d}\mathcal{S}. \tag{5.33}$$

At the free surface $r = a$, we recall that the normal stress balance gives rise to,

$$-p + \tau_{rr} = -\frac{\gamma}{a^2}(L^2-2)\zeta. \tag{5.34}$$

The zero-shear-stress condition is enforced at the free surface

$$\tau_{r\theta} = 0, \qquad \tau_{r\varphi} = 0. \tag{5.35}$$

With these boundary conditions, the mechanical energy equation (5.33) can be expressed as

$$\frac{d}{dt}\int_V \rho\frac{|\mathbf{u}|^2}{2}\mathrm{d}V = -\int_{\mathcal{S}}\frac{\gamma}{a^2}(L^2-2)\zeta u_r \mathrm{d}\mathcal{S} - \int_{\mathcal{S}}\mathbf{n}\cdot 2\mu\mathbf{D}\cdot\mathbf{u}\mathrm{d}\mathcal{S}. \tag{5.36}$$

With $|\mathbf{u}|^2 = u_r^2+u_\theta^2+u_\varphi^2$ and the components of $\mathbf{D}$ expressed in spherical coordinates, the integrals in (5.36) can be evaluated using the formula in Appendix E as well as standard results involving integrals of Legendre functions and Fourier series in complex form (see, for instance, Bowman, Senior, and Uslenghi, 1987, and §14.2 in Joseph et al., 2007). The components of $\mathbf{u}$ and $\mathbf{D}$ in spherical coordinates are found from standard expressions for a Newtonian fluid and the definition of the velocity potential in (5.9) and (5.10). Then, after carrying out the integrals in (5.36), this expression reduces to (Appendix F)

$$\begin{aligned}-\left(\sigma A e^{-\sigma t}+\bar{\sigma}\bar{A}e^{-\bar{\sigma}t}\right) = \frac{\gamma}{\rho a^3}\left(\frac{A}{\sigma}e^{-\sigma t}+\frac{\bar{A}}{\bar{\sigma}}e^{-\bar{\sigma}t}\right)(\ell+2)\ell(\ell-1)\\ -\frac{2\nu}{a^2}\left(Ae^{-\sigma t}+\bar{A}e^{-\bar{\sigma}t}\right)(2\ell+1)(\ell-1),\end{aligned} \tag{5.37}$$

dropping the subscript ℓ. This has the form,

$$\left[-\sigma+\frac{2\nu}{a^2}(2\ell+1)(\ell-1)-\frac{\gamma}{\rho a^3\sigma}(\ell+2)\ell(\ell-1)\right]Ae^{-\sigma t}+\text{c.c.}=0. \tag{5.38}$$

Therefore, the dissipation approximation gives rise to the dispersion relation

$$\sigma^2-\frac{2\nu}{a^2}(2\ell+1)(\ell-1)\sigma+\frac{\gamma}{\rho a^3}(\ell+2)\ell(\ell-1)=0. \tag{5.39}$$

In dimensionless form, this expression becomes,

$$\hat{\sigma}^2-\frac{2}{\sqrt{J}}(2\ell+1)(\ell-1)\hat{\sigma}+(\ell+2)\ell(\ell-1)=0. \tag{5.40}$$

where the dimensionless parameter $\hat{\sigma}$ and J have been defined in (5.18) and (5.20), respectively. The eigenvalues are

$$\hat{\sigma}=\frac{(2\ell+1)(\ell-1)}{\sqrt{J}}\pm\sqrt{\left[\frac{(2\ell+1)(\ell-1)}{\sqrt{J}}\right]^2-(\ell+2)\ell(\ell-1)}, \tag{5.41}$$

which has two different real roots or a complex-conjugate pair of roots. For $\mathrm{Im}(\hat{\sigma})=0$, the decay rate for monotonically decaying waves is obtained. In the case of de-

caying oscillations ($\mathrm{Im}(\hat{\sigma}) \neq 0$), the decay rate $(2\ell+1)(\ell-1)/\sqrt{J}$ was obtained by Lamb (1932) in §355 through the dissipation method. In the present calculations, the relation (5.41) also gives rise to viscous effects in the frequency of the oscillations, which determine the crossover from the oscillatory-wave regime to the monotonically-decaying-wave regime. Such effects were not predicted by Lamb's dissipation method. Hence, no crossover from oscillatory waves to monotonically decaying ones can be obtained from his calculation. Expression (5.41) can be compared with (5.23) from VPF and (5.24) from IPF.

As $\sqrt{J} \to 0$, (5.41) produces two real roots for the decay rate; the following gives the lowest value for the aperiodic motion,

$$\hat{\sigma} = \hat{\sigma}_D^{*2}\sqrt{J}\frac{1}{2(2\ell+1)(\ell-1)}. \tag{5.42}$$

In the case of $\sqrt{J} \to \infty$ the eigenvalues are complex,

$$\hat{\sigma} = \frac{(2\ell+1)(\ell-1)}{\sqrt{J}} \pm \mathrm{i}\hat{\sigma}_{\mathrm{D}}^{*}. \tag{5.43}$$

Hence, one finds oscillatory decaying waves. The definition of $\hat{\sigma}_D^*$ is given in (5.24).

Prosperetti (1977) studied the initial value problem posed by small departures from the spherical shape of a viscous drop surrounded by another viscous liquid. In the case of a drop in a vacuum, he found (5.41) in the limit of time $t \to 0$ if an irrotational initial condition is assumed. We remark that (5.41) was obtained here by a different method.

5.3.2 Dissipation approximation for a spherical bubble

Following the same steps as those described for the drop, the dispersion relation for a spherical bubble immersed in liquid can also be obtained from the dissipation method. In this case, the eigenvalues are

$$\hat{\sigma} = \frac{(2\ell+1)(\ell+2)}{\sqrt{J}} \pm \sqrt{\left[\frac{(2\ell+1)(\ell+2)}{\sqrt{J}}\right]^2 - (\ell+2)(\ell+1)(\ell-1)}, \tag{5.44}$$

with J determined from the liquid properties. In the case of decaying oscillations, the decay rate given in (5.44) as $(2\ell+1)(\ell+2)/\sqrt{J}$ is the same as the rate computed by Lamb (1932) using the dissipation method without the explicit inclusion of the surface tension effects in the formulation.

Expression (5.44) yields the following result as $\sqrt{J} \to 0$ ($\nu \to \infty$, say) for the

bubble,

$$\hat{\sigma} = \hat{\sigma}_B^{*2}\sqrt{J}\frac{1}{2(2\ell+1)(\ell+2)}, \tag{5.45}$$

and thus monotonically decaying waves take place with $\hat{\sigma}_B^*$ defined in (5.28).

In the case of $\sqrt{J} \to \infty$ ($\nu \to 0$, say), the dissipation method predicts oscillatory decaying waves with eigenvalues

$$\hat{\sigma} = \frac{(2\ell+1)(\ell+2)}{\sqrt{J}} \pm \mathrm{i}\hat{\sigma}_{\mathrm{B}}^*. \tag{5.46}$$

5.4 Exact solution of the linearized fully viscous problem

In this section we summarize the results from the solution of the linearized equations of motion, dropping the assumption of irrotational flow, for a drop immersed in a vacuum and a bubble of negligible density and viscosity embedded in a viscous liquid. The result for the drop was presented by Reid (1960) whereas the solution for the bubble can be obtained following a similar path. In both cases, the dispersion relation coincides with the corresponding limiting results presented by Miller and Scriven (1968) and Prosperetti (1980a), who posed and solved the most general two-fluid problem. The predictions from these dispersion relations are compared with results from the irrotational approximations in §5.5.

The linearized Navier–Stokes equations govern this problem

$$\rho\frac{\partial \mathbf{u}}{\partial t} = -\nabla p + \mu\nabla^2\mathbf{u}, \tag{5.47}$$

with $\nabla\cdot\mathbf{u} = 0$ in $0 \leqslant r < a$ for the drop and in $a < r < \infty$ for the bubble. Continuity of shear stresses at $r = a$ is satisfied.

5.4.1 Exact solution for a spherical drop in a vacuum

Reid (1960) obtained the dispersion relation for the eigenvalue σ

$$\alpha^4 = 2q^2\,(\ell-1)\left[\ell + (\ell+1)\,\frac{q - 2\ell Q^J_{\ell+1/2}}{q - 2Q^J_{\ell+1/2}}\right] - q^4, \tag{5.48}$$

with

$$Q^J_{\ell+1/2}(q) = J_{\ell+3/2}(q)/J_{\ell+1/2}(q), \tag{5.49a}$$

$$\alpha^2 = \frac{\sigma_D^* a^2}{\nu} = \hat{\sigma}_D^*\sqrt{J}, \tag{5.49b}$$

$$\frac{q^2}{\alpha^2} = \frac{\sigma}{\sigma_D^*} = \frac{\hat{\sigma}}{\hat{\sigma}_D^*}, \tag{5.49c}$$

where σ_D^* is the frequency of oscillations from inviscid potential flow (IPF) given in (5.24). A thorough discussion on the solution of (5.48) is presented by Chandrasekhar (1959, 1961) when q is real. Considering ℓ fixed, the right-hand side of (5.48) is a function of q, $\Phi(q)$ say. On the axis of positive q, there is an infinite number of intervals where $\Phi(q)$ is positive. The first of these intervals, which contains $q = 0$, encloses a maximum ($\alpha^2_{\max}$). For $\alpha^2 < \alpha^2_{\max}$ this first interval gives two real roots of (5.48), which determine the slowest decay rate. Since $\alpha^2 = \hat{\sigma}_D^* \sqrt{J}$, for every mode ℓ, the magnitude of J defines the roots. In the other intervals, one also has $0 \leqslant \Phi(q) < \infty$. When $\alpha^2 > \alpha^2_{\max}$, (5.48) admits complex-conjugate eigenvalues with positive real parts which give the lowest decay rate; these waves oscillate as they decay.

As $J \to 0$, the decay rate from the exact solution for monotonically decaying waves on a drop surrounded by gas behaves as

$$\hat{\sigma} = \hat{\sigma}_D^{*2} \sqrt{J} \frac{2\ell + 1}{2(\ell - 1)(2\ell^2 + 4\ell + 3)}, \tag{5.50}$$

given by Miller and Scriven (1968). From the exact solution (5.48), the trend of the complex eigenvalue $\hat{\sigma}$ for the drop as $\sqrt{J} \to \infty$ was presented by Chandrasekhar (1959, 1961) and Miller and Scriven (1968) and follows the same result (5.43) from the dissipation method.

5.4.2 Exact solution for a spherical bubble

A procedure similar to the one applied to the drop gives rise to the following dispersion relation for the bubble

$$\alpha^4 = (\ell + 2)\, q^2 \frac{(2\ell + 1)\, q^2 - 2\,(\ell + 1)\,(\ell - 1)\left[(2\ell + 1) - q Q^H_{\ell+1/2}\right]}{(2\ell + 1) + q^2/2 - q Q^H_{\ell+1/2}} - q^4, \tag{5.51}$$

with

$$Q^H_{\ell+1/2} = H^{(1)}_{\ell+3/2}(q) / H^{(1)}_{\ell+1/2}(q), \tag{5.52}$$

and α^2 and q given in (5.49). In these relations, σ_B^* from IPF given in (5.28) for a bubble is used instead of σ_D^*.

Expression (5.51) is the same dispersion relation found by Miller and Scriven (1968). This dispersion relation only admits complex roots as a consequence of the character of the Hankel functions (Prosperetti, 1980a). Therefore, for a bubble, only

oscillatory decaying waves are predicted. For a drop, we recall that real eigenvalues can be found.

For a gas bubble in a viscous liquid, the decay rate σ follows, as $\sqrt{J} \to 0$,

$$\hat{\sigma} = \hat{\sigma}_B^{*2}\sqrt{J}\frac{2\ell+1}{2(2\ell^2+1)(\ell+2)}. \tag{5.53}$$

For $\sqrt{J} \to \infty$ (5.51) yields the same expression (5.46) obtained with the dissipation method. These results for small and large J were presented by Miller and Scriven (1968).

5.5 Results and discussion

In this section, the comparison of the results for the decay rate and frequency of the waves according to viscous potential flow (VPF) and the dissipation method (DM) with the exact solutions of the fully viscous linear problem are presented for a drop and a bubble. A wide interval is selected for the mode number ℓ starting with $\ell = 2$. The smallest value of $\ell = 2$ is chosen since lower values yield compressive or expansive motions of the drop interface which are not compatible with the incompressibility assumption or a non-physical static disturbed interface. For higher values of ℓ, the exact fully viscous solution for the drop predicts oscillations that decay faster (Miller and Scriven, 1968). The same lowest value of $\ell = 2$ is selected for the bubble case.

Figure 5.1(a) shows the critical Reynolds number J_c as a function of ℓ for a drop. The number J_c is defined as the value of J at a given ℓ for which transition from monotonically decaying waves (aperiodic waves) to decaying oscillations occurs. For $J \leqslant J_c$, the eigenvalues $\hat{\sigma}$ are real and monotonically decaying waves take place, whereas for $J > J_c$ the eigenvalues are complex and the waves decay through oscillations. For systems with $J < 0.5$, the viscous theories predict monotonically decaying waves for a drop and for all modes. Figure 5.1(b) presents the trends of J_c with ℓ for VPF and DM for a bubble. Recall that the exact solution always predicts decaying oscillations (i.e. complex eigenvalues) in the bubble case. Therefore, the exact solution does not give rise to a critical J. If DM predicts oscillatory decaying waves, then VPF gives the same outcome. If VPF predicts monotonically decaying waves, then the same behavior is obtained from DM. The viscous irrotational theories give rise to monotonically decaying waves for a bubble with $J < 10$ and for all modes.

For a drop, the decay rate and wave frequency as a function of J are presented

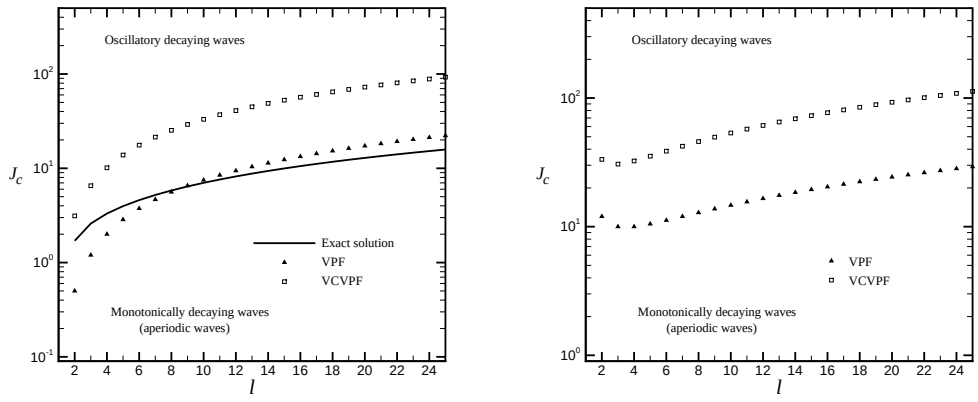

(a) drop (b) bubble

Figure 5.1: Critical Reynolds number J_c as a function of the mode number ℓ for a *drop* and a *bubble*.

in Figures 5.2(a) and (b), respectively, for $\ell = 2$ as predicted by VPF, DM and the exact solution. The wave frequency given by IPF is also included for comparison. For large J, DM and the exact solution show excellent agreement (see §5.4.1), whereas VPF is off the mark as anticipated from the comparison of (5.26) with (5.43). The wave frequencies from the three viscous theories tend to the inviscid solution for large J. As J decreases (below $J = 10$, say), transition from the oscillatory-wave regime to the monotonically-decaying-wave regime occurs. In the point of transition, the frequency becomes identically zero and the curve of the decay rate bifurcates yielding two real and different roots. In Figure 5.2, the eigenvalue $\hat{\sigma}_1$, representing the least damped mode of decay, is plotted. For small J, DM predicts the decay rate with a discrepancy of, nearly, 20% with respect to the exact solution. Figures 5.2(a) and (b) reveal that the viscous irrotational theories qualitatively follow the trend described by the exact solution and are able to predict an oscillatory-to-aperiodic-wave crossover J_c by considering viscous effects in the frequency.

For a bubble, the decay rate and wave frequency are presented in Figures 5.2(c) and (d), respectively for $\ell = 2$. Notice that the decay rate follows somewhat similar trends as those described for the drop. For small J, VPF shows the lowest discrepancy, of nearly 40%, with the exact decay rate. Figure 5.2(d) shows that the exact solution does not predict transition to the monotonically-decaying-wave regime, but the wave frequency tends smoothly to zero as J decreases (the viscosity increases, say). On the other hand, VPF and DM do render a crossover J_c for which transition

to monotonically decaying waves occurs.

For large values of J, if one of the fluids has negligible density and viscosity, a thin boundary layer results (Miller and Scriven, 1968). Thus, an irrotational velocity field works as a good approximation. In terms of the dissipation approximation, such a thin boundary layer yields a negligible contribution to the total viscous dissipation, which is thus determined by the irrotational flow over the interior of the fluid domain (see, for instance, Landau and Lifshitz, 1959, §25). At the free surface, however, the zero-shear-stress condition is enforced in the formulation. Indeed, expression (5.43), obtained from (5.41) as a first order approximation in the dimensionless viscosity $\epsilon \equiv J^{-1/2}$, and the results in §5.4.1, indicate that DM and the exact solution agree to first order in ϵ. This can also be said for the bubble. By contrast, as ϵ increases (e.g., the liquid viscosity increases), the boundary layer becomes thicker and the performance of the dissipation method deteriorates as the difference for the higher order terms in ϵ between DM and the exact solution becomes significant. A non-negligible boundary layer flow contributes substantially to the rate of viscous dissipation, hence the decay rate increases. However, the increasing trend of the decay rate is reversed as J continues decreasing because the motion for small J, as discussed by Prosperetti (1980a), is restrained in such a drastic way that the energy dissipation per unit time, and thus the decay rate, has to decrease as J goes to zero. In the case of the drop, the oscillatory-to-aperiodic-wave crossover sharply represents this change in the trend of the decay rate.

For a bubble (Figure 5.2(c)), oscillatory decaying waves are always predicted by the exact linearized theory yet the smooth region where the decay-rate graph reaches a maximum as a function of J suggests a transition in the structure of the flow that follows on the lines explained above.

Computations carried out for several higher modes ($\ell = 3$, 4 and 10) have shown that the features commented for the fundamental mode are also observed for these other modes (not plotted here). The general trend is that the decay rate increases with increasing ℓ. The analysis of the predictions from the exact solution indicates that the change-over from oscillatory waves to monotonically decaying waves takes place for a larger critical J as ℓ increases for a drop. Even though no transition to over-damped aperiodic waves occur for the bubble, the interval of J for which very low frequencies are obtained becomes wider as ℓ increases. These results show that viscosity damps the motion more effectively for shorter waves. The viscous irrotational theories follow these tendencies.

For a drop, when $J << 1$ in the monotonically-decaying-wave regime, VPF shows good agreement with the exact solution for short waves or large ℓ (not plotted).

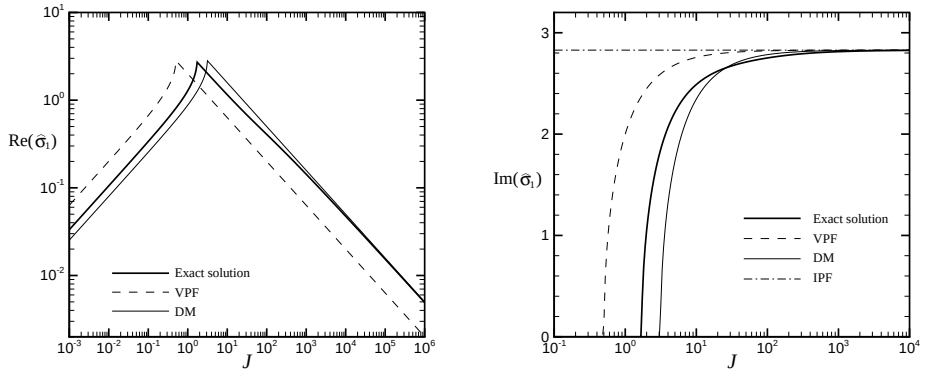

(a) Decay rate - *drop* (b) Wave frequency - *drop*

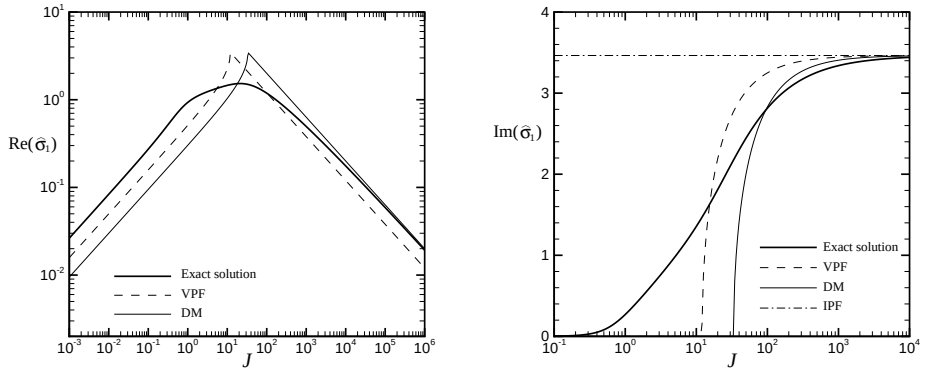

(c) Decay rate - *bubble* (d) Wave frequency - *bubble*

Figure 5.2: Decay rate $\mathrm{Re}(\hat{\sigma}_1)$ and wave frequency $\mathrm{Im}(\hat{\sigma}_1)$ for the fundamental mode $\ell = 2$ as function of the Reynolds number J for a *drop* and a *bubble* from the exact solution, VPF, DM and IPF. The decay rate predicted by IPF is identically zero for all ℓ.

This tendency can be anticipated from (5.25) and (5.50). The same response is observed for a bubble. In the case of large mode number ℓ, the dynamics of the short waves may be modeled as small disturbances about a horizontal, plane free surface. This problem was solved by Lamb (1932) §349. For large viscosity (i.e. small $\sqrt{J}$), he argues that the least damped mode "represents a slow creeping of the fluid towards a state of equilibrium with a horizontal surface". From Lamb's analysis, it is clear that this flow is nearly irrotational, thus explaining the good agreement between VPF and the exact solution. Viscous potential flow is restricted to "small" vorticity, but it is not restricted to "small" viscosity (Joseph and Wang, 2004).

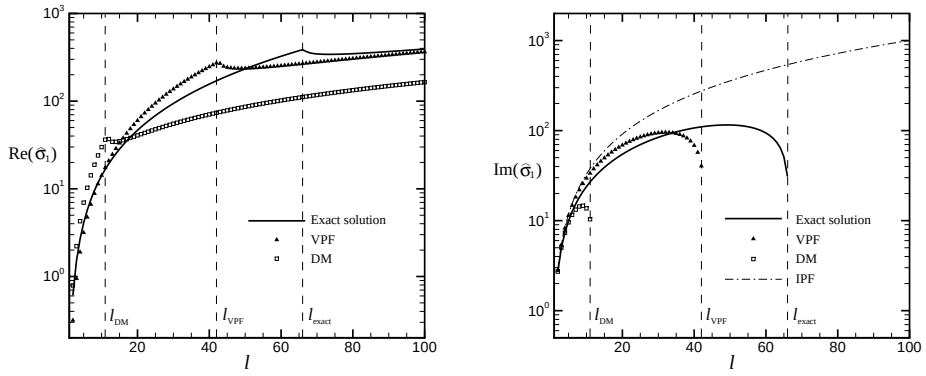

(a) Decay rate (b) Wave frequency

Figure 5.3: Decay rate $\mathrm{Re}(\hat{\sigma}_1)$ and wave frequency $\mathrm{Im}(\hat{\sigma}_1)$ for $J = 40$ versus the mode number ℓ for a *drop*. In this case, the eigenvalues are a pair of complex conjugates for the interval of $\ell \leq \ell_{\mathrm{c}}$ and they are real and different for $\ell > \ell_{\mathrm{c}}$. For the latter case, the lowest decay rate is plotted in (a). The symbol ℓ_{c} stands for the highest value of ℓ for which a non-zero imaginary part is obtained, i.e. decaying oscillations occur. For instance, $\ell_{\mathrm{c}} = \ell_{\mathrm{exact}}$ from the exact solution.

As J increases, waves of certain length becomes oscillatory waves. For instance, in the case of $J = 40$ shown in Figure 5.3 , the crossover values of ℓ according to every viscous theory enters into the analysis. In this case, oscillatory waves exist according to the viscous theories for $\ell < \ell_{\mathrm{DM}}$, whereas these theories agree and predict monotonically decaying waves for $\ell > \ell_{\mathrm{exact}}$. For large J, the crossover ℓ_c obtained from each viscous theory may also be large (e.g., $\ell_c > 100$ for $J = 10^6$), since viscous effects are weak and short waves oscillate. In the regime of decaying oscillatory waves, $\ell \leqslant \ell_c$, there exists a region of good agreement between DM and the exact solution that extends to higher values of $\ell \geqslant 2$, whereas VPF shows poor agreement in comparison. At least for values of $\ell << \ell_{\mathrm{exact}}$ in the neighborhood of $\ell = 2$ and large J, DM provides the best approximation of the decay rate for the drop or the bubble.

5.6 Concluding remarks

The results obtained from the viscous purely irrotational approximations for the decay rate and frequency of the oscillations for a drop and a bubble follow the trends described by the exact solution, showing qualitative agreement with most of the features depicted by this theory. The damping role of viscosity in the dynamics of the waves is adequately described by the viscous irrotational theories through

the modeling of the decay rate and frequency of the oscillations, in contrast to the classical inviscid theory, which predicts undamped oscillations. Quantitative agreement is also demonstrated for certain intervals of modes and dimensionless viscosity. Some notable features from the comparison carried out in this study for the drop and the bubble are:

- In the case of short waves (i.e. large mode number ℓ) and large viscosity, VPF gives a very good approximation of the decay rate for both the drop and the bubble. On the other hand, the dissipation method gives rise to values of the decay rate in closer agreement with the exact solution within a certain ℓ interval, including $\ell = 2$, in the oscillatory-wave regime (i.e. long waves) for large values of the Reynolds number J or "small" viscosity. This trend resembles the tendencies obtained for free gravity waves perturbing a plane interface by Wang and Joseph (2006). Nonetheless, a notable difference between their results and those given here is that surface tension has a stronger regularizing effect on short waves than gravity does.

- VPF approximates the variation of frequency with the mode number with the lowest discrepancy for a fixed J. In particular, the transition from oscillatory to monotonically decaying waves predicted by this irrotational theory occurs at a higher critical value of ℓ than the threshold given by the dissipation method.

- The viscous irrotational approximations predict effects of viscosity on the frequency of the oscillations. For every mode, there exists a J for which transition from oscillatory decaying waves to monotonically decaying waves occurs for either the drop or the bubble. Whereas a transitional value of J is predicted by the exact solution for a drop, only oscillations are found by this theory for a bubble. In this case, very small frequencies are obtained as $\sqrt{J} \to 0$ (e.g., $\nu \to \infty$) from the exact solution.

- The viscous irrotational theories do not give rise to a continuos spectrum of eigenvalues for the bubble as has been found for the exact solution by Prosperetti (1980a).

Chapter 6

Stress-induced cavitation for the streaming motion of a viscous liquid past a sphere*

The theory of stress induced cavitation is a revision of the classical maximum pressure criterion. While the latter postulates that a liquid will cavitate where the pressure becomes lower than a cavitation threshold, the former establishes that a cavity will open where the maximum tensile stress exceeds the breaking strength of the liquid. These theories are applied here to the problem of cavitation of a viscous liquid in the streaming flow past a stationary sphere. This study considers single phase flow and the objective is to find the region of the fluid domain where the risk of cavitation is the greatest. The flow field is obtained from three different methods, namely, the numerical solution of the incompressible Navier–Stokes equations, the analytical solution with the assumption of irrotational motion of a viscous fluid and, in the case of inertialess flow, with the Stokes flow approximation.

6.1 Introduction

Winer and Bair (1987) and, independently, Joseph (1995, 1998) proposed the maximum tension criterion for cavitation which states that the flowing liquid will cavitate if the maximum tensile stress exceeds a critical value. Since this maximum stress is associated with a principal direction, this criterion is not isotropic. Winer and Bair (1987) introduced the idea that stress-induced cavitation may enter into the appar-

*Reprinted with permission from Padrino, J. C.; Joseph, D. D.: Funada, T.; Wang, J.; Sirignano, W.A. *J. Fluid Mech.*, Vol. 578, Issue 8, 381-411, 2007.

ent shear thinning of liquid lubricants. They remarked that shear thinning may be the result of a yielding or cavitation event that takes place at a critical value of the liquid's tensile stress. They further note that "for some high shear rate viscosity data at atmospheric pressure the principal normal stress may approach quite low values relative to one atmosphere suggesting the possibility of cavitation or fracture of the material resulting in a reduced shear stress". In a private communication, Prof. Bair noted that "...There was little interest from tribologists, so we dropped it until recently. In the original work we were able to see to the voids by eye using a clear plastic outer cylinder...".

The maximum tension criterion is embedded as one possibility for liquid failure presented by analysis of the state of stress in Joseph's theory. A comparison of these two theories can be found in the study of cavitation in creeping shear flows by Kottke, Bair and Winer (2005). Numerous examples of cavitation in shear flow by other researchers are discussed by Kottke *et al.* (2005). Examples of stress-induced cavitation in extensional flow and shear flow were discussed by Joseph (1998). Pereira *et al.* (2001) did a theoretical study of cavitation in a journal bearing with axial throughput. They found that the inception of cavitation in a moving fluid is always stress induced. Funada *et al.* (2006) carried out an analysis of stress induced cavitation in a two-dimensional aperture flow modeling atomizers in which cavitation is well documented. The aperture flow was expressed using a complex potential and the stress calculated using viscous potential flow. They found that the viscous stress was huge near the tips of the aperture, thus cavitation could be induced. The region at risk to cavitation is larger, for a fixed cavitation number, when the Reynolds number is smaller.

In this chapter, we study stress-induced cavitation in the streaming motion past a sphere. This kind of study differs from the typical one based solely upon the local pressure; it is necessary to compute the field of principal stresses as well as the pressure. This program is carried, without approximation, by numerical simulation of the Navier–Stokes equations. We also analyze the same problem for two cases in which simple explicit formulas for cavitation inception may be derived. The first case, Stokes flow, is an asymptotic limit in which inertia – the Reynolds number– is not in play. In the general case, in which inertia is important, the criterion for cavitation inception is a relation between the cavitation number and the Reynolds number; the region at risk to cavitation increases when the cavitation number increases and the Reynolds number decreases. This dependence is shown explicitly by the analysis based on potential flow of a viscous fluid (VPF) presented in §6.5 and by the numerical simulation of the Navier–Stokes equation presented in §6.6.

6.2 Theory of stress-induced cavitation

The stress in an incompressible Newtonian fluid is given by

$$\mathbf{T} = -p\mathbf{1} + 2\mu\mathbf{D}\left[\mathbf{u}\right], \tag{6.1}$$

where $\mathbf{D}\left[\mathbf{u}\right]$ is the symmetric part of the velocity gradient, $\mathbf{u}$ is the velocity field and $\mathrm{tr}\mathbf{D}\left[\mathbf{u}\right] = 0$, such that

$$\mathrm{tr}\mathbf{T} = T_{11} + T_{22} + T_{33} = -3p. \tag{6.2}$$

We define the stress at the cavitation threshold as p_c. It is positive when compressive and negative when tensile. Classically, the vapor pressure is taken as the threshold stress; however, in the next section, we discuss examples where different values, including tensile values, should be used for the cavitation threshold.

In the pressure criterion, the viscous part of the stress tensor is not considered and the liquid will cavitate when

$$-p + p_\mathrm{c} > 0. \tag{6.3}$$

The pressure criterion assumes that cavitation inception is determined by the average stress, called the pressure. The fluid cannot average its stresses; it sees only principal stresses and when the actual state of stress is considered there is at least one stress which is more compressive and another which is more tensile than the average stress. The most conservative criterion is the one which requires that the most compressive stress is larger than the cavitation threshold; suppose T_{22} is the most compressive and T_{11} is the most tensile (or least compressive) stress, then if

$$T_{22} + p_\mathrm{c} > 0 \tag{6.4}$$

for cavitation, it will surely be true that

$$-p + p_\mathrm{c} > 0 \quad \text{and} \quad T_{11} + p_\mathrm{c} > 0. \tag{6.5}$$

The maximum tension theory, which perhaps embodies the statement that liquids which are not specially prepared will cavitate when they are subject to tension, can be expressed by the condition that supposing T_{11} to be the maximum of the three principal stresses,

$$T_{11} + p_\mathrm{c} > 0. \tag{6.6}$$

The cavitation number K compares the cavitation threshold p_c with a typical pressure; here in our sphere problem, with the pressure p_∞ at infinity. We define

$$K = \frac{p_\infty - p_c}{N_R} \tag{6.7}$$

where $N_R = \mu U/L$ for Stokes flow and $N_R = \rho U^2/2$ when inertia acts; L is a characteristic length scale. Later, the analysis will show that the stress difference between the free-stream pressure and the cavitation threshold $p_\infty - p_c$ is the critical value rather than the cavitation threshold by itself.

The maximum tension criterion (6.6) has recently been studied in a numerical simulation of bubble growth in Newtonian and viscoelastic filaments undergoing stretching by Foteinopoulou et al. (2004). They base their analysis on the Navier–Stokes equations for Newtonian fluids and the Phan-Thien/Tanner model for viscoelastic fluids. They compute the principal stresses and evaluate the cavitation threshold for the maximum tension criterion (6.6), the pressure theory (6.3) and the minimum principal theory (6.4). They find that the capillary number at inception is smallest for (6.6). As remarked by Kottke et al. (2005), the cavitation threshold p_c could be negative or positive. In the case of $p_c < 0$, the liquid shows tensile strength; for $p_c = 0$, a cavity will open if the maximum principal stress becomes positive (i.e., tensile), and, if $p_c > 0$, the cavitation threshold is given by a positive pressure (i.e., compressive stress). The latter case is typified by the pressure theory of cavitation determined by the local pressure dropping below the vapor pressure.

To each principal stress there corresponds a principal direction, which plays a role in the physics of cavity inception. Joseph (1998) asserts that "if a cavitation bubble opens up, it will open in the direction of maximum tension. Since this tension is found in the particular coordinate system in which the stress is diagonal, the opening direction is in the direction of maximum extension, even if the motion is a pure shear. It may open initially as an ellipsoid before flow vorticity rotates the major axis of ellipsoid away from the principal tension axis of stress, or it may open abruptly into a "slit" vacuum cavity perpendicular to the tension axis before vapour fills the cavity as in the experiments of Kuhl et al. (1994)". These ideas are illustrated in cartoons showing the orientation of the principal directions on the surface of the sphere for each approach considered in this study.

Consider the expression for the stress tensor for a Newtonian fluid given in (6.1). Adding the diagonal tensor $p_c\mathbf{1}$ to both sides and decomposing $p = p_\infty + p^*$ yields

$$\mathbf{T} + p_c\mathbf{1} = -(p_\infty - p_c)\,\mathbf{1} - p^*\mathbf{1} + 2\mu\mathbf{D}. \tag{6.8}$$

Dividing through by the normalizing factor N_R, (6.8) becomes

$$\frac{\mathbf{T}+p_{\mathrm{c}}\mathbf{1}}{N_R}=-\left(K+\frac{p^*}{N_R}\right)\mathbf{1}+\frac{2\mu}{N_R}\mathbf{D}. \tag{6.9}$$

The strain–rate tensor can be readily diagonalized. Thus the principal stresses and directions can be determined. Suppose now that $K=K_{\mathrm{c}}$ at the marginal state separating cavitation from no cavitation. For shortness, let us call K_{c} the incipient cavitation number. This marginal state is defined by an equality in one of the three criteria (6.3), (6.4) or (6.6). For the maximum tension theory $K=K_{\mathrm{c}}$ when $T_{11}+p_{\mathrm{c}}=0$. In particular, for the maximum principal stress T_{11}, (6.9) yields

$$\left(T_{11}+p_{\mathrm{c}}\right)/N_R=-(K+p^*/N_R)+2\mu D_{11}/N_R, \tag{6.10}$$

where D_{11} denotes the maximum principal rate of strain. Then, $K_{\mathrm{c}}=\left(-p^*+2\mu D_{11}\right)/N_R$ is, in general, a scalar function of the position in the fluid domain. For a positive cavitation number, consider $K=K_{\mathrm{c}}+K^*$ such that $\left(T_{11}+p_{\mathrm{c}}\right)/N_R=-K^*$. It is thus clear from (6.10) that

$$T_{11}+p_{\mathrm{c}}<0 \text{ when } K>K_{\mathrm{c}}, \tag{6.11}$$

and

$$T_{11}+p_{\mathrm{c}}>0 \text{ when } K<K_{\mathrm{c}}. \tag{6.12}$$

The latter condition implies that the liquid is at the most risk to cavitation in regions where $K<K_{\mathrm{c}}$. For instance, for a fixed cavitation number K, no cavity will open if $K>K_{\mathrm{c,max}}$, the maximum value that K_{c} takes in the entire fluid domain. On the other hand, the cavitation number K based on the actual hydrodynamics, may vary in the fluid domain, since the cavitation threshold p_{c} may also change with position. For example, Singhal et al. (2002) included in their cavitation model the effect of the local turbulence pressure fluctuations in the phase-change threshold pressure.

6.3 Cavitation threshold

Cavitation can be defined as the formation, expansion and collapse of a cavity in a liquid. In general, the "formation" of a cavity implies both the appearance of a new void or the growth of a preexisting nucleus beyond a critical size large enough to be observed with the unaided eye (Young, 1989). The idea of the opening of a cavity in

the liquid continuum brings into consideration the concept of liquid tensile strength, which is a material property. The pressure criterion for cavitation states that the liquid cavitates when the local pressure reaches the vapor pressure somewhere in the domain. Knapp, Daily, and Hammit (1970) discusses that, although the inception of a cavity has been observed in experiments when local pressure is near the vapor pressure, deviations of various degrees have been reported for different liquids such that the results do not agree with the vapor pressure criterion. Knapp et al. define the vapor pressure as "the equilibrium pressure, at a specified temperature, of the liquid's vapor which is in contact with an *existing* free surface." They argue that the stress required to rupture the continuum in a homogeneous liquid is determined by the tensile strength, not by the vapour pressure. The literature on the tensile strength of liquids is vast and a good account of experimental results is given in the book by Knapp et al. (1970) for various liquids. In particular for water, values ranging from 13 to 200 atm are listed. Briggs (1950) reports inception of cavities in water induced by centrifugal force for pressures between vapor presssure and -300 atm (tension). Recently, Kottke, Bair, and Winer (2003) measured the tensile strength of nine liquids, including water, lubricant and polymeric liquids. Theoretical estimates of the tensile strength of water render large negative values in the interval -500 atm to -10,000 atm, which, however, have never been reported from experiments (Strassberg, 1959). Both observed phenomena, the wide scatter of the experimental results and the inception of cavitation at pressures much higher than the theoretical tensile strength reported in the literature indicate the existence of weak spots in the fluid that allows breaking of the continuum. Plesset (1969) comments that bubbles can grow to macroscopic dimensions starting from voids of size already beyond the molecular level under tensile stresses much lower than the theoretical values predicted for pure liquids.

Fisher (1948) reasons that, in a similar manner as very greatly subcooled liquids (such as glass) may fail by the nucleation and growth of a crack, a fluid may fail under tension by the growth of a cavity starting from very small holes. By applying methods of nucleation theory, Fisher predicts fracture tensions for several liquids with values, however, one order of magnitude higher than the experimental evidence. Some mechanism is required to stabilize preexisting nuclei in the liquid. For a very small bubble suspended in the liquid, the pressure inside the bubble is much higher than the pressure in the surrounded liquid because of surface–tension forces. This pressure difference diffuses the gas out of the gas void until it vanishes. On the other hand, bubbles not so small will rise and escape through the surface. Harvey and collaborators (1944a) introduced the idea of stabilized gas pockets attached to

submicroscopic and hydrophobic crevices in the surface of the liquid container or in solid impurities. The size of these nuclei can be of the order of microns. Harvey et al. (1944b) supported their theory with results from a series of experiments in which previously pressurized and unpressurized samples of water were boiled at atmospheric pressure such that the saturation pressure corresponding to the boiling temperature was taken as a rough measure of the effective tensile strength. Although quite broad scatter was observed in the results for the pressurized samples, they all boiled at temperatures much higher than the saturation temperature for atmospheric pressure, which was the boiling temperature showed by the unpressurized samples. Tensile strength of 16 atm were reported in some samples previously pressurized.

Harvey et al. (1947) performed a different type of experiments to investigate tensile strength of water by high-speed removal of a squared-ended glass rod from a narrow glass tube containing the liquid. Meticoulous cleaning of the glass surfaces and pressurization of the sample with the rod in position were done to remove hydrophobic spots and gas nuclei. In terms of the rod-withdrawal speed, they found that "if the rod surface contained glass nuclei, or was hydrophobic and free of gas nuclei, cavitation ocurred at the rear end when the velocity was less than 3 m/s, but if completely hydrophilic and free of gas nuclei, the velocity could be 37 m/s (...) without cavitation." Knapp (1958) confirmed Harvey's results performing experiments at a rather larger scale. Strasberg (1959) explored the onset of acoustically-induced cavitation in tap water finding that microscopic undissolved air cavities, which show a slow motion toward the surface, play an important role as nuclei. Apfel (1970) extended Harvey's theory to consider the condition required in a liquid for the inception of a vapor cavity from a solid impurity in the liquid. Crum (1970) examined the crevice model of Harvey et al. comparing its predictions with experimental evidence.

From the standpoint of hydrodynamic cavitation, stream nuclei carried by the moving liquid as particulates or microbubbles have a greater contribution as sites for onset of cavitation than the surface nuclei originated in crevices or cracks on the solid boundaries (Billet 1985 and references therein). Turbulence has been shown to influence cavitation inception and its effect has been accounted for in models through the phase-change threshold (Singhal et al. 2002).

The inception of a cavity can be an abrupt event, where the liquid must rupture, instead of a continuous one. Chen and Israelachvili (1991) and Kuhl et al. (1994) monitored the elastohydrodynamic deformations of two curve surfaces that move relative to each other separated by a thin–liquid film of nanoscopic dimensions. A low molecular weight polymer liquid of polybutadiene and bare mica smooth surfaces

having strong adhesion to the liquid were utilized in the tests. When the surfaces move normally with a slow separation speed they bulge outward becoming pointed at the location of the shortest surface separation. This shape indicates the existence of a tensile stress acting on the surface. If the separation speed is increased beyond a critical value, a vapor cavity opens in the liquid at the position of the shortest separation, reducing the tensile stress, while the pointed surfaces suddenly recover their original shape. Chen and Israelachvili (1991) also used surfactant–coated mica surfaces, which have weak adhesion to the liquid, resulting in cavity formation at the liquid–solid interface. Kuhl et al. (1994) considered lateral sliding of a curved surface over a mostly plane surface with a thin liquid film in between. Describing the shape of the sliding element, they observed that "the leading edge becomes more rounded and lifts off while the trailing edge becomes more pointed." For a sliding speed larger than some critical value, the pointed trailing edge snaps back, while a small cavity opens in the wake.

Cavitation inception has been observed in liquids undergoing shearing, suddenly changing the rhelogical response of the samples. Bair and Winer (1990) inferred cavitation inception by detecting yielding of a synthetic oil during rheological tests using a rotating concentric cylinder rheometer for a shear stress near the hydrostatic pressure (1.73 MPa). A similar phenomenon was noticed by Bair and Winer (1992) for polybutene in simple shear at low pressures (0.1 to 1 MPa) for a shear stress of 0.075 MPa in excess of the internal absolute pressure. This magnitude may represent the amount of tension that this liquid can resist without the opening of a cavity. Archer, Ternet, and Larson (1997) visualized the opening of bubbles within a sample of low–molecular–weight polysterene subjected to start-up of steady shearing flow. They noticed that bubbles seemed to appear near dust particles. As a consequence of cavitation, the shear stress abruptly drops after it reaches a maximum of 0.1 MPa. Kottke et al. (2005) observed the inception of cavities in polybutene undergoing shearing tests using a Couette viscometer. Cavities become visible when the measured shear stress matches the ambient pressure. According to their principal normal stress cavitation criterion (PNSCC), this result implies that the sample liquid is not able to withstand tension. They suggest that cavitation grows from preexisting nuclei stabilized in some cracks or crevices on the solid boundaries.

The previous survey has shown that the idea of minute gas and vapor pockets in the liquid acting as nucleation sites is plausible and generally accepted. Nevertheless, a precise definition of the cavitation threshold and a clear description of the wide gamut of factors that influence this critical value is yet to be accomplished. We use

the words "cavitation threshold" and "breaking strength" as synonymous with the threshold at which the liquid continuum will fracture. This threshold can vary from place to place in a sample. The threshold need not be a material parameter. In the case of heterogeneous nucleation, the cavitation threshold depends on the sample preparation, the density and nature of nucleation sites. In the case of homogeneous nucleation, the threshold may be taken as the vapor pressure. The vapor pressure is a thermodynamic quantity which is defined for uniform isotropic samples for which the stress tensor is isotropic; for static samples, bubble nucleation is a function of pressure and nothing else. In this work, the cavitation threshold, p_c, is not necessarily the vapor pressure; this value is regarded as given and is not a subject for study here. For liquid which cannot withstand tension, $p_c = 0$.

In §§6.4, 6.5 and 6.6 we discuss three parallel solutions approached using the maximum tension criterion, namely, Stokes flow, viscous potential flow and the numerical solution of the incompressible Navier–Stokes equations, which can be read in any order.

6.4 Cavitation of Stokes flow

The problem of heterogeneous nucleation of bubbles in the creeping flow of a viscous liquid sheared between parallel plates has been considered by Kottke, Bair, and Winer (2005). They find good agreement between experiments and cavitation based on the maximum tension criterion. These authors indicate:

> Liquid failure has been observed in low Reynolds number (Stokes) shear flows where reduction of the hydrodynamic pressure should not occur. Cavitation in Stokes flows has implications in lubrication, polymer processing, and rheological measurements. Such cavitation can be predicted by a principal normal stress cavitation criterion (PNSCC). We present results of a direct experimental test of the PNSCC. Imaging of the cavitation events suggests that the cavitation is gaseous and originates from preexisting nuclei. Crevice–stabilized gas nuclei are assumed, and numerical simulations are used to investigate the cavitation event for a Newtonian liquid. The inception of cavitation from a preexisting nucleus, the persistence of suitable nuclei, and the growth and deformation of shed bubbles are considered.

.

Ashmore, del Pino, and Mullin (2005) study the Stokesian fluid dynamics around a sphere free to move inside a rotary cylinder filled with viscous liquid, showing that

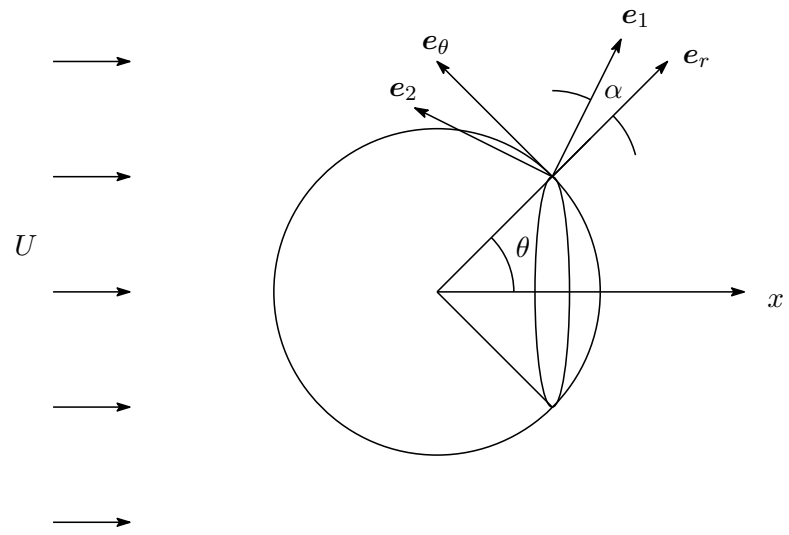

Figure 6.1: Streaming flow of a liquid past a sphere of radius a. The spherical-polar coordinates basis vectors that lie in the plane of motion are shown. The angle α puts the stresses into principal axes.

the inception of cavitation breaks the symmetry of the flow field, creating a net normal force that prevents contact between the sphere and the boundary. We analyze in this section stress-induced cavitation when the stream is creeping in the Stokes flow limit. A cartoon of the flow is given in figure 6.1 using spherical–polar coordinates, showing the angle α, which sets the stresses into principal directions. For this type of fluid motion, the principal strain–rates and stresses and their corresponding principal directions can be determined. The velocity and pressure fields for Stokes flow past a sphere are given by the expressions

$$u_r = U\left[1 - \frac{3}{2}\frac{a}{r} + \frac{1}{2}\frac{a^3}{r^3}\right]\cos\theta, \qquad u_\theta = -U\left[1 - \frac{3}{4}\frac{a}{r} - \frac{a^3}{4r^3}\right]\sin\theta, \tag{6.13}$$

$$p = p_\infty - \frac{3\mu a U}{2r^2}\cos\theta. \tag{6.14}$$

The components of the viscous stress tensor $2\mu\mathbf{D}[\mathbf{u}]$ with respect to the spherical polar reference frame of figure 6.1 are determined using (6.13) and the formulae

$$D_{rr} = \frac{\partial u_r}{\partial r}, \qquad D_{\theta\theta} = \left(\frac{1}{r}\frac{\partial u_\theta}{\partial\theta} + \frac{u_r}{r}\right),$$

$$D_{\varphi\varphi} = \left(\frac{u_r}{r} + \frac{u_\theta}{r}\cot\theta\right), \qquad D_{r\theta} = \frac{1}{2}\left[r\frac{\partial}{\partial r}\left(\frac{u_\theta}{r}\right) + \frac{1}{r}\frac{\partial u_r}{\partial\theta}\right]. \tag{6.15}$$

Thus, the viscous stress tensor $2\mu\mathbf{D}[\mathbf{u}]$ may be written in matrix form as

$$2\mu\begin{bmatrix} D_{rr} & D_{r\theta} & 0 \\ D_{r\theta} & D_{\theta\theta} & 0 \\ 0 & 0 & D_{\varphi\varphi} \end{bmatrix} = \\ = \frac{3}{2}\mu U\frac{a^3}{r^4}\begin{bmatrix} 2\left[\left(\frac{r}{a}\right)^2-1\right]\cos\theta & -\sin\theta & 0 \\ -\sin\theta & -\left[\left(\frac{r}{a}\right)^2-1\right]\cos\theta & 0 \\ 0 & 0 & -\left[\left(\frac{r}{a}\right)^2-1\right]\cos\theta \end{bmatrix}, \quad (6.16)$$

which is rotated by an angle α to obtain its diagonalized form

$$\frac{3}{2}\mu U\frac{a^3}{r^4}\begin{bmatrix} \frac{1}{2}\left[\left(\frac{r}{a}\right)^2-1\right]\cos\theta-\frac{\sin\theta}{\sin 2\alpha} & 0 & 0 \\ 0 & \frac{1}{2}\left[\left(\frac{r}{a}\right)^2-1\right]\cos\theta+\frac{\sin\theta}{\sin 2\alpha} & 0 \\ 0 & 0 & -\left[\left(\frac{r}{a}\right)^2-1\right]\cos\theta \end{bmatrix}. \quad (6.17)$$

The angle of rotation α is related to the polar angle θ by the expression

$$\cot 2\alpha = -\frac{3}{2}\left[\left(\frac{r}{a}\right)^2-1\right]\cot\theta \quad (6.18)$$

Expression (6.18) can be solved to find the rotation angle α ($-0.5 \leq \alpha/\pi \leq 0.5$) required to rotate the polar coordinates (r,θ) such that the direction defined by the unit vector $\mathbf{e}_\mathrm{r}$ coincides with the principal direction associated with the most tensile (or the least compressive) principal stress on the plane of motion. The orientation of the principal axes on the surface of the sphere $r = a$ in the plane of motion is illustrated in figure 6.2.

Expression (6.1) can be modified by adding $p_\mathrm{c}\mathbf{1}$ to both sides and substituting (6.14) for the pressure p and (6.17) for the viscous stress $2\mu\mathbf{D}$. Defining the cavitation number and the Reynolds number, respectively, as

$$K = \frac{p_\infty - p_\mathrm{c}}{\mu U/a}, \quad (6.19)$$

and

$$Re = \frac{\rho U a}{\mu}, \quad (6.20)$$

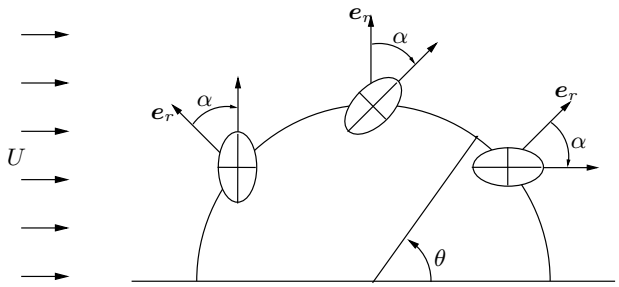

Figure 6.2: Schematic view of the orientation of the principal directions in the plane of motion from the Stokes flow analysis (6.18) on the surface of the sphere. In this case, $\alpha = -45^\circ$ for all θ. The major axis in the ellipse represents the maximum tensile stress. The angle α puts the direction defined by the unit outward normal vector $\mathbf{e}_\mathrm{r}$ into the principal direction of the maximum tensile stress.

the following expression results after arranging

$$\frac{\mathbf{T}+p_\mathrm{c}\mathbf{1}}{\frac{\mu U}{a}} = -\left[K-\frac{3}{2}\left(\frac{a}{r}\right)^2\cos\theta\right]\begin{bmatrix}1&0&0\\0&1&0\\0&0&1\end{bmatrix} + \frac{3}{2}\left(\frac{a}{r}\right)^4\begin{bmatrix}\frac{1}{2}\left[\left(\frac{r}{a}\right)^2-1\right]\cos\theta-\frac{\sin\theta}{\sin 2\alpha} & 0 & 0\\ 0 & \frac{1}{2}\left[\left(\frac{r}{a}\right)^2-1\right]\cos\theta+\frac{\sin\theta}{\sin 2\alpha} & 0\\ 0 & 0 & -\left[\left(\frac{r}{a}\right)^2-1\right]\cos\theta\end{bmatrix}. \quad (6.21)$$

Since the right hand side is diagonal, (6.21) gives the principal stresses. Not surprisingly, this expression is independent of the Reynolds number. For the Stokes flow solution given in (6.21), one can show that at any point the most tensile (least compressive) and most compressive (least tensile) principal stresses lie on the plane of motion. Suppose that for a point (r, θ) in the fluid domain, T_{11} is the maximum of the three principal stresses. Then, the maximum tension criterion for cavitation (6.6) can be applied to this fluid motion. Let K_c be the cavitation number in the marginal state determined by $T_{11} + p_\mathrm{c} = 0$, then (6.21) gives rise to a functional relation $K_\mathrm{c} = f(r, \theta)$, from which a contour plot with lines of constant K_c can be readily obtained.

For fluid motions in which inertia effects are dominant, it is customary to use the dynamic pressure, $\rho U^2/2$, as the normalization factor for pressure. For the purpose of analysis, one may wish to compare results from creeping flows with results from fluid motions with higher Reynolds numbers. In such a case, the following relations

can be useful,

$$\frac{p_\infty - p_\mathrm{c}}{\mu U/a} = \frac{Re}{2}\frac{p_\infty - p_\mathrm{c}}{\frac{1}{2}\rho U^2}, \tag{6.22}$$

for the cavitation number and,

$$\frac{\mathbf{T} + p_\mathrm{c}\mathbf{1}}{\mu U/a} = \frac{Re}{2}\frac{\mathbf{T} + p_\mathrm{c}\mathbf{1}}{\frac{1}{2}\rho U^2}, \tag{6.23}$$

for the stress tensor. Thus the quantities defined in terms of the viscous forces scale with their counterpart defined in terms of the dynamic pressure by a factor of $Re/2$ everywhere in the fluid domain.

Lines of constant K_c for the marginal state of cavitation according to (6.21) are presented in §6.7 and compared with solutions from direct numerical simulation and viscous potential flow for $Re = 0.01$ (see figure 6.9).

In particular, on the surface of the sphere, $r = a$, (6.21) reduces to

$$\begin{bmatrix} T_{11}+p_\mathrm{c} & 0 & 0 \\ 0 & T_{22}+p_\mathrm{c} & 0 \\ 0 & 0 & T_{33}+p_\mathrm{c} \end{bmatrix} / (\mu U/a) = -K \begin{bmatrix} 1 & 0 & 0 \\ 0 & 1 & 0 \\ 0 & 0 & 1 \end{bmatrix} + \frac{3}{2}\begin{bmatrix} \cos\theta + \sin\theta & 0 & 0 \\ 0 & \cos\theta - \sin\theta & 0 \\ 0 & 0 & \cos\theta \end{bmatrix}. \tag{6.24}$$

It is shown in Appendix G that the maximum of K under the condition $T_{11} + p_\mathrm{c} = 0$ occurs at $\theta = 45°$. Therefore, the position $r = a$, $\theta = 45°$ is the location most vulnerable to cavitation.

The principal axes representation of this tensor is achieved for $\alpha = -45°$, which satisfies (6.18) for $r = a$. Expression (6.24) can be used to form the cavitation criteria. The maximum tension is achieved at $\theta = 45°$. From the right-hand side of (6.24) it can be noticed that $T_{11} \geq T_{33} \geq T_{22}$ for the array shown in its left-hand side for all $0 \leq \theta \leq \pi$ since $\sin\theta \geq 0$ for this interval. This trend is presented in §6.7 (figure 6.12) where K_c versus θ/π have been plotted for the three principal stresses on the surface of the sphere for $Re = 0.01$.

6.5 Irrotational flow of a viscous fluid

Kuhn de Chizelle, Ceccio and Brennen (1995) studied the interactions between a travelling cavity and the potential flow exterior to the thin boundary layer around an axisymmetric headform. Liu and Brennen (1998) presented a mechanistic model for hydrodynamic cavitation event rate for flow over a headform that utilizes the pressure distribution given by potential flow modified to accomodate boundary layer effects. There is no literature other than the paper of Funada et al. (2006) on analysis of stress-induced cavitation using potential flow. The analysis of this problem, given below, is completely transparent; the effects of vorticity on cavitation on a solid sphere are mainly associated with the formation of wakes and the displacement of the region of irrotational flow (see §6.6). Considering the irrotational flow of a viscous fluid, the principal strain-rates and stresses and their corresponding principal directions can be determined. Then, the maximum tension criterion is applied to evaluate the cavitation threshold. The theory of viscous potential flow considered here includes the viscous components in the definition of the state of stress in the flowing liquid.

Irrotational flows of incompressible viscous fluids satisfy the Navier–Stokes equations and give rise to the usual Bernoulli equation because

$$\mu\nabla^2\mathbf{u} = \mu\nabla\nabla^2\phi = 0, \tag{6.25}$$

no matter what the value of μ. The stresses are given by

$$\mathbf{T} = -p\mathbf{1} + 2\mu\nabla\otimes\nabla\phi = \frac{1}{3}\mathrm{tr}\,(\mathbf{T})\,\mathbf{1} + 2\mu\nabla\otimes\nabla\phi, \tag{6.26}$$

where p is the average stress given by (6.2).

The flow is axisymmetric and steady and the potential $\phi(r,\theta)$ satisfies $\nabla^2\phi = 0$. In this analysis, spherical-polar coordinates as shown in figure 6.1 are utilized.

The potential for this flow is

$$\phi = U\left(r + \frac{1}{2}\frac{a^3}{r^2}\right)\cos\theta. \tag{6.27}$$

The velocity $\mathbf{u} = \mathbf{e}_r u_r + \mathbf{e}_\theta u_\theta$ is given by

$$u_r = \frac{\partial\phi}{\partial r} = U\left(1 - \frac{a^3}{r^3}\right)\cos\theta, \qquad u_\theta = \frac{1}{r}\frac{\partial\phi}{\partial\theta} = -U\left(1 + \frac{1}{2}\frac{a^3}{r^3}\right)\sin\theta. \tag{6.28}$$

Note that the no-slip condition must be relaxed for viscous potential flow. So, the

boundary layer is not resolved. The pressure is given by

$$\begin{aligned} p &= p_\infty + \rho\frac{U^2}{2} - \frac{\rho}{2}\left(u_r^2 + u_\theta^2\right) \\ &= p_\infty + \rho\frac{U^2}{2}\left[1 - \left(1 - \frac{a^3}{r^3}\right)^2 \cos^2\theta - \left(1 + \frac{1}{2}\frac{a^3}{r^3}\right)^2 \sin^2\theta\right], \end{aligned} \tag{6.29}$$

where p_∞ is the constant value of the pressure at infinity. The non-zero components of the viscous stress

$$2\mu\mathbf{D}\left[\nabla\phi\right] \tag{6.30}$$

are determined using the standard formulae (6.15) and the velocity field (6.28). This yields to the matrix of components

$$2\mu\begin{bmatrix} D_{rr} & D_{r\theta} & 0 \\ D_{r\theta} & D_{\theta\theta} & 0 \\ 0 & 0 & D_{\varphi\varphi} \end{bmatrix} = 3\mu U\frac{a^3}{r^4}\begin{bmatrix} 2\cos\theta & \sin\theta & 0 \\ \sin\theta & -\cos\theta & 0 \\ 0 & 0 & -\cos\theta \end{bmatrix}, \tag{6.31}$$

which can be rotated into diagonal form through an angle α satisfying

$$\tan 2\alpha = \frac{2}{3}\tan\theta. \tag{6.32}$$

From (6.32) we look for the angle α that puts by rotation with axis $\mathbf{e}_\varphi$ the direction given by the unit vector $\mathbf{e}_\mathrm{r}$ into the principal direction corresponding to the most tensile (or the least compressive) principal stress in the plane of the motion. Without lack of generality, we consider this angle α to be in the interval $-0.5 \leq \alpha/\pi \leq 0.5$.

The diagonal form of $2\mu\nabla\otimes\nabla\phi$ is given by

$$3\mu U\frac{a^3}{r^4}\begin{bmatrix} \frac{1}{2}\cos\theta + \frac{\sin\theta}{\sin 2\alpha} & 0 & 0 \\ 0 & \frac{1}{2}\cos\theta - \frac{\sin\theta}{\sin 2\alpha} & 0 \\ 0 & 0 & -\cos\theta \end{bmatrix}. \tag{6.33}$$

At $\theta = \pi/2$, where the pressure is smallest, $\alpha = \pi/4$ and the diagonal form is

$$3\mu U\frac{a^3}{r^4}\begin{bmatrix} 1 & 0 & 0 \\ 0 & -1 & 0 \\ 0 & 0 & 0 \end{bmatrix}, \tag{6.34}$$

giving rise to tension and compression.

Following the analysis presented in §6.2, we next consider the whole stress using

(6.26), which may be written as

$$\mathbf{T} + p_{\mathrm{c}}\mathbf{1} = (-p + p_{\mathrm{c}})\,\mathbf{1} + 2\mu\nabla \otimes \nabla\phi \tag{6.35}$$

with the addition of the cavitation threshold p_{c}. After arranging, expression (6.35) becomes

$$\begin{aligned}\frac{\mathbf{T} + p_{\mathrm{c}}\mathbf{1}}{\frac{1}{2}\rho U^2} &= -\left[K + 1 - \left(1 - \frac{a^3}{r^3}\right)^2 \cos^2\theta - \left(1 + \frac{a^3}{2r^3}\right)^2 \sin^2\theta\right]\begin{bmatrix} 1 & 0 & 0 \\ 0 & 1 & 0 \\ 0 & 0 & 1 \end{bmatrix} \\ &\quad + \frac{3}{Re}\left(\frac{a}{r}\right)^4 \begin{bmatrix} \cos\theta + \frac{2\sin\theta}{\sin 2\alpha} & 0 & 0 \\ 0 & \cos\theta - \frac{2\sin\theta}{\sin 2\alpha} & 0 \\ 0 & 0 & -2\cos\theta \end{bmatrix}\end{aligned} \tag{6.36}$$

where

$$K = \frac{p_\infty - p_{\mathrm{c}}}{\frac{1}{2}\rho U^2} \tag{6.37}$$

is the cavitation number and

$$Re = \frac{\rho U a}{\mu} \tag{6.38}$$

is the Reynolds number.

For the viscous potential flow solution (6.36), one can show that at any point the most tensile (least compressive) and most compressive (least tensile) principal stresses lie in the plane of motion (i.e., the plane where the velocity vector is contained). Suppose now that T_{11} is the largest of the three principal values of stress. Then, according to the maximum tension theory, the locus of the cavitation threshold is given by

$$T_{11} + p_{\mathrm{c}} = 0, \tag{6.39}$$

giving rise to isolines $(a/r, \theta) = f(K_{\mathrm{c}}, Re)$ for the cavitation threshold. The largest values of the viscous irrotational stress are at the boundary $r = a$ where the neglected vorticity is largest. In Appendix G, it is shown that $\theta = 0$ for very low Re and $\theta = \pi/2$ for very high Re are the points most vulnerable for cavitation under the respective conditions.

Equation (6.36) gives the form of the diagonalized stress tensor at each point

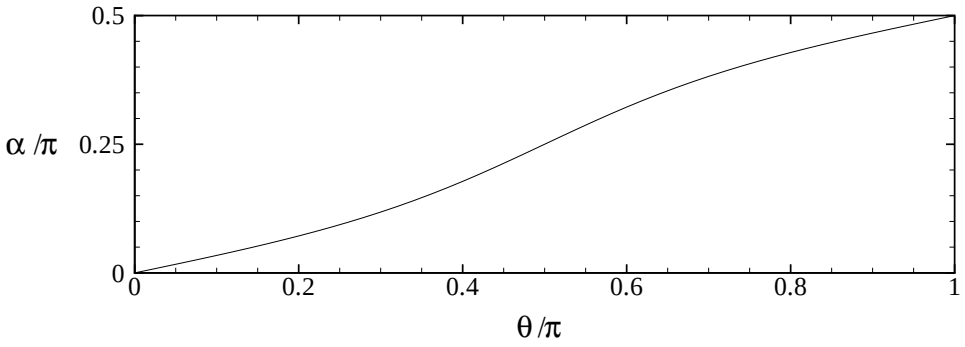

Figure 6.3: Rotation angle α/π versus angular position θ/π, derived from $\tan 2\alpha = \frac{2}{3}\tan\theta$ for irrotational flow of a viscous fluid. A linear approximation of this graph is $\alpha = 0.5\theta$. A cavitation bubble will open asymmetrically with the axis of maximum tension rotated through an angle α at each point r, θ as in this figure.

(r, θ) in the axially symmetric flow. T_{11}, T_{22} and $T_{33} = T_{\varphi\varphi}$ are principal stresses in the principal axes coordinates with bases $\mathbf{e}_1$, $\mathbf{e}_2$, $\mathbf{e}_\varphi$. In the present case, the angle α changes with θ, $\tan 2\alpha = \frac{2}{3}\tan\theta$. The solution of this equation (6.32) is displayed graphically in figure 6.3. A representation of the orientation of the principal axes in the plane of motion at the surface of the sphere $r = a$ as predicted by (6.32) is presented in figure 6.4.

It is apparent from (6.36) that the largest stresses are at the boundary of the sphere where $r = a$. Certainly the liquid will cavitate when $K = (p_\infty - p_c) \,/\, \left(\frac{\rho}{2}U^2\right) < 0$; only $K > 0$ is of interest. Using now the maximum tension criterion, we see that cavitation occurs for $0 < K < K_c$ and the fluid is most at risk to cavitation for θ at which $K_c(\theta)$ is greatest. For viscous potential flow, this most dangerous θ is at $\theta = 0$ when Re is small and at $\theta = \pi/2$ when Re is large. It follows that the place most at risk to cavitation runs from the rear stagnation point at $\theta = 0$ when Re is small to $\theta = \pi/2$ when Re is large.

In §6.7 contour plots with lines of constant K representing the cavitation threshold from (6.36) for various Re are presented and compared with the results from the numerical simulation and the Stokes solution for the lowest Re (see figures 6.9, 6.10 and 6.11). Also, in §6.7 we have plotted K_c versus θ/π for the three principal stresses at $r = a$ for $Re = 0.01$, 10 and 100, comparing these results with the corresponding graphs obtained with direct numerical simulation and, for $Re = 0.01$, with the Stokes flow analysis (see figures 6.12, 6.13 and 6.14).

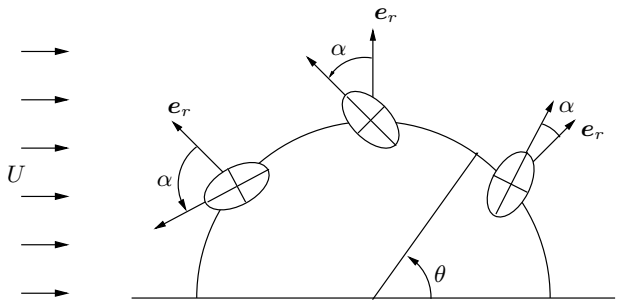

Figure 6.4: Schematic view of the orientation of the principal directions in the plane of motion for irrotational flow of a viscous fluid according to (6.32) on the surface of the sphere. The major axis in the ellipse represents the maximum tensile stress. The angle α puts the direction defined by the unit outward normal vector $\boldsymbol{e}_r$ into the principal direction of the maximum tensile stress.

6.6 Numerical solution of the incompressible Navier–Stokes equations

Numerical investigations of the fundamental aspects of cavitation formation from a wall–stabilized nucleus (Kottke et al. 2005 and references therein) or the interaction between the flow field and traveling cavitation bubbles (Kuhn de Chizelle and Brennen 1993) can be encountered in the literature. On the other hand, some effort has been devoted to develop engineering tools based on computational fluid dynamics to model cavitation through different approaches of the multiphase flow (Singhal et al. 2002; Farrell, 2003). In this section, the numerical simulation of streaming flow past a sphere is carried out for various values of the Reynolds number Re as defined before. The hydrodynamics is predicted for a single phase, Newtonian, non-cavitating fluid. The velocity and pressure fields computed in this numerical study are used to determine the principal stresses and directions. Therefore, the cavitation criteria can be formed based on these results and a comparison with the theoretical models from §6.4 and §6.5 can be presented.

6.6.1 Numerical set-up and flow field computations

The numerical solution of the incompressible unsteady Navier–Stokes equations for streaming flow past a sphere is performed using the computational-fluid-dynamics package Fluent® 6.1. This program is based on the finite-volume method which is utilized to integrate the governing equations and then a set of algebraic equations is constructed. An implicit segregated scheme is used to solve the discretized

governing equations sequentially. The convective term in the momentum equation is discretized using a Quadratic Upwind Interpolation for Convective Kinematics (QUICK). The pressure-velocity coupling is accomplished through the Pressure-Implicit with Splitting of Operators (PISO) scheme. The time integration of the unsteady momentum equations is carried out using a second-order approximation.

We are interested in the steady-state limit of the solution. The interval for the Reynolds number based on the free-stream velocity U and the radius of the sphere as considered in this simulation is $0 < Re \leq 100$. For this interval of Re, the steady-state-flow motion is described as axisymmetric (see, for instance, Johnson and Patel, 1999). Then, a semi O-type mesh is employed in the numerical simulations. Figure 6.5 shows a scheme of the computational domain as well as the boundary conditions, where the horizontal edge represents the axis of symmetry and the stream flows from left to right. The outflow boundary condition implies that the diffusion flux in the direction normal to the exit surface is zero for all variables. Therefore, the flow variables at the outflow plane are computed from inside the domain through extrapolation. The interested reader is referred to the Fluent® 6.1's User Guide for details about the numerical schemes and boundary conditions available in the package. Quadrilateral cells in a structured mesh are used to discretize the domain. The position of the outer spherical edge of the computational domain is fixed as $H = 150a$ measured from the center of the sphere. For the selected geometry, the number of cells of the domain is 11680 and the number of nodes is 11907. Using a similar node density, a larger domain was considered by increasing the distance from the center of the sphere to the outer spherical edge ($H = 200a$). The comparison of the drag coefficient computed for these two computational domains indicates that the relative difference is below 1% for $Re = 0.01$ and $Re = 100$. Therefore, we decided to use the mesh with $H = 150a$ to perform further computations. The smallest cells of the domain were located attached to the surface of the sphere and their size increases as the distance from the wall increases. Good resolution of the boundary layer attached to the surface is provided with the selected cells' sizes. The dimensionless time step used in the simulations was $\Delta tU/a = 0.04$. In addition, tests were also conducted with a dimensionless time step of 0.02 and a much finer grid rendering results very close to the previous ones. The initial velocity field is set equal to the free-stream velocity everywhere in the computational domain.

With these settings, computations are performed for different values of the Reynolds number, $Re = 0.01$, 10, 25, 50, 75 and 100. Therefore, the steady axisymmetric flow conditions reported in the literature from experiments and three-dimensional simulations are expected in all the cases, being consistent with our

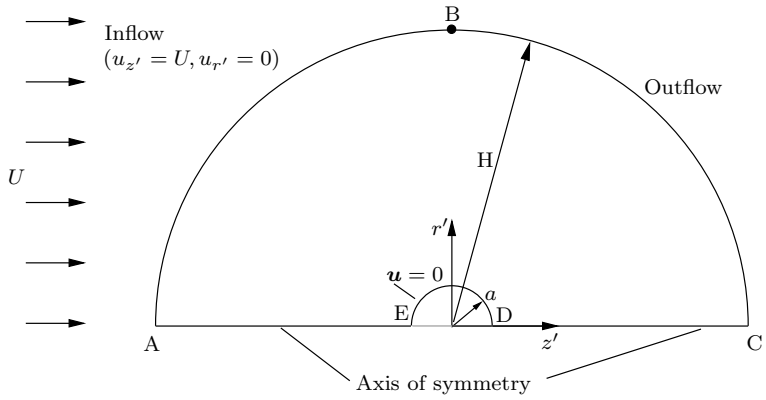

Figure 6.5: Computational domain showing the boundary conditions.

numerical set-up.

The validation of the numerical setup is carried out by comparing our numerical results for various parameters with results from different sources as compiled and presented in the work of Johnson and Patel (1999). These parameters are the drag coefficient, the separation angle and the separation length. Their definition and the results of the comparison are presented in Appendix H. Satisfactory agreement with previous numerical and experimental results is obtained. Furthermore, the computed flow field is presented in this Appendix through the streamline pattern and contours of vorticity for three values of de Reynolds number.

6.6.2 Principal stresses and cavitation inception

In order to compute the principal stresses and directions from the velocity and pressure field obtained from the numerical simulations consider the reference frame shown in figure 6.6 for axysimmetric flow past a sphere. This reference frame is defined by the cylindrical coordinates (z', r', θ'). The corresponding vector basis is defined by the set of unit vectors $\{\boldsymbol{e}_{z'}, \boldsymbol{e}_{r'}, \boldsymbol{e}_{\theta'}\}$. The vector $\boldsymbol{e}_{\theta'}$ is normal to the page in figure 6.6(a). The cylindrical coordinates have been used here instead of the spherical polar coordinates utilized in previous sections since the computational solver applied for the direct numerical simulation imposes this system of coordinates for axysimmetric problems with the direction of the axis of symmetry indicated by $\boldsymbol{e}_{z'}$. Therefore, the package computes the derivatives of the components of the velocity with respect to this cylindrical reference frame.

The components of the viscous stress tensor $2\mu\mathbf{D}$ with respect to this set of

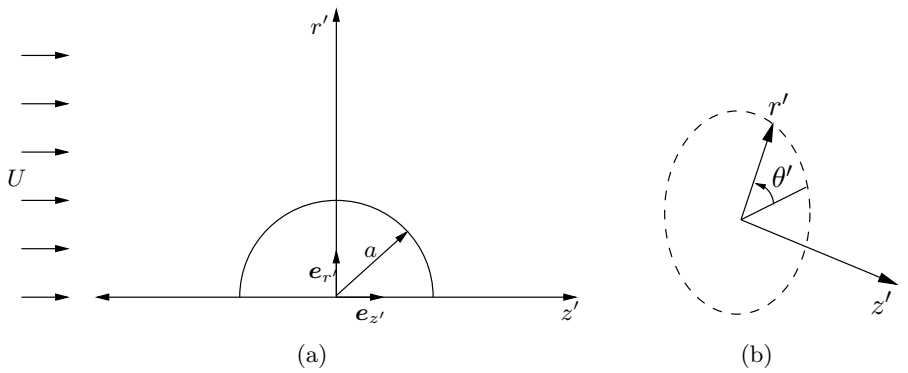

Figure 6.6: Cartoon showing (a) a representation of the axisymmetric flow past a sphere of radius a, and (b) cylindrical coordinates.

vectors may be written in matrix form as

$$2\mu \begin{bmatrix} D_{z'z'} & D_{z'r'} & 0 \\ D_{z'r'} & D_{r'r'} & 0 \\ 0 & 0 & D_{\theta'\theta'} \end{bmatrix}, \tag{6.40}$$

where,

$$D_{z'z'} = \frac{\partial u_{z'}}{\partial z'}, \quad D_{r'r'} = \frac{\partial u_{r'}}{\partial r'}, \quad D_{\theta'\theta'} = \frac{u_{r'}}{r'}, \quad D_{z'r'} = \frac{1}{2}\left(\frac{\partial u_{r'}}{\partial z'} + \frac{\partial u_{z'}}{\partial r'}\right) \tag{6.41}$$

and $D_{r'\theta'} = D_{\theta'r'} = D_{z'\theta'} = D_{\theta'z'} = 0$.

The diagonalized form of the stress $2\mu\mathbf{D}$ can be found by rotating the coordinates (z', r') through an angle β such that (6.40) becomes

$$2\mu \begin{bmatrix} \frac{1}{2}\left(D_{z'z'} + D_{r'r'}\right) + \frac{D_{z'r'}}{\sin 2\beta} & 0 & 0 \\ 0 & \frac{1}{2}\left(D_{z'z'} + D_{r'r'}\right) - \frac{D_{z'r'}}{\sin 2\beta} & 0 \\ 0 & 0 & D_{\theta'\theta'} \end{bmatrix}. \tag{6.42}$$

The rotation angle β such that the direction defined by the unit vector $\boldsymbol{e}_{r'}$ reaches the principal direction corresponding to the maximum strain-rate in the plane of the fluid motion is related to the components of the strain-rate tensor given in (6.41) according to the expression

$$\tan 2\beta = \frac{2D_{z'r'}}{D_{z'z'} - D_{r'r'}}. \tag{6.43}$$

The angle α associated with the rotation with axis $\boldsymbol{e}_{\varphi}$ of the orthogonal reference

frame defined by the sphere's outward normal unit vector $\boldsymbol{e}_r$ and the sphere's tangential unit vector $\boldsymbol{e}_\theta$ (figure 6.1) is related to the angle β associated with the rotation with axis $\boldsymbol{e}_{\theta'}$ of the cylindrical coordinates defined by $\boldsymbol{e}_{z'}$ and $\boldsymbol{e}_{r'}$ (figure 6.6) through the formula

$$\alpha = \beta - \theta. \tag{6.44}$$

The angle α corresponds to the rotation of the spherical polar coordinates (r, θ) in the plane of motion such that the direction of the unit vector $\boldsymbol{e}_\mathrm{r}$ coincides with the principal direction associated with the most tensile (or the least compressive) principal stress. The angle α is restricted to the interval -0.5 $\leq \alpha/\pi \leq$ 0.5. The rotation angle α/π as a function of the polar angle θ/π on the surface of the sphere $r = a$ is computed from the numerical simulation results and is presented for various Re in figure 6.7. For $Re = 0.01$ and $Re = 10$ the angle $\alpha = -45^\circ$ coincides with the principal direction of maximum tension for simple shearing. This result was also obtained in the Stokes flow solution and is enforced by the no-slip condition. In the case of $Re = 100$, the angle α shows a similar behavior from the front stagnation point until the point of separation. Beyond this point, the principal axes rotates 90° and the direction of the maximum principal stress is reached for $\alpha = 45^\circ$. Figure 6.8 presents a cartoon showing the orientation of the principal axes on the plane of motion at different angular positions on the surface of the sphere for $Re = 100$.

Recalling expression (6.1), the total stress tensor for an incompressible Newtonian fluid can be written as

$$\mathbf{T} = -p\mathbf{1} + 2\mu\mathbf{D}.$$

The pressure p can be expressed in terms of the pressure coefficient, which is defined as

$$c_\mathrm{p} = \frac{p - p_\infty}{\frac{1}{2}\rho U^2}, \tag{6.45}$$

where p_∞ is a constant reference pressure corresponding to the limiting pressure as $r \to \infty$. Then, using (6.45), expression (6.1) becomes,

$$\mathbf{T} = -p_\infty\mathbf{1} - \frac{1}{2}\rho U^2 c_\mathrm{p}\mathbf{1} + 2\mu\mathbf{D}. \tag{6.46}$$

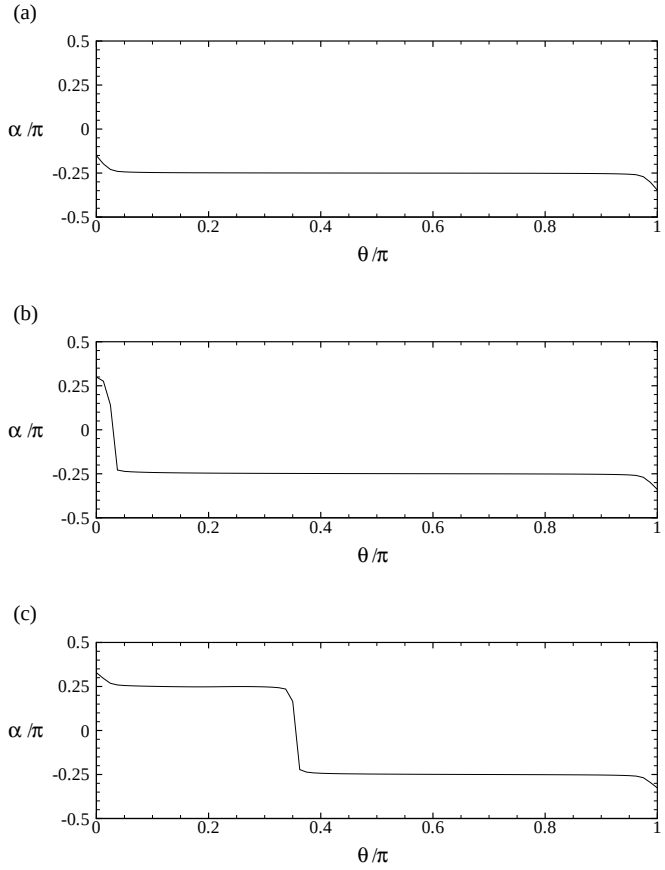

Figure 6.7: Rotation angle α as defined in (6.44) versus θ/π on the surface of the sphere, r/a= 1, from the numerical solution for (a) Re= 0.01, (b) Re= 10, (c) Re= 100. The position $\theta = 0$ corresponds to the rear stagnation point. Notice that for $Re = 100$ the jump on the curve occurs at $\theta \approx 63°$, which coincides with the corresponding separation angle θ_s (see figure H.2).

Adding $p_{\mathrm{c}}\mathbf{1}$ to both sides of (6.46) yields,

$$\mathbf{T} + p_{\mathrm{c}}\mathbf{1} = -(p_\infty - p_{\mathrm{c}})\mathbf{1} - \frac{1}{2}\rho U^2 c_{\mathrm{p}}\mathbf{1} + 2\mu\mathbf{D}, \tag{6.47}$$

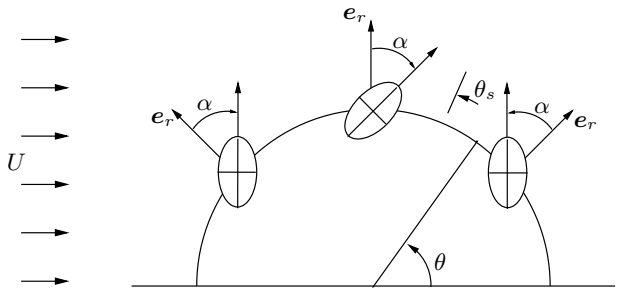

Figure 6.8: Schematic view of the orientation of the principal directions in the plane of motion on the surface of the sphere according to (6.44) from direct numerical simulation of the Navier–Stokes equations and $Re = 100$. In this case, $\alpha \approx -45°$ for $\theta > \theta_s$ and $\alpha \approx 45°$ for $\theta < \theta_s$ (from figure 6.7 (c)). The angle θ_s refers to the separation angle measured from the rear stagnation point. The major axis in the ellipse represents the maximum tensile stress. The angle α puts the direction defined by the unit outward normal vector $\boldsymbol{e}_r$ into the principal direction of the maximum tensile stress.

where p_c is the cavitation threshold. After arranging, (6.47) may be written as

$$\frac{\mathbf{T} + p_\mathrm{c}\mathbf{1}}{\frac{1}{2}\rho U^2} = -\left(K + c_\mathrm{p}\right)\begin{bmatrix} 1 & 0 & 0 \\ 0 & 1 & 0 \\ 0 & 0 & 1 \end{bmatrix} + \frac{4}{Re}\begin{bmatrix} \frac{1}{2}\left(\tilde{D}_{z'z'} + \tilde{D}_{r'r'}\right) + \frac{\tilde{D}_{z'r'}}{\sin 2\beta} & 0 & 0 \\ 0 & \frac{1}{2}\left(\tilde{D}_{z'z'} + \tilde{D}_{r'r'}\right) - \frac{\tilde{D}_{z'r'}}{\sin 2\beta} & 0 \\ 0 & 0 & \tilde{D}_{\theta'\theta'} \end{bmatrix}, \quad (6.48)$$

where the dimensionless strain-rate tensor is defined as $\tilde{\mathbf{D}} = \mathbf{D}(a/U)$, and K is the cavitation number as presented in (6.37). The Reynolds number is defined as in (6.38). The principal stresses are thus determined by (6.48).

The velocity field obtained from the numerical solution is used to compute (6.41) and then all the required quantities, including the principal stresses, also utilizing the numerical pressure field. The derivatives of the velocity components in cylindrical coordinates required in (6.41) are approximated by the computational fluid dynamics package using the discrete values of the velocity components obtained from the numerical solution stored at every node.

Consider (6.48) and let T_{11} be the maximum of the principal stresses. Then, the maximum tension criterion (6.6) can be formed. Notice that the maximum principal stress T_{11} may be given by the stress normal to the plane of motion, $T_{\theta'\theta'}$. In the

next section, plots of lines of constant K obtained from the numerical simulations corresponding to the cavitation threshold for various Re are presented (figures 6.9, 6.10 and 6.11). In addition, the critical values of the cavitation threshold K_c versus θ/π for the three principal stresses on the surface of the sphere from the numerical results are shown and compared with the viscous potential flow solution and, for a low $Re = 0.01$, with the Stokes flow solution (figures 6.12, 6.13 and 6.14).

6.7 Discussion

This work is motivated by the desire to understand the effect of viscosity on stress-induced cavitation of liquids. The study is performed in the framework of direct numerical simulation of the incompressible Navier–Stokes equations to predict the flow field. Analyzes are also presented based on the irrotational flow of viscous fluids around a sphere and, for low Reynolds number flows, on the Stokes-flow-limit solution. These formulations allow for a particularly transparent analysis in which all the predictions are given by simple explicit expressions. These formulations relate two dimensionless parameters, the cavitation number associated with the inception of cavitation and the Reynolds number. In the case of the Stokes-flow solution, the formulation is made independent of the Reynolds number by choosing a characteristic viscous-stress scale. The results of this investigation apply to any viscous Newtonian liquid. For all the cases considered, the results from the simplified analytical models are contrasted with the computations from direct numerical simulation.

The main points about stress-induced cavitation, in particular the role of the maximum tensile stress in principal axes coordinates, and the comparison of this criterion with the criterion depending only on pressure and the most conservative one which requires that all the principal stresses be in tension, are very clearly expressed in the simple analyses based on either viscous potential flow or Stokes flow. In addition, the criteria for cavitation can be neatly formed and evaluated using the velocity and pressure fields from numerical simulations of the governing equations.

Contour plots of lines of constant critical cavitation number K_c from the maximum tension criterion are presented in figures 6.9, 6.10 and 6.11 for $Re = 0.01$, 10 and 100, respectively. In these figures, the results obtained from the analysis of viscous potential flow and from direct numerical simulation are included. For $Re = 0.01$, the Stokes flow solution is also presented for comparison. Notice that the results from the Stokes limit and the results from direct numerical simulation are very

similar, as expected (figures 6.9 (a) and (c)). The analytical models predict that the risk of cavitation is higher for low Reynolds number flows. This result is confirmed by the numerical experiments. The comparison of the cavitation regions for viscous potential flow and numerical simulation of the Navier–Stokes equations (NS) for $Re = 10$ and 100 is interesting; the cavitation regions shift to the right for NS because of the formation of wakes not present in the irrotational flow solution. As Re increases, the contour plots corresponding to viscous potential flow become symmetric with respect to an axis passing through the center of the sphere, perpendicular to the direction of the free stream velocity, since the contribution of the viscous stress vanishes and the classical "inviscid" potential flow result is approached. As we mentioned, in the case of the numerical solution of NS, the principal stress in the normal direction to the plane of motion may become the largest in some regions of the domain. In such a case, the cavitation inception is determined by this principal stress.

The pressure criterion can readily be presented in dimensionless form as $K_{\mathrm{c}} = -c_{\mathrm{p}}$, in the marginal state separating cavitation from no cavitation. Using the pressure field from the numerical solution of NS equations, contour plots of K_{c} following the pressure criterion are presented in figures 6.9 (d), 6.10 (c) and 6.11 (c). Comparison of these results with the corresponding results from the maximum tension criterion (figures 6.9 (c), 6.10 (b) and 6.11 (b)) indicates that the later shifts the region of higher critical cavitation number upstream on the surface of the sphere. The difference is notorious for the lowest $Re = 0.01$. In this case, the region of higher K_{c} is predicted at 45^o from the rear stagnation point by the maximum tension criterion, whereas the pressure criterion indicates that the fluid is at the most risk to cavitation (i.e. maximum K_{c}) at the rear stagnation point. This result can also be obtained using the pressure field in (6.14) for Stokes flow to define the pressure coefficient c_{p}. Furthermore, notice that the maximum tension criterion is more conservative than the pressure criterion since $K_{\mathrm{c,max}}$ from the former approach is larger than $K_{\mathrm{c,max}}$ from the latter. As Re increases, both approaches tend to the same distribution since the effects of viscosity carried by the viscous deviator are substantially lessened.

In particular for $r = a$, the surface of the sphere, the profiles of the cavitation number K_{c} from the maximum tension criterion as a function of θ/π are computed independently for the three principal stresses and presented in figures 6.12, 6.13 and 6.14 for $Re = 0.01$, 10 and 100, respectively. In each of these figures, the comparison is performed between the VPF solution and the results from the numerical analysis. Also, the predictions from the pressure criterion $K_{\mathrm{c}} = -c_{\mathrm{p}}$, using the numerical

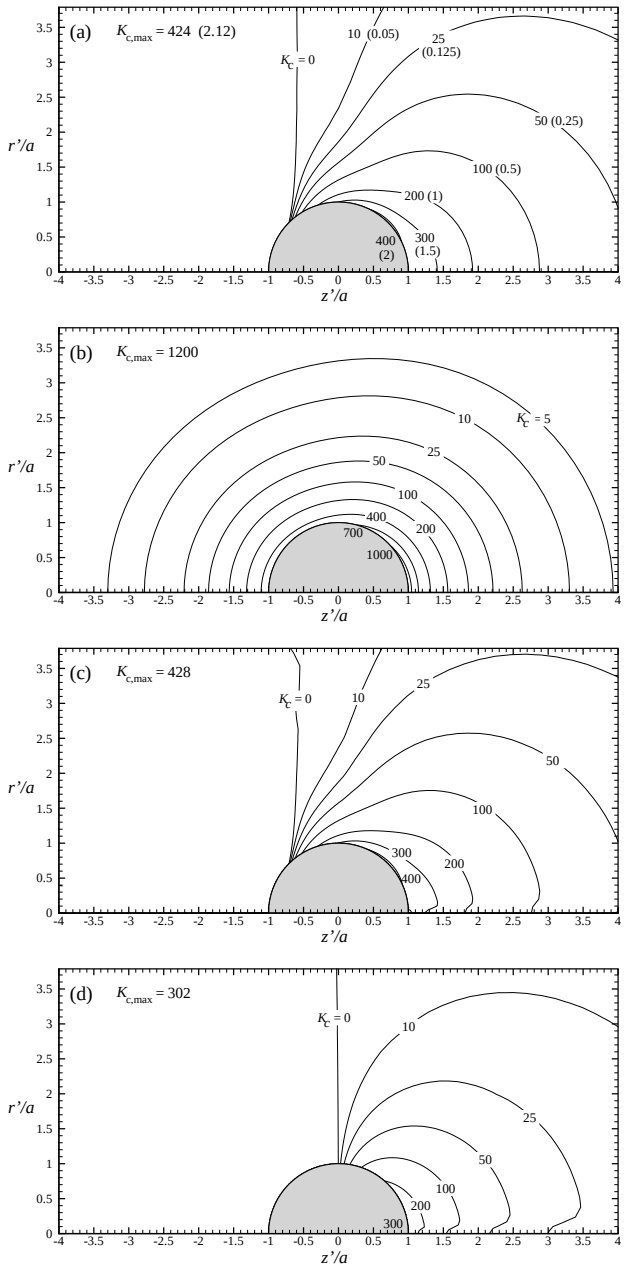

Figure 6.9: Contours of critical cavitation number K_c given by the condition $T_{11}+p_c = 0$ according to the maximum tension criterion for a Reynolds number $Re = 0.01$ from (a) Stokes flow (6.21); (b) the irrotational flow of a viscous fluid (6.36), and (c) numerical solution (6.48); the pressure criterion given by $K_c = -c_p$ is shown in (d) using the numerical pressure field. The cavitation number K is defined in terms of the dynamic pressure $\rho U^2/2$ (Caption continues on next page).

Figure 6.9: (Caption continued from previous page) For a given cavitation number K, cavitation occurs in the region where $K < K_c$. A different normalization of the cavitation number and of the critical cavitation number is used for Stokes flow (6.19) rather than the normalization used for the other cases (6.37). The contour lines for the normalization of $p_\infty - p_c$ with the viscous-stress scale $\mu U/a$ in (6.19) are presented in parenthesis in (a). The ratio of the normalization factors is $Re/2$ (6.22).

solution of the Navier–Stokes equations, are presented. For $Re = 0.01$, the results from the Stokes flow limit are included as well. In these figures, T_{11} represents the maximum principal stress and $T_{11} \geq T_{33} \geq T_{22}$. At the surface of the sphere, the pressure criterion coincides with the curve for which $T_{33} + p_c = 0$ because of the no-slip condition. The discrepancies between the predictions from the maximum tension criterion and the pressure criterion discussed above are better appreciated when observed at the surface of the sphere, in particular for the lowest $Re = 0.01$ (figure 6.12 (c)). In this case, the maximum tension criterion predicts the location of the point where K_c is maximum at $\theta = 45^o$ using the pressure field from the numerical simulations (the Stokes' approximation yields the same result as shown in Appendix G). With this pressure distribution, the pressure criterion predicts the location of $K_{c,\max}$ at $\theta = 0^o$ (the rear stagnation point). The same position is determined from the maximum tension criterion using the pressure field from VPF, though the maximum K_c is much higher in this case (figure 6.12 (b)). Figures 6.13 and 6.14 show that the results from the maximum tension criterion tend to the results from the pressure criterion theory for the inception of cavitation as Re increases.

This study has focused on cavitation by homogeneous nucleation. However, important implications are found for heterogeneous nucleation. The results show that the K value is maximized at the surface of the sphere and that viscous normal stresses are important there. This can explain the greater likelihood for heterogeneous nucleation. Furthermore, if the flow around the sphere in figure 6.1 contained particles that were sufficiently small so that the flow is not modified substantially in a global sense, certain inferences can be made. The normal compressive stress which is locally reduced (or made tensile) by flow around the sphere can be further reduced due to relative motion between a small particle and the liquid. That is, in a frame of reference fixed to a moving small particle, the liquid will, in some domain, accelerate around and past the small particle, thereby further increasing the local K value when viewed with a finer resolution than we have allowed in our analysis.

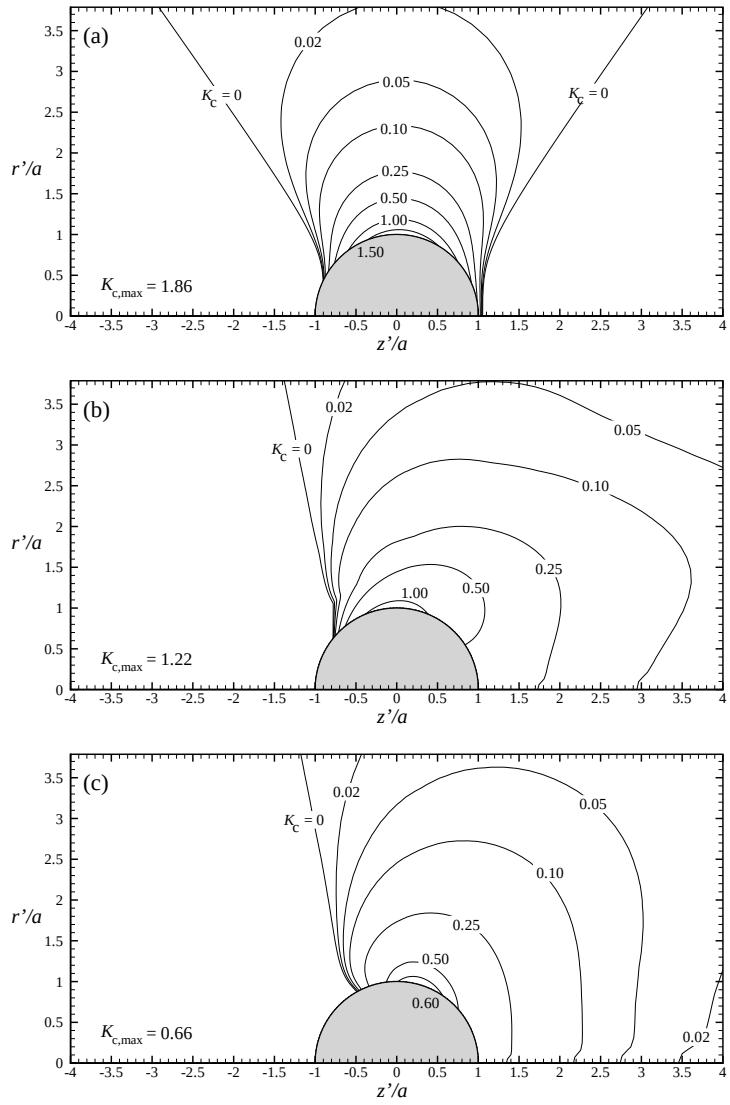

Figure 6.10: Contours of critical cavitation number K_c given by the condition $T_{11}+p_c = 0$ according to the maximum tension criterion for a Reynolds number $Re = 10$ from (a) the irrotational flow of a viscous fluid (6.36), and (b) numerical solution (6.48); the pressure criterion given by $K_c = -c_p$ is shown in (c) using the numerical pressure field. The cavitation number K is defined in terms of the dynamic pressure $\rho U^2/2$. For a given cavitation number K, cavitation occurs in the region where $K < K_c$.

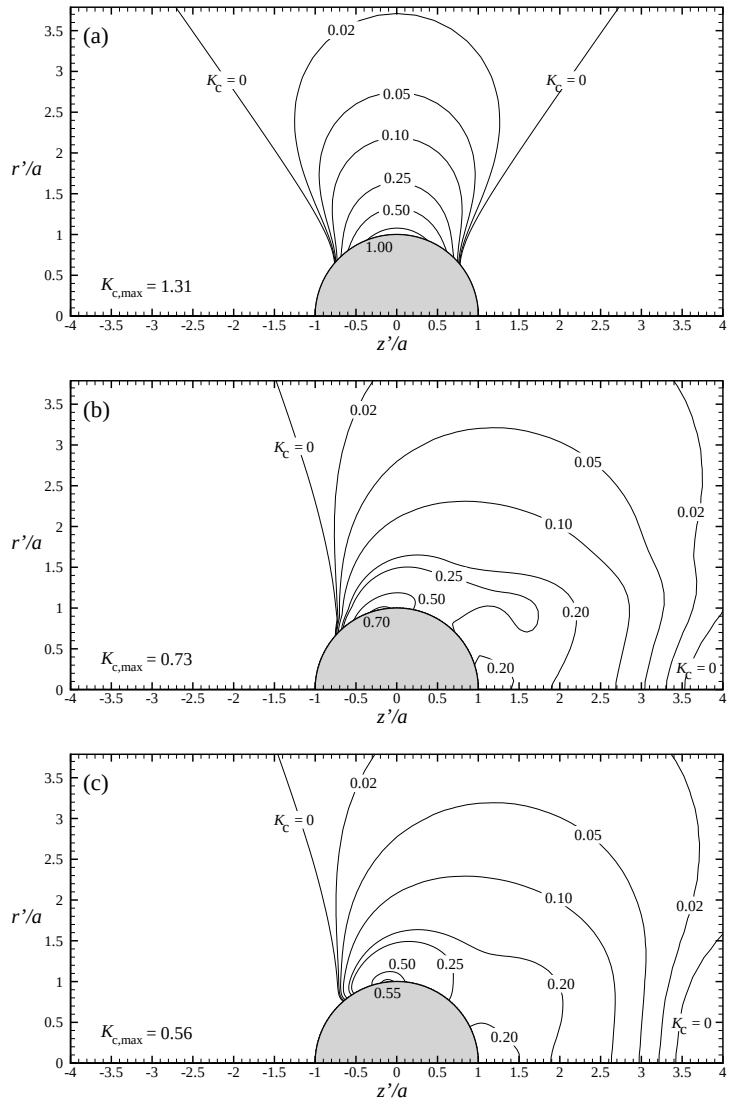

Figure 6.11: Contours of critical cavitation number K_c given by the condition $T_{11}+p_c = 0$ according to the maximum tension criterion for a Reynolds number $Re = 100$ from (a) the irrotational flow of a viscous fluid (6.36), and (b) numerical solution (6.48); the pressure criterion given by $K_c = -c_p$ is shown in (c) using the numerical pressure field. The cavitation number K is defined in terms of the dynamic pressure $\rho U^2/2$. For a given cavitation number K, cavitation occurs in the region where $K < K_c$.

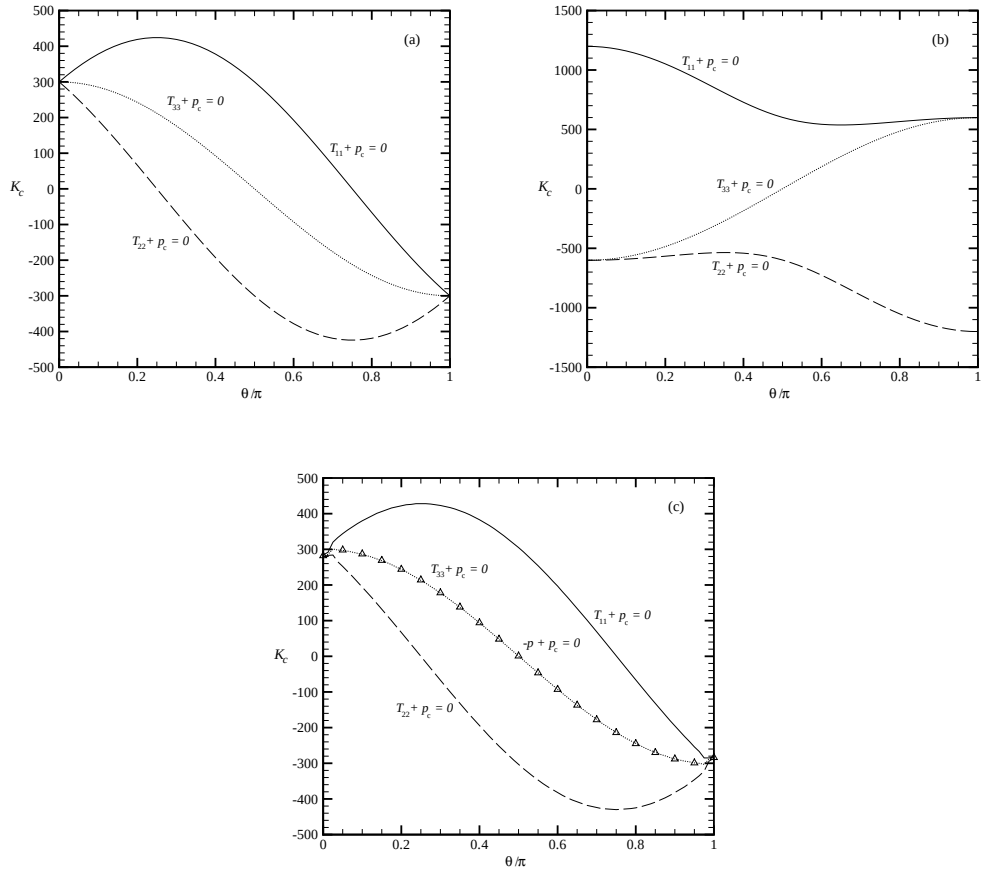

Figure 6.12: Critical cavitation number $K_{\rm c}$ versus angular position θ/π on the surface of the sphere $r = a$ for $Re = 0.01$ and (a) Stokes flow (6.21); (b) the irrotational flow of a viscous fluid (6.36), and (c) numerical solution (6.48). In addition, the pressure criterion $K_{\rm c} = -c_{\rm p}$ has also been included in (c) with the symbol Δ. $K_{\rm c}$ is defined in terms of the dynamic pressure $\rho U^2/2$. In the figure, three values of the critical cavitation number $K_{\rm c}$ are determined for every polar angular position θ, with $T_{11} + p_{\rm c} = 0$, $T_{22} + p_{\rm c} = 0$ and $T_{33} + p_{\rm c} = 0$. The position $\theta = 0$ corresponds to the rear stagnation point. For all values of Re, we consider T_{11} as the most tensile principal stress and $T_{11} \geq T_{33} \geq T_{22}$. By multipliying the values in the vertical axis by a factor of $Re/2$, the results for Stokes flow in (a) can be readily presented in terms of the viscous–stress scale $\mu U/a$ instead, according to (6.22).

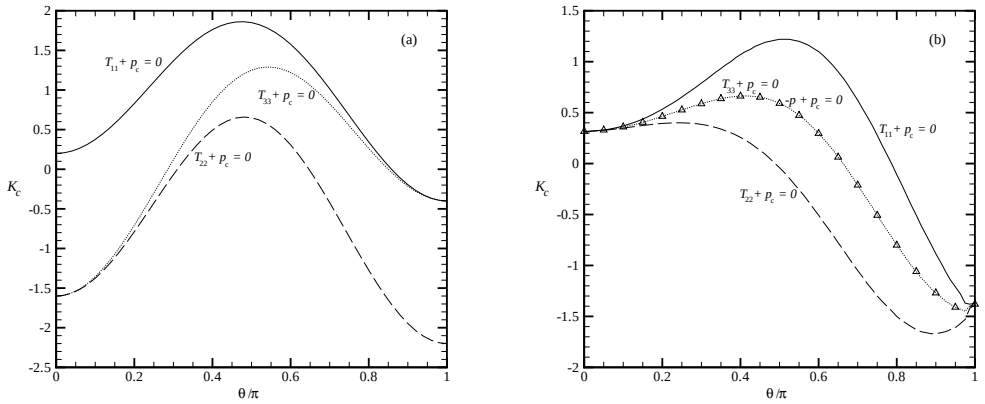

Figure 6.13: Critical cavitation number K_c versus angular position θ/π on the surface of the sphere $r = a$ for $Re = 10$ and (a) the irrotational flow of a viscous fluid (6.36), and (b) numerical solution (6.48). In addition, the pressure criterion $K_c = -c_p$ has also been included in (b) with the symbol Δ. In the figure, three values of the critical cavitation number K_c are determined for every polar angular position θ, with $T_{11} + p_c = 0$, $T_{22} + p_c = 0$ and $T_{33} + p_c = 0$. The position $\theta = 0$ corresponds to the rear stagnation point. For all values of Re, we consider T_{11} as the most tensile principal stress and $T_{11} \geq T_{33} \geq T_{22}$.

So, the likelihood of both homogeneous and heterogeneous nucleation is increased by the presence of these small particles[†].

Irrotational motions of viscous liquids account for viscous stresses but not for vorticity created by the no slip condition at the boundary of solids which is neglected. The analysis is not restricted to small viscosity but is restricted to small vorticity. In steady flows over a sphere the effects of vorticity are greatest in the wake regions behind the separated boundary layers. The irrotational theory cannot be used in the wake region. However, this theory predicts that the liquid is at greatest risk to cavitation close to $\theta = 90^\circ$ when Re is high, which is in good agreement with numerical simulation (see figures 6.13 and 6.14). Moreover, the cavitation region computed from the irrotational theory is in fair agreement with the numerical simulations with $Re = 10$ and $Re = 100$ for $K > 0.5$ (see figures 6.10 and 6.11). On the front face of the sphere including the neighbourhood of the position $\theta = 90^\circ$ we expect a thin boundary layer and an exterior flow closely irrotational for high Reynolds numbers (e.g., $Re = 100$). A good discussion of this can be found in White (2006). There, it is shown that the skin friction based on the surface velocity of the

[†]This paragraph has been contributed by Prof. W. A. Sirignano of the University of California, Irvine.

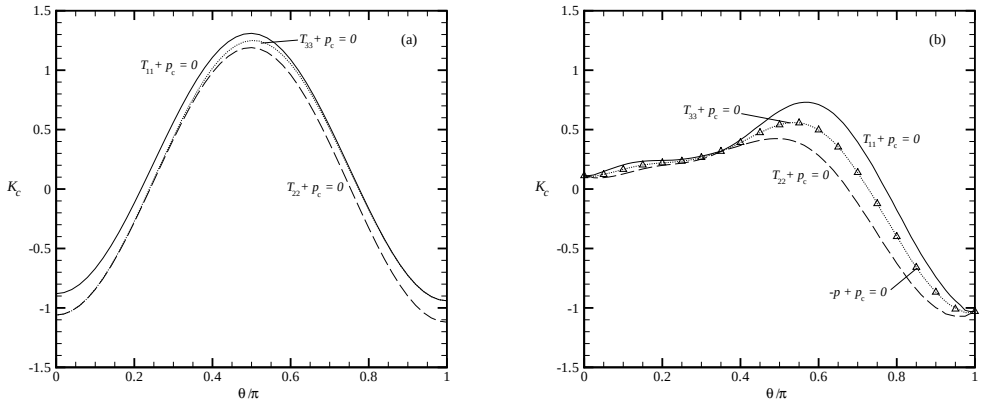

Figure 6.14: Critical cavitation number K_c versus angular position θ/π on the surface of the sphere $r = a$ for $Re = 100$ and (a) the irrotational flow of a viscous fluid (6.36), and (b) numerical solution (6.48). In addition, the pressure criterion $K_c = -c_p$ has also been included in (b) with the symbol Δ. In the figure, three values of the critical cavitation number K_c are determined for every polar angular position θ, with $T_{11} + p_c = 0$, $T_{22} + p_c = 0$ and $T_{33} + p_c = 0$. The position $\theta = 0$ corresponds to the rear stagnation point. For all values of Re, we consider T_{11} as the most tensile principal stress and $T_{11} \geq T_{33} \geq T_{22}$.

irrotational flow is close to the actual friction near the front stagnation point and not so hugely different up to the point of separation. The irrotational flow theory given here is off the mark not because the flow is rotational but due to the displacement of the irrotational flow by the separated wake.

The theory of stress-induced cavitation does not require one to assume irrotational flow; we worked the same theory for Stokes flow and Navier–Stokes flow. The predictions for Stokes flow are for very thick fluids creeping around a sphere. We find that the cavities would develop at $\theta = 45°$, at $-45°$ from the direction of shearing. The theory of stress-induced cavitation can be applied to exact numerical simulation, even for turbulent flow.

A clear description of the effects of viscosity in the inception of cavitation was reported by Harvey and collaborators (1947). They carried out experiments of withdrawal of a rod from a liquid container similar to the ones depicted in §6.3 but using gas-nucleus-free corn syrup (2010 cP and density 1.383 at 23°C) instead of water. Two rods of different materials, aluminum and glass, were drawn from the liquid at a maximum speed of 12.2 m/s. Experiments showed that several minute bubbles formed at the end and side of the rod at the very start of its motion, growing into a long cylindrical bubble. After the rod left the container, the bubble started to

collapse. Experiments were repeated for a syrup having viscosity of 56 cP at 25°C and for citrated cat blood plasma, having viscosity slightly greater than water, and no cavities appeared in any case. A maximum rod velocity of 18 m/s was reached in both experiments. These results suggest that cavitation inception presumably induced by the motion of an immersed body is promoted by increasing the liquid viscosity.

As noted by Joseph (1998) the effect of viscosity in cavitation phenomena has been indirectly accounted for through its impact on the structure of the fluid motion, as in the case of separation spots and pressure profiles. For flow past axisymmetric bodies that exhibit laminar boundary layer separation, Arakeri and Acosta (1973) observed that cavitation inception occurs within the region of separated flow. Similarly, Franc and Michel (1985) noticed that detachment of cavities occurs in the recirculation zone, behind laminar boundary layer separation, instead of nearby the point of minimum pressure for flow past circular and elliptical cylinders. Photographs included in the book by Young (1989) for flow past a 1-in-diameter sphere show that inception of cavitation occurs in the shear layer formed between the main stream and the recirculation zone in the wake behind the body. Decreasing the cavitation number associated with the experiment expands the region of cavitation over the surface of the shear layer. By comparing figure H.3 (c) for the streamlines and figure 6.11 (b) for the critical cavitation number distribution in the case of Re =100, one can conjecture, on qualitative grounds, that cavitation events may be generated as traveling nuclei pass through the region of high K_c (the equator of the sphere), where their growth is triggered, and immediately enter the shear layer region carried by the external flow, while becoming visible to the unaided eye. Inside the recirculation zone, the higher values of the critical cavitation number occur in the neighbourhood of the point of boundary layer separation (about $\theta = 60^o$; see figures H.2 (b) and H.3 (c)), which is also a low velocity region. Thus, it seems likely that cavities become visible in this region of the wake.

The main prediction of this work is that highly viscous fluids are at greater risk to cavitation at a fixed cavitation number. This prediction appears to be new since the question seems, surprisingly, not to have been addressed in the theoretical cavitation literature.

Bibliography

Abramowitz, M.; Stegun, I.A. (Ed.) 1964 *Handbook of Mathematical Functions with Formulas, Graphs, and Mathematical Tables.* U.S. Department of Commerce. Tenth printing, December 1972.

Ackeret, J. 1952 Über exakte Lösungen der Stokes–Navier–Gleichungen inkompressibler Flüssigkeiten bei veränderten Grenzbedingungen. *Z. Angew. Math. Phys.*, **3**, 259–270.

Andersson, R.; Andersson, B. 2006 On the breakup of fluid particles in turbulent flows. *AIChE J.*, **52**, 2020–2030.

Apfel, R.E. 1970 The role of impurities in cavitation–threshold determination. *J. Acoust. Soc. Am.*, **48**, 1180–1186.

Arakeri, V.H.; Acosta, A.J. 1973 Viscous effects in the inception of cavitation on axisymmetric bodies. *J. Fluids Eng.*, **95**, 519–527.

Archer, L.A.; Ternet, D.; Larson, R.G. 1997 'Fracture' phenomena in shearing flow of viscous liquids. *Rheol. Acta.*, **36**, 579–584.

Ashmore, J.; del Pino, C.; Mullin, T. 2005 Cavitation in a lubrication flow between a moving sphere and a boundary. *Phys. Rev. Lett.*, **94**, 124501.

Bair, S.; Winer, W.O. 1990 The high shear stress rheology of liquid lubricants at pressure 0f 2 to 200 MPa. *J. Tribol.*, **114**, 246–253.

Bair, S.; Winer, W.O. 1992 The high pressure high shear stress rheology of liquid lubricants. *J. Tribol.*, **114**, 1–13.

Baker G. R.; Meiron D. I.; Orszag S. A. 1980 Vortex simulations of the Rayleigh-Taylor instability. *Phys. Fluids,* **23**, 1485–1490.

Baker G. R.; Meiron D. I.; Orszag S. A. 1982 Generalized vortex methods for free-surface flow problems. *J. Fluid Mech.,* **123**, 477–501.

Baker G. R.; Meiron D. I.; Orszag S. A. 1984 Boundary integral methods for axisymmetric and three-dimensional Rayleigh-Taylor instability problems. *Physica,* **12 D**, 19–31.

Banerjee, P. K.; Butterfield, R. 1981 *Boundary Element Methods in Engineering Science*. McGraw-Hill, Inc.

Basaran, O. 1992 Nonlinear oscillations of viscous liquid drops. *J. Fluid Mech.*, **241**, 169–198.

Basset, A. B. 1888 A Treatise on Hydrodynamics with Numerous Examples, vol. 2. Deighton, Bell and Co., Cambridge. Reprinted by Dover, New York, in 1961.

Batchelor, G. K. 1967 *An Introduction to Fluid Dynamics*. Cambridge University Press.

Becker, A. A. 1992 *The Boundary Element Method in Engineering–A Complete Course*. McGraw-Hill.

Bialecki, R.A.; Herding, U.; Köhler, O.; Kuhn, G. 1996 Weakly singular 2D quadratures for some fundamental solutions. *Eng. Anal. Boundary Elements,* **18**, 333-336.

Billet, M.L. 1985 Cavitation nuclei measurements–A review. *ASME Cavitation and Multiphase Flow Forum–1985*, ASME, New York, FED **23**, 31–38.

Blake, J.R.; Gibson, D.C. 1987 Cavitation bubbles near boundaries. *Ann. Rev. Fluid Mech.*, **19**, 99–123.

Bolaños-Jiménez, R.; Sevilla, A.; Martínez-Bazán, C.; van der Meer, D.; Gordillo, J. M. 2009 The effect of liquid viscosity on bubble pinch-off. *Phys. Fluids*, **21**, 072103.

Bowman, J. J.; Senior, T. B. A.; Uslenghi, P. L. E. (Ed.) 1987 *Electromagnetic and Acoustic Scattering by Simple Shapes*. Hemisphere Publishing Corporation.

Brebbia C. A.; Telles J. C. F.; Wrobel L. C. 1984 *Boundary Element Techniques: Theory and Applications in Engineering*. Springer-Verlag.

Briggs, L.J. 1950 Limiting negative pressure of water. *J. Appl. Phys.*, **21**, 721–722.

Bunner, B.; Tryggvason, G. 2002a Dynamics of homogeneous bubbly flows. Part 1. Rise velocity and microstructure of the bubbles. *J. Fluid Mech.*, **466**, 17–52.

Bunner, B.; Tryggvason, G. 2002b Dynamics of homogeneous bubbly flows. Part 2. Velocity fluctuations. *J. Fluid Mech.*, **466**, 53–84.

Byatt-Smith, J. G. B.; Longuet-Higgins, M. S. 1976 On the speed and profile of steep solitary waves. *Proc. Roy. Soc. Lond. A,* **350**, 175–189.

Burton, J. C.; Waldrep, R.; Taborek, P. 2005 Scaling and instabilities in bubble pinch-off. *Phys. Rev. Lett.*, **94**, 184502.

Canot E.; Davoust L.; Hammoumi M. E.; Lachkar D. 2003 Numerical simulation of the buoyancy-driven bouncing of a 2-D bubble at a horizontal wall. *Theort. Comput. Fluid Dynamics,* **17**, 51–72.

Chandrasekhar, S. 1959 *The oscillations of a viscous liquid globe.* Proc. London Math. Soc., **9**, 141–149.

Chandrasekhar, S. 1961 *Hydrodynamic and Hydromagnetic Stability.* Oxford University Press.

Chen, Y.; Israelachvili, J. 1991 New mechanism of cavitation damage. *Science*, **252**, 1157–1160.

Chen, Y.J.; Steen, P.H. 1997 Dynamics of inviscid capillary breakup: Collapse and pinchoff of a film bridge. *J. Fluid Mech.*, **341**, 245-267.

Chhabra, R. P. 1995 Further remarks on the drag of a swarm of bubbles. *Int. J. Engng Sci.*, **33**, 1849–1852.

Cohen, I; Brenner, M. P.; Eggers, J.; Nagel, S. R. 1999 Two fluid drop snap-off problem: Experiments and theory. *Phys. Rev. Lett.*, **83**, 1147–1150.

Crum, L.A. 1982 Nucleation and stabilization of microbubbles in liquids. *Appl. Sci. Res.*, **38**, 101–115.

Cunningham, E. 1910 On the velocity of steady fall of spherical particles through fluid medium. *Proc. Roy. Soc. A*, **83**, 357.

Day R. F.; Hinch E. J.; Lister J. R. 1998 Self-similar capillary pinchoff of an inviscid fluid. *Phys. Rev. Lett.,* **80**, 704–707.

Dodd, T.L.; Hammer, D.A.; Sangani, A.S.; Koch, D.L. 1995 Numerical simulations of the effect of hydrodynamic interactions on diffusivities of integral membrane proteins. *J. Fluid Mech.*, **293**, 147–180.

Doshi, P.; Cohen, I.; Zhang, W. W.; Siegel, M.; Howell, P.; Basaran, O. A.; Nagel, S. R. 2003 Persistence of memory in drop breakup: The breakdown of universality. *Science*, **302**, 1185–1188.

Dryden, H.; Murnaghan, F.; Bateman, H. 1956 *Hydrodynamics*; Dover (a complete unabridged reprinting of the National Research Council's Bulletin 84, 1931). (Part II, §1.1).

Eastwood, C. D.; Armi, L.; Lasheras, J. C. 2004 The breakup of immiscible fluids in turbulent flows. *J. Fluid Mech.*, **502**, 309–333.

Eggers, J. 1993 Universal pinching of 3D axisymmetric free-surface flows. *Phys. Rev. Lett.*, **71**, 3458–3460.

EGGERS, J.; FONTELOS, M. A.; LEPPINEN, D. M.; SNOEIJER, J. 2007 Theory of the collapsing axisymmetric cavity. *Phys. Rev. Lett.*, **98**, 094502.

EGGERS, J.; VILLERMAUX, E. 2008 Physics of liquids jets. *Rep. Prog. Phys.*, **71**, 1–79.

EL-KAISSY, M. M.; HOMSY, G. M. 1973 A theoretical study of pressure drop and transport in packed beds at intermediate Reynolds numbers. *Ind. Eng. Chem. Fundam.*, **12**, 82–90.

ESMAEELI, A.; TRYGGVASON, G. 1998 Direct numerical simulations of bubbly flows. Part I-Low Reynolds number arrays. *J. Fluid Mech.*, **377**, 313–345.

ESMAEELI, A.; TRYGGVASON, G. 1999 Direct numerical simulations of bubbly flows. Part II-Moderate Reynolds number arrays *J. Fluid Mech.*, **385**, 325–358.

ESMAEELI, A.; TRYGGVASON, G. 2005 A direct numerical simulation study of the buoyant rise of bubbles at $O(100)$ Reynolds number. *Phys. Fluids*, **17**, 093303.

FARRELL, K.J. 2003 Eulerian/Lagrangian analysis for the prediction of cavitation inception. *J. Fluids Eng.*, **125**, 46–52.

FISHER, J.C. 1948 The fracture of liquids. *J. Appl. Phys.*, **19**, 1062–1067.

Fluent 6.1. 2003 User's Guide. Fluent Inc. Lebanon, NH.

FOSDICK, R.; ROYER-CARFAGNI, G. 2005 A Stokes theorem for second order tensor fields and its implications in continuum mechanics. *Int. J. Non-Linear Mech.*, **40**, 381–386.

FOTEINOPOULOU, K.; MAVRANTZAS, V. G.; TSAMOPOULOS, J. 2004 Numerical simulation of bubble growth in Newtonian and viscoelastic filaments undergoing stretching. *J. Non-Newtonian Fluid Mech.*, **122**, 177–200.

FRANC, J. P.; MICHEL, J. M. 1985 Attached cavitation and the boundary layer; experimental investigation and numerical treatment. *J. Fluid Mech.*, **154**, 63–90.

FUNADA, T.; JOSEPH, D.D. 2001 Viscous potential flow analysis of Kelvin-Helmholtz instability in a channel. *J. Fluid Mech.*, **445**, 263–283.

FUNADA, T.; JOSEPH, D. D. 2002 Viscous potential flow analysis of capillary instability. *Int. J. Multiphase Flow*, **28**, 1459–1478.

FUNADA, T.; WANG, J.; JOSEPH, D. D. 2006 Viscous potential flow analysis of stress induced cavitation of aperture flow. *Atomization and Sprays*, **16**, 763–776.

GAVRILYUK, S. L.; TESHUKOV, V. M. 2005 Drag force acting on a bubble in a cloud of compressible spherical bubbles at large Reynolds numbers. *Eur. J. Mech. B/Fluids*, **24**, 468–477.

GEORGESCU S. C.; ACHARD J. L.; CANOT E. 2002 Jet drops ejection in bursting gas bubbles processes. *Eur. J. Mech. B/Fluids,* **21**, 265–280.

Gordillo, J. M. 2008 Axisymmetric bubble collapse in a quiescent liquid pool. I. Theory and numerical simulations. *Phys. Fluids*, **20**, 112103.

Gordillo, J. M.; Fontelos, M. A. 2007 Satellites in the inviscid breakup of bubbles. *Phys. Rev. Lett.*, **98**, 144503.

Gordillo, J. M.; Sevilla, A.; Rodríguez-Rodríguez, J.; Martínez-Bazán, C. 2005 Axisymmetric bubble pinch-off at high Reynolds numbers. *Phys. Rev. Lett.*, **95**, 194501.

Grilli, S. T.; Guyenne P.; Dias, F. 2001 A fully non-linear model for three-dimensional overturning waves over an arbitrary bottom. *Int. J. Numer. Meth. Fluids,* **35**, 829–867.

Grilli, S. T.; Horrillo, J. 1997 Numerical generation and absorption of fully nonlinear periodic waves. *J. Eng. Mech.,* October, 1060–1069.

Grilli, S. T.; Skourup, J.; Svendsen, I. A. 1989 A efficient boundary element method for nonlinear water waves. *Eng. Anal. Boundary Elements,* **6**, 97–107.

Grilli, S. T.; Subramanya, R. 1994 Quasi-singular integrals in the modeling of nonlinear water waves in shallow water. *Eng. Anal. Boundary Elements,* **13**, 181–191.

Grilli, S. T.; Subramanya, R. 1996 Numerical modeling of wave breaking induced by fixed or moving boundaries. *Comput. Mech.,* **17**, 374–391.

Guido, S.; Greco, F. 2004 Dynamics of a liquid drop in a flowing immiscible liquid. In *Rheology Reviews 2004*; Binding, D.M.; Walters, K., Eds. The British Society of Rheology, 99–142.

Happel, J. 1958 Viscous flow in multiparticle systems: Slow motion of fluids relative to beds of spherical particles. *A.I.Ch.E. Journal*, **4**, 197–201.

Happel, J.; Brenner, H. 1965 *Low Reynolds Number Hydrodynamics*; Prentice-Hall, Inc. (§8.4).

Harvey, E.N.; Barnes, D.K.; McElroy, W.D.; Whiteley, A. H.; Pease, D.C.; Cooper, K.W. 1944a Bubble formation in animals, I. Physical factors. *J. Cell. Comp. Physiol.*, **44**, 1–22.

Harvey, E.N.; Whiteley, A.H.; McElroy, W.D.; Pease, D.C.; Barnes, D.K. 1944b Bubble formation in animals, II. Gas nuclei and their distribution in blood and tissues. *J. Cell. Comp. Physiol.*, **44**, 23–34

Harvey, E.N.; McElroy, W.D.; Whiteley, A. H. 1947 On cavity formation in water. *J. Appl. Phys.*, **18**, 162–172.

Heister, S.D. 1997 Boundary element methods for two-fluid free surface flows. *Eng. Anal. Boundary Elements*, **19**, 309–317.

Hilbing, J.H.; Heister, S.D.; Spangler, C.A. 1995 A boundary-element method for atomization of a finite liquid jet. *Atomization and Sprays*, **5**, 621–638.

Hinze, J. O. 1955 Fundamentals of the hydrodynamics mechanism of splitting in dispersion processes. *AIChE J.*, **1**, 289–295.

Ilinskii, Y.; Hamilton, M. F.; Zabolotskaya, E. A. 2007 Bubble interaction dynamics in Lagrangian and Hamiltonian mechanics. *J. Acoustic. Soc. Am.*, **121**, 786–795.

Ishii, M.; Zuber, N. 1979 Drag Coefficient and Relative Velocity in Bubbly, Droplet or Particulate Flows. *AIChE J.*, **25**, 843–855.

Jaiswal, A. K.; Sundararajan, T.; Chhabra, R. P. 1992 Simulation of Non-Newtonian fluid flow through fixed and fluidized beds of spherical particles. *Numer. Heat Transfer, Part A*, **21**, 275–297.

Jaswon M. A.; Symm G. T. 1977 *Integral Equation Methods in Potential Theory and Elastostatics*. Academic Press INC.

Johnson, T. A.; Patel, V. C. 1999 Flow past a sphere up to a Reynolds number of 300. *J. Fluid Mech.,* **378**, 19–70.

Joseph, D. D. 1995 Cavitation in a flowing liquid. *Physical Review E*, **51**, R1649–R1650.

Joseph, D. D. 1998 Cavitation and the state of stress in a flowing liquid. *J. Fluid Mech.*, **366**, 367–378.

Joseph, D. D. 2003 Viscous potential flow. *J. Fluid Mech.*, **479**, 191–197.

Joseph, D. D. 2006 Potential flow of viscous fluids: Historical notes. *Int. J. Multiphase Flow*, **32**, 285–310.

Joseph, D. D. 2006 Helmholtz decomposition coupling rotational to irrotational flow of a viscous fluid. *Proc. Nat. Acad. Sci. U.S.A.*, **103**, 14272–14277.

Joseph, D. D. 2008 The role of potential flow in the theory of the Navier–Stokes equations. In *Advances in Mathematical Fluid Mechanics*. (Dedicated to Giovanni Paolo Galdi on the occasion of his 60th birthday); Rannacher, R.; Sequeira, A., Eds.; Springer.

Joseph, D. D.; Funada, T.; Wang, J. 2007 *Potential Flows of Viscous and Viscoelastic Fluids*. Cambridge University Press.

Joseph, D. D.; Liao, T.Y. 1994a Potential flows of viscous and viscoelastic fluids. *J. Fluid Mech.,* **265**, 1–23.

Joseph, D. D.; Liao, T.Y. 1994b Viscous and viscoelastic potential flow. In *Trends and Perspectives in Applied Mathematics.* vol. 100; Sirovich, S.; Arnol'd, V., Eds.; pp. 1–54. Springer.

Joseph, D. D.; Liao, T. Y.; Hu, H. H. 1993 Drag and Moment in Viscous Potential Flow. *Eur. J. Mech.* B/*Fluids*, **12**, 97–106.

Joseph, D.D.; Renardy, Y.Y. 1993 *Fundamentals of Two-Fluid Dynamics, Part I: Mathematical Theory and Applications*. Springer-Verlag.

Joseph, D. D.; Wang, J. 2004 The dissipation approximation and viscous potential flow. *J. Fluid Mech.*, **505**, 365–377.

Kang, I.S.; Leal, L.G. 1987 Numerical solution of axisymmetric, unsteady free boundary problems at finite Reynolds number. I. Finite-difference scheme and its application to the deformation of a bubble in a uniaxial straining flow. *Phys. Fluids*, **30**, 1929–1940.

Kang, I. S.; Leal, L. G. 1988 The drag coefficient for a spherical bubble in a uniform streaming flow. *Phys. Fluids*, **31**, 233–237.

Kang, I.S.; Leal, L.G. 1990 Bubble dynamics in time-periodic straining flows. *J. Fluid Mech.*, **218**, 41–69.

Kang, S-Y.; Sangani, A.S.; Tsao, H-K.; Koch, D.L. 1997 Rheology of dense bubble suspensions. *Phys. Fluids*, **9**, 1540–1561.

Keim, N. C.; Møller, P.; Zhang, W. W.; Nagel, S. R. 2003 Breakup of air bubbles in water: Memory and breakdown of cylindrical symmetry. *Phys. Rev. Let.*, **97**, 144503.

Keller J. B.; Miksis M. J. 1983 Surface tension driven flows. *SIAM J. Appl. Math.,* **43**, 268–277.

Keller, J. B.; Miksis, M. J. 1983 Surface tension driven flows. *SIAM J. Appl. Math.*, **43**, 268–277.

Kendoush, A. A. 2001 Hydrodynamic model for bubbles in a swarm. *Chem. Eng. Sci.*, **56**, 235–238.

Knapp, R.T. 1958 Cavitation and nuclei. *Trans. ASME*, **80**, 1315–1324.

Knapp, R.T.; Daily, J.W.; Hammit, F.G. 1970 Cavitation. McGraw-Hill, Inc.

Kolmogorov, A. N. 1949 On the breakage of drops in a turbulent flow. *Dokl. Akad. Navk. SSSR*, **66**, 825–828.

Koo, S.; Sangani, A.S. 2002 Effective-medium theories for predicting hydrodynamics transport properties of bidisperse suspensions. *Phys. Fluids*, **14**, 3522–3533.

Koo, S.; Sangani, A.S. 2003 Mass transfer coefficients for laminar longitudinal flow in hollow-fibre contactors. *J. Fluid Mech.*, **484**, 255–282.

Kottke, P.A.; Bair, S.; Winer, W.O. 2003 The measurement of viscosity of liquids under tension. *J. Tribol.*, **125**, 260–266.

KOTTKE, P.A.; BAIR, S.; WINER, W.O. 2005 Cavitation in creeping shear flows. *AIChE J.*, **51**, 2150–2170.

KUHL, T.; RUTHS, M.; CHEN, Y.; ISRAELACHVILI, J. 1994 Direct visualization of cavitation and damage in ultrathin liquid films. *J. Heart Valve Disease*, **3**, 117–127.

KUHN DE CHIZELLE, Y.; BRENNEN, C.E. 1993 Comparison of observed and calculated shapes of travellingcavitation bubbles. *Proc. IUTAM Symp. on Bubble Dynamics and Interface Phenomena, Birmingham, UK.* 207–217.

KUHN DE CHIZELLE, Y.; CECCIO, S.L.; BRENNEN, C.E. 1995 Observations and scaling of travelling bubble cavitation. *J. Fluid Mech.*, **293**, 99–126.

KULKARNI, A.; JOSHI, J. 2005 Bubble Formation and Bubble Rise Velocity in Gas-Liquid Systems: A Review. *Ind. Eng. Chem. Res.*, **44**, 5873–5931.

KUSHCH, V.; SANGANI, A. S.; SPELT, P. D. M.; KOCH, D. 2002 Finite-Weber-number motion of bubbles through a nearly inviscid liquid. *J. Fluid Mech.*, **460**, 241–280.

KUWABARA, S. 1959 The forces experienced by randomly distributed parallel circular cylinders or spheres in a viscous flow at small Reynolds numbers. *J. Phys. Soc. Japan*, **14**, 527–532.

LAMB, H. 1881 On the oscillations of a viscous spheroid. *Proc. Lond. Math. Soc.*, **13**, 51–66.

LAMB, H. 1932 *Hydrodynamics*. Sixth edition. Cambridge University Press. Reprinted by Cambridge University Press, 1993.

LANDAU, L.D.; LIFSHITZ, E.M. 1959 *Fluid Mechanics*. Volume 6 of *Course of Theoretical Physics*. First edition. Pergamon Press. Reprinted by Pergamon Press in 1986.

LECLAIR, B. P.; HAMIELEC, A. E. 1971 Viscous flow through particle assemblages at intermediate Reynolds numbers—A cell model for transport in bubble swarms. *Can. J Chem. Engng.*, **49**, 713–720.

LÉGER, D.; ASKOVIC, R. 2006 Viscid contributions to the hydrodynamic flows past a rising spherical gas bubble with a time-dependent radius. *Int. J. Non-Linear Mech.*, **41**, 247–257.

LEPPINEN, D.; LISTER, J.R. 2003 Capillary pinch-off in inviscid fluids. *Phys. Fluids*, **15**, 568–578.

LEVICH, V. G. 1949 The motion of bubbles at high Reynolds numbers. *Zh. Eksp. Teor. Fiz.*, **19**, 18–24.

LEVICH, V. G. 1962 *Physicochemical Hydrodynamics*; Prentice-Hall, Inc. (§§80-83).

LIGGUET, J. A.; LIU, P. L.-F. 1984 Application of Boundary Element Methos in Fluid Mechanics. Vol. 1 of Topics in Boundary Element Research (ed. C. A. Brebbia.) Springer-Verlag, Chapter 4.

LISTER, J. R.; STONE, H. 1998 Capillary breakup of a viscous thread surrounded by another viscous fluid. *Phys. Fluids*, **10**, 2758–2764.

LIU, Z.; BRENNEN, C. E. 1998 Cavitation nuclei population and event rates. *J. Fluids Eng.*, **120**, 728–737.

LONGUET-HIGGINS, M. 1997 Viscous dissipation in steep capillary-gravity waves. *J. Fluid Mech.*, **344**, 271–289.

LONGUET-HIGGINS, M. S.; COKELET, E. D. 1976 The deformation of steep surface waves on water. I. A numerical method of computation. *Proc. R. Soc. London Ser. A*, **350**, 1-26.

LORD KELVIN 1890 Oscillations of a liquid sphere, in *Mathematical and Physical Papers.* Clay and Sons, London, Vol. 3, pp. 384–386.

LORD RAYLEIGH 1896 *The Theory of Sound.* Second edition. MacMillan, London. Reprinted by Dover, New York, 1945. Vol. 2, p. 371.

LUNDGREN, T.S.; MANSOUR, N.N. 1988 Oscillations of drops in zero gravity with weak viscous effects. *J. Fluid Mech.*, **194**, 479–510.

LUNDGREN T. S.; MANSOUR N. N. 1991 Vortex ring bubbles. *J. Fluid Mech.,* **224**, 177–196.

MACHANE R.; CANOT E. 1997 High-order schemes in boundary element methods for transient non-linear free surface problems. *Int. J. Numer. Methods Fluids,* **24**, 1049–1072.

MAGNAUDET, J.; EAMES, I. 2000 The motion of high-Reynolds-number bubbles in inhomogeneous flows. *Annu. Rev. Fluid Mech.*, **32**, 659–708.

MAGNAUDET, J.; RIVERO, M.; FABRE, J. 1995 Accelerated flows past a rigid sphere or a spherical bubble. Part 1. Steady straining flow. *J. Fluid Mech.*, **284**, 97–135.

MAGNAUDET, J.; LEGENDRE, D. 1998 The viscous drag force on a spherical bubble with a time-dependent radius. *Phys. Fluids*, **10**, 550–554.

MANJUNATH, M.; TRIPATHI, A.; CHHABRA, R. P.; SUNDARARAJAN, T. 1994 Numerical simulation of the drag on a swarm of bubbles. *Int. J. Engng. Sci.*, **32**, 927–933.

MANSOUR N. N.; LUNDGREN T. S. 1990 Satellite formation in capillary jet breakup. *Phys. Fluids,* A **2**, 1141–1144.

MARRUCCI, G. 1965 Rising velocity of a swarm of spherical bubbles. *Ind. Engng. Chem. Fundam.*, **5**, 224–229.

MARTÍNEZ-BAZÁN, C.; MONTAÑES, J. L.; LASHERAS, J. C. 1999a On the breakup of an air bubble injected into a fully developed turbulent flow. Part 1. Breakup frequency. *J. Fluid Mech.*, **401**, 157–182.

MARTÍNEZ-BAZÁN, C.; MONTAÑES, J. L.; LASHERAS, J. C. 1999b On the breakup of an air bubble injected into a fully developed turbulent flow. Part 2. Size PDF of the resulting daughter bubbles. *J. Fluid Mech.*, **401**, 183–207.

MARTÍNEZ-MERCADO, J.; PALACIOS-MORALES, C.A.; ZENIT, R. 2007 Measurement of pseudoturbulence intensity in monodispersed bubbly liquids for $10 < Re < 500$. *Phys. Fluids*, **19**, 103302.

MELVILLE, W. K. 1996 The role of surface-wave breaking in air-sea interaction. *Ann. Rev. Fluid Mech.*, **18**, 279–321.

MEIRON, D. I.; SAFFMAN, P. G. 1983 Overhanging interfacial gravity waves of large amplitude. *J. Fluid Mech.,* **129**, 213–218.

MIKSIS, M.; VANDEN–BROECK, J. M. V.; KELLER, J. B. 1981 Axisymmetric bubble or drop in a uniform flow. *J. Fluid Mech.,* **108**, 89–100.

MIKSIS, M.; VANDEN–BROECK, J.-M.; KELLER, J. B. 1982 Rising bubbles. *J. Fluid. Mech.*, **123**, 31–41.

MILLER, C. A.; SCRIVEN, L. E. 1968 The oscillations of a fluid droplet immersed in another fluid. *J. Fluid Mech.*, **32**, 417–435.

MILNE-THOMSON, L. M. 1968 *Theoretical Hydrodynamics*. Fifth Edition, Macmillan & Co. Ltd (unabridge republication by Dover, New York, in 1996). (§3.75).

MOORE, D. W. 1959 The rise of a gas bubble in a viscous liquid. *J. Fluid. Mech.*, **6**, 113–130.

MOORE, D. W. 1963 The boundary layer on a spherical gas bubble. *J. Fluid. Mech.*, **16**, 161–176.

MOORE, D. W. 1965 The Velocity of Rise of Distorted Gas Bubbles in a Liquid of Small Viscosity. *J. Fluid Mech.*, **23**, 749–766.

NICKLIN, D. J. 1962 Two-phase bubble flow. *Chem. Eng. Sci.*, **17**, 693–702.

OĞUZ H.; PROSPERETTI A. 1989 Surface-tension effects in the contact of liquid surfaces. *J. Fluid Mech.,* **203**, 149–171.

OĞUZ H.; PROSPERETTI A. 1990 Bubble entrainment by the impact of drops on liquid surfaces. *J. Fluid Mech.,* **219**, 143–179.

OĞUZ H.; PROSPERETTI A. 1993 Dynamics of bubble growth and detachment from a needle. *J. Fluid Mech.,* **257**, 111–145.

Ohl, C. D.; Tijink, A.; Prosperetti, A. 2003 The added mass of an expanding bubble. *J. Fluid Mech.*, **482**, 271–290.

Padrino, J.C.; Funada, T.; Joseph, D.D. 2008 Purely irrotational theories for the viscous effects on the oscillations of drops and bubbles. *Int. J. Multiphase Flow*, **34**, 61–75.

Panton, R. L. 2005 *Incompressible Flow*. Third Edition, J. Wiley. (§10.7).

Papageorgiou, D.T. 1995 On the breakup of viscous liquid threads. *Phys. Fluids*, **7**, 1529–1544.

Park, H.; Heister, S. D. 2006 Nonlinear simulation of free surfaces and atomization in pressure swirl atomizers. *Phys. Fluids*, **18**, 052103.

Patzek, T.W.; Benner, R.E.; Basaran, O.A.; Scriven, L.E. 1991 Nonlinear oscillations of inviscid free drops. *J. Comp. Phys.*, **97**, 489–515.

Pereira, A.; McGrath, G.; Joseph, D.D. 2001 Flow and stress induced cavitation in a journal bearing with axial throughput. *J. Tribol.*, **123**, 742–754.

Plesset, M. 1969 Tensile strength of liquids. *Office of Naval Res. Rep.* 85–4.

Poletto, M.; Joseph, D. D. 1995 Effective density and viscosity of a suspension. *J. Rheol.*, **39**, 323–343.

Pozrikidis, C. 1992 *Boundary Integral and Singularity Methods for Linearized Viscous Flow*. Cambridge University Press.

Press, W. H.; Teukolsky, S. A.; Vetterling, W. T.; Flannery, B. P. 2002 *Numerical Recipes in Fortran 90: The Art of Parallel Scientific Computing. Volume 2 of Fortran Numerical Recipes.* Second Edition.

Prosperetti, A. 1976 Viscous effects on small-amplitude surface waves. *Phys. Fluids*, **19**, 195–203.

Prosperetti, A. 1977 Viscous effects on perturbed spherical flows. *Quart. Appl. Math.*, **35**, 339–352.

Prosperetti, A. 1980a Normal-mode analysis for the oscillations of a viscous liquid drop in an immiscible liquid. *J. Méc.*, **19**, 149–182.

Prosperetti, A. 1980b Free oscillations of drops and bubbles: the initial value problem. *J. Fluid Mech.*, **100**, part 2, 333–347.

Pruppacher, H. R.; Le Clair, B. P.; Hamiliec, A. E. 1970 Some relations between drag and flow pattern of viscous flow past a sphere and a cylinder at low an intermediate Reynolds numbers. *J. Fluid Mech.*, **44**, 781–790.

QUAN, S.; HUA, J. 2008 Numerical studies of bubble necking in viscous liquids. *Phys. Rev. Lett.*, **77**, 066303.

RAMASWAMY, S.; LEAL, L. G. 1997 A note on inertial effects in the deformation of Newtonian drops in a uniaxial extensional flow. *Int. J. Multiphase Flow*, **23**, 561–574.

REID, W.H. 1960 The oscillations of a viscous liquid drop. *Quart. Appl. Math.*, **18**, 86–89.

REVUELTA, A.; RODRÍGUEZ-RODRÍGUEZ, J.; MARTÍNEZ-BAZÁN, C. 2006 Bubble break-up in a straining flow at finite Reynolds numbers. *J. Fluid Mech.*, **551**, 175–184.

RICHARDSON, J. F.; ZAKI, W. N. 1954 Sedimentation and fluidisation: Part I. *Trans. Instn. Chem. Engrs.*, **32**, 35–53.

RISSO, F; FABRE, J. 1998 Oscillations and breakup of a bubble immersed in a turbulent field. *J. Fluid Mech.*, **372**, 323–355.

RODRÍGUEZ-RODRÍGUEZ, J. 2004 *Estudio de la rotura de gotas y burbujas en flujos a altos números de Reynolds.* PhD thesis Universidad Carlos III de Madrid, Madrid.

RODRÍGUEZ-RODRÍGUEZ, J; GORDILLO, J. M.; MARTÍNEZ-BAZÁN, C. 2006 Breakup time and morphology of drops and bubbles in a high-Reynolds-number flow. *J. Fluid Mech.,* **548**, 69–86.

RODRÍGUEZ-RODRÍGUEZ, J.; MARTÍNEZ-BAZÁN, C.; MONTAÑES, J. L. 2003 A novel particle tracking and break-up detection algorithm: application to the turbulent break-up of bubbles. *Meas. Sci. Technol.*, **14**, 1328–1340.

ROOS, F. W.; WILLMARTH, W. W. 1971 Some experimental results on sphere and disk drag. *AIAA J.*, **9**, 285–291.

RYSKIN, G; LEAL, L.G. 1984 Numerical solution of free boundary problems in fluid mechanics. Part 3. Bubble deformation in an axisymmetric straining flow. *J. Fluid Mech.*, **148**, 37–43.

SANGANI, A. S. 1991 A pairwise interaction theory for determining the linear acoustic properties of dilute bubbly liquids. *J. Fluid Mech.*, **232**, 221–284.

SANGANI, A. S.; DIDWANIA, A. K. 1993 Dynamic Simulations of Flow of Bubbly Liquids at Large Reynolds Numbers. *J. Fluid Mech.*, **250**, 307–337.

SANGANI, A.S.; MO, G. 1997 Elastic interactions in particulate composites with perfect as well as imperfect interfaces. *J. Mech. Phys. Solids*, **45**, 2001–2031.

SANKARANARAYANAN, K.; SHAN, X.; KEVREKIDIS, I.G.; SUNDARESAN, S. 2002 Analysis of Drag and Virtual Mass Forces in Bubbly Suspensions using an Implicit Formulation of the Lattice Boltzmann Method. *J. Fluid Mech.*, **452**, 61–96.

SHERWOOD, J. D. 1999 The force on a growing bubble in potential flow. *Int. J. Multiphase Flow*, **25**, 705–713.

SIEROU, A.; LISTER, J. R. 2003 Self-similar solutions for viscous capillary pinch-off. *J. Fluid Mech.*, **497**, 381–403.

SINGHAL, A. K.; ATHAVALE, M. M.; LI, H.; JIANG, Y. 2002 Mathematical basis and validation of the full cavitation model. *J. Fluids Eng.*, **124**, 617–624.

SMEREKA, P. 1993 On the motion of bubbles in a periodic box. *J. Fluid Mech.*, **254**, 79–112.

SPELT, P. D. M.; NORATO, M.A.; SANGANI, A.S.; GREENWOOD, M.S.; TAVLARIDES, L. 2001 Attenuation of sound in concentrated suspensions: Theory and experiments. *J. Fluid Mech.*, **430**, 51–86.

SPELT, P. D. M.; SANGANI, A.S. 1998 Properties and average equations for flows of bubbly liquids. *Appl. Sci. Res.*, **58**, 337–386.

STOKES, G.G. 1851 On the effect of the internal friction of fluids on the motion of pendulums. *Trans. Cambr. Phil. Soc.* **IX**, 8, 106 (read on Dec. 9, 1850) *Mathematical and physical papers* **3**, 1.

STRASBERG, M. 1959 Onset of ultrasonic cavitation in tap water. *J. Acoust. Soc. Am.*, **31**, 163–176.

STRAUSS, W. A. 1992 *Partial Differential Equations, an Introduction.* John Wiley & Sons, Inc.

STROUD, A.H.; SECREST, A.H. 1966 *Gaussian Quadrature Formulae.* Prentice Hall.

SURYO, R.; DOSHI, P.; BASARAN, O. A. 2004 Non-self-similar, linear dynamics during pinch-off of a hollow annular jet. *Phys. Fluids*, **16**, 4177–4184.

TAKEMURA, F.; MAGNAUDET, J. 2004 The history force on a rapidly shrinking bubble rising at finite Reynolds number. *Phys. Fluids*, **16**, 3247–3255.

TAM, P. D. 1982 The unsteady drag on a spherical bubble at large Reynolds Numbers. *Appl. Sci. Res.*, **38**, 247–254.

TANEDA, S. 1956 Experimental investigation of the wake behind a sphere at low Reynolds numbers.. *J. Phys. Soc. Japan*, **11**, 1104–1108.

THORODDSEN, S. T.; ETOH, T. G.; TAKEHARA, K. 2007 Experiments on bubble pinch-off. *Phys. Fluids*, **19**, 042101.

TOMBOULIDES, A. G. 1993 Direct and large-eddy simulation of wake flows: flow past a sphere. PhD thesis, Princeton University.

Tomotika, S. 1935 On the stability of a cylindrical thread of a viscous liquid surrounded by another viscous fluid. *Proc. R. Soc. Lond.* A, **150**, 322–337.

Tsamopoulos, J.A.; Brown, R.A. 1983 Nonlinear oscillations of inviscid drops and bubbles. *J. Fluid Mech.*, **127**, 519–537.

Valentine, R.S.; Sather, N.F.; Heideger, W.J. 1965 The motion of drops in viscous media. *Chem. Eng. Sci.*, **20**, 719–728.

Verdon C. P.; McCory R. L.; Morse R. L.; Baker G. R.; Meiron D. I.; Orszag S. A. 1982 Nonlinear effects of multifrequency hydrodynamic instabilities on ablatively accelerated thin shells. *Phys. Fluids,* **25**, 1653–1674.

Voinov, O. V; Golovin, A. M. 1970 Lagrange equations for a system of bubbles of varying radii in a liquid of small viscosity. *Fluid Dynamics*, **5**, 458–464.

Wang, J.; Joseph, D.D. 2006 Purely irrotational theories of the effect of the viscosity on the decay of free gravity waves. *J. Fluid Mech.*, **559**, 461–472.

Wang, J.; Joseph, D.D.; Funada, T. 2005a Pressure corrections for potential flow analysis of capillary instability of viscous fluids. *J. Fluid Mech.*, **522**, 383–394.

Wang, J.; Joseph, D.D.; Funada, T. 2005b Viscous contributions to the pressure for potential flow analysis of capillary instability of two viscous fluids. *Phys. Fluids*, **17**, 052105.

Wang, N.; Smereka, P. 2003 Effective equations for sound and void wave propagation in bubbly fluids. *SIAM J. Appl. Math.*, **63**, 1849–1888.

White, F. M. 2006 *Viscous Fluid Flow*. 3rd. ed., McGraw-Hill. (§4-10-4).

White, F. M. 1974 *Viscous Fluid Flow*. McGraw-Hill, Inc. (§3.10).

Winer, W.O.; Bair, S. 1987 The influence of ambient pressure on the apparent shear thinning of liquid lubricants–an overlooked phenomena. Conference Publication 1987-5. Vol. 1. London: Inst. Mech. Eng. C190-87, 395–398.

Wrobel, L. C. 2002 *The Boundary Element Method. Vol. 1, Applications in Thermo-Fluids and Acoustics.* John Wiley & Sons, Ltd.

Yang, B.; Prosperetti, A.; Takagi, S. 2003 The transient rise of a bubble subject to shape or volume changes. *Phys. Fluids*, **15**, 2640–2648.

Yin, X.; Koch, D.; Verberg, R. 2006 Lattice-Boltzmann method for simulating spherical bubbles with no tangential stress boundary conditions. *Phys. Rev. E*, **73**, 026301.

Yoon, S. S.; Heister, S. D. 2004 A nonlinear atomization model based on a boundary layer instability mechanism. *Phys. Fluids*, **16**, 47–61.

YOUNG, F.R. 1989 *Cavitation.* McGraw-Hill, Inc.

ZENIT, R.; KOCH, D. L.; SANGANI, A. 2001 Measurements of the average properties of a suspension of bubbles rising in a vertical channel. *J. Fluid Mech.*, **429**, 307–342.

ZHANG, D. Z.; PROSPERETTI, A. 1994 Ensemble phase-averaged equations for bubbly flows. *Phys. Fluids*, **6**, 2956.

ZUBER, N. 1964 On the dispersed two-phase flow in the laminar flow regime. *Chem. Eng. Sci.*, **19**, 897–917.

ZUBER, N.; HENCH, J. 1962 Steady state and transient void fraction of bubbling systems and their operating limits, Part 1: Steady state operation. General Electric Company, General Engineering Laboratory. Report No. 62GL100.

Appendix A

Computation of the coefficients for the quintic splines*

Consider the interval $\ell_1 \leqslant \ell \leqslant \ell_{N+1}$ and let

$$\ell_1 < \ell_2 < \cdots < \ell_N < \ell_{N+1}$$

determine a partition of that interval into N subintervals. Consider also the associated set of ordinates

$$y_1 < y_2 < \cdots < y_N < y_{N+1}$$

as prescribed. We seek a collection of piecewise polynomials of degree five

$$S^{(j)}(\ell) = y_j + \sum_{m=1}^{5} C_m^{(j)} (\ell - \ell_j)^m, \tag{A.1}$$

such that $S^{(j)}(\ell)$ interpolates the values of y in the subinterval $\ell_j \leqslant \ell \leqslant \ell_{j+1}$ for $1 \leqslant j \leqslant N$. These piecewise functions satisfy

$$S^{(j)}(\ell_j) = y_j \qquad \text{for } 1 \leqslant j \leqslant N, \tag{A.2}$$

and $S^{(N)}(\ell_{N+1}) = y_{N+1}$. Moreover, the piecewise functions $S^{(j)}$ and their first fourth derivatives are continuous across the interior points $2 \leqslant j \leqslant N$, i.e.

$$S^{(j-1)}(\ell_j) = S^{(j)}(\ell_j), \tag{A.3a}$$

*The algorithm presented here has been written based upon the routines for quintic splines kindly provided by Prof. David Leppinen of the University of Birmingham to whom we are indebted.

$$\frac{\mathrm{d}^p S^{(j-1)}}{\mathrm{d}\ell^p}(\ell_j) = \frac{\mathrm{d}^p S^{(j)}}{\mathrm{d}\ell^p}(\ell_j), \tag{A.3b}$$

with $1 \leqslant p \leqslant 4$. Such a collection of piecewise fifth-degree polynomials is said to be a set of *quintic splines*. The coefficients $C_m^{(j)}$ are uniquely determined by specifying an appropriate set of end conditions at $\ell = \ell_1$ and $\ell = \ell_{N+1}$. The objective of this Appendix is to briefly describe the computation of the coefficients $C_m^{(j)}$ such that (A.1) satisfies two different sets of end conditions that are suitable for the applications discussed in Chapter 2.

Enforcing constraints (A.3a) and (A.3b), with $p = 1, 2$, in (A.1) leads to the following system of linear equations

$$C_3^{(j-1)}h_{j-1}^3 + C_4^{(j-1)}h_{j-1}^4 + C_5^{(j-1)}h_{j-1}^5 = y_j - y_{j-1} - C_1^{(j-1)}h_{j-1} - C_2^{(j-1)}h_{j-1}^2, \tag{A.4a}$$

$$3C_3^{(j-1)}h_{j-1}^2 + 4C_4^{(j-1)}h_{j-1}^3 + 5C_5^{(j-1)}h_{j-1}^4 = - C_1^{(j-1)} - 2C_2^{(j-1)}h_{j-1} + C_1^{(j)}, \tag{A.4b}$$

$$6C_3^{(j-1)}h_{j-1} + 12C_4^{(j-1)}h_{j-1}^2 + 20C_5^{(j-1)}h_{j-1}^3 = -2C_2^{(j-1)} + 2C_2^{(j)}, \tag{A.4c}$$

where $h_{j-1} = \ell_j - \ell_{j-1}$. After solving this system for the coefficients $C_3^{(j-1)}$, $C_4^{(j-1)}$ and $C_5^{(j-1)}$ we find

$$C_3^{(j-1)}h_{j-1}^3 = 10(y_j - y_{j-1}) - 6C_1^{(j-1)}h_{j-1} - 3C_2^{(j-1)}h_{j-1}^2 - 4C_1^{(j)} + C_2^{(j)}h_{j-1}^2, \tag{A.5a}$$

$$C_4^{(j-1)}h_{j-1}^4 = -15(y_j - y_{j-1}) + 8C_1^{(j-1)}h_{j-1} + 3C_2^{(j-1)}h_{j-1}^2 + 7C_1^{(j)}h_{j-1} - 2C_2^{(j)}h_{j-1}^2, \tag{A.5b}$$

$$C_5^{(j-1)}h_{j-1}^5 = 6(y_j - y_{j-1}) - 3C_1^{(j-1)}h_{j-1} - 3C_1^{(j)}h_{j-1} - C_2^{(j-1)}h_{j-1}^2 + C_2^{(j)}h_{j-1}^2. \tag{A.5c}$$

Continuity of the third derivative at the interior points (A.3b), with $p = 3$, leads

to

$$\lambda^3 C_3^{(j-1)} h_{j-1}^3 + 4\lambda^3 C_4^{(j-1)} h_{j-1}^4 + 10\lambda^3 C_5^{(j-1)} h_{j-1}^5 = C_3^{(j)} h_j^3 \tag{A.6}$$

where $\lambda = h_j/h_{j-1}$. Substitution of (A.5) into (A.6) yields

$$\begin{aligned} 8\lambda^2 C_1^{(j-1)} h_j + \lambda \hat{C}_2^{(j-1)} h_j^2 + 12(\lambda^2 - 1) C_1^{(j)} h_j - 3(1+\lambda)\hat{C}_2^{(j)} h_j^2 \\ - 8C_1^{(j+1)} h_j + \hat{C}_2^{(j+1)} h_j^2 = -20 y_{j+1} + 20(1+\lambda^3) y_j - 20\lambda^3 y_{j-1}, \end{aligned} \tag{A.7}$$

for $2 \leqslant j \leqslant N-1$, where $\hat{C}_2^j = 2C_2^{(j)}$ has been introduced for convenience. Finally, continuity of the fourth derivative at the interior points (A.3b), with $p = 4$, yields

$$\lambda^4 C_4^{(j-1)} h_{j-1}^4 + 5\lambda^4 C_5^{(j-1)} h_{j-1}^5 = C_4^{(j)} h_j^4. \tag{A.8}$$

Substitution of (A.5) into (A.8) results in

$$\begin{aligned} 14\lambda^3 C_1^{(j-1)} h_j + 2\lambda^2 \hat{C}_2^{(j-1)} h_j^2 + 16(1+\lambda^3) C_1^{(j)} h_j + 3(1-\lambda^2)\hat{C}_2^{(j)} h_j^2 \\ + 14C_1^{(j+1)} h_j - 2\hat{C}_2^{(j+1)} h_j^2 = 30 y_{j+1} + 30(\lambda^4 - 1) y_j - 30\lambda^4 y_{j-1}, \end{aligned} \tag{A.9}$$

for $2 \leqslant j \leqslant N-1$.

Taking $2 \leqslant j \leqslant N$ in expressions (A.7) and (A.9) one obtains a set of $2N-2$ equations with $2N+2$ unknowns. Therefore, four additional equations are needed. These come from the constraints imposed at the end points $j = 1$ and $j = N+1$. Two different sets of constraints are enforced at those points, hence leading to two different sets of equations. First, consider the following constraints,

$$\frac{\mathrm{d}S^{(1)}}{\mathrm{d}\ell}(\ell_1) = 0, \qquad \frac{\mathrm{d}^3 S^{(1)}}{\mathrm{d}\ell^3}(\ell_1) = 0, \tag{A.10a}$$

for the first point of the sequence $j = 1$, and

$$\frac{\mathrm{d}S^{(N)}}{\mathrm{d}\ell}(\ell_{N+1}) = 0, \qquad \frac{\mathrm{d}^3 S^{(N)}}{\mathrm{d}\ell^3}(\ell_{N+1}) = 0, \tag{A.10b}$$

for the last point $j = N+1$. Expressions (A.10a) yield

$$C_1^{(1)} = 0, \tag{A.11}$$

and

$$-36C_1^{(1)} h_1 - 9\hat{C}_2^{(1)} h_1^2 - 24C_1^{(2)} h_1 + 3\hat{C}_2^{(2)} h_1^2 = -60(y_2 - y_1), \tag{A.12}$$

respectively, where expression (A.5a) with $j = 2$ has been used to obtain the latter.

To apply conditions (A.10b) it is convenient to introduce a "ghost" subinterval $\ell_{N+1} \leqslant \ell \leqslant \ell_{N+2}$ such that (A.3) are satisfied at point $j = N + 1$. By taking $\mathrm{d}S^{(N+1)}/\mathrm{d}\ell = 0$ at $\ell = \ell_{N+1}$ we find

$$C_1^{(N+1)} = 0, \tag{A.13}$$

and by virtue of (A.3b), with $p = 1$, the first constraint in (A.10b) is satisfied. The second constraint in (A.10b) together with expressions (A.5) with $j = N + 1$ leads to

$$-24C_1^{(N)}h_N - 3\hat{C}_2^{(N)}h_N^2 - 36C_1^{(N+1)}h_N + 9\hat{C}_2^{(N+1)}h_N^2 = -60(y_{N+1} - y_N). \tag{A.14}$$

Expression (A.11) through (A.14) represent the additional four equations needed to close the system of equations (A.7) and (A.9). Thus, the $2N + 2$ unknowns $C_1^{(j)}$ and $\hat{C}_2^{(j)}$ for $1 \leqslant j \leqslant N + 1$ can be found. The constraints given in (A.10) that led to expressions (A.11) through (A.14) are labeled here as "z-type" constraints, because they fit the variation of the z-coordinate at points $\ell = \ell_1$ and $\ell = \ell_{N+1}$; accordingly, they are used to obtain the C_z coefficients needed in (2.40a) of Chapter 2 corresponding to the data for the z-coordinate.

An heptadiagonal system of equations can be formed by arranging the equations in the following order: First, (A.11) and (A.12); next (A.7) and (A.9), one after the other for a given j, varying $2 \leqslant j \leqslant N$, and, finally, (A.13) and (A.14) close the system. This heptadiagonal system can be efficiently solved for the vector of $2N+2$ unknowns

$$\left\{C_1^{(1)}, \hat{C}_2^{(1)}, \ldots, C_1^{(j-1)}, \hat{C}_2^{(j-1)}, C_1^{(j)}, \hat{C}_2^{(j)}, C_1^{(j+1)}, \hat{C}_2^{(j+1)}, \ldots, C_1^{(N+1)}, \hat{C}_2^{(N+1)}\right\}$$

using a banded-matrix solver routine, as the one available from Numerical Recipes (Press et al., 2002).

Turning now our attention to the second set of constraints,

$$S^{(1)}(\ell_1) = 0, \qquad \frac{\mathrm{d}^2 S^{(1)}}{\mathrm{d}\ell^2}(\ell_1) = 0, \qquad \frac{\mathrm{d}^4 S^{(1)}}{\mathrm{d}\ell^4}(\ell_1) = 0, \tag{A.15a}$$

for the first point of the sequence $j = 1$, and

$$S^{(N)}(\ell_{N+1}) = 0, \qquad \frac{\mathrm{d}^2 S^{(N)}}{\mathrm{d}\ell^2}(\ell_{N+1}) = 0, \qquad \frac{\mathrm{d}^4 S^{(N)}}{\mathrm{d}\ell^4}(\ell_{N+1}) = 0, \tag{A.15b}$$

for the last point $j = N+1$. Notice that the first expressions in (A.15a) and (A.15b)

are automatically satisfied provided $y_1 = 0$ and $y_{N+1} = 0$ are specified in the data set. The condition imposed on the fourth derivative in (A.15a) leads to

$$8C_1^{(1)}h_1 + \frac{3}{2}\hat{C}_2^{(1)}h_1^2 + 7C_1^{(2)}h_1 - \hat{C}_2^{(2)}h_1^2 = 15(y_2 - y_1), \tag{A.16}$$

where used has been made of expressions (A.5b) with $j = 2$. The vanishing of the second derivative in (A.15a) results in

$$\hat{C}_2^{(1)} = 0. \tag{A.17}$$

Again, adding a "ghost" subinterval as introduced above and using expressions (A.5) with $j = N + 1$ yields

$$-168C_1^{(N)}h_N - 24\hat{C}_2^{(N)}h_N^2 - 192C_1^{(N+1)}h_N + 36\hat{C}_2^{(N+1)}h_N^2 = -360(y_{N+1} - y_N), \tag{A.18}$$

as a result of the condition on the fourth derivative given in (A.15b), whereas

$$\hat{C}_2^{(N+1)} = 0, \tag{A.19}$$

is obtained from the constraint on the second derivative in (A.15b). Conditions (A.15), which gave rise to expressions (A.16) to (A.19), are labeled as "r-type" end conditions because they specify the correct variation of the r-coordinate in the neighborhood of $\ell = \ell_1$ and $\ell = \ell_{N+1}$, and therefore are adequate to determining the quintic splines coefficients C_r appearing in (2.40b) associated with the r-coordinate data. Expressions (A.16)-(A.19) with (A.7) and (A.9) for $2 \leqslant j \leqslant N$ define a set of $2N + 2$ equations with $2N + 2$ unknowns that can also be arranged as an heptadiagonal system of equations.

Interpolating function

Once the coefficients $C_m^{(j)}$ have been determined, expression (A.1) for the quintic spline can be used to interpolate the values of y or its derivatives with respect to ℓ within the subinterval $\ell_j \leqslant \ell \leqslant \ell_{j+1}$ for $1 \leqslant j \leqslant N$. For coding purposes, it is convenient to write (A.1) in the form

$$S^{(j)}(\ell) = \hat{S}^{(j)}(\hat{t}) = y_j + \hat{t}\Big(C_1^{(j)}h_j + \hat{t}\Big(C_2^{(j)}h_j^2 + \hat{t}\Big(C_3^{(j)}h_j^3 + \hat{t}\Big(C_4^{(j)}h_j^4 + C_5^{(j)}h_j^5\hat{t}\Big)\Big)\Big)\Big), \tag{A.20}$$

where $\hat{t} = (\ell - \ell_j)/h_j$. Differentiation of (A.20) yields

$$\frac{\mathrm{d}S^{(j)}}{\mathrm{d}\ell}(\ell) = \frac{1}{h_j}\frac{\mathrm{d}\hat{S}^{(j)}}{\mathrm{d}\hat{t}}(\hat{t}) = \frac{1}{h_j}\Big(C_1^{(j)}h_j + \hat{t}\Big(2C_2^{(j)}h_j^2 + \hat{t}\Big(3C_3^{(j)}h_j^3 + \hat{t}\Big(4C_4^{(j)}h_j^4 + 5C_5^{(j)}h_j^5\hat{t}\Big)\Big)\Big)\Big), \quad \text{(A.21)}$$

which is used to interpolate values for the first derivative of y. After differentiation of (A.21), the approximation of the second derivative of y with respect to ℓ at the jth-point is given by $\hat{C}_2^{(j)}$ for $1 \leqslant j \leqslant N+1$.

Appendix B

Force on the outer boundary by the dissipation method

In this analysis we obtain an expression for the force D_2 that the fluid in V exerts on the outer boundary S_2 in the $\mathbf{e}_x$-direction by used of the dissipation method. The analysis involves writing the equations of motion with respect to a noninertial coordinate system. This procedure parallels that of §3.2.3 for the force D_1 on the bubble interface S_1 when the outer boundary S_2 is a free surface.

The incompressible Navier–Stokes equations relative to the laboratory reference frame are

$$\rho\left(\frac{\partial \mathbf{u}}{\partial t} + \mathbf{u}\cdot\nabla\mathbf{u}\right) = -\nabla p + \mu\nabla^2\mathbf{u}, \tag{B.1}$$

$$\nabla\cdot\mathbf{u} = 0. \tag{B.2}$$

Consider a noninertial reference frame with an origin that moves with velocity $U\mathbf{e}_x$ relative to the laboratory frame and does not rotate. The transformation between coordinate systems is governed by the relations

$$\hat{\mathbf{x}} = \mathbf{x} - \int_0^t U(t')\mathbf{e}_x dt', \tag{B.3a}$$

$$\hat{t} = t, \tag{B.3b}$$

$$\mathbf{v} = \mathbf{u} - U\mathbf{e}_x. \tag{B.3c}$$

The form of the incompressible Navier–Stokes equations is invariant under the transformation (B.3) provided a pseudo-pressure $\hat{p}$ is defined as (Panton, 2005)

$$\hat{p} \equiv p + \rho\dot{U}\mathbf{e}_x\cdot\hat{\mathbf{x}}, \tag{B.4}$$

so that the governing equations in the noninertial reference frame may be written as

$$\rho\left(\frac{\partial \mathbf{v}}{\partial \hat{t}} + \mathbf{v}\cdot\hat{\nabla}\mathbf{v}\right) = -\hat{\nabla}\hat{p} + \mu\hat{\nabla}^2\mathbf{v}, \tag{B.5}$$

$$\hat{\nabla}\cdot\mathbf{v} = 0. \tag{B.6}$$

With $\hat{\mathbf{T}} \equiv -\hat{p}\mathbf{1} + \mu\left(\hat{\nabla}\mathbf{v} + \hat{\nabla}\mathbf{v}^T\right)$, the right-hand side of (B.5) is $\hat{\nabla}\cdot\hat{\mathbf{T}}$. Moreover, with (B.4),

$$\hat{\mathbf{T}} = \mathbf{T} - \rho\dot{U}\mathbf{e}_x\cdot\hat{\mathbf{x}}. \tag{B.7}$$

Let

$$\hat{D}_2 \equiv -\int_{S_2}\mathbf{n}_2\cdot\hat{\mathbf{T}}\cdot\mathbf{e}_x dA. \tag{B.8}$$

With (3.8) and (B.7), (B.8) yields

$$\hat{D}_2 = D_2 + \int_{S_2}\rho\dot{U}\mathbf{e}_x\cdot\hat{\mathbf{x}}(\mathbf{n}_2\cdot\mathbf{e}_x)dA. \tag{B.9}$$

The fluid motion is subjected to the following boundary conditions:
On S_1,

$$\mathbf{n}_1\cdot\mathbf{v} = \hat{q}_1, \tag{B.10}$$

$$\mathbf{n}_1\cdot\hat{\mathbf{T}}\cdot\mathbf{t}_1^{(\alpha)} = \mathbf{n}_1\cdot\mathbf{T}\cdot\mathbf{t}_1^{(\alpha)} = 0, \qquad \text{for} \quad \mathbf{t}_1^{(\alpha)}\perp\mathbf{n}_1. \tag{B.11}$$

On S_2,

$$\mathbf{n}_2\cdot\mathbf{u} = q_2, \tag{B.12}$$

$$\mathbf{n}_2\cdot\hat{\mathbf{T}}\cdot\mathbf{t}_2^{(\alpha)} = \mathbf{n}_2\cdot\mathbf{T}\cdot\mathbf{t}_2^{(\alpha)} = 0, \qquad \text{for} \quad \mathbf{t}_2^{(\alpha)}\perp\mathbf{n}_2, \tag{B.13}$$

and thus both surfaces are taken as free surfaces. Taking the inner product of (B.5) with $\mathbf{v}$ and invoking (B.6), leads to the mechanical energy equation for the motion relative to the noninertial reference frame. That is, in integral form,

$$\frac{d\hat{E}}{d\hat{t}} = -\int_{S_1}\mathbf{n}_1\cdot\hat{\mathbf{T}}\cdot\mathbf{v}\ dA + \int_{S_2}\mathbf{n}_2\cdot\hat{\mathbf{T}}\cdot\mathbf{v}\ dA - \int_V 2\mu\hat{\mathbf{D}}[\mathbf{v}]:\hat{\mathbf{D}}[\mathbf{v}]\ d\mathcal{V}, \tag{B.14}$$

where,

$$\frac{d\hat{E}}{d\hat{t}} = \frac{d}{d\hat{t}}\int_V \rho\frac{|\mathbf{v}|^2}{2}\,d\mathcal{V} = \int_V \mathbf{v}\cdot\rho\left(\frac{\partial\mathbf{v}}{\partial\hat{t}} + \mathbf{v}\cdot\hat{\nabla}\mathbf{v}\right)d\mathcal{V}, \tag{B.15}$$

and $\hat{\mathbf{D}}[\mathbf{v}] = \frac{1}{2}\left(\hat{\nabla}\mathbf{v} + \hat{\nabla}\mathbf{v}^T\right)$.

With (B.3c) and (B.8), (B.11) and (B.13), (B.14) may be written as

$$\hat{D}_2 = \frac{1}{U}\left(\frac{d\hat{E}}{d\hat{t}} + \int_V 2\mu\hat{\mathbf{D}}[\mathbf{v}] : \hat{\mathbf{D}}[\mathbf{v}]\; d\mathcal{V} - \hat{W}\right), \tag{B.16}$$

where,

$$\hat{W} = -\int_{S_1}\mathbf{n}_1\cdot\hat{\mathbf{T}}\cdot\mathbf{n}_1\hat{q}_1\; dA + \int_{S_2}\mathbf{n}_2\cdot\hat{\mathbf{T}}\cdot\mathbf{n}_2 q_2\; dA. \tag{B.17}$$

Now, the integrals in the left-hand side of (B.16) are evaluated in potential flow, $\mathbf{v} = \hat{\nabla}\hat{\phi}$. Momentum balance (B.5) reduces to the Bernoulli equation for potential flow, i.e.

$$\frac{\hat{p}}{\rho} + \frac{\partial\hat{\phi}}{\partial\hat{t}} + \frac{|\mathbf{v}|^2}{2} = B(\hat{t}). \tag{B.18}$$

Then, (B.15) yields

$$\frac{d\hat{E}}{d\hat{t}} \;=\; -\int_{S_1}(-\hat{p})\hat{q}_1 dS + \int_{S_2}(-\hat{p})q_2 dS - U\int_{S_2}(-\hat{p})\mathbf{n}_2\cdot\mathbf{e}_x dS. \tag{B.19}$$

Denoting $\hat{\mathbf{D}} = \hat{\mathbf{D}}[\mathbf{v} = \nabla\hat{\phi}]$, the dissipation integral in (B.16) becomes

$$\begin{aligned}\int_V 2\mu\hat{\mathbf{D}} : \hat{\mathbf{D}}d\mathcal{V} =& -\int_{S_1}\mathbf{n}_1\cdot 2\mu\hat{\mathbf{D}}\cdot\mathbf{v}dA + \int_{S_2}\mathbf{n}_2\cdot 2\mu\hat{\mathbf{D}}\cdot\mathbf{v}dA \\ =& -\int_{S_1}\mathbf{n}_1\cdot 2\mu\hat{\mathbf{D}}\cdot\mathbf{n}_1\hat{q}_1 dA - \int_{S_1}\mathbf{n}_1\cdot 2\mu\hat{\mathbf{D}}\cdot\mathbf{t}_1^{(\alpha)}(\mathbf{t}_1^{(\alpha)}\cdot\mathbf{v})dA \\ & - U\int_{S_2}\mathbf{n}_2\cdot 2\mu\hat{\mathbf{D}}\cdot\mathbf{e}_x dA + \int_{S_2}\mathbf{n}_2\cdot 2\mu\hat{\mathbf{D}}\cdot\mathbf{n}_2 q_2 dA \\ & + \int_{S_2}\mathbf{n}_2\cdot 2\mu\hat{\mathbf{D}}\cdot\mathbf{t}_2^{(\alpha)}(\mathbf{t}_2^{(\alpha)}\cdot\mathbf{u})dA,\end{aligned} \tag{B.20}$$

using the relation $\mathbf{v} = \mathbf{u} - U\mathbf{e}_x$ and boundary conditions (B.10) and (B.12). Substitution of (B.19) and (B.20) into (B.16), with (B.17) given by potential flow, leads

to

$$\hat{D}_2 = -\int_{S_2} \left(-\hat{p} + \mathbf{n}_2 \cdot 2\mu\hat{\mathbf{D}} \cdot \mathbf{n}_2\right) \mathbf{n}_2 \cdot \mathbf{e}_x dA + \frac{1}{U}\int_{S_2} \mathbf{n}_2 \cdot 2\mu\hat{\mathbf{D}} \cdot \mathbf{t}_2^{(\alpha)} \left(\mathbf{t}_2^{(\alpha)} \cdot \mathbf{v}\right) dA$$
$$- \frac{1}{U}\int_{S_1} \mathbf{n}_1 \cdot 2\mu\hat{\mathbf{D}} \cdot \mathbf{t}_1^{(\alpha)} \left(\mathbf{t}_1^{(\alpha)} \cdot \mathbf{v}\right) dA. \tag{B.21}$$

Using (B.4) and (B.9), with $\mathbf{D} = \mathbf{D}[\mathbf{u}] = \hat{\mathbf{D}}[\mathbf{v}]$ from the transformation (B.3), expression (B.21) results in (3.34) that is given in §3.2.3.

Finally, expression (3.35) for $D_1 + D_2$ is obtained using the self-equilibration of irrotational viscous stresses. This implies,

$$\int_V \nabla \cdot 2\mu\mathbf{D} \cdot \mathbf{e}_x d\mathcal{V} = -\int_{S_1} \mathbf{n}_1 \cdot 2\mu\mathbf{D} \cdot \mathbf{e}_x dA + \int_{S_2} \mathbf{n}_2 \cdot 2\mu\mathbf{D} \cdot \mathbf{e}_x dA = 0, \tag{B.22}$$

which gives rise to the relation,

$$\int_{S_1} \mathbf{n}_1 \cdot 2\mu\mathbf{D} \cdot \mathbf{n}_1 (\mathbf{n}_1 \cdot \mathbf{e}_x) dA + \int_{S_1} \mathbf{n}_1 \cdot 2\mu\mathbf{D} \cdot \mathbf{t}_1^{(\alpha)} (\mathbf{t}_1^{(\alpha)} \cdot \mathbf{e}_x) dA =$$
$$\int_{S_2} \mathbf{n}_2 \cdot 2\mu\mathbf{D} \cdot \mathbf{n}_2 (\mathbf{n}_2 \cdot \mathbf{e}_x) dA + \int_{S_2} \mathbf{n}_2 \cdot 2\mu\mathbf{D} \cdot \mathbf{t}_2^{(\alpha)} (\mathbf{t}_2^{(\alpha)} \cdot \mathbf{e}_x) dA = 0. \tag{B.23}$$

The reason why *each* of the surface integrals in (B.22) vanishes is shown in Appendix C.

Appendix C

The net resultant of the viscous stress on a closed surface in potential flow*

Consider a closed surface S bounding a region V of incompressible Newtonian fluid in which the motion is irrotational. The deviatoric stress is given by $\boldsymbol{\tau} = 2\mu\nabla \otimes \nabla\phi$, where ϕ is the velocity potential that satisfies Laplace's equation in V, by continuity, and μ is the dynamic viscosity. Then, the divergence of $\boldsymbol{\tau}$ is zero in V. As a consequence, the statement "the traction vectors $\mathbf{n} \cdot \boldsymbol{\tau}$ have no net resultant on each and every closed surface in the domain V of flow"Joseph (2006) follows immediately, since

$$\int_D \nabla \cdot \boldsymbol{\tau} d\mathcal{V} = \int_\Gamma \mathbf{n} \cdot \boldsymbol{\tau} dA = 0, \tag{C.1}$$

by used of the divergence theorem, where D is an arbitrary volume in V with boundary Γ, and $\mathbf{n}$ is the outward normal unit vector to Γ. The surface integral in (C.1) represents the net irrotational viscous stress over Γ.

A proof of the above statement that the surface integral in (C.1) vanishes for every closed surface in the fluid domain is not obvious for a "periphractic" region. A three-dimensional region is periphractic "when it is bounded internally by one or more closed surfaces" (Milne-Thomson, 1968, p. 97). Thus, a periphractic region has one or more holes embedded in it, but no hole runs through the outer boundary, and thus the volume is simply connected.

*Appendix by R. Fosdick and J. C. Padrino, Department of Aerospace Engineering and Mechanics, University of Minnesota, Minneapolis, Minnesota 55455, USA.

Consider now a periphractic three-dimensional region bounded externally by a surface S enclosing a fluid volume V and one or more embedded holes. Suppose the fluid motion in V is irrotational. Consider a closed surface Γ immersed in V. This surface may surround a volume totally filled with fluid or there can be one or more holes enclosed by Γ. We wish to show that

$$\int_\Gamma \mathbf{n}\cdot\boldsymbol{\tau}dA = \int_\Gamma \mathbf{n}\cdot 2\mu\nabla\otimes\nabla\phi dA = 0\,. \tag{C.2}$$

Using Cartesian index notation, since $\tau_{ij} = 2\mu\phi_{,ij}$ and $\phi_{,ii} = 0$, where "," denotes partial differentiation with respect to the Cartesian coordinates indexed after it, we may write

$$\tau_{ij} = \varepsilon_{ikt}\varepsilon_{jrs}B_{rk,st}\ , \tag{C.3}$$

provided we take

$$B_{rk} \equiv -2\mu\delta_{rk}\phi\ , \tag{C.4}$$

where ε_{ijk} is the permutation symbol and δ_{ij} is the Kronecker delta. This follows by simple reduction of indices, since, with (C.4), (C.3) yields

$$\tau_{ij} = -2\mu\varepsilon_{ikt}\varepsilon_{jrs}\delta_{rk}\phi_{,st} = -2\mu\varepsilon_{ikt}\varepsilon_{jks}\phi_{,st} = -2\mu(\delta_{ts}\delta_{ij}-\delta_{tj}\delta_{is})\phi_{,st} = 2\mu\phi_{,ij}\,. \tag{C.5}$$

The form of (C.3) is known as a "Beltrami representation" of the stress (see §4 in the work of Fosdick and Royer-Carfagni, 2005). Note that τ_{ij} is symmetric provided B_{ij} is also symmetric. Now, with this representation and using Stokes' theorem, we have

$$\int_\Gamma n_i\tau_{ij}dA = \int_\Gamma n_i\varepsilon_{ikt}\varepsilon_{jrs}B_{rk,st}dA = 0 \tag{C.6}$$

for every closed surface Γ in V. Thus, (C.2) holds and the net viscous irrotational stress on any closed surface Γ in V is zero.

It is also true that, because of the Beltrami representation above, the moment of the irrotational viscous stress on every closed surface Γ in V about any fixed point (say, the origin of the coordinate system) is zero. That is,

$$\int_\Gamma \mathbf{x}\times(\mathbf{n}\cdot\boldsymbol{\tau})\,dA = 0\ , \tag{C.7}$$

or, in Cartesian index notation,

$$\int_{\Gamma} \varepsilon_{lmj} x_m n_i \tau_{ij} dA = 0\,. \tag{C.8}$$

By applying the divergence theorem, Joseph (2008) obtained (C.7) without using representation (C.3) for a region with no embedded holes.

Both balances together say that any closed surface Γ in V is "self-equilibrated". Results (C.2) and (C.7) apply, in particular, to the outer and inner boundaries of V.

Appendix D

Velocity potential coefficients

The expression for q_1 in (3.44) may be rewritten in terms of Legendre polynomials as

$$q_1 = \dot{R}_1 + \dot{\epsilon} P_1(z) - \frac{2}{3}\frac{\epsilon\dot{\epsilon}}{R_1}\left(1 - P_2(z)\right) + O(\epsilon^2), \tag{D.1}$$

where $z = \cos\theta$. Using (3.43) for the potential ϕ, expressions (3.49) for coefficients A_l and B_l, and (3.46) for $\mathbf{n}_1$, we can compute

$$\begin{aligned}
\mathbf{n}_1 \cdot \nabla\phi\big|_{S_1} \;=\; & -B_0 R_1^{-2} + 2\epsilon B_0 R_1^{-3} P_1(z) + \sum_{l=1}^{\infty}\left[lA_l^{(0)}R_1^{l-1} - (l+1)B_l^{(0)}R_1^{-l-2}\right]P_l(z) \\
& + \epsilon\sum_{l=1}^{\infty}\left[lA_l^{(1)}R_1^{l-1} - (l+1)B_l^{(1)}R_1^{-l-2}\right]P_l(z) \\
& + \epsilon\sum_{l=2}^{\infty}\left[(l-1)^2 A_{l-1}^{(0)}R_1^{l-3} + \{(l+1)^2 - 2\}B_{l-1}^{(0)}R_1^{-l-2}\right]\frac{l}{2l-1}P_l(z) \\
& + \epsilon\sum_{l=0}^{\infty}\left[(l^2-2)A_{l+1}^{(0)}R_1^{l-1} + (l+2)^2 B_{l+1}^{(0)}R_1^{-l-4}\right]\frac{l+1}{2l+3}P_l(z) \\
& + O(\epsilon^2).
\end{aligned} \tag{D.2}$$

Then, satisfying (3.44) with (D.1) and (D.2), applying orthogonality of Legendre polynomials and equating terms of alike powers of ϵ, gives rise to this set of relations

for the coefficients in (3.49):

$$-B_o R_1^{-2} = \dot{R}_1 \tag{D.3}$$

$$A_1^{(0)} - 2B_1^{(0)} R_1^{-3} = \dot{\epsilon} \tag{D.4}$$

$$2B_0 R_1^{-3} + A_1^{(1)} - 2B_1^{(1)} R_1^{-3} + \frac{2}{5}\left(-A_2^{(0)} + 9B_2^{(0)} R_1^{-5}\right) = 0 \tag{D.5}$$

$$2A_2^{(0)} R_1 - 3B_2^{(0)} R_1^{-4} = 0 \tag{D.6}$$

$$2A_2^{(1)} R_1 - 3B_2^{(1)} R_1^{-4} + \frac{2}{3}\left(A_1^{(0)} R_1^{-1} + 7B_1^{(0)} R_1^{-4}\right) + \frac{3}{7}\left(2A_3^{(0)} R_1 + 16B_3^{(0)} R_1^{-6}\right) = \frac{2}{3}\frac{\dot{\epsilon}}{R_1}, \tag{D.7}$$

and, for $l \geqslant 3$,

$$lA_l^{(0)} R_1^{l-1} - (l+1)B_l^{(0)} R_1^{-l-2} = 0 \tag{D.8}$$

$$lA_l^{(1)} R_1^{l-1} - (l+1)B_l^{(1)} R_1^{-l-2} + \left[(l-1)^2 A_{l-1}^{(0)} R_1^{l-3} + \{(l+1)^2 - 2\}B_{l-1}^{(0)} R_1^{-l-2}\right]\frac{l}{2l-1} + \left[(l^2-2)A_{l+1}^{(0)} R_1^{l-1} + (l+2)^2 B_{l+1}^{(0)} R_1^{-l-4}\right]\frac{l+1}{2l+3} = 0. \tag{D.9}$$

Furthermore, we recall (3.47) and (3.48),

$$B_0 = -R_2^2 \dot{R}_2 = -R_1^2 \dot{R}_1, \tag{3.47}$$

$$A_l l R_2^{l-1} = B_l (l+1) R_2^{-l-2} \quad \text{for} \quad l \geqslant 1, \tag{3.48}$$

respectively. Note that (D.3) is satisfied by (3.47).

From (D.6) and (D.8), using expression (3.48), we obtain $A_l^{(0)} = B_l^{(0)} = 0$ for $l \geqslant 2$. Then, using these results in (D.9), combined with (3.48), yields $A_l^{(1)} = B_l^{(1)} = 0$ for $l \geqslant 3$.

Next, the system (D.4)-(D.7) gives rise to expressions for $A_1^{(0)}$, $B_1^{(0)}$, $A_1^{(1)}$ and $B_1^{(1)}$. This leads to (3.50), and also to $A_2^{(1)}$ and $B_2^{(1)}$ after some algebra. That is, to first order in ϵ,

$$A_2 = -\frac{3\epsilon\dot{\epsilon} R_1^3 R_2^3}{2(R_2^3 - R_1^3)(R_2^5 - R_1^5)}, \qquad B_2 = -\frac{\epsilon\dot{\epsilon} R_1^3 R_2^8}{(R_2^3 - R_1^3)(R_2^5 - R_1^5)}. \tag{D.10}$$

Notice that, although $A_2 = B_2 = 0$ for $\epsilon = 0$, their time derivatives, needed in the unsteady Bernoulli equation, do not vanish, in general, at $\epsilon = 0$. However, it turns out that the $l = 2$ terms do not contribute at all to the forces on S_1 and S_2 in the $\mathbf{e}_x$-direction with $\epsilon = 0$ because of orthogonality of Legendre polynomials.

Appendix E

Integration formula

In the analysis presented in §4.3 and §4.4, the following formula is used,

$$\int_{\mathcal{S}} \big(B+\bar{B}\big)\big(C+\bar{C}\big)\mathrm{d}\mathcal{S} = 2\int_{\mathcal{S}} \mathrm{Re}\big[BC+B\bar{C}\big]\mathrm{d}\mathcal{S} = 2\,\mathrm{Re}\bigg[\int_{\mathcal{S}} \big(BC+B\bar{C}\big)\mathrm{d}\mathcal{S}\bigg], \quad \text{(E.1)}$$

where $\mathcal{S}$ denotes the region of integration and B and C are complex fields. The bar indicates complex conjugate and $\mathrm{Re}\,[\cdot]$ is a linear operator that returns the real part of a complex number.

Appendix F

Integrals of the mechanical energy equation

Performing the integrals in (5.36) gives rise to the following results:

$$\frac{d}{dt}\int_V \rho\frac{|\mathbf{u}|^2}{2}\mathrm{d}V = \sum_{\ell=0}^{\infty}\sum_{m=0}^{\ell} F_{\ell m} 4\pi a\rho \left(A_\ell e^{-\sigma_\ell t} + \bar{A}_\ell e^{-\bar{\sigma}_\ell t}\right) \left(-\sigma_\ell A_\ell e^{-\sigma_\ell t} - \bar{\sigma}_\ell \bar{A}_\ell e^{-\bar{\sigma}_\ell t}\right) \frac{\ell}{2\ell+1}\frac{(\ell+m)!}{(\ell-m)!}, \quad \text{(F.1)}$$

$$\int_{\mathcal{S}} \frac{\gamma}{a^2}(L^2-2)\zeta u_r \mathrm{d}\mathcal{S} = \sum_{\ell=0}^{\infty}\sum_{m=0}^{\ell} F_{\ell m} 4\pi \frac{\gamma}{a^2}\left(A_\ell e^{-\sigma_\ell t} + \bar{A}_\ell e^{-\bar{\sigma}_\ell t}\right) \left(-\frac{A_\ell}{\sigma_\ell}e^{-\sigma_\ell t} - \frac{\bar{A}_\ell}{\bar{\sigma}_\ell}e^{-\bar{\sigma}_\ell t}\right) \frac{(\ell+2)\ell^2(\ell-1)}{2\ell+1}\frac{(\ell+m)!}{(\ell-m)!}, \quad \text{(F.2)}$$

and

$$\int_{\mathcal{S}} \mathbf{n}\cdot 2\mu\mathbf{D}\cdot\mathbf{u}\mathrm{d}\mathcal{S} = \sum_{\ell=0}^{\infty}\sum_{m=0}^{\ell} F_{\ell m}\frac{8\pi\mu}{a}\left(A_\ell e^{-\sigma_\ell t} + \bar{A}_\ell e^{-\bar{\sigma}_\ell t}\right)^2 \ell(\ell-1)\frac{(\ell+m)!}{(\ell-m)!}, \quad \text{(F.3)}$$

where we have reckoned with standard formulae for integrals concerning spherical harmonics. $F_{\ell m}$ denotes real constants that follows from (5.11).

Appendix G

An analysis for maximum K^*

Here we look for the angular position on the surface of the sphere at which the maximum value of the cavitation number K occurs. This position is the most vulnerable to cavitation.

For the potential flow solution, the stress tensor is given in (6.36). Suppose that T_{11} is the maximum tensile stress such that $T_{11} \geq T_{33} \geq T_{22}$. If we consider the surface of the sphere $r = a$ and use the cavitation criterion $T_{11} + p_c = 0$, we obtain from (6.36)

$$K = \frac{9}{4}\sin^2\theta - 1 + \frac{3}{Re}\left(\cos\theta + \frac{2\sin\theta}{\sin 2\alpha}\right), \tag{G.1}$$

Considering the expression for α given in (6.32)

$$\tan 2\alpha = \frac{2}{3}\tan\theta, \tag{G.2}$$

we can write (G.1) as

$$K = \frac{9}{4}\sin^2\theta - 1 + \frac{3}{Re}\left[\cos\theta + 3\cos\theta\sqrt{1 + \frac{4}{9}\tan^2\theta}\right], \tag{G.3}$$

for $0 \leq \theta \leq \pi/2$, whereas

$$K = \frac{9}{4}\sin^2\theta - 1 + \frac{3}{Re}\left[\cos\theta - 3\cos\theta\sqrt{1 + \frac{4}{9}\tan^2\theta}\right], \tag{G.4}$$

*Prof. W. A. Sirignano, of the University of California, Irvine, contributed to this appendix.

for $\pi/2 < \theta \leq \pi$. Taking the derivative of K in (G.3), we find

$$\frac{\partial K}{\partial \theta} = \frac{9}{2}\sin\theta\cos\theta - \frac{3}{Re}\sin\theta\left[1 + \frac{5}{\sqrt{9+4\tan^2\theta}}\right]. \tag{G.5}$$

It is obvious that $\theta = 0$ is a solution of $\partial K/\partial\theta = 0$ at any Reynolds number. We compute $\partial^2 K/\partial\theta^2$ to determine whether K at $\theta = 0$ is a local maximum or minimum. From (G.5), the second derivative of K is

$$\frac{\partial^2 K}{\partial \theta^2} = \frac{9}{2}\cos 2\theta + \frac{60\sec\theta\tan^2\theta}{Re\,(9+4\tan^2\theta)^{3/2}} - \frac{\cos\theta}{Re}\left(3 + \frac{15}{\sqrt{9+4\tan^2\theta}}\right). \tag{G.6}$$

When $\theta = 0$, we have

$$\frac{\partial^2 K}{\partial \theta^2}(\theta = 0) = \frac{9}{2} - \frac{8}{Re}. \tag{G.7}$$

Thus $\partial^2 K/\partial\theta^2$ at $\theta = 0$ is negative when $Re < 16/9$ and positive when $Re > 16/9$. This result indicates that K at $\theta = 0$ is a local maximum when $Re < 16/9$ and is a local minimum when $Re > 16/9$. Substitution of $\theta = 0$ in (G.3) yields

$$K(\theta = 0) = \frac{12}{Re} - 1, \tag{G.8}$$

which is a local maximum of K for $Re < 16/9$ in the interval $0 \leq \theta \leq \pi/2$.

Besides $\theta = 0$, there is a second solution for $\partial K/\partial\theta = 0$ which depends on Re and has a very complicated expression. If the value of Re is very high, then $\partial K/\partial\theta \approx 9\sin(2\theta)/4$. The second solution is close to $\theta = \pi/2$. We also notice that $\partial^2 K/\partial\theta^2 < 0$ at $\theta = \pi/2$ when Re is high. Therefore, the maximum value of K occurs near $\theta = \pi/2$ when Re is high in the interval $0 \leq \theta \leq \pi/2$.

Similarly, from (G.4), K has a local maximum at $\theta = \pi$ when $Re < 4/9$ and has a local minimum at this position when $Re > 4/9$ in the interval $\pi/2 < \theta \leq \pi$. Substitution of $\theta = \pi$ into (G.4) gives this local maximum for $Re < 4/9$ in the interval $\pi/2 < \theta \leq \pi$,

$$K(\theta = \pi) = \frac{6}{Re} - 1. \tag{G.9}$$

A second solution, as a complicated function of Re, can be written for $\partial K/\partial\theta = 0$. For high Re, this solution gives that K goes to a maximum when θ approaches $\pi/2$.

A comparison of (G.8) and (G.9) allows us to discard the position $\theta = \pi$. Summarizing our findings for viscous potential flow, K reaches a maximum at $\theta = 0$ when $Re < 16/9$ in the interval of interest $0 \leq \theta \leq \pi$. In addition, in the limit of

high Re, K is maximum at $\theta = \pi/2$ in this interval. These results are verified in figures 6.9 (b) and 6.12 (b) for low Re and figures 6.11 (a) and 6.14 (a) for high Re.

For the Stokes flow solution, the stress tensor on the surface of the sphere is given in (6.24). With $T_{11} + p_c = 0$, we obtain

$$K = \frac{3}{2}(\cos\theta + \sin\theta). \tag{G.10}$$

The maximum K occurs at $\theta = \pi/4$ or $45°$. Thus $\theta = 45°$ is the location most vulnerable to cavitation on the surface of the sphere. This result is illustrated in figures 6.9 (a) and 6.12 (a) when $Re = 0.01$.

Appendix H

Validation of the numerical setup used in Chapter 6

The numerical strategy implemented in this work is validated by comparing our results with those from various publications collected by Johnson and Patel (1999). The evaluation is performed in terms of the drag coefficient and two relevant geometric parameters of the flow, namely, the separation angle θ_s and the separation length x_s as a function of the Reynolds number Re. The separation angle θ_s represents the angle, measured from the rear stagnation point, where the flow separates from the sphere. The separation length x_s represents the distance along the axis of symmetry, measured from the rear stagnation point, where the separated flow rejoins. These two parameters, the separation angle and length, are described in figure H.1. The drag coefficient is defined as:

$$C_D = \frac{F_{z'}}{\frac{1}{2}\rho U^2 \pi a^2} \tag{H.1}$$

where $F_{z'}$ represents the force that the fluid motion produces on the body in the streamwise direction.

The data considered in this study embraces the experimental results of Taneda (1956) and the numerical results of Pruppacher, Le Clair and Hamiliec (1970), Tomboulides (1993) and Magnaudet, Rivero and Fabre (1995). In addition, the results presented by Roos and Willmarth (1971) as well as the data owed to Johnson and Patel (1999) are included. Excellent agreement between our numerical values and the corresponding results from the literature is observed in figure H.2.

Once the velocity field has been determined from the numerical solution of the governing equations, the stream function and vorticity fields can be computed by

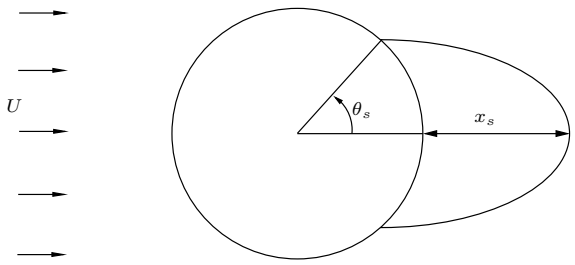

Figure H.1: Sketch showing two geometric parameters of the axisymmetric flow past a sphere: polar separation angle θ_s and separation length x_s.

the computational fluid dynamics package using the velocity components known at every node. The stream function is expressed in terms of the connection between conservation of mass and the definition of streamlines. Since a streamline is determined by a constant value of the stream function, the mass rate of flow between two streamlines is given by the difference of the stream function's values corresponding to these streamlines (Fluent 6.1 User's Guide, 2003). Figure H.3 presents the streamlines for streaming flow past a sphere for $Re = 0.01$, 10 and 100. For the former case, the classic symmetric pattern with respect to the equator of the sphere ($\theta = \pi/2$) is observed. As Re increases, this symmetry disappears and the separation of the laminar boundary layer for $Re = 10$ is about to occur (Johnson and Patel, 1999). For $Re = 100$, separation has taken place and a well defined stable axisymmetric recirculation region is formed behind the sphere. For $Re = 0.01$, 10 and 100, the vorticity contours $\omega a/U$ are presented in figure H.4. For the lower Re, the diffusion of vorticity prevails and the levels of vorticity show symmetry with respect to the axis $\theta = \pi/2$. For $Re = 10$ and $Re = 100$ the vorticity is convected by the fluid motion.

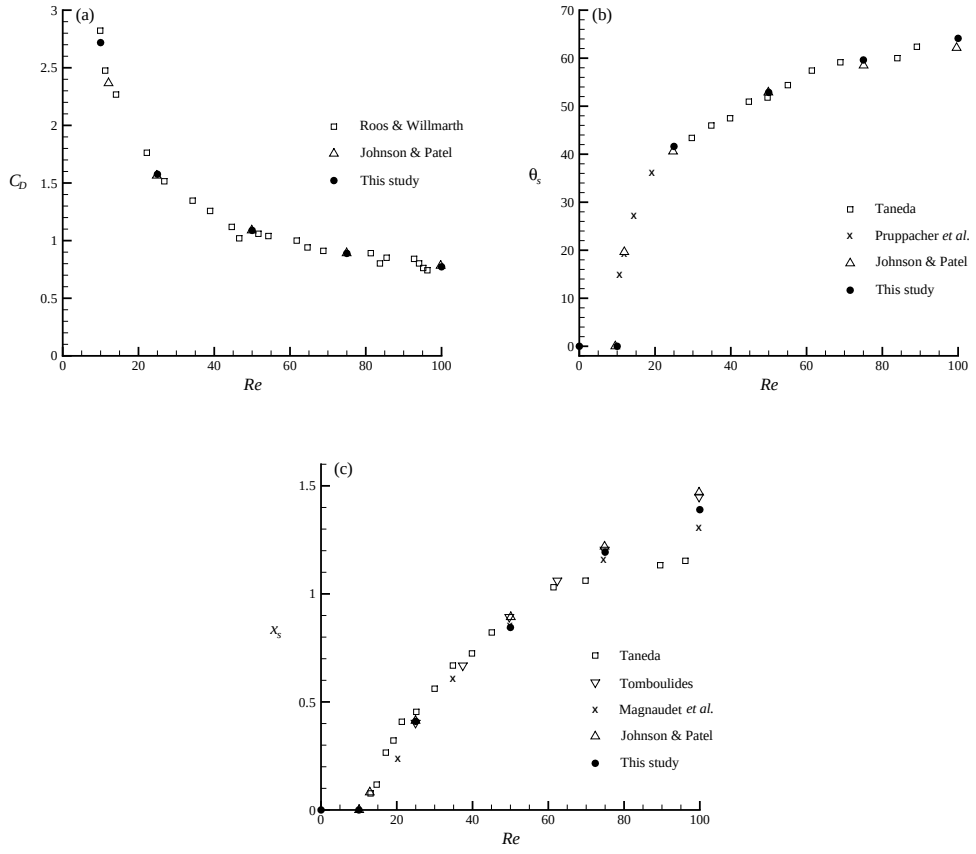

Figure H.2: Comparison between the numerical results from this study with data from the literature: (a) Drag coefficient C_D; (b) polar separation angle θ_s (is zero at the rear stagnation point), and (c) separation length x_s versus Re. All the data from previous works is extracted from the paper of Johnson and Patel (1999).

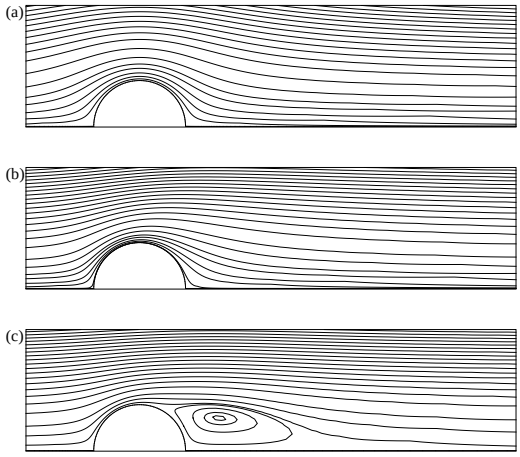

Figure H.3: Streamline pattern ψ/aU^2 for streaming flow past a sphere from the numerical solution for various Reynolds numbers; (a) $Re = 0.01$, (b) $Re = 10$, (c) $Re = 100$. The streamline $\psi = 0$ corresponds to the axis of symmetry and the sphere's surface.

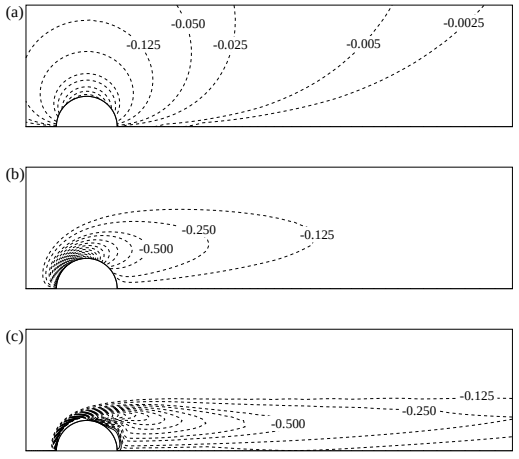

Figure H.4: Vorticity contours $\omega a/U$ for various Re from the numerical solution. (a) $Re = 0.01$, (b) $Re = 10$, (c) $Re = 100$. The solid lines (for $Re = 100$) represent contours of positive vorticity.

Appendix I

Copyright permission

Part of the material presented in Chapters 2, 4, 5 and 6 of this work is reprinted with permission from Joseph, D. D.; Funada, T.; Wang, J. *Potential flows of viscous and viscoelastic fluids.* Cambridge University Press, 2007. Copyright Daniel Joseph, Toshio Funada, Jing Wang 2008. (Padrino, J.C. is author in Sections 12.7, 14.2, 14.3, 17.1, 17.3, 18.3, 22.2 and 22.3 of this book).

According to the copyright policies of Cambridge University Press cited below, I have permission from this publisher to include material of which I am the author, and contained in the sections mentioned above, as part of my PhD dissertation submitted to the University of Minnesota.

From http://www.cambridge.org/us/information/rights/authors.htm.

Permissions request from authors:

In certain circumstances, permission requests are not required from authors, who wish to reuse original material they have written for a Cambridge publication, provided that the subsequent use includes a full acknowledgement of the original publication together with the copyright notice and the phrase 'Reprinted with permission'. Permission requests are waived if:

- The author wishes to reproduce a single chapter (not exceeding 20% of his/her work), journal article or shorter extract in a subsequent work (i.e. with a later publication date) of which he or she is to be the author, co-author or editor.
- The author wishes to photocopy a single chapter (not exceeding 20% of his/her work as a whole), journal article or shorter extract for his/her own teaching purposes, provided that such photocopies are not made available for sale.
- The author wishes to reproduce a single chapter (not exceeding 20% of his/her work as a whole), journal article or shorter extract on his/her personal or institution web site for teaching and research purposes.